Dissertation

submitted to the

Combined Faculty of Mathematics, Engineering, and Natural Sciences

of Heidelberg University, Germany

for the degree of

Doctor of Natural Sciences

Put forward by

Sven Fabian

born in Neustadt am Rübenberge, Germany

Oral examination: 31.10.2024

Dark Matter models in light of Effective Field Theories, the Baryon Asymmetry, and Neutrino Properties

1st Referee: Dr. Florian Goertz

2nd Referee: Prof. Dr. Joerg Jaeckel

Contents

List of Figures

iii

List of Tables

List of Publications

The results of my independent studies presented in this thesis are based on the following articles that were published in peer-reviewed journals (or are available as preprints at the time of submission) during my doctoral studies or are in preparation. In addition, information about my contributions to the individual projects is provided.

(1) **Dark matter and nature of electroweak phase transition with an inert doublet** [1]

Using the results from my Master's thesis [2], I contributed to this project by performing the numerical computation of the DM relic abundance and the annihilation cross sections. Furthermore, I investigated the characteristics of the EWPhT by deploying a self-developed (software) code.

(2) **Minimal Inert Doublet benchmark for dark matter and the baryon asymmetry** [3]

My contribution encompasses the generation of the model files and the numerical computation of the DM relic abundance, the annihilation cross sections, and the DM direct-detection cross sections. Moreover, I created the final results for the baryon asymmetry and calculated the lepton electric dipole moments presented in the appendices. In addition to that, I derived the expressions for the relevant operators for DM annihilation as well as the UV realizations in the appendices.

(3) **Flavor-Specific Dark Matter Signatures through the Lens of Neutrino Oscillations** [4]

My contributions include the calculation of the branching ratios and mean number of leptons in both models, the generation of the model file, and the numerical computation of the DM relic abundance, the calculation of the DM direct detection cross section, and lastly the results for the collider analysis (with the cross sections provided by a co-author).

(4) **Dark Particles at the LHC: LHC-Friendly Dark Matter Characterization via Non-Linear EFT**

Besides the analytical analysis of the UV models, including their theoretical and experimental constraints, I contributed so far to the numerical calculation of the DM relic abundance and conducted the computation of the collider cross sections. The paper is in preparation.

Bibliography

[1] S. Fabian, F. Goertz and Y. Jiang, *Dark matter and nature of electroweak phase transition with an inert doublet*, *JCAP* **09** (2021) 011 [2012.12847].

[2] S. Fabian, *Study of the inert doublet model in the light of dark matter physics and electroweak phase transition*, 2020.

[3] M.D. Astros, S. Fabian and F. Goertz, *Minimal Inert Doublet benchmark for dark matter and the baryon asymmetry*, *JCAP* **02** (2024) 052 [2307.01270].

[4] S. Bhattacharya, S. Fabian, J. Herms and S. Jana, *Flavor-Specific Dark Matter Signatures through the Lens of Neutrino Oscillations*, [2407.09614].

Acknowledgements

First and foremost, I would like to thank my PhD advisor Dr. Florian Goertz for the opportunity to continue my studies and research with him after my Master's thesis. The past few years allowed me to embrace the chance to dive into several different topics in high-energy physics for my research and gained insights into different research fields. Moreover, I'm very grateful to him for encouraging and supporting me in participating in conferences, workshops, and schools and presenting my work in multiple occasions.

Among many delightful events like the group's own workshop 'New Physics Directions in the LHC era and beyond', the workshop 'CP2023' was one of the highlights. Its wealth of inspiring and further motivating discussions about theoretical and experimental aspects of high-energy physics and great meetings in a fantastic environment render this workshop an awesome event with many new insights.

Another highlight of my doctoral studies was my research trip to Messina (Sicily) with the goal to advance the project with Dr. Giorgio Arcadi and David Cabo Almeida. Besides the great collaboration, I enjoyed the time at Messina University for the terrific atmosphere in the research groups with its dazzling social energy. I would like to thank the entire division at Messina University for the wonderful stay that I will never forget.

Furthermore, I'm grateful for delightful and inspiring conversations about a broad range of topics with many speakers and co-organizers during the Heidelberg Graduate Days either after the courses or during the speakers' dinners. They offered me valuable insights into various aspects of research and scientific outreach. Talking of scientific outreach, I would like to thank Dr. Florian Goertz and the public relations team at MPIK (in particular Dr. Renate Hubele) for the opportunity to offer the high energy physics-themed 'Escape Room' for students which was fun for everyone, sparked interest in this field, and triggered many great questions about the topic itself and research in general. In line of this, I'm also grateful to the students who attended my tutorials at the University and enriched them by smart questions and enlightening discussions.

Talking of discussions, I would like to thank many colleagues of mine for taking the time to clarify aspects in projects and to think together about various topics in

ACKNOWLEDGEMENTS

Summary

This thesis addresses several observations in nature that cannot be explained by the Standard Model of particle physics. The overarching topic is the theoretical description of dark matter (DM) which constitutes the framework for two further conundrums: the baryon asymmetry of the Universe and neutrino masses. In the context of effective field theories (EFTs) we first compare an extended DM EFT to UV theories and investigate its range of validity. Making use of the power of EFTs in the next chapter, we augment the Inert Doublet Model by a CP-violating effective operator which can thereby explain the imbalance between matter and antimatter in the Universe and simultaneously account for DM while eluding constraints from electron electric dipole moment searches and DM direct detection. We further discuss possible UV realizations of the effective operators. Lastly, we turn to the unknown origin of neutrino masses and connect this puzzle to DM via the analysis of potential DM indirect detection signals as well as of collider signatures that offer insights into the free neutrino oscillation parameters and the neutrino mass hierarchy. We find potential for synergies between the different experimental approaches to determine neutrino properties.

Zusammenfassung

Diese Thesis behandelt mehrere Beobachtungen in der Natur, die nicht mit dem Standardmodell der Teilchenphysik erklärt werden können. Das übergeordnete Thema ist die theoretische Beschreibung der Dunklen Materie (DM), welches den Rahmen für zwei weitere Rätsel bildet: die Baryonasymmetry im Universum und Neutrinomassen. Im Kontext der effektiven Feldtheorien (EFTs) stellen wir eine 'erweiterte DM EFT' UV-Theorien gegenüber und untersuchen ihren Gültigkeitsbereich. Das Potenzial der EFTs nutzend, erweitern wir anschließend das 'Inertes Dublett'-Modell um einem CP-verletzenden effektiven Operator, welches dadurch das Ungleichgewicht zwischen Materie und Antimaterie sowie die Existenz von DM erklären kann, während Experimente zum elektrischen Dipolmoments des Elektrons und zur DM-Streuung die Theorie nicht ausschließen. Des Weiteren diskutieren wir mögliche UV-Realisierungen der effektiven Operatoren. Zum Schluss widmen wir uns dem Ursprung der Neutrinomassen und verbinden dieses Rätsel mit der Analyse von indirekten Suchen nach DM sowie Teilchenbeschleunigersignaturen, die Auskunft über Oszillationsparameter und die Massenhierarchie von Neutrinos geben können. Wir finden die Möglichkeit für Synergien zwischen den verschiedenen experimentellen Herangehensweisen zur Bestimmung der Neutrinoeigenschaften.

Chapter 1

The Standard Model and its shortcomings

This chapter aims at providing a coarse overview of the building blocks of the Standard Model of particle physics (SM) and motivating the examinations of SM extensions which shall be presented in the next chapters. For a comprehensive summary of the various aspects, phenomenological discussions, and the rigorous mathematical formulation, the reader is referred to Refs. [5–10].

One cornerstone of the SM is the concept of symmetries and the description of the strong, weak, and electromagnetic forces by the exchange of spin-1 mediators. These mediators arise from local (*i.e.* gauge) symmetries which form the underlying symmetry group of the SM. With Emmy Noether's proof of a conserved current and charge associated with every continuous symmetry of the action of the theory [11], the concept of symmetries became even more appealing in theoretical particle physics. The symmetry group of the SM is

$$\mathcal{G}_{\mathrm{SM}} = SU(3)_c \times SU(2)_L \times U(1)_Y \tag{1.1}$$

and is associated with Quantum Chromodynamics (QCD) and the electroweak (EW) sector. A unitary gauge group $U(N)$ features N^2 generators, whereas a special unitary group $SU(N)$ has $N^2 - 1$ generators. The SM $U(1)_Y$ is an abelian group. In general, the generators of the symmetry groups are associated with *massless* gauge bosons.

The symmetry group manifests itself today in $SU(3)_c \times U(1)_Q$ and describes eight gluons as the gauge fields of QCD and one photon for Quantum Electrodynamics (QED). Both theories are described well by massless mediators, whereas the weak interactions are mediated by massive particles and therefore short-ranged. To reconcile the fact of

1

massive force mediators for the weak interactions with the descriptions via gauge symmetries, the EW theory was proposed by Glashow [12], Salam [13], and Weinberg [14] (hence known as the GSW theory) which evolves spontaneously via electroweak symmetry breaking (EWSB) to the present gauge symmetry group $SU(3)_c \times U(1)_Q$.[1] With the particles and interactions observed in experiments and the SM gauge symmetry, one can find proper representations of these fields with respect to the SM gauge group $\mathcal{G}_{SM}$. We shall specify the representations below when needed. The renormalizable operators of the Lagrangian are prescribed by the gauge and Lorentz symmetries and the Lagrangian can be categorized into different sectors, reading

$$\mathcal{L}_{SM} = \mathcal{L}_{gauge} + \mathcal{L}_{Dirac} + \mathcal{L}_{Yukawa} + \mathcal{L}_{Higgs} \,. \tag{1.2}$$

Beginning with the first part, the gauge sector describes the dynamics (including potential self-interactions) of the gauge fields which transform under the adjoint representation of the respective gauge group. Defining the field strength tensor for the abelian symmetry group $U(1)_Y$,

$$B_{\mu\nu} = \partial_\mu B_\nu - \partial_\nu B_\mu \,, \tag{1.3}$$

and for the non-abelian group $SU(2)_L$,

$$W_{\mu\nu}^I = \partial_\mu W_\nu^I - \partial_\nu W_\mu^I + g\varepsilon^{IJK} W_\mu^J W_\nu^K \tag{1.4}$$

with the indices $I, J, K = 1, 2, 3$, the gauge coupling parameter g, and the Levi-Civita tensor ε^{IJK} as the structure function (similar for $SU(3)_c$ with the field strength tensors $G_{\mu\nu}^a$, the color index $a = 1, \ldots, 8$, and the structure function f^{abc}), the Lagrangian of the SM gauge sector reads

$$\mathcal{L}_{gauge} = -\frac{1}{4} G_{\mu\nu}^a G^{a\mu\nu} - \frac{1}{4} W_{\mu\nu}^I W^{I\mu\nu} - \frac{1}{4} B_{\mu\nu} B^{\mu\nu} \,. \tag{1.5}$$

A notable difference between the abelian and non-abelian symmetry groups is the presence of self-interactions of gauge fields in non-abelian symmetry groups. Neither Lorentz nor gauge symmetries prohibit the CP-violating operators $V_{\mu\nu}^i \widetilde{V}^{i\mu\nu}$ with the gauge field strength tensors $V_{\mu\nu}^i$ and their duals $\widetilde{V}^{i\mu\nu} \equiv V_{\alpha\beta}^i \varepsilon^{\mu\nu\alpha\beta}/2$. As stated in Ref. [15] and discussed below in Section 4.1, the operator for the abelian gauge fields vanishes and the renormalizable operator with the $SU(2)_L$ gauge field strength tensors

---

[1]Note that the former symmetry is rather *hidden* than broken.

can be eliminated by making use of the anomalous global $U(1)_{B+L}$ symmetry of the SM [16–18]. The QCD θ-term, on the other hand, can be present and shall be discussed below in the list of shortcomings.

Moving on to the second sector of the SM, the dynamics of the fermions are described, in particular their interactions with the gauge fields. Omitting the indices for generation, color, and flavor, the Lagrangian reads

$$\mathcal{L}_{\text{Dirac}} = \overline{Q}i\slashed{D}Q + \overline{L}i\slashed{D}L + \overline{u_R}i\slashed{D}u_R + \overline{d_R}i\slashed{D}d_R + \overline{\ell_R}i\slashed{D}\ell_R \tag{1.6}$$

with the short-hand notation $\slashed{D} \equiv \gamma^\mu D_\mu$ for the product of Dirac matrices γ^μ and the gauge covariant derivative D_μ (see below). Its building blocks are the left-handed (LH) Dirac fermion fields Q, L and the right-handed (RH) fields u_R, d_R, e_R which transform as doublets and singlets, respectively, upon an $SU(2)_L$ gauge transformation. The isospin doublets are given by $Q : (\mathbf{3}, \mathbf{2}, 1/3)$ and $L : (\mathbf{1}, \mathbf{2}, -1)$, while the singlets are $\ell_R : (\mathbf{1}, \mathbf{1}, -2)$, $u_R : (\mathbf{3}, \mathbf{1}, 4/3)$, and $d_R : (\mathbf{3}, \mathbf{1}, -2/3)$. For instance, the first generation of leptons is embedded in $L_1 = (\nu_e, e^-)^T$ and the second generation of quarks in $Q_2 = (c, s)^T$. In the present work we shall work with the gauge covariant derivative

$$D_\mu = \partial_\mu - ig_s \frac{\lambda^a}{2} G_\mu^a - ig \frac{\sigma^I}{2} W_\mu^I - ig' \frac{Y}{2} B_\mu. \tag{1.7}$$

The generators of $SU(3)_c$ are related to the Gell-Mann matrices λ^a which obey the commutation relation $[\lambda^a, \lambda^b] = 2if^{abc}\lambda^c$. For $SU(2)_L$ the generators are proportional to the Pauli matrices σ^I, satisfying $[\sigma^I, \sigma^J] = 2i\varepsilon^{IJK}\sigma^K$. As seen above, the structure function for the abelian symmetry group $U(1)_Y$ is zero, preventing the gauge field of an abelian symmetry group from interacting with other gauge fields of the same symmetry group. The gauge fields B_μ, $W_\mu^{(3)}$ in the weak eigenbasis do not equal the corresponding mass eigenstates. After EWSB the gauge fields in the mass eigenbasis read

$$\begin{pmatrix} A_\mu \\ Z_\mu \end{pmatrix} = \begin{pmatrix} \cos\theta_W & \sin\theta_W \\ -\sin\theta_W & \cos\theta_W \end{pmatrix} \begin{pmatrix} B_\mu \\ W_\mu^{(3)} \end{pmatrix}. \tag{1.8}$$

The weak mixing angle θ_W which governs the rotation of the gauge fields is related to the elementary electric charge via $e = g\sin\theta_W = g'\cos\theta_W$ with the $SU(2)_L \times U(1)_Y$ gauge coupling parameters g, g'. With the electric charge Q, the third component T_3 of the weak isospin, and the weak hypercharge Y, we shall use the convention $Q = T_3 + Y/2$ throughout this thesis.

The third part of the SM Lagrangian connects the fermions to the Higgs field which shall be defined below in Eq. (1.11). Besides describing the Yukawa interactions between the scalar Higgs boson and the fermions, it serves as the sector in which the fermion masses are generated via EWSB. The Yukawa Lagrangian reads

$$\mathcal{L}_{\text{Yukawa}} = - \left(y_{ij}^d \overline{Q_i} \Phi d_{j,R} + y_{ij}^u \overline{Q_i} \widetilde{\Phi} u_{j,R} + y_{ij}^\ell \overline{L_i} \Phi \ell_{j,R} + \text{h.c.} \right) \tag{1.9}$$

with the 3×3 Yukawa matrices with the generation indices $i, j = 1, 2, 3$.[2] One can show that the Yukawa matrices are generally complex for more than two fermion generations as the phases can be absorbed via proper field redefinitions. The three Yukawa matrices can be diagonalized via $U(3)$ rotations of the fermion fields, with the consequence that the mass eigenstates of one of the quark types (either up- or down-type quarks) are not any longer identical to their weak eigenstates. The rotations are dictated by the Cabibbo–Kobayashi–Maskawa (CKM) matrix for that type of quarks.

The last part of the Lagrangian that shall be relevant for this thesis is the scalar sector which is described by

$$\mathcal{L}_{\text{Higgs}} = (D_\mu \Phi)^\dagger (D^\mu \Phi) - \mu^2 |\Phi|^2 - \lambda |\Phi|^4 \tag{1.10}$$

with the Higgs doublet

$$\Phi = \frac{1}{\sqrt{2}} \begin{pmatrix} \sqrt{2} G^+ \\ v + h + i G^0 \end{pmatrix} \tag{1.11}$$

and its dual $\widetilde{\Phi} \equiv i\sigma^2 \Phi^*$ which occurs also in the Yukawa sector. The potential in Eq. (1.10) with a negative bare mass term leads to a ground state at finite field value. This vacuum expectation value (vev) v is given in neutral component of the doublet, alongside the physical Higgs boson h. According to the Goldstone theorem [19], the spontaneous EWSB of the SM gauge group to $SU(3)_c \times U(1)_Q$ via the electroweak phase transition (EWPhT) breaks three generators and hence gives rise to three Goldstone bosons. These Goldstones, which are $G^\pm$ and G^0 from the Higgs doublet in Eq. (1.11), become the longitudinal components of the EW gauge bosons and thus give rise to the masses of $W^\pm$ and Z bosons. This mechanism was proposed almost simultaneously by independent groups and is sometimes referred to as the Brout–Englert–Higgs mechanism [20–23]. Following the widespread terminology in the literature, we refer to

---

[2]The Yukawa sector breaks the accidental, global symmetry $U(3)^5 \equiv U(3)_Q \times U(3)_L \times U(3)_{u_R} \times U(3)_{d_R} \times U(3)_{e_R}$.

this mass-generating mechanism and the doublet as the 'Higgs mechanism' and 'Higgs doublet' in this thesis.

The kinetic term in the Lagrangian of the scalar sector above in Eq. (1.10) describes the interactions between the EW gauge bosons and the Higgs field which result in their masses after EWSB. One finds

$$\mathcal{L}_{\text{Higgs}} \supset -\frac{g^2 v^2}{4} W_\mu^+ W^{-\mu} - \frac{(g^2 + g'^2) v^2}{8} Z_\mu Z^\mu - \frac{(g' \cos\theta_W - g\sin\theta_W)\, v^2}{8} A_\mu A^\mu \,, \tag{1.12}$$

which leads to the tree-level EW gauge boson masses

$$m_W = \frac{gv}{2} \quad, \quad m_Z = \frac{\sqrt{g^2 + g'^2}\,v}{2} \quad, \quad m_A = 0\,. \tag{1.13}$$

The properties of the Higgs multiplet and the interactions of the physical Higgs boson are of utmost importance for the understanding of the fundamental mechanism behind the mass generation of the fermions and of the EW gauge bosons.

The characteristic feature of the Higgs potential at (virtually) zero temperature today is the negative mass parameter μ^2. The resulting non-zero Higgs vev determined as $v = (\sqrt{2}G_F)^{-1/2} \approx 246\,\text{GeV}$ with Fermi's constant G_F is known remarkably precisely and allows, together with the measured mass $m_h = 125.25 \pm 0.17\,\text{GeV}$ of the Higgs boson, to infer the Higgs mass parameter $|\mu| \approx 88.4\,\text{GeV}$ and the Higgs self-coupling parameter $\lambda = m_h^2/(2v^2) \approx 0.13$ [10]. The latter is of great interest as it is – in principle – accessible via the measurement of Higgs self-interactions and indicates directly whether the SM scalar sector describes nature accurately or whether physics beyond the SM (BSM) is at work. On the downside, the accuracy level of dedicated measurements are to date far too low to draw conclusions. Working in the κ-framework in which the SM prediction corresponds to $\kappa_\lambda = 1$, the results by the ATLAS [24] and CMS [25] collaborations at 95% C.L. read

$$-1.2 \lesssim \kappa_\lambda \lesssim 6.5 \quad, \quad -1.4 < \kappa_\lambda < 6.1\,. \tag{1.14}$$

Another interesting property of the Higgs boson is its decay width as it tells whether it decays into sufficiently light BSM fields. The ATLAS [26] and CMS [27] results are

$$\Gamma_h = \begin{cases} 4.5^{+3.3}_{-2.5}\,\text{MeV} & \text{for ATLAS} \\ 3.2^{+2.4}_{-1.7}\,\text{MeV} & \text{for CMS} \end{cases} \tag{1.15}$$

and hence in agreement with the SM prediction $\Gamma_h^{\mathrm{SM}} = 4.1\,\mathrm{MeV}$ [28]. As for the measurement of the Higgs self-coupling λ, an improvement of accuracy in Γ_h could eventually result in evidence for a connection between the Higgs sector and BSM physics.

So far the SM has demonstrated its power in an overwhelmingly large fraction of experiments and experimental anomalies perished with more statistics or improved analyses (see, *e.g.*, Refs. [29–33] for the $750\,\mathrm{GeV}$ diphoton excess and Refs. [34–36] for the $R_{K^{(*)}}$ anomaly).[3] However, the SM falls in fact short in explaining some observations or theoretical curiosities which either suggest or clearly indicate BSM physics. Besides the rather large number of free model parameters, the hierarchical ordering of the fermion masses or the stark difference between the measured Higgs mass and the Planck scale $M_{\mathrm{Pl}} \sim \mathcal{O}(10^{19}\,\mathrm{GeV})$ – just to mention two prime examples for mysterious hierarchies in the SM – lead to the expectation of yet-to-unveil BSM physics. Further curiosities are the mere number of fermion generations, which appear to be copies of each other (except for their masses), and the same number of generations of quarks and leptons. A brief overview of further puzzles within the SM is following.

Strong CP problem

Besides the field strength operators listed in Eq. (1.5), the QCD θ-term can exhibit physical consequences and reads

$$\mathcal{L}_{\theta\text{-QCD}} = \theta \frac{g_s^2}{32\pi^2} G_{\mu\nu}^a \widetilde{G}^{a\mu\nu} \,. \tag{1.16}$$

Since this operator violates the CP symmetry, an enhanced electric dipole moment of the neutron (nEDM) is expected which might be much larger than the SM prediction $|d_n/e| \sim 10^{-34}\,\mathrm{cm}$ [52–54], although it might receive significant QCD contributions, as pointed out in Ref. [55]. A dedicated measurement conducted at Paul Scherrer Institute (PSI) finds for the nEDM $d_n/e = (0.0 \pm 1.1_{\mathrm{stat}} \pm 0.2_{\mathrm{sys}}) \times 10^{-26}\,\mathrm{cm}$, which is suggested to be interpreted as the upper bound $|d_n/e| < 1.8 \times 10^{-26}\,\mathrm{cm}$ at 90% C.L. [56]. Defining the parameter $\bar{\theta} \propto \theta + \arg\det M$ with the quark mass matrix M (*cf.* Eq. (2.18) for the definition), the CP-violating parameter can consequently be constrained to $|\bar{\theta}| \lesssim 10^{-10}$ [57]. Although the proposal of the axion which results in the perfect cancellation of the tiny parameter is intriguing, the answer to this conundrum remains elusive to date. See, *e.g.*, Refs. [18, 57–59] for reviews.

---

[3]Note that the prominent $R_{D^{(*)}}$ anomaly for the charged-current decay $B \to D^{(*)}\ell\bar{\nu}$ tended towards the SM prediction in the recent years, but still exhibits a 3.3σ deviation with respect to the SM prediction and thus poses a possible window for new physics (see Refs. [36–51]).

Neutrino masses

The observation of neutrino flavor oscillation cannot be explained within the SM framework and is clear evidence for BSM physics. There is a plethora of proposals for neutrino mass-generating mechanisms but the fundamental theory for neutrino masses as well as the nature of the neutrino itself (whether it is a Dirac or Majorana particle) is still inconclusive for the lack of clear experimental indications. An introduction to neutrino oscillations as well as an overview of neutrino mass models can be found in Chapter 5 where two specific neutrino mass models shall be investigated.

Baryon asymmetry of the Universe

Furthermore, the obvious imbalance between the amount of ordinary matter and anti-matter in the (visible) Universe serves as a further indication for BSM physics. As we shall examine in detail in Chapter 4, the SM does not fulfil the necessary conditions for generating the baryon asymmetry of the Universe. Although the violation of the CP symmetry, experimentally confirmed in, *e.g.*, K- and B-meson decays, is explained by the complex phase in the CKM matrix, its magnitude is not large enough to explain the excess of ordinary matter. Moreover, the out-of-equilibrium condition during the EWPhT is not given in the SM. In principle, the SM provides the ingredients, but falls short in fulfilling them to a sufficient amount. An extension of the SM for generating the measured baryon asymmetry of the Universe shall be elaborated on in the last section of Chapter 4.

Dark matter

As the last shortcoming of the SM focused on in this thesis, we shall discuss the experimental evidence for the still-unknown type of matter which we shall refer to as dark matter (DM). Besides its gravitational effects in weak-lensing observations, we know from experiments that this new type of matter does effectively not interact via the electromagnetic and strong force. Furthermore, the DM must be stable on cosmological time scales. The SM does not feature an appropriate candidate which can account for the entire amount of DM. More details shall be presented in the next chapter, including prominent DM candidates and detection methods.

Chapter 2

Introduction to Dark Matter

As pointed out in the previous section, the SM is a very successful theory but fails in numerous aspects. In this section we want to delve into one of these, namely DM. After discussing the various observations which all lead to the conclusion of the existence of DM, we provide a broad overview of DM models and detection strategies.

2.1 Experimental Evidence

The experimental evidence for the existence of DM spans a wide range of length scales (see, *e.g.*, Refs. [60, 61] for reviews) which we shall briefly summarize in the following.

Evidence at galactic scale

The measurements of the circular velocities of the stars and gas of a galaxy for different radii allow to compare the rotation curves to the expectations from Newtonian dynamics, namely

$$v\left(r\right) = \sqrt{\frac{G_N M\left(r\right)}{r}} \tag{2.1}$$

with Newton's constant G_N as well as the mass $M(r) = \int \mathrm{d}^3 r\, \rho(r)$ of the sphere with radius r and mass density $\rho(r)$, and feature a stark discrepancy for large radii. This disagreement between prediction and observation strongly suggests the presence of a new kind of matter which cannot be observed through optical telescopes and whose mass density profile must be $\rho_{\mathrm{DM}}(r) \propto r^{-2}$ for large radii to reproduce a flat velocity distribution (see Fig. 2.1) [60]. An historical overview of this field's development can be found in Ref. [62] for instance.

A spherically symmetric DM halo encompassing the galactic disk with the density $\rho_{\mathrm{DM}}(r) \propto r^{-2}$ for large radii ameliorates the problem. However, the density profile of the inner part of the galaxy is inconclusive and known as the *core-cusp problem*, based on the difference between some observations suggesting a rather radius-independent DM density at the center and N-body simulations finding a cuspy profile (see Ref. [63] for a review).

Further evidence for the existence of DM from galactic-scale measurements comes from the Oort discrepancy which refers to the discrepancy between the amount of stars in the Milky Way and the induced gravitational potential (see Refs. [60, 64] for details).

Evidence at galaxy cluster scale

Another indication for the existence is the study of galaxy clusters and the application of the Virial theorem. Following the investigation conducted by Zwicky in 1937 [65], the Virial theorem is based on the fundamental law of motion for a galaxy labelled by the index i in the cluster,

$$\mathbf{F}_i = m_i \frac{\mathrm{d}^2 \mathbf{r}_i}{\mathrm{d}t^2} \,, \tag{2.2}$$
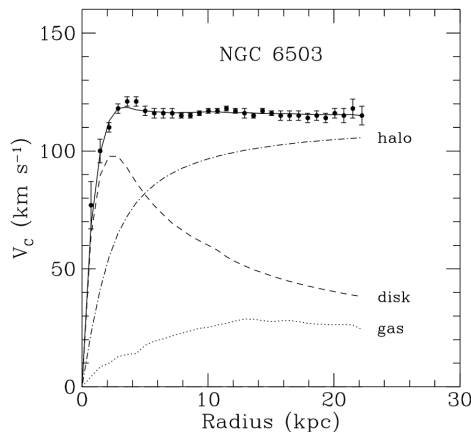
Figure 2.1: Velocity distribution of the galaxy with the number 6503 in the New General Catalogue (NGC). The contributions from the visible components are presented as dashed and dotted lines. The putative DM halo contribution is shown as a dot-dashed line. The contribution from the DM halo is clearly necessary to explain the experimental data. Taken from Ref. [60].

with the force $\mathbf{F}_i$, mass $\mathbf{m}_i$, and distance $\mathbf{r}_i$, which leads to

$$\frac{1}{2}\sum_i m_i \frac{\mathrm{d}^2 \mathbf{r}_i^2}{\mathrm{d}t^2} = \underbrace{\sum_i \mathbf{F}_i \mathbf{r}_i}_{\equiv \mathrm{Vir}} + \underbrace{\sum_i m_i \left(\frac{\mathrm{d}\mathbf{r}_i}{\mathrm{d}t}\right)^2}_{\equiv 2 \times K_\mathrm{T}} \tag{2.3}$$

after scalar multiplication with the distance $\mathbf{r}_i$ [65]. The lefthand side of this equation is proportional to the time derivative of the cluster's polar moment of inertia and zero after averaging over time. Hence, we obtain the Virial theorem

$$\overline{\mathrm{Vir}} = -2 \times \overline{K_\mathrm{T}} \tag{2.4}$$

for the averaged virial Vir and the kinetic energy of translation K_T of the whole galaxy cluster. Applying the Virial theorem, Zwicky found the conversion factor of approximately 500 from luminosity to the cluster's mass which is much larger than his expectations and can be explained by a non-luminous kind of matter in the Coma cluster.

The last point in this list of astronomical evidence is the collision of galaxy clusters, *e.g.* in the 'bullet cluster' (with the designation 1E 0657-558) [66–70] and MACS J0025.4-1222 [71]. The spatial difference between the bary-centers of the subclusters and the originating regions of the X-rays produced by the collisions of the intergalactic gas lead to the conclusion of the existence of a type of matter that causes weak-lensing effects while it interacts at most weakly with the ordinary matter.
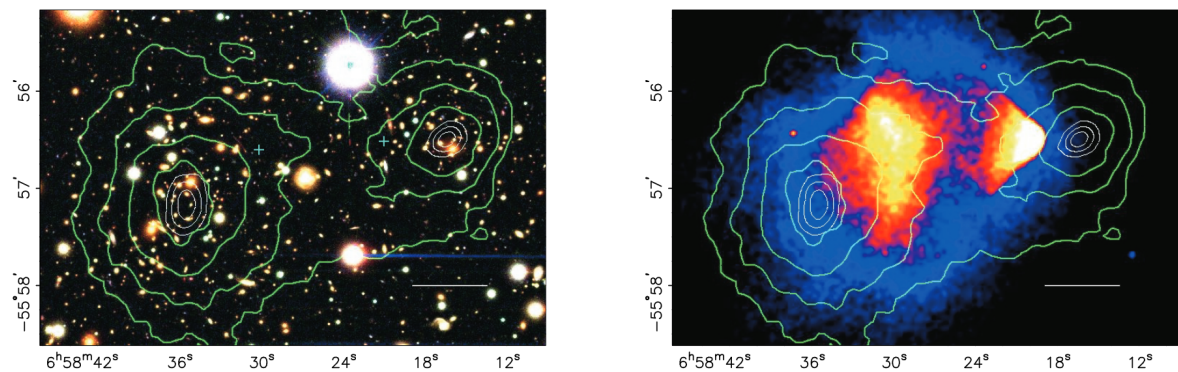
Figure 2.2: Observations of the cluster 1E 0657-558 in the visible (*left*) and X-ray spectrum (*right*). The green contours correspond to different magnitudes of weak-lensing effects and the color-encoded regions between the bary-centers of the two subgroups of galaxies indicate the origin of the detected X-rays. Images taken from Ref. [69].

Evidence at cosmological scale

After the prediction of background photons propagating since the Early Universe [72, 73] and their Nobel prize-awarded discovery by Penzias and Wilson in 1965 [74], the measurements of the cosmic microwave background (CMB) were continuously improved and serve as an excellent source for extracting information about the Early Universe.

The temperature anisotropies in the CMB can be expanded as [60]

$$\frac{\delta T}{T}(\theta, \varphi) = \sum_{\ell=2}^{\infty} \sum_{m=-\ell}^{\ell} a_{\ell m} Y_{\ell m}(\theta, \varphi) \qquad (2.5)$$

with the spherical harmonics $Y_{\ell m}$. If the temperature anisotropies obey a Gaussian distribution, the CMB can be transformed into a power spectrum which is typically presented as $\mathcal{D}_\ell \equiv \ell(\ell+1)C_\ell/(2\pi)$ in terms of the multipole ℓ. Here, the variance C_ℓ of the coefficients $a_{\ell m}$ is defined as [60]

$$C_\ell \stackrel{\text{def}}{=} \langle |a_{\ell m}|^2 \rangle \equiv \frac{1}{2\ell+1} \sum_{m=-\ell}^{\ell} |a_{\ell m}|^2. \qquad (2.6)$$

The CMB power spectrum is depicted in Fig. 2.3 and the blue line, corresponding to the fit of the cosmological ΛCDM model which describes both dark energy Λ and cold
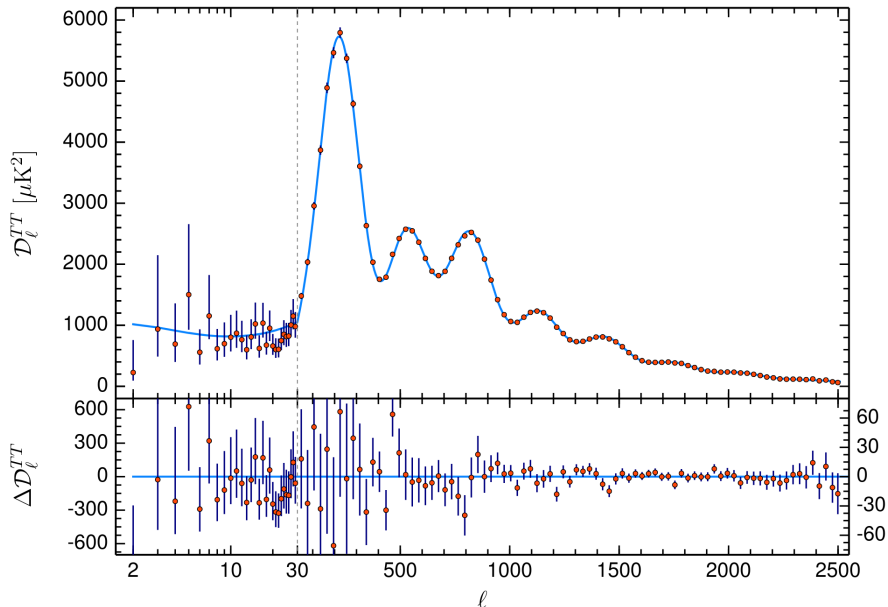
Figure 2.3: The CMB power spectrum measured by the Planck satellite. The data (red) matches well the ΛCDM fit (blue). See Refs. [75, 76] for details.

dark matter (CDM), fits the data impressively well and allows to extract cosmological parameters. In particular, the pattern of the baryon acoustic oscillations, which originate from the competing processes of contraction due to gravity and expansion due to thermal pressure, strongly suggests the large proportion of DM in the energy budget of the Universe. The anisotropies of the CMB are imprints of the cosmological density fluctuations at the time of recombination[1] and allow to determine the relic abundance of cold DM of

$$\Omega_{\mathrm{DM}} h^2 = 0.1200(12) \,, \tag{2.7}$$

which quantifies the DM relic abundance in terms of the DM energy density ρ_{DM} in units of the critical energy density ρ_{crit}, $i.e.$ $\Omega_{\mathrm{DM}} \equiv \rho_{\mathrm{DM}}/\rho_{\mathrm{crit}}$, and the reduced Hubble constant $h \equiv H_0/(100\,\mathrm{km\,s^{-1}\,Mpc^{-1}})$ with today's Hubble constant $H_0 \approx 67.4(5)\,\mathrm{km\,s^{-1}\,Mpc^{-1}}$ [75]. Besides the DM content of the Universe, the CMB power spectrum allows to infer the abundance Ω_{b} of baryonic matter and the total abundance Ω_{m} of any kind of matter in the Universe, quantified as [75]

$$\Omega_{\mathrm{b}} h^2 = 0.02237(15) \quad , \quad \Omega_{\mathrm{m}} h^2 = 0.1430(11) \,. \tag{2.8}$$

Another finding on very large scales is the formation of large scale structures in the Universe which was compared to N-body simulations (*cf.* Fig. 2.4). The structure of galaxies, and whole galaxy clusters in respectively opposite slices in Fig. 2.4 resemble each other astonishingly well, providing additional support for the hypothesis of the existence of DM. Simulations like the one in Fig. 2.4 demonstrate that *cold*, that is non-relativistic, DM is a vital ingredient for the structure formation on large scales.

2.2 Overview of Dark Matter Candidates

Since neither the SM nor the former cosmological standard model (*i.e.*, without DM) provide an explanation for the observations above, new physics is expected to be responsible for these. Besides theories like modified Newtonian dynamics (MOND) [78, 79] and massive astrophysical compact halo objects (MACHOs) [80, 81] like primordial black holes (PBHs) [82–84], it is not excluded that a yet unknown particles species

---

[1]The term *recombination* refers to the point in time at which the plasma got cold enough to facilitate the nuclei bind electrons and thus form electrically neutral atoms. By that, the mean free path of the photons increased substantially and the photons could travel through the neutral medium for the first time.

constitutes the full or a fraction of the measured DM energy density. In this thesis we pursue the hypothesis of particle DM which needs to fulfil a set of requirements to constitute the type of matter that these measurements suggest (see, *e.g.*, Refs. [10, 85, 86] for further details on the experimental evidence and DM models).

One striking feature of DM results from the large range of distances (from galactic up to cosmological scales) which translates into a large range in time at which DM must have been in place. Consequently, DM is required to be stable on cosmological time scales. DM models can account for this via additional symmetries.[2]

Moreover, the measurement of the CMB and the analysis of the 'bullet cluster' in light of X-rays and weak gravitational lensing require zero or at least close-to-zero electric charge of the DM particle. Assuming that DM is decoupled from the baryon-photo plasma at the time of recombination, the authors of Ref. [87] find $\epsilon \equiv Q_{DM}/e \lesssim 10^{-6}$ for $m_{DM} = 1\,\mathrm{GeV}$ and $\epsilon \lesssim 10^{-4}$ for $m_{DM} = 10\,\mathrm{TeV}$ for the upper limits on the DM electric charge Q_{DM} in units of the elementary charge e.

As the second-to-last aspect, the mass of fermionic and bosonic DM is subject to constraints which limit the mass from below. In case of DM fermions, Pauli's exclusion principle results in an upper limit for the viable phase space of the dark fermions and hence in the lower limit $m_{fDM} \gtrsim 100\,\mathrm{eV}$ [10, 88] for the DM mass (known as the

---

[2]It cannot be concluded from this observation that DM must be absolutely stable but its decay rate must be sufficiently slow such that many DM models feature non-decaying DM particle(s).
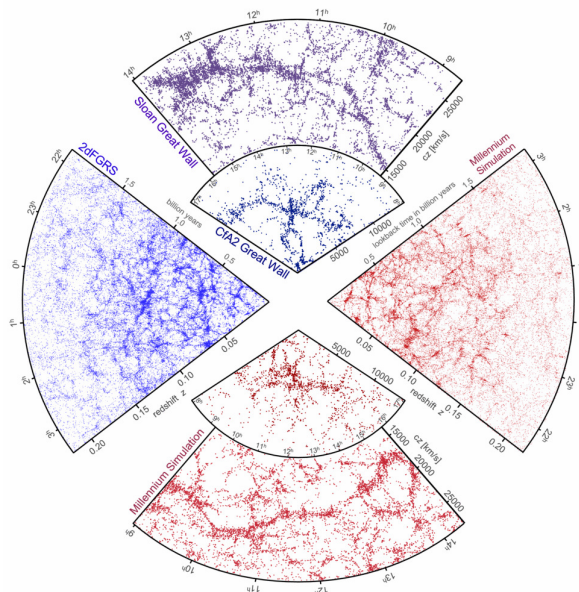
Figure 2.4: Comparison of galaxy surveys (*left* and *top*) to simulation of structure formation on large scales with DM contribution (*right* and *bottom*). Taken from Ref. [77].

Tremaine-Gunn bound [89]). Similarly, the mass of bosonic DM cannot be smaller than a certain value because its Compton wavelength could be larger than galactic scale structures which in turn would be washed out (see, *e.g.*, Ref. [90]). One finds as lower limit for the bosonic DM mass $m_{\mathrm{bDM}} \gtrsim 10^{-22}\,\mathrm{eV}$ [10].

Lastly, a key feature of DM is its small interaction strength with ordinary matter. The observation of the 'bullet cluster' 1E 0657-558 and the comparison of the gravitational center of mass to the origin of the X-ray emission strongly suggests a small interaction strength between DM and ordinary matter as well as between DM particles themselves (see, *e.g.*, Ref. [91]). This finding was already used for putting an upper bound on the electric charge of the DM particle, but can be applied also to QCD interactions as well as BSM forces.

After the discussion of the requirements a particle has to fulfil in order to serve as a DM candidate, we shall elaborate on different proposals for DM models in the following.

Weakly and feebly interacting massive particles

One very prominent DM candidate is the weakly interacting massive particle (WIMP) which we shall consider in the investigations in Chapters 3–5. The reader may be referred to the studies and reviews in the Refs. [92–95] for details.

If the DM particles are in thermal equilibrium with the SM particles in the Early Universe, the evolution of the DM number density n_{DM} obeys the Boltzmann equation [95]

$$\frac{\mathrm{d}n_{\mathrm{DM}}}{\mathrm{d}t} + 3Hn_{\mathrm{DM}} = -\langle\sigma v\rangle \left(n_{\mathrm{DM}}^2 - n_{\mathrm{DM,eq}}^2\right) \tag{2.9}$$

with the time-dependent Hubble parameter H, the thermally averaged DM annihilation cross section $\langle\sigma v\rangle$, and the DM number density in thermal equilibrium $n_{\mathrm{DM,eq}}$ (see Refs. [96, 97] for detailed calculations). Using the comoving DM number density, which is defined as

$$Y_{\mathrm{DM}} \overset{\mathrm{def}}{=} \frac{n_{\mathrm{DM}}}{s} \tag{2.10}$$

with the entropy density

$$s \overset{\mathrm{def}}{=} \frac{2\pi^2}{45} h_{\mathrm{eff}}\left(T\right) T^3 \tag{2.11}$$

in terms of the effective number h_{eff} of entropy degrees of freedom, and the entropy conservation $\mathrm{d}s/\mathrm{d}t = -3Hs$, the evolution of Y_{DM} is described by

$$\frac{\mathrm{d}Y_{\text{DM}}}{\mathrm{d}t} = \frac{\mathrm{d}s}{\mathrm{d}t} \frac{\langle \sigma v \rangle}{3H} Y_{\text{DM}}^2 \left(1 - \frac{Y_{\text{DM,eq}}^2}{Y_{\text{DM}}^2} \right) . \tag{2.12}$$

At a sufficiently early time in the Early Universe, *i.e.* at sufficiently high temperatures, the DM annihilation rate $\Gamma_{\text{DM-ann}} = \langle \sigma v \rangle Y_{\text{DM}} s$ is larger than the Hubble expansion rate H and the DM particles are hence in thermal equilibrium with the SM bath, provided the interaction strength between particles in the dark sector and the SM sector is large enough to guarantee thermalization. The expansion of the Universe causes a drop in temperature which in turn leads to an increasingly inefficient DM production in the thermal bath as the DM production cross section scales with $\exp\left(-m_{\text{DM}}/T\right)$ and hence gets Boltzmann suppressed for temperatures smaller than the DM mass. If the DM interaction rate Γ_{DM} is large enough, the DM destruction continues and the comoving DM number density decreases. Once the DM interaction rate drops below the Hubble rate, DM annihilation processes get suppressed and eventually shut off effectively. Consequently, the comoving DM number density Y_{DM} tends to approach a constant value, *i.e.* to *freeze out*. The corresponding freeze-out temperature is labelled as $T_{\text{f.o.}}$. The comoving DM number density today at temperature $T = T_0$ can be estimated as

$$Y_{\text{DM}} (T = T_0) \approx \sqrt{\frac{\pi}{45}} M_{\text{Pl}} \left(\int_{T_0}^{T_{\text{f.o.}}} \mathrm{d}T \, g_*^{1/2} \langle \sigma v \rangle \right)^{-1} \tag{2.13}$$

with

$$g_*^{1/2} = \frac{h_{\text{eff}}}{g_{\text{eff}}^{1/2}} \left(1 + \frac{T}{3h_{\text{eff}}} \frac{\mathrm{d}h_{\text{eff}}}{\mathrm{d}T} \right) \tag{2.14}$$

in terms of the effective number g_{eff} of relativistic degrees of freedom. The comoving DM number density in terms of the dimensionless parameter $x \equiv m_{\text{DM}}/T$ is shown in Fig. 2.5.

The comoving DM number density today in Eq. (2.13) involves the thermally averaged DM annihilation cross section $\langle \sigma v \rangle$. Adopting the formal definition from Ref. [95] with the modified Bessel function of the first (second) kind $K_{1(2)}(x)$, it reads

$$\langle \sigma v \rangle = \frac{1}{8m_{\text{DM}}^4 T K_2 \left(m_{\text{DM}}/T\right)^2} \int_{4m_{\text{DM}}^2}^{\infty} \mathrm{d}s \, \sigma\left(s\right) \sqrt{s} \left(s - 4m_{\text{DM}}^2\right) K_1 \left(\sqrt{s}/T\right) \tag{2.15}$$

and the DM relic abundance can be evaluated as

$$\Omega_{\mathrm{DM}}h^2 \approx 8.76 \times 10^{-11}\,\mathrm{GeV}^{-2} \left(\int_{T_0}^{T_{\mathrm{f.o.}}} \mathrm{d}T\, g_*^{1/2} \frac{\langle\sigma v\rangle}{m_{\mathrm{DM}}} \right)^{-1} \qquad (2.16)$$

with the today's critical energy density $\rho_{\mathrm{crit}}\,(T = T_0) \approx 10^{-5}\,\mathrm{GeV\,cm}^{-3}$. It turns out that the measured DM relic abundance in Eq. (2.7) requires the thermally averaged annihilation cross section

$$\langle\sigma v\rangle \sim \mathcal{O}\left(10^{-26}\right)\,\mathrm{cm}^3\,\mathrm{s}^{-1}, \qquad (2.17)$$

which translates into the freeze-out temperature $T_{\mathrm{f.o.}} \approx m_{\mathrm{DM}}/20$ (see, $e.g.$, Ref. [94]). The freeze-out temperature can be read off Fig. 2.5 for a specific WIMP DM mass.

Surprisingly, the measured DM relic abundance can be obtained with a interaction strength comparable to the EW interactions in the SM and a DM mass of the order $\mathcal{O}(0.1 - 1)\,\mathrm{TeV}$ [95]. This 'miraculous' coincidence was dubbed $WIMP\ miracle$ and sparked great excitement and expectations. However, a large fraction of this energy range can be probed in collider experiments nowadays and present DM direct detection (DMDD) experiments like XENONnT, LZ, and PandaX-II are sensitive to the expected cross sections for scattering off a nucleon. The null results in these experiments exclude a substantial fraction of the parameter space in WIMP models.[3]

---

[3]Note that the terminology 'null results' refers only to the fact that the searches did not lead to
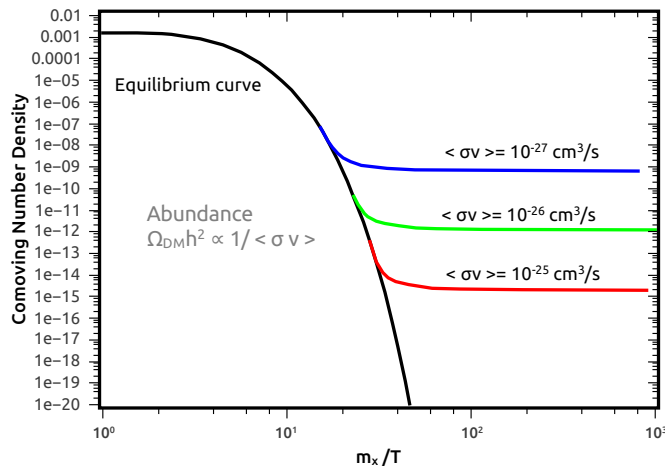
Figure 2.5: Comoving DM number density Y_{DM} in freeze-out models for different values of the thermally averaged DM annihilation cross section $\langle\sigma v\rangle$. Taken from Ref. [94].

Besides the weakly interacting massive particles, there are models involving *feebly interacting massive particle* (FIMP; see, *e.g.*, Refs. [100, 101] for details). The distinct feature of FIMP DM models is the DM production mechanism which is not described by the freeze-out but rather by the *freeze-in* mechanism. Briefly summarized, a small abundance of heavy DM particles is present in the Early Universe at high temperatures $T \gg m_{\mathrm{DM}}$. The DM particles are virtually decoupled from the thermal SM bath due to the feeble interaction strength but can be produced nevertheless by interactions in the thermal bath. As a consequence, the DM abundance builds up steadily until the temperature of the thermal bath becomes comparable to the DM mass and renders the DM production inefficient due to Boltzmann suppression. The gain in DM abundance flattens and eventually reaches a practically constant value for the entire further evolution of the Universe.

Weakly interacting slim particles

Based on reviews by Jaeckel *et al.* [102] and Graham *et al.* [103], we shall briefly present the axion as a prominent example for weakly interacting slim particles (WISPs).

As motivated in the (incomplete) list of shortcomings of the SM in Chapter 1, the SM gauge group allows the CP-violating QCD term in Eq. (1.16) which in turn predicts the contribution to the neutron EDM that scales as

$$|d_n/e| \sim \frac{m_q}{m_n^2} \underbrace{|\theta + \arg \det M|}_{\equiv \bar{\theta}} \tag{2.18}$$

with the masses m_n and m_q of the neutron and light quarks, respectively, and the quark mass matrix M. The proposal by Peccei and Quinn [104, 105] explains the smallness of the effective QCD θ parameter by promoting the QCD θ parameter to a dynamical field which transforms under the global $U(1)_{\mathrm{PQ}}$ symmetry. By that, the Lagrangian gains additional terms, reading

$$\mathcal{L}_{\mathrm{axion}} \supset \frac{g_s^2}{32\pi^2} \left(\frac{a}{f_a} \right) G_{\mu\nu}^a \widetilde{G}^{a\mu\nu} \tag{2.19}$$

for instance, which demonstrates that the axion decay constant f_a governs the interaction strengths. The non-trivial QCD vacuum structure features a minimum at $\langle a + \bar{\theta} f_a \rangle = 0$ such that the contribution to the nEDM vanishes.

---

the discovery of a DM particle yet. The experiments provide valuable bounds for DM model building and are poised to enter a new era after the announcement of having dived into the neutrino fog for the first time in DMDD experiments (see Refs. [98, 99]).

The mass of the axion as the pseudo-Nambu-Goldstone boson from the explicit $U(1)_{\text{PQ}}$ symmetry breaking is determined by the axion decay constant on the one hand and the pion mass m_π, its decay constant f_π, and the light quark masses $m_{u,d}$ on the other hand. The relation reads

$$m_a \approx m_\pi \left(\frac{f_\pi}{f_a} \right) \frac{\sqrt{m_u m_d}}{m_u + m_d} \, . \tag{2.20}$$

In spite of its small mass, the axion can account for the amount of cold DM in the Universe thanks to the misalignment mechanism (see, *e.g.*, Refs. [106, 107]).

2.3 Strategies of Detection

Before concluding this chapter, we shall turn to the experimental endeavours to detect DM. The strategies can be divided into three categories: (*i*) DM direct detection, (*ii*) DM indirect detection, and (*iii*) collider searches for DM. In the following, we shall briefly summarize the basics of the first two search strategies which are depicted in Fig. 2.6, while we refer the reader to Refs. [90, 108] for a comprehensive overview of the variety of collider searches and bounds on a wealth of DM models.

Dark Matter direct detection

Although to date we only have evidence for DM interacting gravitationally, it is not excluded that the DM particle couples to SM particles via the exchange of SM gauge bosons (if the DM particle is charged under the SM gauge group or an extension of it) or via the Higgs portal. The possibility of those interactions are probed in DMDD experiments whose characteristic feature is a target which triggers an interaction between an atom in the target material and a bypassing DM particle by enhancing the scattering
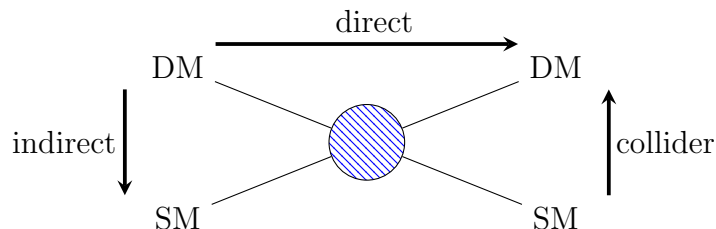
Figure 2.6: Three possible strategies for DM searches involving SM particles. The blue blob at the center represents any particle physics model that describes the interaction.

cross section due to an appropriate selection of the target material. The cross section for a DM particle scattering off a nucleus scales with its atomic number, *i.e.* $\sigma \propto A^2$, and a large atomic number of the target material is therefore one of the selection criteria [90, 95]. In the case of an interaction, the detector is sensitive to recoil events of either the whole nucleus or an electron in the atomic shell of the target material due to elastic DM-target scattering. The differential rate of WIMP DM scattering off a nucleus reads

$$\frac{\mathrm{d}R_{\mathrm{DM}}\left(E, t\right)}{\mathrm{d}E} = \frac{N_{\mathrm{nucleus}}\rho_{\mathrm{DM}}}{m_{\mathrm{DM}}m_{\mathrm{nucleus}}} \int_{v_{\min}}^{v_{\mathrm{esc}}} \mathrm{d}^3 v\, v f_{\mathrm{Earth}}\left(v, t\right) \frac{\mathrm{d}\sigma\left(v, E\right)}{\mathrm{d}E} \tag{2.21}$$

with the recoil energy E, the number N_{nucleus} of nuclei with mass m_{nucleus} in one kilogram of target material, the velocity v of the DM particle in the reference frame of the Earth, and the velocity distribution f_{Earth} [95]. The minimum velocity leading to an observable signal is given by $v_{\min} = \sqrt{m_{\mathrm{nucleus}}E/(2\mu^2)}$ with the reduced mass μ of the DM-nucleus system and the escape velocity v_{esc} is the DM velocity beyond which the DM particle is not gravitationally bound to the Milky Way any longer. The differential scattering cross section reads

$$\frac{\mathrm{d}\sigma}{\mathrm{d}E} = \frac{m_{\mathrm{nucleus}}}{2\left(\mu v\right)^2} \left(\sigma_{\mathrm{SI}}F\left(q\right)^2 + \sigma_{\mathrm{SD}}S\left(q\right)\right) \tag{2.22}$$

with the momentum transfer-dependent form factors $F(q)$ and $S(q)$ and the spin-independent (spin-dependent) scattering cross section $\sigma_{\mathrm{SI(SD)}}$ in the limit of zero momentum transfer [95]. A wealth of experiments is dedicated to detect DM scattering events. In the upcoming chapters we shall focus on WIMP DM, so we present in Fig. 2.7 current exclusion limits set by several experiments, in particular by XENONnT and LZ [109, 110], alongside the development of the experimental sensitivity by comparing to other, less stringent upper limits. The yellow region in the lower part of the exclusion plot corresponds to the *neutrino fog* for experiments with a xenon target, for which neutrino-target scatterings are expected to mimic DM scattering processes and hence to render the identification of DM scattering events in the target material more complicated (see Refs. [117, 118] for further information).

Dark Matter indirect detection

A second possibility of looking for DM is DM indirect detection (DMID) which is based on DM annihilations in a region of a high DM density (*e.g.*, the Galactic center) and the measurement of the produced SM particles like photons, positrons, or neutrinos. In

addition to these, also the flux of composite particles like antiprotons or anti-deuterium is measured and potentially serves as an indicator for DM annihilations. A comprehensive review of the different approaches to DMID and current experiments can be found in Refs. [60, 85, 90].

The differential flux Φ of photons, for instance, with respect to the solid angle Ω and the energy E is given by

$$\frac{\mathrm{d}\Phi}{\mathrm{d}\Omega\,\mathrm{d}E} = \frac{\sigma v}{8\pi m_{\mathrm{DM}}^2} \times \frac{\mathrm{d}N}{\mathrm{d}E} \times \int_{\mathrm{l.o.s.}} \mathrm{d}^3x\,\rho_{\mathrm{DM}}^2\left(r\left[x, \Omega\right]\right) \tag{2.23}$$

with the DM annihilation cross section σ, the mean velocity v of the DM particles in the region of interest, the energy spectrum $\mathrm{d}N/\mathrm{d}E$, and the integral of the DM density along the line of sight (l.o.s.) x [95].

The advantage of DMID searches is the accessibility of the regime of large DM mass which DMDD experiments nor collider searches are sensitive to. Hence DMID experiments allow to cover a much larger range of DM mass, although astrophysical uncertainties must be taken into account and might render the results less accurate than results from experiments in laboratories.

After this introduction to DM, including its motivation, prominent models, and detection methods, we shall next turn to DM models and a new way of describing multiple DM models in an effective field theory framework.
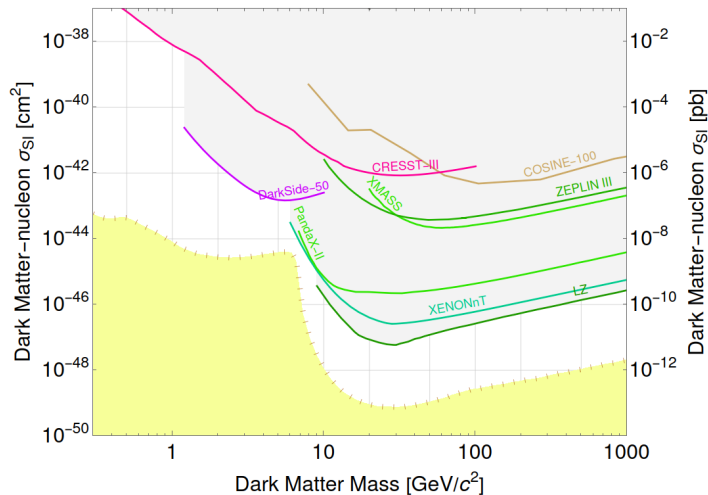
Figure 2.7: DMDD exclusion curves by several experiments [111–116] in light of the practically irreducible neutrino background [117] (indicated in yellow). Plot created with the Dark Matter Limit Plotter v5.18, accessed on July 8th 2024.

Chapter 3

New Effective Field Theory Approach to Dark Matter

Particle physics phenomena in nature occur at different energy scales: while electron transitions in atoms occur at $\mathcal{O}(\text{eV})$ and nuclear processes like excitations and deexcitations involve energies at $\mathcal{O}(\text{MeV})$, weak interactions like β decays are explained by the exchange of heavy mediators with masses around the EW scale $\sim 100\,\text{GeV}$ and gravity is expected to be explained by physics at the Planck scale $\mathcal{O}(10^{19})\,\text{GeV}$ in the context of quantum gravity. Notably, the progress in the past demonstrates that it is not necessary to have a grasp of the high-energy physics to explain processes at comparably low energies. One prime example is the four-fermion theory by Fermi for describing the β decay, which ultimately culminated in the discovery of the W boson. Fermi's effective operator for β decay reads

$$-\mathcal{L}_{\text{Fermi}} \supset G_F J_\mu^\dagger J^\mu \tag{3.1}$$

with the current $J_\mu = \overline{n}\gamma_\mu p + \overline{e}\gamma_\mu \nu_e$ [9]. If the momentum transfer (*i.e.* the characteristic energy scale of the process) is much smaller than the mass of the mediating W boson, Fermi's constant can be related to the W boson mass by [9, 10]

$$G_F \approx \frac{\sqrt{2}g^2}{8m_W^2} \approx 1.17 \times 10^{-5}\,\text{GeV}^{-2}\,. \tag{3.2}$$

The negative mass dimension of Fermi's constant signals the non-renormalizability of the operator in Eq. (3.1) and hence suggests physics at the cutoff scale which can be estimated by assuming values for the couplings $C_i^{(6)}$ in Eq. (3.4). By that the measurement of Fermi's constant suggested $\Lambda \sim \mathcal{O}(100\,\text{GeV})$ which is fairly close to

the measured W boson mass $m_W \approx 80\,\text{GeV}$ [10]. This great success of the EFT approach supports studies in this framework whenever it is reasonable to stay agnostic of the underlying theory and should serve as motivation for analyses in this framework.

Bearing the success of the EFT approach in mind, what follows is an introduction to EFTs and their applications (based on Refs. [119–122]). Formally, the full theory is described by the Lagrangian $\mathcal{L}$ which in turn determines the action $S = \int \mathrm{d}^4 x\, \mathcal{L}$. In line of the decoupling theorem by Appelquist and Carazzone [123], a heavy field Φ is effectively 'integrated out' from the theory by defining the *effective* action $S_{\text{eff}}[\phi_j]$ via

$$e^{iS_{\text{eff}}[\phi_j]} \equiv \int \mathcal{D}\Phi\, e^{iS[\phi_j,\Phi]} \left(\int \mathcal{D}\Phi\, e^{iS[\phi_j,0]} \right)^{-1} \tag{3.3}$$

with the set of sufficiently light fields ϕ_j and the path integral over all possible field values of Φ [121]. This approach allows to describe the physical phenomena at low energies $E \ll \Lambda$, where the cutoff scale Λ is typically set by the mass of the heavy field. The *effective* Lagrangian at the specific mass dimension $D > 4$ is defined by

$$\mathcal{L}_{\text{eff}}^{(D)} = \sum_{i=1}^{n_D} \frac{C_i^{(D)}}{\Lambda^{D-4}} \mathcal{O}_i^{(D)} \tag{3.4}$$

with the Wilson coefficients $C_i^{(D)}$ and the operators $\mathcal{O}_i^{(D)}$ and is renormalizable order by order. The latter are made up by the field content of the specific 'low-energy' theory. Note that the local operators $\mathcal{O}_i^{(D)}$ in the EFT describe non-local interactions in the underlying, high-energy theory *after* integrating out the heavy degree of freedom [119]. In the effective Lagrangian in Eq. (3.4), the effective couplings and the suppression scale are separated, but they can be collectively called Wilson coefficients.

The cutoff scale Λ indicates the energy scale at which the low-energy theory is not reliably applicable any longer. It is one of the key aspects of EFTs that the new physics beyond the cutoff scale Λ is encapsulated in the Wilson coefficients. The ratio $E/\Lambda \ll 1$ serves as an appropriate expansion parameter in the EFT. The closer the energy scale of a process approaches the cutoff scale (*i.e.*, the larger the contributions from the fields integrated out in the EFT), the worse the expansion in this ratio and the more inaccurate the predictions of the EFT. Typically, observables get contributions from these non-renormalizable operators. The accuracy parameter ϵ can be defined as

$$\epsilon \sim \left(\frac{E}{\Lambda} \right)^{D_\epsilon - 4}, \tag{3.5}$$

which consequently leads to $D_\epsilon \sim 4 + \log\left(1/\epsilon\right)/\log\left(\Lambda/E\right)$ as a rough estimate for the dimension D_ϵ required to reach an accuracy goal ϵ [119] (see also Ref. [124] for more details).

The EFT framework can be applied in two ways. In the *bottom up* approach the UV theory is typically not known. By considering the symmetries and degrees of freedom of the 'low-energy theory', the most general effective Lagrangian is built and the Wilson coefficients are free parameters. A typical example for such a 'low-energy' theory is the SM which is incomplete (*cf.* list of shortcomings in Chapter 1) and might need to be augmented by new, heavy fields. Suggested by the absence of particle discoveries at particle colliding experiments like the Large Hadron Collider (LHC) after the one of the Higgs boson in 2012, these new degrees of freedom might reside well separated from the EW scale. The *top down* approach, on the other hand, makes use of the knowledge about the UV theory and usually simplifies the calculation remarkably since the heavy, in the best case at most negligibly contributing degrees of freedom do not appear in the calculations. After matching the UV theory onto the EFT at the cutoff scale Λ, the Wilson coefficients are determined at this energy scale. Since the characteristic energy scale of the process of interest is substantially smaller than the matching scale, the renormalization group running of the full set of Wilson coefficients must be taken into account (see calculation below).

The aforementioned matching of a UV model onto the EFT in the 'top down' approach results in relations between the UV model parameters and the Wilson coefficients. There are several approaches for this, *e.g.* via the path integral, the equations of motion, or the Feynman diagrams for specific processes (see Ref. [9] for examples). As a first attempt for the analysis in this thesis, we shall compare the operators of a specific EFT (will be introduced in Section 3.3) to the operators in the UV model and thereby identify the matching conditions. The shortcomings of this approach and possible improvements shall be discussed at the end of this chapter. But before we begin with our investigation, we shall introduce different EFT frameworks.

3.1 Introduction to the Standard Model EFT

Motivated by the great success of the SM, one may be inclined to take the SM with its gauge symmetries and field representations and construct higher-dimensional, non-renormalizable operators with these. With the definition of an effective Lagrangian in Eq. (3.4) at hand, the general Lagrangian for the SM effective field theory (SMEFT)

without the truncation in mass dimension reads

$$\mathcal{L}_{\text{SMEFT}} = \mathcal{L}_{\text{SM}} + \sum_{D=5}^{\infty} \sum_{i=1}^{n_D} \frac{C_i^{(D)}}{\Lambda^{D-4}} \mathcal{O}_i^{(D)} \tag{3.6}$$

with the operators $\mathcal{O}_i^{(D)}$ being gauge invariant with respect to the SM gauge group $SU(3)_c \times SU(2)_L \times U(1)_Y$ [121, 125].

For practical purposes, the number of mass dimensions D is limited in the EFT of interest and the finite number of non-renormalizable operators can be found systematically. Potentially redundant operators can be identified and eliminated via equations of motion. The 'Warsaw basis' of non-redundant higher-dimensional operators up to $D = 6$ is given in Refs. [126, 127]

Assuming that the SM with its gauge groups and the fields in their respective SM representations is the correct way of describing the physics at low energies, the SMEFT framework provides a powerful tool in addressing experimental anomalies (see Refs. [128–131] for examples for SMEFT analyses).

3.2 Introduction to the Higgs EFT

Unlike the SM and SMEFT with their linear realization of the EW symmetry, the Higgs effective field theory (HEFT) describes the non-linear realization thereof [125]. Instead of the Higgs doublet, the HEFT contains the physical Higgs boson as a scalar singlet and the three Goldstone bosons π^I (which give rise to the mass of the EW gauge bosons) in the Goldstone matrix [121]

$$\Sigma = \exp\left(i\sigma^I \frac{\pi^I}{v}\right), \tag{3.7}$$

which transforms as

$$\Sigma \rightarrow \exp\left(i\varphi_L^I(x) \frac{\sigma^I}{2}\right) \Sigma \exp\left(-i\varphi_Y(x) \frac{\sigma^3}{2}\right) \tag{3.8}$$

under the SM gauge symmetry with spacetime-dependent phases $\varphi_{L,Y}(x)$. The bi-doublet made up by the Higgs doublet Φ and its conjugate $\widetilde{\Phi}$ is related to the Goldstone matrix by

$$\left(\widetilde{\Phi}\,\Phi\right) = \frac{v+h}{\sqrt{2}} \Sigma. \tag{3.9}$$

As a summary, the three theories are related to each other by

$$\text{SM}\left(\Phi, \Lambda \to \infty\right) \subset \text{SMEFT}\left(\Phi, \Lambda < \infty\right) \subset \text{HEFT}\left(h, \Lambda < \infty\right), \qquad (3.10)$$

which showcases the advantage of working in the HEFT framework to allow a high degree of generality and consequently a reduced theoretical bias in the interpretation of experimental data [121].[1] The measurement of Higgs self-couplings (involving three and four scalars) could help shed light on the Higgs embedding as SMEFT predicts self-interactions arising from $\lambda(v+h)^4$, while, *e.g.*, the three- and four-Higgs interactions in HEFT are not necessarily dictated by the same quartic coupling parameter λ. Hence, the measurement of the Higgs quartic coupling, as outlined in Chapter 1, is crucial for the understanding of the scalar sector.

3.3 Introduction to the extended DM EFT

Inspired by the analysis in Ref. [132], in which the SM is extended by a DM particle (in one scenario bosonic, in the other fermionic) and *one* mediator, the following analysis aims at lifting the assumption of the SM Higgs representation in the context of an extended HEFT. Another distinct feature of this extended DM EFT (eDMEFT) is the number of mediators: here we consider *two* scalar mediators $\mathcal{S}_1, \mathcal{S}_2$ (with masses smaller than the cutoff scale Λ) in order to account for resonantly enhanced interactions with the two BSM scalars involved. The eDMEFT approach allows us to stay agnostic of their representation with respect to the underlying gauge group. They can originate either from singlet representations or from higher multiplets like doublets, triplets, or quadruplets for instance. In our scenarios, they shall serve as mediators linking the SM and the dark sector. The latter consists of the fermion χ which is – like the new scalars $\mathcal{S}_i$ and the Higgs boson h – a gauge singlet under $SU(3)_c \times U(1)_Q$.

The operators encoding all interactions between the Higgs boson h and the new scalars $\mathcal{S}_i$ up to dimension D are defined as

$$\mathcal{O}_D^C\left(h, \mathcal{S}_1, \mathcal{S}_2\right) \stackrel{\text{def}}{=} \sum_{k=0}^{D} \sum_{j=0}^{D-k} \sum_{i=0}^{j} C_{i,j-i}^{(k)} h^k \mathcal{S}_1^i \mathcal{S}_2^{j-i}. \qquad (3.11)$$

Although we could go up to an arbitrarily high mass dimension in the expansion, we shall truncate our eDMEFT Lagrangian with a non-linearly realized EW symmetry

---

[1]Note that the SM has not been constructed with an energy cutoff scale but is expected to be superseded by a theory for energies $\gtrsim M_{\text{Pl}}$ at the latest.

at mass dimension $D = 5$. It reads

$$
\begin{aligned}
\mathcal{L} = \ & \mathcal{L}_{\text{gauge-ferm}}^{\text{SM}} + \left(\overline{\chi} i \slashed{\partial} \chi - \mathcal{O}_2^y \left(h, \mathcal{S}_1, \mathcal{S}_2 \right) \overline{\chi_L} \chi_R + \text{h.c.} \right) + \frac{1}{2} \sum_{\phi = \mathcal{S}_1, \mathcal{S}_2, h} \partial_\mu \phi \partial^\mu \phi \\
& - \mathcal{O}_5^\lambda \left(h, \mathcal{S}_1, \mathcal{S}_2 \right) + \frac{v^2}{4} \text{Tr} \left[\left(D_\mu \Sigma \right)^\dagger \left(D^\mu \Sigma \right) \right] \mathcal{O}_3^\kappa \left(h, \mathcal{S}_1, \mathcal{S}_2 \right) \\
& + i \frac{v^2}{4} \text{Tr} \left[\Sigma^\dagger \left(D^\mu \Sigma \right) \sigma^3 \right] \left(\mathcal{O}_2^s \left(h, \mathcal{S}_1, \mathcal{S}_2 \right) \partial_\mu h + \mathcal{O}_2^{s1} \left(h, \mathcal{S}_1, \mathcal{S}_2 \right) \partial_\mu \mathcal{S}_1 + \mathcal{O}_2^{s2} \left(h, \mathcal{S}_1, \mathcal{S}_2 \right) \partial_\mu \mathcal{S}_2 \right) \\
& - \frac{v}{\sqrt{2}} \left(\left(\overline{u_{i,L}} \, , \, \overline{d_{i,L}} \right) \Sigma \begin{pmatrix} Y_{ij}^u u_{j,R} \\ Y_{ij}^d d_{j,R} \end{pmatrix} \mathcal{O}_2^{c_q} \left(h, \mathcal{S}_1, \mathcal{S}_2 \right) + \overline{\ell_{i,L}} \Sigma Y_{ij}^\ell \ell_{j,R} \mathcal{O}_2^{c_\ell} \left(h, \mathcal{S}_1, \mathcal{S}_2 \right) + \text{h.c.} \right) \\
& - \sum_\phi \frac{\phi}{16\pi^2} \left[g'^2 c_B^\phi B_{\mu\nu} B^{\mu\nu} + g^2 c_W^\phi W_{\mu\nu}^I W^{I\mu\nu} + g_s^2 c_G^\phi G_{\mu\nu}^a G^{a\mu\nu} \right] \\
& - \sum_\phi \frac{\phi}{16\pi^2} \left[g'^2 \tilde{c}_B^\phi B_{\mu\nu} \widetilde{B}^{\mu\nu} + g^2 \tilde{c}_W^\phi W_{\mu\nu}^I \widetilde{W}^{I\mu\nu} + g_s^2 \tilde{c}_G^\phi G_{\mu\nu}^a \widetilde{G}^{a\mu\nu} \right] ,
\end{aligned}
\tag{3.12}
$$

with the kinetic term $\mathcal{L}_{\text{gauge-ferm}}^{\text{SM}}$ including the SM fermions and gauge bosons and with the gauge covariant derivative, acting on the Goldstone matrix Σ,

$$
D_\mu \Sigma \equiv \partial_\mu \Sigma - i \frac{g}{2} \sigma^I W_\mu^I \Sigma + i \frac{g'}{2} B_\mu \Sigma \sigma^3 .
\tag{3.13}
$$

As outlined above, the purpose of this eDMEFT is the description of DM models with a dark fermion while minimising the assumptions for the representations of fields in the UV theory beyond the eDMEFT cutoff scale. The scalars are described as singlets in the eDMEFT but can emerge from higher $SU(2)_L$ multiplets. Their representations impact the power counting of the effective operators: singlets $\mathcal{S}_i$ result in $c_V^{\mathcal{S}_i} \sim 1/\Lambda$ from Eq. (3.12), whereas $\mathcal{S}_i$ from an $SU(2)_L$ doublet lead to $c_V^{\mathcal{S}_i} \sim v/\Lambda^2$ with the vev v of the doublet. In an analogous way, the scaling of the other Wilson coefficients can be derived and comparing the scaling behaviour of different field representations to experimental data (*cf.* the processes in Appendix A) might allow to survey the possible representations both of the Higgs scalar and of the BSM scalars $\mathcal{S}_{1,2}$ in a systematic way. In the following sections, we shall compare the eDMEFT to a set of models with a richer scalar sector and investigate whether the eDMEFT is capable of capturing the relevant DM physics and a subset of collider signatures presented in Appendix A. The latter might help identify typical signatures for the models to distinguish one model from another. The model files for the numerical analysis were created with the public `FeynRules` package [133–135] and the DM relic abundance and the cross sections were computed with the `micrOMEGAs` code [136, 137] and `MadGraph5_aMC@NLO` [138, 139].

3.3.1 SM + Complex Scalar Singlet + Fermionic Singlets

With the purpose of a sanity check of our eDMEFT, we shall compare it to a light extension of the SM scalar and fermion sectors. Here the scalar sector with the Higgs doublet Φ is augmented by a complex scalar singlet S which transforms non-trivially under a global, spontaneously broken $U(1)$ symmetry. The scalar multiplets read

$$\Phi = \frac{1}{\sqrt{2}} \begin{pmatrix} \sqrt{2}G^+ \\ v_h + \hat{h} + iG^0 \end{pmatrix} \quad , \quad S = \frac{1}{\sqrt{2}}(v_s + \hat{s} + ia) \,. \tag{3.14}$$

While the three Goldstones $G^{0,\pm}$ and the pseudoscalar singlet a are already mass eigenstates, the two CP-even, neutral scalars generally mix with each other due to the two finite vevs. Throughout our analysis, we shall use the hat notation for indicating weak eigenstates to distinguish them from the mass eigenstates. The scalar potential reads

$$-\mathcal{L} \supset V = \mu_\Phi^2 \left|\Phi\right|^2 + \lambda_\Phi \left|\Phi\right|^4 + \mu_S^2 \left|S\right|^2 + \lambda_S \left|S\right|^4 + \lambda_{\Phi S} \left|\Phi\right|^2 \left|S\right|^2 + \mu_a^2 a^2 \tag{3.15}$$

with the last term explicitly breaking the global $U(1)$ and thereby generating a parametrically small mass $m_a = \sqrt{2}\mu_a$ of the pseudo-Goldstone boson. Furthermore, the fermion sector is extended by four heavy chiral quarks $\mathcal{B}_{L,R}$, $\mathcal{T}_{L,R}$ as well as two chiral DM fermions $\chi_{L,R}$ and is described by

$$-\mathcal{L} \supset y_{\chi S} \overline{\chi_L} S \chi_R + \sum_{\mathcal{Q}} y_{\mathcal{Q}S} \overline{\mathcal{Q}_L} S \mathcal{Q}_R + \text{h.c.} \tag{3.16}$$

with the heavy chiral quarks $\mathcal{Q} = \mathcal{B}, \mathcal{T}$ and the coupling parameters $y_{\chi S}$, $y_{\mathcal{Q}S}$. The heavy quarks $\mathcal{Q}$ are charged under the $SU(3)_c \times U(1)_Y$ like their RH SM siblings, while the DM fermion transforms as a singlet under the SM gauge group. The BSM fermions transform non-trivially under the global $U(1)$ for sake of couplings to the BSM scalar singlet S. The representations of the BSM fields under $\mathcal{G}_{\text{SM}} \times U(1)$ are presented in Tab. 3.1. The resulting loop-induced decay of the pseudo-Goldstone into a pair of photons for instance prevents it from being stable on cosmological time scales. Moreover, the $U(1)$ charges prevent the BSM quarks from mixing with the SM quarks. In order to integrate out the BSM quarks, the mass of the lightest BSM quark $m_{\mathcal{Q}} = y_{\mathcal{Q}S}v_s/\sqrt{2}$, which is generated via spontaneous symmetry breaking (SSB) of the global $U(1)$, equals the cutoff scale Λ of the eDMEFT. In this simplified analysis, we consider a degenerate mass spectrum of the BSM quarks. Note that large BSM quark masses do not pose problems for the comparably small DM mass although the masses are proportional

to the BSM vev v_s altogether. The DM mass can be much smaller than the cutoff scale, *i.e.* $m_\chi = y_{\chi S} v_s / \sqrt{2} \ll \Lambda$, for $y_{\chi S} \ll 1$ and a BSM vev $v_s \lesssim \Lambda$, while $y_{\mathcal{Q}S} \gtrsim 1$ to ensure the high mass of the BSM quarks $\mathcal{Q}$.

The symmetric mass matrix of the two scalar fields in this model is given by the second derivative of the scalar potential in Eq. (3.15) and reads

$$\mathcal{M}_{\mathrm{s}} \equiv \left(\frac{\partial^2 V}{\partial \phi \partial \phi'} \right)_{\phi, \phi' = h, s} = \begin{pmatrix} 2\lambda_\Phi v_h^2 & \lambda_{\Phi S} v_h v_s \\ \lambda_{\Phi S} v_h v_s & 2\lambda_S v_s^2 \end{pmatrix} \tag{3.17}$$

and the masses of the SM Higgs and the BSM scalar are given by

$$m_{h,s}^2 = \lambda_\Phi v_h^2 + \lambda_S v_s^2 \pm \frac{\lambda_\Phi v_h^2 - \lambda_S v_s^2}{\cos 2\theta} \tag{3.18}$$

upon diagonalization. The angle θ in the orthogonal rotation matrix governs the mixing between the weak eigenstate forming the two mass eigenstates, *i.e.*

$$\begin{pmatrix} h \\ s \end{pmatrix} = \begin{pmatrix} \cos\theta & \sin\theta \\ -\sin\theta & \cos\theta \end{pmatrix} \begin{pmatrix} \hat{h} \\ \hat{s} \end{pmatrix} \equiv \mathcal{R}_\theta \begin{pmatrix} \hat{h} \\ \hat{s} \end{pmatrix}, \tag{3.19}$$

and reads

$$\theta = \frac{1}{2} \arctan \frac{\lambda_{\Phi S} v_h v_s}{\lambda_\Phi v_h^2 - \lambda_S v_s^2}. \tag{3.20}$$

Although already clear from the mass matrix in Eq. (3.17), the necessity of both vevs being nonzero for a finite mixing angle θ manifest itself once more in the expression for the mixing angle. The six free model parameters from the Lagrangian above can be traded for a different set of parameters which contains the masses, the BSM vev,

Field	$SU(3)_c$	$SU(2)_L$	$U(1)_Y$	global $U(1)$
S	**1**	**1**	0	$+1$
$\mathcal{T}_L$	**3**	**1**	4/3	$+1/2$
$\mathcal{T}_R$	**3**	**1**	4/3	$-1/2$
$\mathcal{B}_L$	**3**	**1**	$-2/3$	$+1/2$
$\mathcal{B}_R$	**3**	**1**	$-2/3$	$-1/2$
χ_L	**1**	**1**	0	$+1/2$
χ_R	**1**	**1**	0	$-1/2$

Table 3.1: Quantum numbers of BSM fields in one-singlet extension.

and the mixing angle, *i.e.* $\{m_s, m_a, m_\chi, m_\mathcal{Q}, v_s, \theta\}$. The relations for the parameters are relegated to Appendix B.1. The theoretical and experimental constraints are presented in Appendix C.1 and the subsequent numerical investigation is based on sampling random parameter points. Taking the parameters $m_h = 125\,\text{GeV}$, $v_h = 246\,\text{GeV}$, and $m_{\mathcal{B},\mathcal{T}} = \Lambda = 1\,\text{TeV}$, the ranges for the other parameters read

$$
m_s \in [m_h/2, \Lambda] \quad , \quad m_a \in [1\,\text{GeV}, 0.01 m_h] \quad , \quad m_\chi \in [m_h/2, \Lambda] \quad ,
$$
$$
v_s \in [100\,\text{GeV}, 1600\,\text{GeV}] \quad , \quad \sin\theta \in [0, 1] \ . \tag{3.21}
$$

Note the small mass $m_a \propto \mu_a$ of the pseudoscalar in comparison to the other scales in this theory which reflects the soft breaking of the global $U(1)$ in Eq. (3.15). The lower bound of the breaking parameter in the scan was chosen arbitrarily; any choice serves the purpose of comparing this model to the eDMEFT.

We shall now turn to the comparison of the collider cross sections and the predictions for the DM relic abundance. The matching conditions for this model and the eDMEFT at the cutoff scale Λ are presented in Appendix B.1.

Collider signatures

Out of many possible signatures one can study in this model, we select the mono-h and mono-Z processes for this first analysis and compute the cross sections $\sigma_{pp}^{\text{UV(EFT)}}$ in the UV model (eDMEFT) in order to compare the relative difference

$$
\xi \overset{\text{def}}{=} \left(\sigma_{pp}^{\text{EFT}} - \sigma_{pp}^{\text{UV}} \right) / \sigma_{pp}^{\text{UV}} \ . \tag{3.22}
$$

We consider LHC-like beam conditions, *i.e.* proton-proton collisions with a center-of-mass energy of 13 TeV. Since the two new scalar degrees of freedom are sufficiently light and therefore not integrated out in our scenario, we assign $\mathcal{S}_1 = s$ and $\mathcal{S}_2 = a$. The BSM quarks $\mathcal{Q}$, on the other hand, are integrated out in the eDMEFT. The processes for
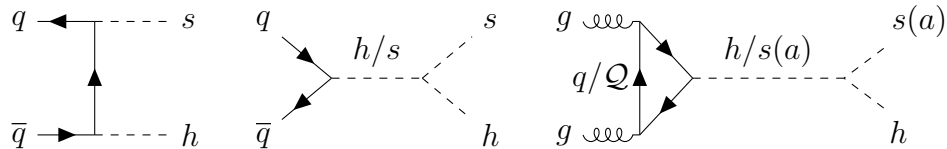
Figure 3.1: Processes for mono-h signatures with and without scalar resonances at hadron colliders. The quark loop in the third diagram involves SM quarks as well as BSM quarks. See text for mono-Z processes.

the mono-h signatures are shown in Fig. 3.1.[2] Processes with SM quarks in the initial state lead to s-channel interactions, mediated by the scalars h, s as well as to t-channel interactions. Those with gluons in the initial state, on the other hand, are possible due to the effective couplings of h, s to gluons via a loop of SM and BSM quarks.[3] For the processes with the BSM scalar s and the Z boson in the final state (*i.e.* mono-Z processes), the scalar mediators in the processes for the mono-h are replaced by the pseudoscalar a or the Z boson. The comparison of the predictions for the cross sections is shown in Fig. 3.2. The eDMEFT describes both processes, *i.e.* mono-h and mono-Z, in the mono-singlet model very well with a numerical inaccuracy of only up to one per cent without a bias for either of the two models. A bias would manifest itself in a substantial relative difference ξ which would result from mismatching contributions to the cross sections. The results in Fig. 3.2 meet our expectation as the eDMEFT contains all the mediating degrees of freedom at tree level.

Dark Matter relic abundance

Besides the pseudoscalar a, also the scalar singlet s couples to the DM fermion χ and hence mediates the DM annihilation. For this reason, a finite mixing angle θ allows the coupling of the SM Higgs to the DM fermions and thus opens more possible annihilation channels. Note that the final state is made of a pair of pseudoscalars for many parameter points in our set of parameter points due to the small mass of the pseudoscalar and a decent coupling strength $\sim \lambda_S v_s$, resulting in a large phase space for this annihilation channel. Since the spin-0 fields h, s, a are comparably light

---

[2]The Feynman diagrams in this thesis have been drawn by using `TikZ-Feynman` [140].

[3]Note that the largest SM contribution comes from the top-quark due to its large Yukawa coupling to the SM Higgs field.
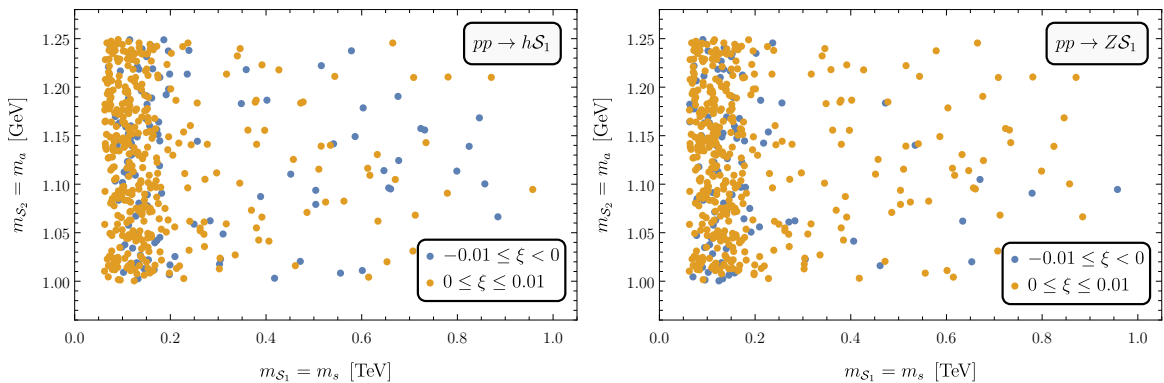
Figure 3.2: Comparison of mono-h (*left*) and mono-Z (*right*) cross sections.

and hence present in the eDMEFT, the DM annihilation processes are fully described by the eDMEFT and the DM relic abundance therein are expected to match the one in the mono-singlet extension. The comparison of the predictions for the DM relic abundance $\Omega_{\mathrm{DM}} h^2$ in the two models is shown in Fig. 3.3.[4] The heavy degrees of freedom (here the heavy chiral quarks $\mathcal{B}, \mathcal{T}$) contribute to the DM annihilation processes as additional particles in the final state via the coupling to the mediators s, a, and – due to the mixing – the SM Higgs boson h. As a result, the DM relic abundance in the mono-singlet model consequently decreases when the center-of-mass energy of the initial state opens further phase space for the DM annihilation into a pair of heavy quarks. The surge of the ratio of the DM relic abundance in the two models begins already for a DM mass smaller than the cutoff scale, $i.e.$ $m_\chi < \Lambda$, due to the kinetic energy of the annihilating DM particles. Note that the kinetic energy is expected to be significantly smaller than the DM mass for the DM to constitute *cold* DM. That is why the mismatch between the predictions sets in close to the cutoff scale $\Lambda = 1\,\mathrm{TeV}$. To sum up, the eDMEFT captures the relevant processes of the singlet extension and the comparison of the predictions for the DM relic abundance shows the DM mass range in which the eDMEFT is valid. In conclusion, the eDMEFT behaves as anticipated and we can move on to a model which features more degrees of freedom.

---

[4]For the sake of readability, the subscript 'DM' for the DM relic abundance $\Omega_{\mathrm{DM}} h^2$ is omitted in the figures of this chapter.
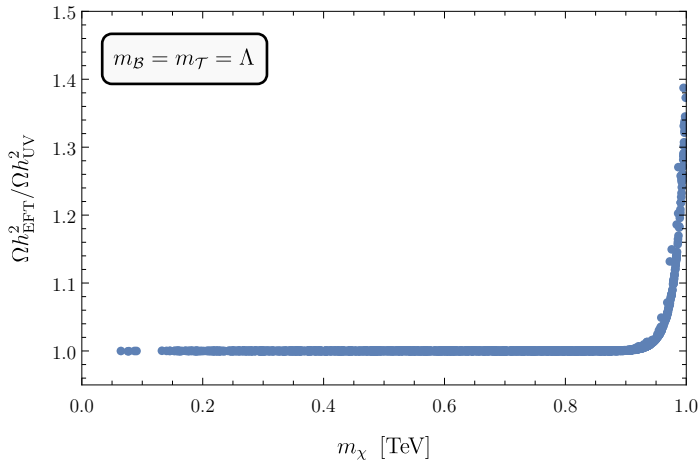
Figure 3.3: Ratio of the DM relic abundance in the eDMEFT and the one in the mono-singlet model. Close to the new-physics scale $\Lambda = 1\,\mathrm{TeV}$ the heavy degrees of freedom impact the DM annihilation cross section and the eDMEFT cannot accurately describe the model any longer.

3.3.2 2HDM + Pseudoscalar Singlet + Fermionic DM

After the sanity check above, we shall compare the eDMEFT to an extension of the two-Higgs doublet model (2HDM) as one of many well motivated new-physics models. The 2HDM has been discussed, *e.g.*, in Refs. [141–145] and Ref. [142] shall be closely followed in the present introduction. The most general Lagrangian of the 2HDM reads

$$
\begin{aligned}
\mathcal{L}_{\text{2HDM}} = &\sum_j |D_\mu \Phi_j|^2 - y^d_{j,mn} \overline{Q_m} \Phi_j d_{n,R} - y^u_{j,mn} \overline{Q_m} \widetilde{\Phi}_j u_{n,R} - y^\ell_{j,mn} \overline{L_m} \Phi_j \ell_{n,R} \\
&- M_{11}^2 |\Phi_1|^2 - M_{22}^2 |\Phi_2|^2 - M_{12}^2 \left(\Phi_2^\dagger \Phi_1 + \text{h.c.}\right) - \frac{\lambda_1}{2}|\Phi_1|^4 - \frac{\lambda_2}{2}|\Phi_2|^4 \\
&- \lambda_3 |\Phi_1|^2 |\Phi_2|^2 - \lambda_4 \left|\Phi_1^\dagger \Phi_2\right|^2 - \frac{1}{2}\lambda_5 \left[\left(\Phi_2^\dagger \Phi_1\right)^2 + \text{h.c.}\right] \\
&- \left(\lambda_6 |\Phi_1|^2 + \lambda_7 |\Phi_2|^2\right)\left(\Phi_2^\dagger \Phi_1 + \text{h.c.}\right)
\end{aligned}
\tag{3.23}
$$

with the gauge covariant derivative D_μ from Eq. (1.7), the usual notation $\widetilde{\Phi}_j \equiv i\sigma^2 \Phi_j^*$, and the two Higgs doublets

$$
\Phi_j = \frac{1}{\sqrt{2}}\begin{pmatrix} \sqrt{2}\hat{\phi}_j^+ \\ v_j + \hat{\rho}_j + i\hat{\eta}_j \end{pmatrix} \quad \text{with } j = 1, 2
\tag{3.24}
$$

in the weak eigenbasis. Like already in the previous sections, those fields dressed with a hat are not mass eigenstates and their rotations to the mass basis shall be discussed below. Rather than the general Lagrangian in Eq. (3.23), it is customary to eliminate the last two terms by imposing a (softly broken) discrete $\mathbb{Z}_2$ symmetry with the doublets transforming as $\Phi_1 \to \Phi_1$ and $\Phi_2 \to -\Phi_2$. This discrete symmetry is softly broken by $M_{12}^2 \neq 0$ in general.[5] Moreover, assuming real parameters M_{12}^2 and λ_5 renders the scalar potential CP invariant. It is useful to introduce the so-called 'Higgs basis' with the two Higgs doublets defined by the orthogonal rotation

$$
\begin{pmatrix} \Phi_h \\ \Phi_H \end{pmatrix} = \begin{pmatrix} c_\beta & -s_\beta \\ s_\beta & c_\beta \end{pmatrix}\begin{pmatrix} \Phi_1 \\ \Phi_2 \end{pmatrix}
\tag{3.25}
$$

and the rotation angle β is determined by the two vevs, *i.e.*

$$
\tan\beta = \frac{v_2}{v_1} \quad \text{with } v_1^2 + v_2^2 = v_h^2 \approx (246\,\text{GeV})^2 \; .
\tag{3.26}
$$

---

[5]We shall examine a 2HDM with an *exact* discrete $\mathbb{Z}_2$ symmetry in Chapter 4.

Defining the angle β in this way results in the characteristic feature of the Higgs basis which is that only one of the two doublets gets a vev. Moreover, the mass matrices of the charged scalars as well as of the neutral pseudoscalars are diagonalized therein. The doublets in the Higgs basis read

$$\Phi_h = \frac{1}{\sqrt{2}} \begin{pmatrix} \sqrt{2}G^+ \\ v_h + \hat{h} + iG^0 \end{pmatrix} \quad , \quad \Phi_H = \frac{1}{\sqrt{2}} \begin{pmatrix} \sqrt{2}H^+ \\ \hat{H} + iA \end{pmatrix} . \tag{3.27}$$

The scalars $\hat{h}$ and $\hat{H}$ are eventually linear combinations of the $125\,\mathrm{GeV}$ scalar, which was discovered at LHC and shall be referred to as the SM Higgs boson h, and the second CP-even physical field H. The mass eigenstates are related to the weak eigenstates and to the eigenstates in the Higgs basis via

$$\begin{pmatrix} h \\ H \end{pmatrix} = \begin{pmatrix} -s_\alpha & c_\alpha \\ -c_\alpha & -s_\alpha \end{pmatrix} \begin{pmatrix} \hat{\rho}_1 \\ \hat{\rho}_2 \end{pmatrix} = \begin{pmatrix} -s_{\alpha-\beta} & c_{\alpha-\beta} \\ -c_{\alpha-\beta} & -s_{\alpha-\beta} \end{pmatrix} \begin{pmatrix} \hat{h} \\ \hat{H} \end{pmatrix} , \tag{3.28}$$

and they equal their respective eigenstate in the Higgs basis for the particular choice $\alpha - \beta = -\pi/2$. This relation of the two angles is called the Higgs alignment limit. Since the observed scalar matches the SM prediction very accurately (see, *e.g.*, Ref. [146] for constraints from the Higgs signal strengths), the Higgs alignment limit shall be imposed in the remainder, *i.e.* we consider $\hat{h} \equiv h$ and $\hat{H} \equiv H$.

The Yukawa sector of the 2HDM in the first line of Eq. (3.23) generally leads to flavor-changing neutral currents (FCNCs) since the two Yukawa matrices for the fermions $f = u, d, \ell$ are not diagonalizable simultaneously. However, contributions must be suppressed in the theory due to compelling experimental evidence (*e.g.* from kaon mixing) for the smallness of FCNCs. One straightforward way to avoid dangerous tree-level contributions in the 2HDM is assuming that the BSM Yukawa matrix is proportional to the SM Yukawa matrix, with different proportionality factors, *i.e.*

$$y_\phi^f = \epsilon_\phi^f y_{\mathrm{SM}}^f \qquad \text{with} \quad y_{\mathrm{SM}}^f \equiv \sqrt{2}\frac{m_f}{v_h} \tag{3.29}$$

for the three generations of fermions $f = u, d, \ell$ with respective masses m_f. This leads to the so-called Aligned Yukawa Model [147–151]. To avoid radiative deviations from the SM Yukawa structure, it is customary to impose additional $\mathbb{Z}_2$ symmetries, such that the doublets couple selectively to the fermion fields.[6] There are four possible ways to

---

[6] In a more extended framework, the $\mathbb{Z}_2$ symmetry can be superseded by a gauge symmetry. See, *e.g.*, Refs. [152, 153].

impose such symmetries, leading to the type-I, type-II, type-X (or 'lepton specific') and type-Y (or 'flipped') variants of the 2HDM. In the Higgs alignment limit (*i.e.* $\epsilon_h^f = 1$), the coupling modifiers of the BSM bosons are functions of $\tan\beta$ and summarized in Tab. 3.2. Conventionally, the second doublet Φ_2 couples to up-type quarks in each type. The characteristic feature of the type-I 2HDM is that the first doublet is decoupled from the fermions, such that only the second doublet Φ_2 couples to the fermions. In contrast, the other three types describe couplings of both doublets to the fermions in different combinations. The second doublet couples in the type-II 2HDM exclusively to the up-type quarks, while Φ_1 can interact with the other two types of fermions. The type-X 2HDM is called lepton specific as only Φ_1 couples to the leptons and type-Y 2HDM features interactions between Φ_1 and down-type quarks.

In the following analysis we shall consider the type-II 2HDM. Its Lagrangian for the Yukawa sector reads

$$-\mathcal{L} \supset y_2^u \overline{Q} \widetilde{\Phi}_2 u_R + y_1^d \overline{Q} \Phi_1 d_R + y_1^\ell \overline{L} \Phi_1 \ell_R + \text{h.c.} \tag{3.30}$$

$$\supset \frac{y_2^u}{\sqrt{2}} \overline{u}u \,(v_2 + \hat{\rho}_2) + \frac{y_1^d}{\sqrt{2}} \overline{d}d \,(v_1 + \hat{\rho}_1) + \frac{y_1^\ell}{\sqrt{2}} \overline{\ell}\ell \,(v_1 + \hat{\rho}_1) \tag{3.31}$$

with the 3×3 Yukawa matrices $y_{1,2}^f$. Identifying the masses $m_u = y_2^u v_2/\sqrt{2}$, $m_{d,\ell} = y_1^{d,\ell} v_1/\sqrt{2}$ and replacing the weak eigenstates by the mass eigenstates via Eq. (3.28), we find

$$-\mathcal{L} \supset \frac{m_u}{v_h} \overline{u}u \left(\frac{c_\alpha}{s_\beta} h - \frac{s_\alpha}{s_\beta} H \right) + \left(\frac{m_d}{v_h} \overline{d}d + \frac{m_\ell}{v_h} \overline{\ell}\ell \right) \left(-\frac{s_\alpha}{c_\beta} h - \frac{c_\alpha}{c_\beta} H \right) \tag{3.32}$$

and the prefactors are recognized as the Yukawa modifiers ϵ_ϕ^f. The modifiers for the four types of 2HDM in the alignment limit are shown in Tab. 3.2.

	Type I	Type II	Type X	Type Y	Inert
Φ_1	$-$	d, ℓ	ℓ	d	$-$
Φ_2	u, d, ℓ	u	u, d	u, ℓ	$-$
ϵ_H^u	$\cot\beta$	$\cot\beta$	$\cot\beta$	$\cot\beta$	0
ϵ_H^d	$\cot\beta$	$-\tan\beta$	$\cot\beta$	$-\tan\beta$	0
ϵ_H^ℓ	$\cot\beta$	$-\tan\beta$	$-\tan\beta$	$\cot\beta$	0

Table 3.2: Types of 2HDMs and modifiers of Yukawa interactions between the BSM Higgs boson and fermions in the Higgs alignment limit, *i.e.* $\epsilon_h^f = 1$. The expressions can be found in Ref. [154].

Furthermore, the scalar and fermion sectors of the type-II 2HDM are extended by $SU(2)_L$ singlets. Allowing for a soft breaking of the CP symmetry in the scalar sector, the Lagrangian with an additional real pseudoscalar $\hat{P} : (\mathbf{1}, \mathbf{1}, 0)$ reads [154]

$$-\mathcal{L} \supset \left(\frac{M_{PP}^2}{2} + \lambda_{11P} |\Phi_1|^2 + \lambda_{22P} |\Phi_2|^2 \right) \hat{P}^2 + \frac{\lambda_P}{4} \hat{P}^4 + \left(i\mu_{12P} \Phi_1^\dagger \Phi_2 \hat{P} + \text{h.c.} \right) \quad (3.33)$$

with the CP-violating interaction in the last term. The CP-conserving Lagrangian for the fermionic DM is given by

$$\mathcal{L}_\chi = \overline{\chi} i \displaystyle{\not}\partial \chi - m_\chi \overline{\chi} \chi - i y_{\chi P} \overline{\chi} \gamma^5 \chi \hat{P} \,. \quad (3.34)$$

EW symmetry breaking triggers the mixing between the singlet field $\hat{P}$ and the pseudoscalar $\hat{A}$ from the second doublet in the Higgs basis, while the mixing with the pseudoscalar G^0 is absent in the Higgs alignment limit. The entries of the pseudoscalar mass matrix read

$$(\mathcal{M}_{\text{ps}})_{22} = - \left(2M_{12}^2 / s_{2\beta} + \lambda_5 v_h^2 \right) \quad (3.35)$$

$$(\mathcal{M}_{\text{ps}})_{23} = -\mu_{12P} v_h \quad (3.36)$$

$$(\mathcal{M}_{\text{ps}})_{33} = M_{PP}^2 + \left(\lambda_{11P} c_\beta^2 + \lambda_{22P} s_\beta^2 \right) v_h^2 \,. \quad (3.37)$$

The mass matrix can be diagonalized via a rotation matrix $\mathcal{R}_\theta$, defined in Eq. (3.19), with the angle that satisfies

$$\tan 2\theta = \frac{2 \left(\mathcal{M}_{\text{ps}} \right)_{23}}{\left(\mathcal{M}_{\text{ps}} \right)_{22} - \left(\mathcal{M}_{\text{ps}} \right)_{33}} \,. \quad (3.38)$$

The theoretical and experimental constraints are discussed in Appendix C.2. The set of the physical scalar mass states is composed by two CP-even states, h, H, two CP-odd states, a, A and two electrically charged Higgs $H^\pm$. Expressing their masses in terms of the model parameters, we find

$$m_h^2 = \left(\lambda_2 \sin^2 \beta + \lambda_{345} \cos^2 \beta \right) v^2 \quad (3.39)$$

$$m_H^2 = -\frac{2M_{12}^2}{\sin 2\beta} + (\lambda_2 - \lambda_{345}) v^2 \sin^2 \beta \quad (3.40)$$

$$m_{H^\pm}^2 = -\frac{2M_{12}^2}{\sin 2\beta} - \frac{\lambda_4 + \lambda_5}{2} v^2 \quad (3.41)$$

$$m_{A,a}^2 = \frac{1}{2\cos 2\theta} \left((\cos 2\theta \pm 1) m_{AA}^2 + (\cos 2\theta \mp 1) m_{PP}^2 \right) \,. \quad (3.42)$$

Imposing the Higgs alignment limit leads to the condition

$$\lambda_1 = \frac{\lambda_2 \sin^2 \beta + \lambda_{345} \cos 2\beta}{\cos^2 \beta} \tag{3.43}$$

and thus reduces the number of free model parameters. Similar to Ref. [155], we shall adopt the following set of free parameters for our numerical study:

$$\{m_H^2, m_{H^\pm}^2, m_A^2, m_a^2, m_\chi, \theta, \beta, \lambda_3, \lambda_P, \lambda_{11P}, \lambda_{22P}, y_{\chi P}\}. \tag{3.44}$$

The relations between the original model parameters and the new set are presented in Appendix B.2. The 2HDM+a will be compared to the eDMEFT in two scenarios. First, we shall consider the case in which both mediator $\mathcal{S}_{1,2}$ in the eDMEFT are pseudoscalar and hence identify $\mathcal{S}_1 \equiv A$ and $\mathcal{S}_2 \equiv a$. Consequently, the scalars $H, H^\pm$ are heavy and integrated out in the eDMEFT. The theoretical and experimental constraints that we have summarized in Appendix C.2 require a rather compressed mass spectrum for the fields originating from the doublet. The mass of the pseudoscalar a is taken lighter than its sibling A and also the DM fermion χ is assumed to be lighter than the heavy pseudoscalar. For the subsequent numerical analysis the model parameters have been varied over the following ranges:

$$m_A \in [\Lambda - 100\,\text{GeV}, \Lambda] \quad , \quad m_a \in [1\,\text{GeV}, m_A] \quad , \quad m_{H,H^\pm} = \Lambda \quad ,$$
$$m_\chi \in [m_a/10, m_A] \quad , \quad \lambda_{P,11P,22P} \in [0, 4\pi] \quad , \quad \lambda_3 \in [0.01, 4\pi] \quad ,$$
$$\beta \in [\pi/4, 0.468\pi] \quad , \quad \theta \in [0, 0.7] \quad , \quad y_{\chi P} \in [0.01, 3] \quad . \tag{3.45}$$

In the second scenario the masses of the neutral scalar and pseudoscalar are interchanged, *i.e.* $m_A = \Lambda$ and $\Lambda - 100\,\text{GeV} \le m_H \le \Lambda$. Note that the Lagrangian in Eq. (3.34) and the mixing of the pseudoscalars does not feature an interaction between DM and the SM Higgs boson. That is why the DM fermion can be much lighter than the SM Higgs mass in spite of the strong constraint from the small difference between the measurement and SM prediction of the Higgs decay width, outlined in Chapter 1.

Dark Matter relic abundance

In analogy to the examination in the previous model, we shall compare the prediction for the DM relic abundance in UV model to the one in the eDMEFT in order to assess the capability of capturing the relevant features of the UV model with the eDMEFT. First, we shall consider the scenario with two comparably light pseudoscalars.

While the t- and u-channel with the pseudoscalars a, A in the final state are the same in both the UV model and in the eDMEFT (as only the pseudoscalars couple to the DM fermion), the pseudoscalar-mediated s-channel can lead to deviation if the mediator goes into a final state that contains particles not present in both theories. Depending on the center-of-mass energy of the two annihilating DM particles, the heavy Higgs H with the mass $m_H = \Lambda$ can be produced, accompanied by the light pseudoscalar a. This process cannot be captured by the eDMEFT and we hence expect an underestimated annihilation cross section in the eDMEFT for DM masses $m_\chi \gtrsim (\Lambda + m_a)/2$ because this process with a different final state contributes constructively to the DM annihilation cross section. Consequently, the DM relic abundance in the UV model is smaller than in the eDMEFT. The results are shown in Fig. 3.4 and the accurate description of the UV model by the eDMEFT is given up to the DM mass slightly larger than half of the cutoff scale. For $m_\chi \gtrsim 540\,\text{GeV}$ the predictions of the DM relic abundance begin to feature deviations in our numerical analysis. Note that there are still parameter points in the mass regime in which the eDMEFT can fail that lead to a good agreement between the two models because of a sufficient suppression of the final state with the heavy scalar H.

It is enlightening to study the second scenario as this appears to render the eDMEFT description for this particular scenario in general futile already for $m_\chi \gtrsim 0.2\Lambda$. In this scenario the light pseudoscalar a as well as the heavy scalar H are the additional propagating degrees of freedom. Unlike the previous scenario, only one of the two mediators in the eDMEFT couples to the DM fermions, although also the heavy pseudoscalar contributes to DM annihilations in the UV model. The DM annihilation can proceed either
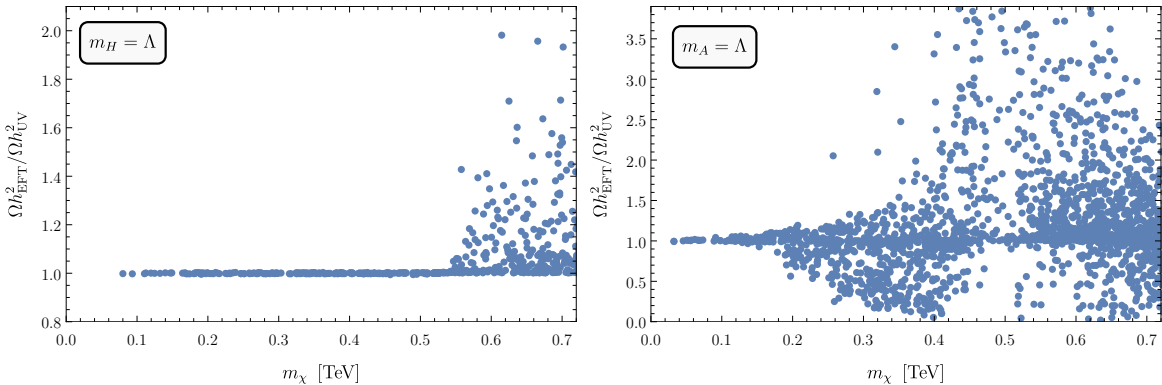
Figure 3.4: Ratio of the DM relic abundance for the eDMEFT and the 2HDM+a with the new-physics scale $\Lambda = 1\,\text{TeV}$. *Left*: The pseudoscalars A, a are the light mediators in the eDMEFT. *Right*: The fields H, a act as mediators in the eDMEFT.

via t-channel annihilation with two pseudoscalars in the final state or via s-channel processes into one pseudoscalar and one scalar. The t-channel DM annihilation is captured by the eDMEFT for DM masses $m_\chi \lesssim (\Lambda + m_a)/2$; larger DM masses lead to differences and the eDMEFT is therefore expected to fail for those DM masses. For the following discussion, we consider the DM mass range to $m_\chi \lesssim \Lambda/2$. In this mass regime, the s-channel DM annihilations create the final state with the light pseudoscalar a and one of the scalars H, h. Since the mass of the former scalar is constrained to be rather close to the mass of the heavy pseudoscalar A and therefore to the cutoff scale (*cf.* Appendix C.2), we can focus on the channels $\overline{\chi}\chi \to A, a \to ha$. The matrix element for the s-channel annihilation mediated by the heavy pseudoscalar A with the light pseudoscalar and the SM Higgs h in the final state scales with $y_{\chi P} \sin\theta \lambda_A v/(s - m_A^2)$, where λ_A corresponds to the vertex factor for Aah. Analogously, the contribution of the s-channel annihilation via a scales with $y_{\chi P} \cos\theta \lambda_a v/(s - m_a^2)$ with the aah vertex factor λ_a. Since the eDMEFT can capture only the a-mediated process, the ratio of the DM relic abundance in the two theories can be estimated as

$$\frac{\Omega h_{\text{EFT}}^2}{\Omega h_{\text{UV}}^2} \sim \frac{\sigma_{\text{UV}}}{\sigma_{\text{EFT}}} \sim \left| 1 - \frac{y_{\chi P} \tan\theta}{m_A^2 - s} \left(s - m_a^2\right) \frac{\lambda_A}{\lambda_a} \right|^2 . \tag{3.46}$$

Note that an accurate calculation requires the evaluation of the integral in Eq. (2.16), but the relation allows to explain the relevant features in Fig. 3.4. While the sign of the first fraction in the second term is positive for any choice of parameters in the DM mass range of consideration, the remaining terms can be positive or negative due to the random values for the center-of-mass energy $\sqrt{s} \approx 2m_\chi$, the pseudoscalar mass m_a, and the couplings $\lambda_{A,a}$. This possibility of a sign flip results in ratios of the DM relic abundance in the two models being larger or smaller than unity. Moreover, the relation in Eq. (3.46) reflects the resonance for $s \to m_A^2$ that is visible in Fig. 3.4.

This feature is absent in the previous scenario (both pseudoscalars are degrees of freedom in the eDMEFT) as the scalar H does not act as a DM mediator at tree level. The analysis of the extended 2HDM demonstrates that the eDMEFT as a model for capturing the relevant physics reveals its limitations if a particle that is not part of the eDMEFT particle spectrum acts as a mediator of, *e.g.*, DM annihilations and possesses a mass not much larger than the masses of the other mediators. It is not surprising that an EFT lacks in accuracy of describing the physics if the cutoff scale is not much larger than the particle masses. If the theoretical and experimental constraints allowed a substantial mass difference between the heavy pseudoscalar A and the other scalar masses from the $SU(2)_L$ doublet, the second term in parentheses in Eq. (3.46) would

get suppressed by the pseudoscalar mass and the ratio of the DM relic abundance in the two models would approach unity – as expected for a well-behaving EFT.

Since the scenario with $m_A = \Lambda$ can generally suffer from large differences between the predictions for the DM relic abundance, an analysis of collider signatures is not promising. Rather limited mass difference between the states from doublets and higher multiplets are expected due to perturbativity constraints on the coupling parameters which determine the scalar masses. Consequently, the fields with masses at the eDMEFT cutoff scale might still contribute to processes to a non-negligible extent and therefore not be eligible to get integrated out. This can be ameliorated by taking the relevant DM annihilation channels and derive the Wilson coefficient for the effective operator $\overline{\chi}\chi ha$. This matching would render the eDMEFT prediction for the DM annihilation more reliable and consequently improve the right plot in Fig. 3.4 in the mass regime $m_\chi \lesssim \Lambda/2$. Neither the resonance nor the annihilation channels with the heavy pseudoscalar in the final state can be described by the eDMEFT as they are outside the range of validity due to the large center-of-mass energy.

With this improvement of the analysis, potentially interesting signatures could be studied as a next step with the two pseudoscalars in the eDMEFT particle spectrum. Besides the mono-h and mono-Z signatures, that have been considered in the study of the one-singlet extension in Section 3.3.1, further signatures from Tab. A.2 in the appendix might reveal which signatures are most promising to distinguish between UV models. Moreover, the pattern of suppression in the Wilson coefficients for several UV models with different representations of the fields is arguably worth being investigated to assess the possibility to differentiate between the UV models.

In conclusion, we demonstrated the capabilities of the eDMEFT in the context of describing the relevant DM annihilation processes and mono-h/Z signatures at colliders. Besides a good agreement for the first, minor extension of the SM in these regards, the comparison to the extended 2HDM revealed limitations of the eDMEFT that we explained and that are not surprising due to the small mass differences for the fields from the BSM doublet. Further UV models with scalar mediators for, *e.g.*, enhancing the mono-h/Z cross sections at colliders are worth being studied in light of additional collider signatures in order to assess the power of the eDMEFT approach in a comprehensive way.

In line of the power of EFTs for capturing many UV theories, we shall study another EFT in the next chapter in the context of a second particle physics puzzle.

Chapter 4

Baryon Asymmetry in Scalar Dark Matter Extensions

After the coarse discussion of a subset of the shortcomings of the SM in Chapter 1 and the introduction to a new EFT approach in light of DM physics in the previous chapter, we shall now take one more shortcoming into account. Before investigating both DM and the generation of the baryon asymmetry of the Universe in an EFT framework for a specific DM model in Section 4.3 (see Ref. [3] for the publication), we shall first examine the experimental and theoretical details of the baryon asymmetry in the next section and then move on to some prominent models in Section 4.2.

4.1 Theoretical and Experimental Background

Following Section 24.4 in Ref. [156], the measurements of the CMB as well as of the primordial abundance of light elements (*e.g.* D, ^{3}He, ^{4}He, ^{7}Li) allow to quantify the baryon-to-photon ratio η as

$$5.8 \times 10^{-10} \leq \eta \equiv \frac{n_B}{n_\gamma} \leq 6.5 \times 10^{-10} \tag{4.1}$$

with the difference n_B of the baryon and anti-baryon number densities and the T-dependent photon number density

$$n_\gamma = \frac{\zeta(3)}{\pi^2} g_* T^3, \tag{4.2}$$

where $\zeta(3) \approx 1.202$ is the Riemann ζ-function and $g_* = 2$ is the number of polarization states of the photon [157]. In the subsequent analysis we shall consider the

mean value $\eta_{\mathrm{ref}} = 6.15 \times 10^{-10}$ as the reference value for the baryon asymmetry. The measurements of the primordial abundance of light elements are confronted with their theoretical predictions of the big bang nucleosynthesis (BBN) model in Fig. 4.1. While the measurement of ^{7}Li poses a discrepancy (known as the *lithium problem*), the measurements and predictions of the abundances of the other isotopes shown in the figure match the results from CMB measurements. The right panel shows the span of results for the baryon-to-photon ratio with respect to different approaches.

Intuitively, one may expect a perfect balance between ordinary matter and antimatter if the particle interactions are independent of the type of matter. The mere absence of antimatter in the observable Universe drives one to think about consequences for the particle physics model to explain the imbalance.[1] Assuming CPT invariance (*i.e.*,

---

[1]Note that antimatter can be produced at colliders and is present in the observable Universe as secondary particles in cosmic rays but not as planets, stars, or gas clouds (see, *e.g.*, Ref. [159]).
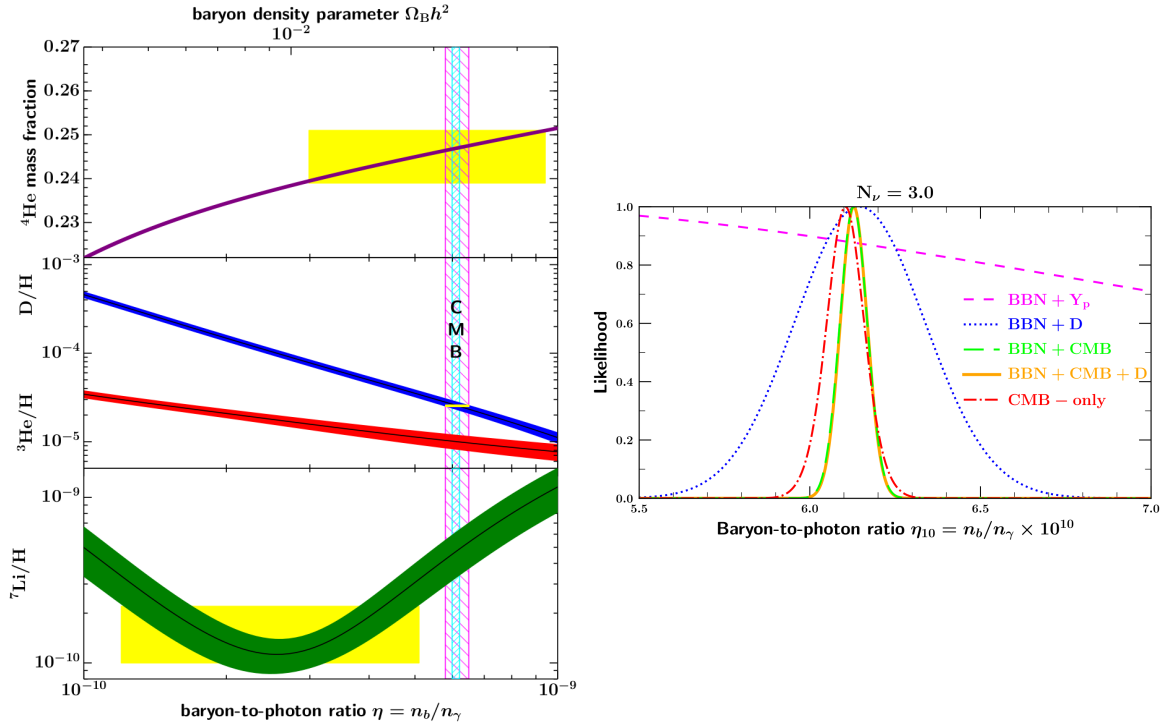
Figure 4.1: Measurements of baryon-to-photon ratio. *Left:* The curved bands show the predicted abundance of light elements with respect to the baryon-to-photon ratio and the baryon density. The measured abundances are indicated by the yellow areas, while the vertical lines correspond to the results of CMB and BBN measurements. *Right:* Results for the baryon-to-photon ratio from various measurements of BBN and CMB. Taken from Refs. [156, 158].

the invariance of a physical process after considering the opposite type of matter and parity and time reversal), it was realized by Sakharov in 1967 [160] that the successful generation of the baryon asymmetry requires three vital ingredients:[2]

(1) B violation: neither baryon nor lepton number is conserved in the SM because of the $U(1)_{B+L}$ anomaly, as shown by 't Hooft in 1976 [162]. At high energies, the B-violating processes are mediated by sphalerons (see details below) [163, 164].

(2) C and CP violation: both the charge conjugation symmetry C and the CP symmetry of charge conjugation and parity transformation are violated in the weak interactions of the SM, as shown, *e.g.*, in Ref. [165] (see also Ref. [15]).

(3) Departure from thermal equilibrium which can be realized, *e.g.*, by either the out-of-equilibrium decay of a heavy particle or a phase transition with a potential barrier between the two local minima (see discussion below).

The three Sakharov conditions and their connections to the SM shall be elaborated on in the following.

Baryon number violation

While the necessity of the first requirement is obvious (because a physical system with initial zero net baryon number cannot evolve to a state with a finite net baryon number if B is not violated), the precise mechanism of B violation in the SM is rather sophisticated, as we shall see in the following.

The vacuum structure of a non-abelian gauge theory, like $SU(2)_L$ for instance, features an infinite number of vacua which are degenerate in energy *in the absence of fermions*. Including fermions in the consideration leads to a modified vacuum structure such that it features a global minimum (*cf.* Fig. 4.2). The subsequent description of the non-conservation of the fermion number closely follows the review by Rubakov and Shaposhnikov [167] and the lecture notes by Bernreuther [15].

The SM features the following classically conserved vector currents for the baryon number B and lepton number L:

$$\partial^\mu J_\mu^B = \frac{1}{3} \sum_q \partial^\mu \left(\overline{q_L} \gamma_\mu q_L + \overline{q_R} \gamma_\mu q_R \right) = 0 \tag{4.3}$$

$$\partial^\mu J_\mu^L = \sum_\ell \partial^\mu \left(\overline{\ell_L} \gamma_\mu \ell_L + \overline{\ell_R} \gamma_\mu \ell_R \right) = 0 \tag{4.4}$$

---

[2]Note that the experimental limits for CPT-violating interactions are remarkably strong and suggest that the CPT symmetry is preserved in nature (*cf.* Refs. [10, 161] for the limits).

The simple Lie group and gauge group $\mathcal{G}$ of dimension $d_{\mathcal{G}}$ features the anomaly equation for the vector currents with different chiralities of the generic fermion field Ψ,

$$\partial^{\mu}\overline{\Psi_{L,R}}\gamma_{\mu}\Psi_{L,R} = \mp c_{L,R}F_{\mu\nu}^{(i)}\widetilde{F}^{(i)\mu\nu}\,, \tag{4.5}$$

with the field strength tensor $F_{\mu\nu}^{(i)}$ for the (non-)abelian gauge group, its dual $\widetilde{F}_{\mu\nu}^{(i)}$, the index $i = 1,\ldots,d_{\mathcal{G}}$, and chirality-dependent constants $c_{L,R}$ [15]. Since QCD is not a chiral theory, *i.e.* gluons do not differentiate between LH and RH quarks in the interactions, the constants are equal ($c_L = c_R$) and QCD does consequently not feature this anomaly. The EW sector, however, does distinguish and the divergences of the two current from above are not conserved at quantum level. One finds

$$\partial^{\mu}J_{\mu}^{B} = \partial^{\mu}J_{\mu}^{L} = \frac{N_f}{32\pi^2}\left(-g^2 W_{\mu\nu}^{I}\widetilde{W}^{I\mu\nu} + g'^2 B_{\mu\nu}\widetilde{B}^{\mu\nu}\right)\,, \tag{4.6}$$

which immediately shows that $B - L$ is a conserved quantity in the SM, whereas the sum $B+L$ is not [15]. The right-hand side can be cast as a divergence of the current [15]

$$K^{\mu} = -\frac{g^2}{16\pi^2}\varepsilon^{\mu\nu\kappa\lambda}W_{\nu}^{I}\left(\partial_{\kappa}W_{\lambda}^{I} + \frac{g}{3}\varepsilon^{IJK}W_{\kappa}^{J}W_{\lambda}^{K}\right) + \frac{g'^2}{32\pi^2}\varepsilon^{\mu\nu\kappa\lambda}B_{\nu}B_{\kappa\lambda}\,. \tag{4.7}$$

The next step involves the integration over spacetime. The term with the weak hypercharge field strength tensor does not contribute to this integral for well-behaving fields, *i.e.* fields vanishing at infinity, and the integration eventually leads to

$$\int \mathrm{d}^4x\,\partial^{\mu}K_{\mu} = \frac{g^3}{96\pi^2}\int_{\partial V_4}\mathrm{d}n^{\mu}\,\varepsilon_{\mu\nu\kappa\lambda}\varepsilon^{IJK}W^{I\nu}W^{J\kappa}W^{K\lambda} = \Delta N_{\mathrm{CS}} \tag{4.8}$$
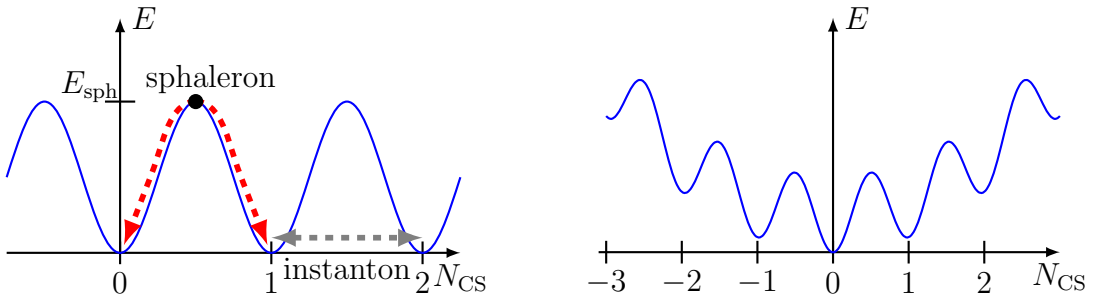
Figure 4.2: Qualitative vacuum structure of non-abelian theories like $SU(2)_L$. *Left*: The instanton and sphaleron processes are indicated. *Right*: The fermion contributions lead to a global minimum at $N_{\mathrm{CS}} = 0$ which eventually results in the washout effect for sufficiently rapid transitions between the local minima (*cf.* Ref. [166]).

with the surface ∂V_4 of the four-dimensional volume, the corresponding unit normal vector n^μ, and the Chern-Simons number N_{CS} [15]. That is, the divergence of the current equals the change in the Chern-Simons number. A one-dimensional slice of the hypersurface is shown in Fig. 4.2. The 'topological charge' ΔN_{CS} governs the change of baryon and lepton number. The integral of the left-hand side in Eq. (4.6) gives rise to the selection rule [15]

$$\Delta B = \Delta L = N_f \Delta N_{\mathrm{CS}} \,. \tag{4.9}$$

A consequence of this selection rule is that both baryon number B and lepton number L change by an integer multiple of the number of fermion generations due to the (non-perturbative) transition from one vacuum to another, as depicted in Fig. 4.2. The SM features three experimentally confirmed fermion generations and does therefore neither permit proton decay ($|\Delta B| = 1$) nor the oscillation of an electrically neutral baryon to its antipartner ($|\Delta B| = 2$). This prediction of the absence of these two B-violating processes both at the perturbative and at the non-perturbative level motivates dedicated searches which we shall summarize towards the end of this section.

We have seen so far that the combination $B + L$ is violated in the SM by the non-perturbative transition from one vacuum state to another and thus allows to fulfil the first Sakharov condition. The fundamental concepts of quantum mechanics allow a field configuration in one vacuum state to either tunnel through (instanton) or passing over (sphaleron) the potential barrier separating distinct vacua. The temperature-dependent height of the potential barrier is associated with the sphaleron energy

$$E_{\mathrm{sph}}\left(T\right) = \frac{2m_W\left(T\right)}{\alpha_W} \times \mathcal{O}\left(1.5 - 2.7\right) \tag{4.10}$$

and is governed by the mass of the W boson and the weak coupling parameter $\alpha_W \equiv g^2/(4\pi)$ [166]. The transition amplitude of the instanton process is exponentially suppressed and with $\sim \mathcal{O}(10^{-160})$ virtually unobservable in experiments today [167, 168]. The sphaleron process, however, turns out to be appealing because of the high temperatures present in the early Universe. It was shown in Refs. [157, 169] that the sphaleron processes are active, in equilibrium with the thermal bath, and effectively prevent the creation of a finite net baryon number at high temperatures $T \lesssim 10^{13}\,\mathrm{GeV}$. The sphaleron rate per unit volume at high temperatures is given by [170]

$$\Gamma_{\mathrm{sph}} \sim \mathcal{O}\left(0.1 - 1\right)\left(\alpha_W T\right)^4 \,. \tag{4.11}$$

For temperatures below a critical temperature, on the other hand, the sphaleron rate per unit volume for transitions between neighbouring vacua gets exponentially suppressed [170]:

$$\Gamma_{\text{sph}} \propto \frac{E_{\text{sph}}\left(T\right)^7}{T^3} e^{-E_{\text{sph}}(T)/T} \ . \tag{4.12}$$

The Boltzmann suppression of the sphaleron rate at temperatures below the critical temperature (and at today's temperature $T_0 \approx 0$ in particular) results in the apparent B-conservation in the SM and the null results of searches for the violation of this accidental, global symmetry.

C and CP violation

Considering a C- and CP-invariant state $|\Psi_0\rangle$ with zero baryon number, $i.e.$ $B\,|\Psi_0\rangle = 0$, one finds that both C and CP invariance must be violated to allow for a finite baryon number. If the C or CP symmetry were respected, $i.e.$ $[\Theta, H] = 0$ with $\Theta \equiv \text{C}, \text{CP}$ and the Hamiltonian H, the time-dependent state $|\Psi\left(t\right)\rangle = e^{iHt}\,|\Psi_0\rangle$ would still be invariant with respect to the C and CP symmetry and the baryon number would remain zero (see, $e.g.$, Ref. [170]).

Departure from thermal equilibrium

The third and last Sakharov condition is associated with the direction of the arrow of time, so that the generated net baryon asymmetry is not erased. Following the description in Ref. [15], a physical system in thermal equilibrium can be described by the Hamiltonian H and the density operator $\rho = \exp(-H/T)$. The expectation value of the time-dependent baryon number operator $B(t)$ reads

$$\langle B\left(t\right)\rangle_T = \text{Tr}\left(\rho\, e^{iHt} B\left(t=0\right) e^{-iHt}\right) = \langle B\left(t=0\right)\rangle_T \tag{4.13}$$

after exploiting the cyclic property of the trace in the last step. This demonstrates that the initial baryon number of the physical system in thermal equilibrium does not change. Moreover, the CPT invariance of the system, $i.e.$ $[\Theta, H] = 0$ with $\Theta \equiv \text{CPT}$, and $\{B, \Theta\} \equiv B\Theta + \Theta B = 0$ result in zero baryon number because

$$\langle B\left(t\right)\rangle_T = \text{Tr}\left(\rho B\left(t\right)\right) = \text{Tr}(\rho\, \underbrace{\Theta B\left(t\right)\Theta^{-1}}_{=-B(t)}) = -\,\langle B\left(t\right)\rangle_T \ . \tag{4.14}$$

The departure from thermal equilibrium can be realized by a first-order phase transition which is characterized by a potential barrier between local minima in the scalar potential of the theory. Focusing on the possibility of baryogenesis at the EW scale (*i.e.*, at $T \approx 100\,\text{GeV}$), a first-order EWPhT can serve as the needed departure from thermal equilibrium which poses an appealing scenario for the comparably low energies associated with it and accessibility in collider experiments.

Considering the evolution of the Higgs potential in Fig. 4.3 from high to low temperatures for a first-order EWPhT, the parabola-like potential at temperatures much higher than the critical temperature, *i.e.* $T \gg T_c$, features one minimum at the origin. The EW symmetry is restored and the EW gauge bosons as well as the fermions are massless. During the expansion of the Universe and the resulting decrease of the temperature, the Higgs potential develops a local minimum at finite field value in addition to the global minimum until the two minima become degenerate in energy at the critical temperature T_c with the two local minima located at $h = 0$ and $h = v_c$. The resulting potential barrier is the characteristic feature of a first-order EWPhT and its height and width drastically impact the following evolution of the vacuum configuration. For temperatures below the critical temperature, the new minimum at finite field value becomes the global minimum and the transition from the former to the new minimum via tunneling is energetically favored. The potential barrier disappears at the temperature $T_b < T_c$ and the Higgs potential ultimately features the vev $v \approx 246\,\text{GeV}$ today. This evolution of the scalar potential occurs at every point in space and causes the formation of bubbles within which the EW symmetry is broken while the EW symme-
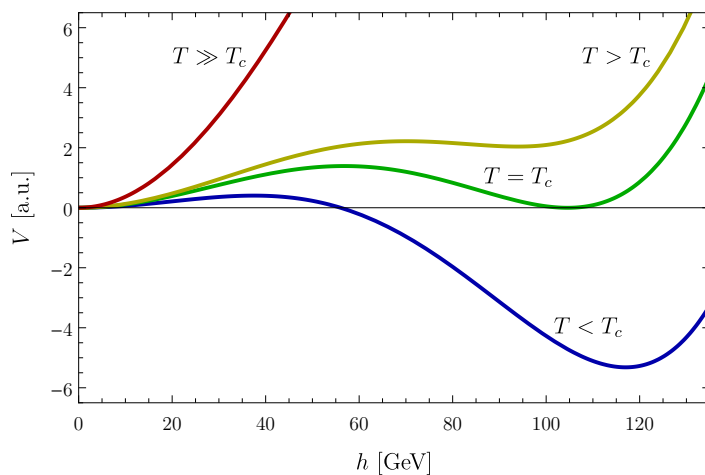
Figure 4.3: Evolution of the scalar potential V in case of a first-order EWPhT. Taken from Ref. [2].

try is restored outside the bubbles. The critical temperature T_c indicates the earliest possible beginning of the phase transition by quantum tunneling, which however might prevent the phase transition from proceeding efficiently due to its suppressed transition amplitude [170]. As a consequence, the phase transition begins at the nucleation temperature $T_n \in [T_b, T_c]$, which depends on the probability for tunneling from the false to the true vacuum. The nucleation rate per unit volume reads

$$\Gamma\left(T\right) = A\left(T\right)e^{-S_3(T)/T} \tag{4.15}$$

with the temperature-dependent prefactor $A(T) \sim \mathcal{O}\left(T^4\right)$ and the three-dimensional bounce action $S_3(T)$ [170]. An efficient nucleation of bubbles and filling of the Universe with the true vacuum requires $S_3/T \sim \mathcal{O}(130 - 140)$ [170]. Considering a theory with n real scalars $\phi_{1,\ldots,n}$, the three-dimensional Euclidean action from Ref. [170] can be written as

$$S_3 = \int \mathrm{d}^3x \left[\frac{1}{2}\sum_{i=1}^{n}\left(\nabla\phi_i\right)^2 + V\left(\phi_1,\ldots,\phi_n,T\right)\right]. \tag{4.16}$$

With time passing, the bubbles grow because the transition from the false to the true vacuum is energetically favored and eventually fill the entire Universe (see the simulation in Fig. 4.4). If more than one bubble is formed (which is a reasonable assumption and results from simulations), the collision of bubbles is inevitable, causing gravitational waves which might be detectable as a stochastic gravitational wave background and offer valuable insights into the dynamics in the early Universe (see, *e.g.*, Refs. [171–175]).
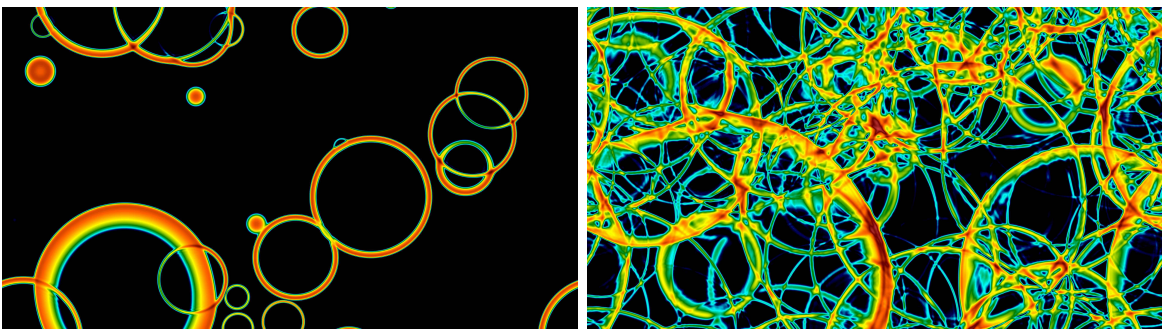
Figure 4.4: Simulation of formation and collision of bubbles. The color indicates the kinetic energy of the particles (*e.g.* 'red' corresponds to a large energy). Taken from Ref. [171].

The three-dimensional Euclidean action in Eq. (4.16) determines the duration of the phase transition. Defining β as the inverse duration, one finds

$$\frac{\beta}{H} = \left(T \frac{\mathrm{d}}{\mathrm{d}T} \frac{S_3(T)}{T} \right) \Bigg|_{T=T_n} \tag{4.17}$$

with the Hubble parameter H at the nucleation temperature T_n [171].

Notably, the baryon asymmetry can be created during the EWPhT if the three Sakharov conditions are satisfied and persist until today if the sphaleron processes are turned off rapidly thereafter. If the departure from thermal equilibrium is not fast enough, the sphalerons might have enough time to *wash out* the generated baryon asymmetry and render the baryogenesis not successful. A sufficiently strong first-order EWPhT in which the scalar potential features a potential barrier and the ratio of the critical vev v_c and the critical temperature T_c is larger than unity can generate such an out-of equilibrium situation described above. This approximation is often applied in examinations of the EWPhT strength but not sufficient as the value of the critical vev v_c in the loop-corrected, effective scalar potential is gauge-dependent (*cf.* Refs. [176–185]). However, this approximation is adopted in the literature and our findings in Ref. [1, 2] are based on this.

Summarizing the three Sakharov conditions and their ties to the SM, the theory is close to accounting for them but falls short in fulfilling them to a sufficient extent.

As one of its shortcomings, the SM Higgs mass $m_h \approx 125\,\mathrm{GeV}$ is too large to facilitate a first-order EWPhT, let alone a *strong* first-order EWPhT. In lattice computations conducted already in the late 1990s, the nature of the EWPhT was determined to be a crossover for a Higgs mass $m_h \gtrsim 72\,\mathrm{GeV}$ [186–191]. It was found in Refs. [192, 193] that the crossover phase transition in the SM occurs at the temperature $T \approx 160\,\mathrm{GeV}$.

In addition to that, the CP violation in the EW sector of the SM seems to be too small to explain the measured baryon asymmetry of the Universe even if the other two Sakharov conditions were fulfilled. The Jarlskog invariant $J = \det\left[M_u^2, M_d^2 \right]$ with the commutator of the mass matrices $M_{u(d)}$ for up-type (down-type) quarks, introduced in Refs. [194, 195], suggests a far too small amount of CP violation in the quark sector. Note, however, the debate on this conclusion, summarized in Ref. [157].

Consequently, any SM extension must feature an additional source of CP violation and an out-of-equilibrium scenario like a strong first-order EWPhT in order to account for the creation of the baryon asymmetry of the Universe. Without specifying the

underlying physics at high energies, the possibility of baryogenesis at EW scales in the context of SMEFT was investigated in Refs. [196, 197].

Before moving on to two prominent models for explaining the baryon asymmetry, we shall briefly review the experimental efforts to search for B-violating processes and CP-violating particle properties.

Searches for proton decay

The baryon number is – like the lepton number – an accidental symmetry in the SM and a prominent example for the 'robustness' of this symmetry is the non-observation of proton decay. The lower limit $\tau_p \geq 3.6 \times 10^{33}$ years on the proton lifetime is set by the Super-Kamiokande experiment [198] via looking for the decay $p \to \mu^+ K^0$ and combining with previous results. Focusing on the decay $p \to e^+ \pi^0$ ($p \to \mu^+ \pi^0$) results in the partial lifetime $\tau_p > 2.4 \times 10^{34}$ years (1.6×10^{34} years) [199]. This rules out a substantial fraction of the parameter space in many BSM theories predicting processes with $|\Delta B| = 1$ and thus proton decay (see, *e.g.*, Refs. [200–203]).

Searches for n-$\overline{n}$ oscillations

Another probe for baryon number violation is the oscillation between neutrons and antineutrons. Such a process would induce $|\Delta B| = 2$ but respect the gauge symmetries of the SM (see Ref. [204, 205] for further details). The search for antineutron appearance in ^{16}O nuclei, conducted at Super-Kamiokande, set the limit $\tau_{n\overline{n}}^{\mathrm{nuc}} > 3.6 \times 10^{32}$ years to this characteristic lifetime [206]. A lower bound on the oscillation time of quasi-free, moving neutrons, characterized by $\tau_{n\overline{n}} \geq 8.6 \times 10^7$ s at 90% C.L., was set by the Institute Laue-Langevin in Grenoble in 1994 [207] and improved to $\tau_{n\overline{n}} \geq 4.7 \times 10^8$ s by the Super-Kamiokande collaboration. The proposal by the HIBEAM/NNBAR collaboration would improve the experimental sensitivity by three orders of magnitude and thereby push the bound on the oscillation time of quasi-free neutrons to higher values [208].

Searches for lepton electric dipole moment

In contrast to the previous strategies for unravelling the nature of baryon number conservation in nature, another vital ingredient for the generation of the baryon asymmetry of the Universe is the violation of C and CP invariance. While the violation of the C and CP symmetries is an established fact in weak interactions of quarks, further

sources of CP violation can arise in BSM models and naturally affect particle properties which are sensitive to CP violation.[3] Such a property is the permanent electric dipole moment of a lepton (ℓEDM) which dictates the coupling strength of the spin of the lepton to an external electric field. For elementary particles like leptons in the SM, the EDM is rather an intrinsic property than a consequence of spatially distributed electric charges, as it is the case for extended objects like atoms or molecules. The Hamiltonian for the ℓEDM reads

$$\mathcal{H}_{\ell\text{EDM}} = -d_\ell \vec{S} \cdot \vec{E} \tag{4.18}$$

with the ℓEDM parameter d_ℓ, the spin $\vec{S}$ of the lepton, and the electric field $\vec{E}$ (see, e.g., Ref. [209]). In case of a CP-invariant theory, the ℓEDM exactly vanishes and the lepton does not exhibit an EDM. Since the weak sector does not respect the CP symmetry, the SM predicts an ℓEDM which arises at four-loop level (see diagram in Ref. [210], for instance) and is therefore largely suppressed.

The low-energy $D = 5$ operator in an effective Lagrangian, associated with the CP violation-inducing ℓEDM, is given by

$$\mathcal{L}_{\text{eff}}^{\ell\text{EDM}} = -\frac{i}{2}d_\ell\,\bar{\ell}\sigma^{\mu\nu}\gamma^5\ell F_{\mu\nu} \tag{4.19}$$

with the electromagnetic field strength tensor $F_{\mu\nu}$ (see, e.g., Refs. [210–212]).[4]

The evolution of the experimental precision of the eEDM d_e is very impressive and hence worth being summarized. After the proposal by Purcell and Ramsey [213] in 1950, searches for the eEDM were conducted and reached a limit of $d_e/e \sim 10^{-16}$ cm. In 1965, Sandars proposed the use of atoms instead of the elementary electron [214] which lead to a further improvement by about eleven orders of magnitude. Nowadays, molecules with their strong internal electric field are deployed for the searches and yield the upper limits we shall list below. For an illustration of the evolution of the upper limit on the eEDM as well as further details, we refer to the dissertation by Ang [209] and the references therein.

To date the sensitivity of dedicated experiments is too low by several orders of magnitude to probe the SM prediction $d_e^{\text{SM}} \sim 10^{-35}e$ cm [215] for the electron, which is by three orders of magnitude larger than calculated before [216]. The current

---

[3]Note that the quark sector of the SM might not be the only source of CP violation. The measurement of the Dirac CP phase in the PMNS neutrino mixing matrix (cf. Chapter 5) is still inconclusive and, strictly speaking, the QCD sector might contribute to CP violation as well.

[4]The reader is referred to Appendix D for further details of this operator. Note the negative mass dimension of the ℓEDM parameter, i.e. $[d_\ell] = -1$.

best upper bound on the eEDM, set by the Joint Institute for Laboratory Astrophysics (JILA) [217], and the projection of the ACME collaboration read [210, 218]

$$|d_e^{\mathrm{JILA}}/e| < 4.1 \times 10^{-30}\,\mathrm{cm} \approx 2.1 \times 10^{-16}\,\mathrm{GeV}^{-1} \tag{4.20}$$

$$|d_e^{\mathrm{ACME\,III}}/e| < 0.3 \times 10^{-30}\,\mathrm{cm} \approx 1.5 \times 10^{-17}\,\mathrm{GeV}^{-1}\,. \tag{4.21}$$

These upper limits on the eEDM are still about five orders of magnitude larger than the SM prediction. Therefore, the SM contribution could be neglected and a signal in a dedicated experiment would clearly serve as a *bona fide* indicator for BSM physics.

Based on the finding in Ref. [219] and the assumption of lepton universality, the ratio of ℓEDMs is governed by the respective mass ratio, *i.e.*

$$d_{\ell'} = \frac{m_{\ell'}}{m_{\ell}}d_{\ell}\,, \tag{4.22}$$

and consequently leads to the SM prediction $d_\mu^{\mathrm{SM}} \sim 10^{-33}e\,\mathrm{cm}$ for the μEDM. The current limit on the μEDM is set by the muon $g-2$ experiment at Brookhaven National Laboratory (BNL) and the projected limits by J-PARC and PSI muEDM read [220–222]

$$|d_\mu^{\mathrm{BNL}}/e| < 1.9 \times 10^{-19}\,\mathrm{cm} \approx 9.6 \times 10^{-6}\,\mathrm{GeV}^{-1} \tag{4.23}$$

$$|d_\mu^{\mathrm{J-PARC}}/e| < 1.5 \times 10^{-21}\,\mathrm{cm} \approx 7.6 \times 10^{-8}\,\mathrm{GeV}^{-1} \tag{4.24}$$

$$|d_\mu^{\mathrm{PSI}}/e| < 6 \times 10^{-23}\,\mathrm{cm} \approx 3 \times 10^{-9}\,\mathrm{GeV}^{-1}\,. \tag{4.25}$$

The absence of signals helps rule out models which predict a large contribution to the leptons' electric dipole moments. These measurements need to be taken into account whenever the BSM theory features new sources of CP violation.

With this we close the brief excursion to experimental searches for insights into the conditions facilitating the baryon asymmetry of the Universe in nature and take a closer look at two distinct realizations thereof in the next section. One could argue that a finite net baryon number was one of the initial conditions of the Universe. This, however, is disfavored by the present paradigm of cosmic inflation (see, *e.g.*, Ref. [223]) and supports the notion of a particle physics reason for the baryon asymmetry.

4.2   Prominent Models for Generating the Baryon Asymmetry

Before delving into one particular realization of generating the baryon asymmetry of the Universe, it is worth presenting a coarse overview of two prominent mechanisms. A plethora of models have been invented and a summary of those can be found in Refs. [224, 225] for instance.

Leptogenesis

The measurement of the baryon asymmetry of the Universe described in the previous section requires a mechanism for generating an imbalance between baryons and antibaryons. The sphaleron processes, however, connect the baryon number with the lepton number by violating $B + L$ while preserving $B - L$. This feature is exploited by models of leptogenesis: A net lepton number is generated at sufficiently high temperatures which is converted into a baryon asymmetry via the sphaleron processes afterwards (see Ref. [226] for the original proposal by Fukigita and Yanagida and, *e.g.*, Refs. [227–230] for comprehensive reviews).

The key feature of leptogenesis models is a heavy lepton that drops out of equilibrium via CP-violating decays in the Early Universe when the sphalerons are active (see Fig. 4.5). With that, the three Sakharov conditions are fulfilled and the successful generation of the baryon asymmetry is possible.

For this description we consider a model with three heavy, RH neutrinos N_i which transform as singlets under the SM gauge group. We shall encounter this model a second time in Section 5.2 in the context of neutrino mass generation. This is the attractive feature of this leptogenesis model: it can account for both baryon asymmetry and neutrino masses. The relevant operators for the production and decay of the RH
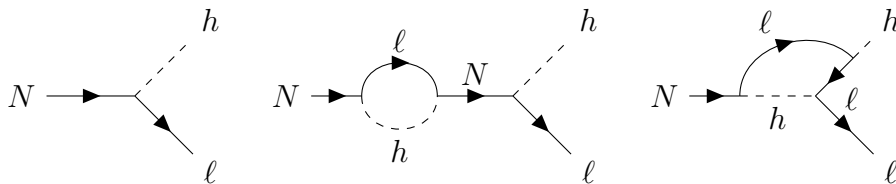
Figure 4.5: Overview of tree-level and one-loop level decay processes of the heavy neutrino N. [225]

Majorana neutrino read

$$-\mathcal{L} \supset \frac{M_{ij}}{2}\overline{N_i^c}N_j + (y_\nu)_{ij}\,\overline{L}_i\widetilde{\Phi}N_j + \text{h.c.} \tag{4.26}$$

with the RH neutrino mass matrix M_{ij} and the complex Yukawa matrix y_ν [230]. The CP-violating decays of the heavy neutrino at tree as well as one-loop level are shown in Fig. 4.5 and lead to a mismatch between leptonic matter and antimatter.

For temperatures above the RH neutrino mass, the production and depletion of the heavy neutrinos are balanced and no persistent lepton asymmetry is generated. Once the temperature drops below the RH neutrino mass, the thermal production gets Boltzmann suppressed and the heavy RH neutrino leaves thermal equilibrium, yielding a lepton asymmetry via CP-violating decay (see, *e.g.*, Ref. [228] for details). Owing to the sphaleron processes, the lepton asymmetry is partially converted into a baryon asymmetry which can eventually give rise to the baryon asymmetry of the Universe. The net baryon number and lepton number are related to each by [230]

$$B = \frac{8N_f + 4}{22N_f + 13}L \overset{\text{SM}}{=} -\frac{28}{51}L\,. \tag{4.27}$$

The evolution of the baryon and lepton number is depicted in Fig. 4.6. The conservation of $B - L$ and the equilibration via Yukawa and gauge interactions can drive the sphaleron processes, indicated by the teal dashed arrow, to generate a net lepton and baryon number. An initial state with $B \neq L$ yields finite net lepton and baryon number.[5]

---

[5]A recent EMPRESS measurement suggests an asymmetry in the lepton sector between the abundance of electron neutrinos and antineutrinos which is translated to the lepton asymmetry
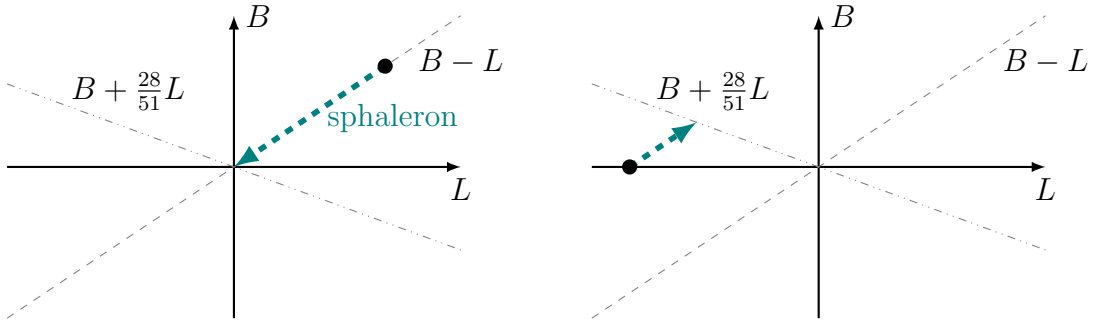
Figure 4.6: Evolution of baryon and lepton number in leptogenesis models. The left panel shows the evolution for an initial state with $B = L$, while the scenario in the right one is $L \neq 0$ for zero baryon number. Inspired by Ref. [230].

Electroweak Baryogenesis

Unlike leptogenesis models which rely on CP-violating out-of-equilibrium decays of heavy particles, another class of models describes the creation of the baryon asymmetry at much lower temperatures and without the generation of a lepton asymmetry as the seed for the baryon asymmetry. Since the transition from the phase in which the EW symmetry is restored to the phase with a finite Higgs vev takes place in the SM, it is worth investigating whether the baryon asymmetry can be generated in this epoch.

The basic principle of electroweak baryogenesis (EWBG) is the creation of a baryon asymmetry in the vicinity of the bubble wall in the symmetric phase which is eventually captured by the expanding bubble. The baryon asymmetry that might be produced anywhere else in the symmetric phase is rapidly eliminated by the sphaleron processes that are active outside the bubble. If a baryon asymmetry is created in a region of space just prior to being swallowed by the expanding bubble, the baryon asymmetry enters the region of space in which the EW symmetry is broken and the sphaleron processes are exponentially suppressed. This, however, is not sufficient to generate a persistent baryon asymmetry in this phase as the dynamics of the suppression of the sphaleron process is important. In case of an EWPhT which does not feature a drop of the sphalerons out of equilibrium, the sphalerons can reduce (if not even totally erase) the captured baryon asymmetry. A strong first-order EWPhT, on the other hand, prevents the sphaleron processes from washing out the baryon asymmetry and is therefore a necessary condition for successful baryogenesis during the EWPhT.

This scenario of baryogenesis has been studied extensively in the literature (see, *e.g.*, Refs. [166, 169, 170, 185, 235–242]) and will be subject of the next chapter.

4.3 Baryon Asymmetry and Dark Matter in the Inert Doublet Model

After the introduction to the current status of the baryon asymmetry of the Universe and two possible mechanisms of generating the asymmetry, this section is dedicated to our results in a specific framework. The results are based on our publication [3]. A few results can be found in my colleague's Master's thesis [243] which emerged from our investigation.

---

parameter $\eta_L \sim 5 \times 10^{-3}$ [231, 232]. A CMB analysis [233] constrains the lepton asymmetry to $-0.085 < \eta_L < +0.084$ (95% C.L.). As stated in Ref. [234], drawing a conclusion on the lepton asymmetry might be premature due to the small number of examined galaxies in the study.

The framework in which we want to investigate the interplay between DM and the generation of the baryon asymmetry of the Universe is the Inert Doublet Model (IDM) (see, *e.g.*, Refs. [1, 2, 244–261] for further details on this model in the context of DM and EWPhT). In addition to the Higgs doublet defined in Eq. (1.11), the scalar sector of this model hosts a second $SU(2)_L$ doublet $\Phi_2 : (\mathbf{1}, \mathbf{2}, 1)$ which transforms as $\Phi_2 \to -\Phi_2$ with respect to a discrete $\mathbb{Z}_2$ symmetry while the SM fields are invariant with respect to this symmetry. The $SU(2)_L$ doublet scalars in this theory read

$$\Phi_1 = \frac{1}{\sqrt{2}} \begin{pmatrix} \sqrt{2}G^+ \\ v_1 + h + iG^0 \end{pmatrix} \quad , \quad \Phi_2 = \frac{1}{\sqrt{2}} \begin{pmatrix} \sqrt{2}H^+ \\ v_2 + H + iA \end{pmatrix} . \tag{4.28}$$

The characteristic feature of the IDM is the vanishing vev v_2 of the second doublet at zero temperature, which in turn prevents the Higgs bosons from mixing with each other. Consequently, the vev of the first doublet equals the SM vev, *i.e.* $v_1 = v \approx 246\,\mathrm{GeV}$ at zero temperature. Furthermore, the $\mathbb{Z}_2$ symmetry prohibits dangerous contributions to FCNCs due to absent Yukawa interactions between the fields from the second Higgs doublet and fermions and stabilizes the lightest field from Φ_2. In the remainder of this analysis we choose the scalar H to be the lightest BSM field and therefore the DM candidate in this model.

With the definition of the gauge covariant derivative in Eq. (1.7), the Lagrangian of the scalar sector reads

$$\mathcal{L} \supset \sum_j \left(D_\mu \Phi_j \right)^\dagger \left(D^\mu \Phi_j \right) - \mu_j^2 \left| \Phi_j \right|^2 - \lambda_j \left| \Phi_j \right|^4$$
$$- \lambda_3 \left| \Phi_1 \right|^2 \left| \Phi_2 \right|^2 - \lambda_4 \left| \Phi_1^\dagger \Phi_2 \right|^2 - \frac{1}{2} \left[\lambda_5 \left(\Phi_1^\dagger \Phi_2 \right)^2 + \mathrm{h.c.} \right] \tag{4.29}$$

and the tree-level masses of the scalars are given by

$$m_h^2 = 2\lambda_1 v_1^2 \ , \ m_H^2 = \mu_2^2 + \lambda_{345} \frac{v_1^2}{2} \ , \ m_A^2 = m_H^2 - \lambda_5 v_1^2 \ , \ m_{H^\pm}^2 = \mu_2^2 + \lambda_3 \frac{v_1^2}{2} \tag{4.30}$$

with the short-hand notation $\lambda_{345} \equiv \lambda_3 + \lambda_4 + \lambda_5$. Since the complex phase of the (generally complex) coupling parameter λ_5 can be absorbed by the inert Higgs doublet Φ_2 and is therefore without any physical meaning, the IDM does not feature BSM CP-violating interactions. For the theoretical and experimental constraints (perturbative unitarity, vacuum stability, invisible SM Higgs decays into a pair of inert scalars, or EW precision tests, for instance) as well as for the parameter space allowing for the correct DM abundance the reader is referred to Refs. [1, 2] and the references therein.

As listed above, the IDM with an exact discrete $\mathbb{Z}_2$ symmetry at zero temperature as its prominent feature was studied extensively in the past, even in the spirit of a new source of CP violation (see, *e.g.*, Refs. [262–264]). In this thesis we shall investigate the impact of the CP-violating $D = 6$ operator

$$\mathcal{L} \supset \tilde{c}_2 \, |\Phi_2|^2 \, V_{\mu\nu} \widetilde{V}^{\mu\nu} \equiv \frac{\tilde{c}_2}{2} \varepsilon^{\mu\nu\alpha\beta} \, |\Phi_2|^2 \, V_{\mu\nu} V_{\alpha\beta} \tag{4.31}$$

with at least one heavy beyond-IDM particle integrated out and hence giving rise to the effective vertex. Consequently, we refer to this effective model as an Inert Doublet Model effective field theory (IDMEFT) and consider $V_{\mu\nu} \widetilde{V}^{\mu\nu} = W_{\mu\nu}^I \widetilde{W}^{I\mu\nu} + B_{\mu\nu} \widetilde{B}^{\mu\nu}$ as the sum of products of the $SU(2)_L$ isospin and $U(1)_Y$ hypercharge field strength tensors and their respective duals. Since the sphalerons which will serve as the baryon asymmetry-generating processes correspond to the $SU(2)_L$ sector, the term $W_{\mu\nu}^I \widetilde{W}^{I\mu\nu}$ determines the resulting baryon asymmetry and the assumption of equal coefficients for the field strengths could be lifted without any consequences for the results. A natural choice of coefficients would include the $SU(2)_L$ and $U(1)_Y$ gauge couplings.

The reader might wonder why we focus on a model with an effective operator instead of a model with renormalizable operators only. The absent signal in ℓEDM experiments suggests to expect CP violation at a higher energy scale for which an EFT approach seems to be reasonable.[6] It is these experimental constraints which render this operator advantageous over its SMEFT sibling $\tilde{c}_1 \, |\Phi_1|^2 \, V_{\mu\nu} \widetilde{V}^{\mu\nu}$ with the SM Higgs doublet Φ_1. Unlike the SMEFT operator which was studied recently by Kley *et al.* in Ref. [210] and contributes at one-loop level to the ℓEDM, the IDMEFT operator does not couple to fermions at tree level due to the discrete $\mathbb{Z}_2$ symmetry at zero temperature and the leading-order contributions are expected to arise at two-loop level. The complete calculation of the contributions to the ℓEDMs from both effective operators is presented in Appendix D. While the SMEFT operator is taking into account here for comparison, we shall focus in particular on the IDMEFT operator in the light of the baryon asymmetry and the DM relic abundance.

As required by the Sakharov conditions, creating the baryon asymmetry calls for a BSM theory which provides an additional source of CP violation and departure from thermal equilibrium. In the IDMEFT a strong first-order EWPhT serves as the departure from thermal equilibrium and the effective operator from Eq. (4.31) is not expected to affect the evolution of the scalar potential significantly, *i.e.*, the findings for the EWPhT in the IDM apply to the IDMEFT. The IDM features a strong first-

---

[6]See Refs. [265–268] for scenarios where the EWPhT is lifted accordingly to such higher scales.

order EWPhT via one and multiple steps (*cf.* Fig. 4.7) and we explore the multi-step EWPhT (see Ref. [1] for the study of a multi-step EWPhT in the original IDM). Beginning at sufficiently high temperatures at which the EW symmetry is restored, *i.e.* both vevs are zero, the evolution of the scalar potential can feature either one transition in Φ_1 direction, *i.e.* $\langle \Phi_1, \Phi_2 \rangle = (0,0) \rightarrow \left(v_1/\sqrt{2}, 0 \right)$, or multiple steps in different directions. The IDM predicts a vanishing BSM vev at zero temperature and we shall study the discrete two-step EWPhT $\langle \Phi_1, \Phi_2 \rangle = (0,0) \rightarrow \left(0, v_2/\sqrt{2} \right) \rightarrow \left(v_1/\sqrt{2}, 0 \right)$. Note that this series of phase transitions features at least one zero vev at any point in time after EWSB. The scenario with two simultaneous vevs was investigated recently by Benincasa *et al.* [269] and its ramifications for the baryon asymmetry are yet to be studied. For this analysis we keep the scenario with only one finite vev at a time.

Results for the baryon asymmetry

In the following we shall investigate the impact of the $D = 6$ operator in Eq. (4.31) on the baryon asymmetry of the Universe. For this we adopt the analytical results from Dine *et al.* in Ref. [270] and the IDMEFT operator can be re-formulated as

$$\tilde{c}_2 \left| \Phi_2 \right|^2 W_{\mu\nu}^I \widetilde{W}^{I\mu\nu} = \frac{32\pi^2}{N_f g^2} \tilde{c}_2 J_B^\mu \, \partial_\mu \left| \Phi_2 \right|^2 \tag{4.32}$$

with the Wilson coefficient $\tilde{c}_2 \equiv \lambda_{\rm CP}/\Lambda^2$ comprising both the coupling parameter $\lambda_{\rm CP}$ entering CP-violating interactions in the fundamental theory and the energy scale Λ
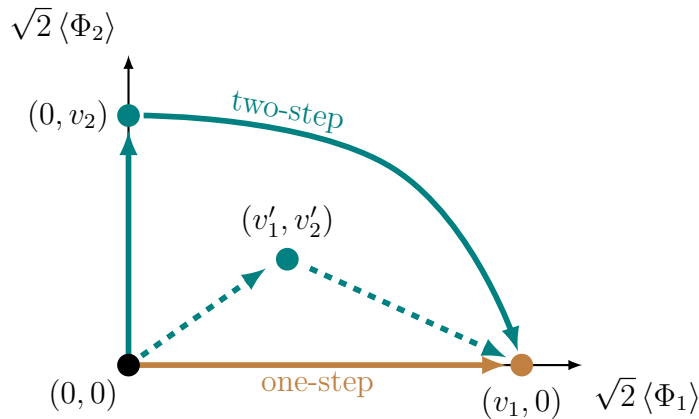
Figure 4.7: Possible scenarios for the evolution of the EW vacuum. A two-step EWPhT (teal lines) features either two discrete transitions with one vanishing vev in each phase or a non-trivial vev configuration (dashed line).

which is larger than any IDM-related energy scale, and the baryon current J_B^μ (see also Refs. [271–273]). This formulation can be derived from Eq. (4.6) via integration by parts. Similar operators involving scalar multiplets have been examined in the literature (see, *e.g.*, Refs. [252, 270, 274]), but – to our knowledge – this particular operator has not. The operator in Eq. (4.32) causes an effective chemical potential and non-degenerate energy levels for baryons and antibaryons in the thermal distribution which drive the sphalerons to generate a baryon asymmetry in front of the bubble wall during a moderate change of $\langle \Phi_2 \rangle$ in time. This baryon asymmetry is captured by the expanding bubble in which the sphalerons are highly suppressed, such that the baryon asymmetry cannot get washed out.

We aim at finding the range of Wilson coefficients which gives rise to the measured baryon asymmetry of the Universe. In the remainder of this investigation we shall take $N_f = 3$ for the three experimentally confirmed generations of fermions. The shift in the free energy results in a minimum associated with an equilibrium value for the baryon number density of [270]

$$n_B^{\rm eq} = \tilde{c}_2 \frac{8\pi^2}{3g^2} \partial_t |\Phi_2|^2 T^2 \tag{4.33}$$

and the evolution of the baryon number density is governed by the differential equation

$$\frac{{\rm d}n_B}{{\rm d}t} = -18 \frac{\Gamma_{\rm sph}}{T^3} \left(n_B - n_B^{\rm eq} \right) \tag{4.34}$$

with the sphaleron rate from Eq. (4.11). Adopting the result from Ref. [270], the assumption of a rapid strong first-order EWPhT, which was justified in Ref. [269], allows to estimate the resulting baryon number density

$$n_B \sim 4\pi \tilde{c}_2 \left| v_c \right|^2 \alpha_W^4 \ \Delta t \ T_c^4 \tag{4.35}$$

in terms of the BSM vev $\langle \Phi_2 \rangle \equiv v_c/\sqrt{2}$ at the critical temperature T_c, where Δt is the time needed by the transition to occur in a sphere with a radius given by the correlation length $\xi \sim (\alpha_W T_c)^{-1}$. Without taking the details of the dynamics into account, the bubble expansion is simplified here in the sense that its growth is assumed to occur with a constant velocity $v_{\rm wall}$, such that the transition time is $\Delta t = \xi/v_{\rm wall}$.[7] The resulting dependence of the baryon asymmetry on the critical vev, the bubble wall velocity, and the Wilson coefficient $\tilde{c}_2$ is presented in Fig. 4.8. Assuming the new coupling

---

[7]As found in Refs. [275, 276], an ultra-relativistic bubble wall velocity changes the bubble dynamics.

parameter $\lambda_{\text{CP}} \sim \mathcal{O}(0.1)$, we find that new physics resides at $50\,\text{TeV} \lesssim \Lambda \lesssim 140\,\text{TeV}$ and results in the measured value of the baryon asymmetry of the Universe for a viable value of v_c (gray band in Fig. 4.8) and a wide range of bubble wall velocities for the CP-violating IDMEFT operator. Note that the SMEFT operator requires a somewhat higher scale for new physics but it is still $\Lambda \sim \mathcal{O}(100\,\text{TeV})$.

Since the energy scales at which the model predicts new physics are far out of reach of the current LHC with a center-of-mass energy $\sqrt{s} \approx 14\,\text{TeV}$, the model appears to be experimentally not accessible today at the first glance.[8] However, the putative heavy particles do not need to be produced at colliders as precision experiments are sensitive (up to a certain extent) to new physics contributions at loop level. In the following we shall confront the model predictions for the ℓEDM with the current and projected upper limits, presented above in Section 4.1.

Beginning with the SMEFT operator whose analytical expression for contribution to the ℓEDM is presented in Section D.1, we choose $4\,\text{PeV}^{-2} \le \tilde{c}_1 = 15\,\text{PeV}^{-2} \le 25\,\text{PeV}^{-2}$ at the energy scale $\mu = m_h$, that gives the measured baryon asymmetry (*cf.* Fig. 4.8). Due to the large separation between the energy scale $\mu = m_h$ and the energy scale at which the experiment is performed ($\mu = m_\ell$), the running of the model parameters must

---

[8]The proposed Future Circular Collider (FCC) with colliding hadrons might reach a center-of-mass energy $\sqrt{s} \approx 100\,\text{TeV}$ and hence open the door for probing the physics beyond the IDM at the collider. [277]
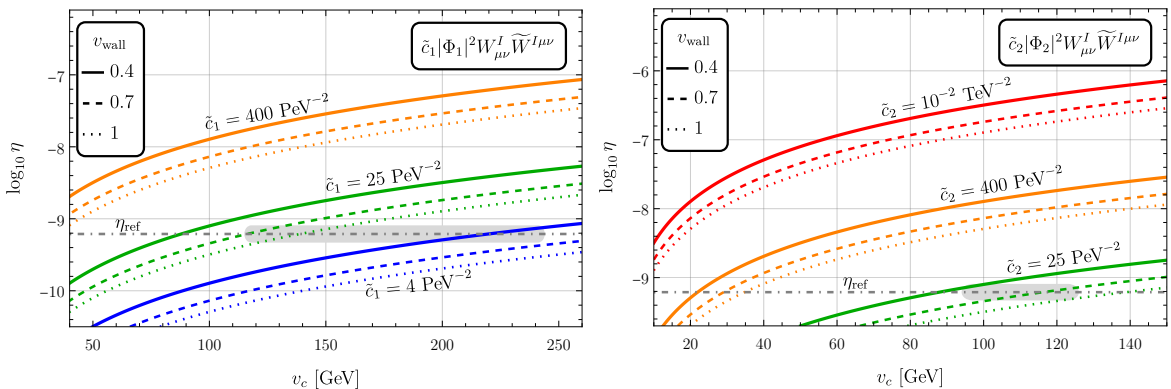
Figure 4.8: The baryon asymmetry parameter η in terms of the critical vev $v_c = \sqrt{2}\langle\Phi_i(T_c)\rangle$, the bubble wall velocity v_{wall}, and the Wilson coefficients $\tilde{c}_i$ for the SMEFT (*left*) and IDMEFT operators (*right*). The bubble wall velocity is indicated by the line style, whereas the values of the Wilson coefficients are color-encoded. The light-gray parameter space corresponds to the range of possible critical vevs at the first stage of a two-step EWPhT found in Ref. [1]. Similar to the plots in Ref. [3].

be taken into account which is dictated by the renormalization group equation (RGE)

$$\frac{\mathrm{d}\lambda}{\mathrm{d}\log\mu} = \frac{1}{16\pi^2}\beta_\lambda \tag{4.36}$$

for the generic model parameter λ. This is accounted for by using the Mathematica package `DsixTools 2.0` [278, 279] and we find for the ℓEDM of the three leptons

$$\left|\frac{d_\ell^{\Phi_1}}{e}\right|_{\mu=m_\ell} \approx \begin{cases} 2.6 \times 10^{-16}\,\mathrm{GeV}^{-1} \text{ for } \ell = e \\ 5.6 \times 10^{-14}\,\mathrm{GeV}^{-1} \text{ for } \ell = \mu \\ 9.7 \times 10^{-13}\,\mathrm{GeV}^{-1} \text{ for } \ell = \tau \end{cases}. \tag{4.37}$$

Notice that the scaling of the ℓEDMs meets our expectation in Eq. (4.22). These contributions are much less suppressed than the SM ones which means that the induced ℓEDM is effectively given by the SMEFT contributions. Note that the results are already in tension with the experimental upper limits in Eq. (4.20), but corners of the parameter space can still be open to create the baryon asymmetry while the induced ℓEDM is smaller than the corresponding limit.

Owing to the loop suppression of the IDMEFT contribution with respect to the one by the SMEFT operator, we expect a smaller induced ℓEDM. Its full calculation is presented in Section D.2. Making use of the findings in Refs. [1, 2] and therefore assuming the DM mass $m_H = 71\,\mathrm{GeV}$, the other inert states being degenerate in mass in the entire analysis with $\Delta m \equiv m_{H^\pm,A} - m_H = 410\,\mathrm{GeV}$, and the Higgs portal coupling $\lambda_{345} = -2 \times 10^{-3}$, the result for the Wilson coefficient $\tilde{c}_2 = 25\,\mathrm{PeV}^{-2}$ from Fig. 4.8 leads to

$$\left|\frac{d_\ell^{\Phi_2}}{e}\right|_{\mu=m_\ell} \approx \begin{cases} 5.9 \times 10^{-17}\,\mathrm{GeV}^{-1} \text{ for } \ell = e \\ 1.3 \times 10^{-14}\,\mathrm{GeV}^{-1} \text{ for } \ell = \mu \\ 2.2 \times 10^{-13}\,\mathrm{GeV}^{-1} \text{ for } \ell = \tau \end{cases}. \tag{4.38}$$

These results suggest that the IDMEFT operator can indeed account for the baryon asymmetry of the Universe while the induced eEDM is not large enough to cause a signal in the JILA experiment (*cf.* Eq. (4.20)) and the other two EDMs are far out of experimental reach. It is remarkable though that the projected sensitivity of the ACME III experiment in Eq. (4.21) includes the predicted eEDM. Hence, we live in exciting times in which near-future experiments might shed light on the mechanism investigated here for the generation of the baryon asymmetry on the Universe!

Results for the Dark Matter relic abundance

Next, we shall investigate whether the finding for the Wilson coefficient $\tilde{c}_2 \sim 25\,\text{PeV}^{-2}$ for the baryon asymmetry gives rise to the measured DM relic abundance. We compute the DM relic abundance as well as the DMDD cross sections with the public `micrOMEGAs` code.

As it was shown in previous studies (see, *e.g.*, Refs. [246, 280]), the DM mass range in the IDM is either $55\,\text{GeV} \lesssim m_H \lesssim 80\,\text{GeV}$ or $m_H \gtrsim 500\,\text{GeV}$. Note that the first range can be expanded towards smaller DM masses to $\sim 44\,\text{GeV}$ for a narrow BSM mass spectrum [261]. A strong first-order EWPhT via one step or two steps requires a large mass difference, which is possible in the low-mass regime without spoiling the results for the DM relic abundance. Following the estimate in Chapter 2, the freeze-out temperature is $T_{\text{f.o.}} \sim \mathcal{O}(1)\,\text{GeV}$ in this DM mass regime and thus below the temperature at which the EWPhT takes place. Consequently, the intermediate phase with $v_2 > 0$ is expected not to affect the computation of the DM relic abundance.

As long as the IDMEFT operator does not contribute significantly, the DM relic abundance can be accomplished by the IDMEFT alongside the results for the baryon asymmetry of the Universe. Therefore, we shall first investigate the thermally averaged annihilation cross section $\langle \sigma v \rangle$ in the light of the IDMEFT Wilson coefficient (see Fig. 4.9). Regardless of the sign of $\tilde{c}_2$, the effective operator contributes *constructively* to the total thermally averaged annihilation cross section. The DM annihilation cross section $\langle \sigma v \rangle$ and thus the resulting DM relic abundance are virtually identical for $|\tilde{c}_2| \lesssim 10^{-1}\,\text{TeV}^{-2}$ in the IDM and the effective theory. From that we conclude that the
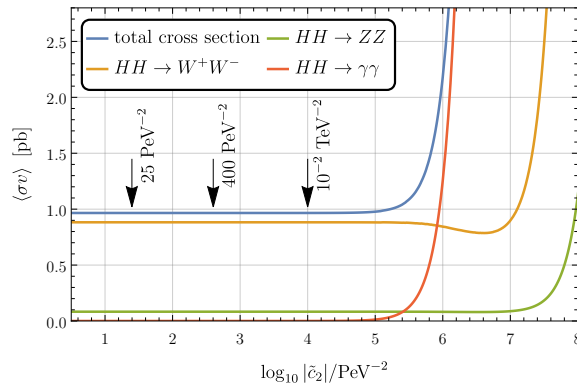
Figure 4.9: Thermally averaged DM annihilation cross section $\langle \sigma v \rangle$ in terms of the Wilson coefficient $\tilde{c}_2$. The DM mass is $m_H = 71\,\text{GeV}$, the mass splitting $\Delta m = 410\,\text{GeV}$, and the Higgs portal coupling $\lambda_{345} = -2 \times 10^{-3}$. The arrows indicate the values of the Wilson coefficients considered in Fig. 4.8. Taken from Ref. [3]

Wilson coefficients in Fig. 4.8 do not substantially affect the DM relic abundance. In particular, the Wilson coefficient $\tilde{c}_2 = 25 \, \text{PeV}^{-2}$ does not alter the DM relic abundance and gives rise to the measured baryon asymmetry. The parameter space in the low-mass regime is presented in the left panel of Fig. 4.10. The parameter space for $m_H < m_h/2$ is insensitive to the sign of the Higgs portal coupling which is because of the main DM annihilation channel $HH \to h^* \to b\bar{b}$ with an off-shell SM Higgs boson. The DM annihilation cross section hence scales with $\lambda_{345}^2/(s - m_h^2)$ and the parameter space for the measured DM relic abundance consequently tends towards smaller $|\lambda_{345}|$ as the momentum transfer, *i.e.* $s \approx 4m_H^2$ for non-relativistic DM, approaches the resonance at $m_H = m_h/2$. The shape of the parameter space beyond the resonance is dictated by the interplay between the on-shell Higgs production and the DM annihilations with mediating EW gauge bosons. The red lines represent the XENONnT [109] and LZ [110] DMDD bounds which rule out the parameter space with Higgs-portal couplings $|\lambda_{345}| \gtrsim 0.01$ in this mass regime. It is worth pointing out that the parameter space in this regime of mass splitting is virtually insensitive to even larger mass splittings as co-annihilations of the DM particle H and another inert scalar are greatly suppressed.

One may wonder whether the viable parameter space for $70 \, \text{GeV} \lesssim m_H \lesssim 74 \, \text{GeV}$ in the left panel of Fig. 4.10 can be broadened in the present IDMEFT framework in a *natural* way. Connecting the results in Figs. 4.9 and 4.10, one could open the parameter space which overcloses the Universe for $\tilde{c}_2 = 25 \, \text{PeV}^{-2}$ by assuming a larger value for the Wilson coefficient. Owing to the constructive contribution to the thermally averaged annihilation cross section, the currently excluded parameter space would open, but at the same time the baryon asymmetry of the Universe gets too large. As a conclusion, the CP-violating operator alone cannot account for the new parameter space. Remarkably however, a UV theory generating the operator in Eq. (4.31) would naturally give rise to the CP-*conserving* operator

$$\mathcal{L} \supset c_2|\Phi_2|^2 V_{\mu\nu}V^{\mu\nu} \tag{4.39}$$

with the same nomenclature as for the CP-violating operator in Eq. (4.31). The right panel in Fig. 4.10 clearly shows that further viable parameter space opens for contributions from the new, CP-conserving $D = 6$ operator. The right panel in Fig. 4.10 shows the corresponding DM parameter space for $c_2 = 6 \times 10^{-7} \, \text{GeV}^{-2}$. Note that this CP-conserving operator could be generated by new physics which includes particles not much heavier than $\sim \mathcal{O}(1 \, \text{TeV})$ with $\mathcal{O}(1)$ CP-conserving couplings.

After having discussed the DM phenomenology of the IDMEFT and identified a new parameter space with an additional, yet naturally arising effective operator, we shall elaborate on possible realizations in a UV theory before we move on to the mass regime with large DM masses.

The power of the description in the EFT framework manifests itself in the fact that the new physics at a higher energy scale is encapsulated in the Wilson coefficient. The effective operators $\Phi_2^\dagger \Phi_2 B_{\mu\nu} \widetilde{B}^{\mu\nu}$ and $\Phi_2^\dagger \Phi_2 W_{\mu\nu}^I \widetilde{W}^{I\mu\nu}$ in Eq. (4.31) can be generated either via tree-level interactions mediated by a sufficiently heavy field beyond the IDM spectrum or via loop processes which might also account for the large suppression scale.

Applying the results of Ref. [281] to the IDM, we find that the effective operators can be induced by the following operators including heavy scalar and vector fields:

$$-\mathcal{L}_{\mathcal{V},\mathcal{S}} \supset \left[\gamma_{\mathcal{V}} \mathcal{V}_\mu^\dagger D^\mu \Phi_2 + \text{h.c.}\right] + ig_{\mathcal{V}}^W \mathcal{V}_\mu^\dagger \sigma^I \mathcal{V}_\nu W^{I\mu\nu} + ig_{\mathcal{V}}^{\widetilde{W}} \mathcal{V}_\mu^\dagger \sigma^I \mathcal{V}_\nu \widetilde{W}^{I\mu\nu}$$

$$+ ig_{\mathcal{V}}^B \mathcal{V}_\mu^\dagger \mathcal{V}_\nu B^{\mu\nu} + ig_{\mathcal{V}}^{\widetilde{B}} \mathcal{V}_\mu^\dagger \mathcal{V}_\nu \widetilde{B}^{\mu\nu} + \varepsilon_{\mathcal{S}\mathcal{V}} \mathcal{S} \mathcal{V}_\mu^\dagger \mathcal{V}^\mu + \kappa_{\mathcal{S}} \mathcal{S} \Phi_2^\dagger \Phi_2$$

$$+ h_{\mathcal{V}}^{(1)} \mathcal{V}_\mu^\dagger \mathcal{V}^\mu \Phi_2^\dagger \Phi_2 + h_{\mathcal{V}}^{(2)} \left(\mathcal{V}_\mu^\dagger \Phi_2\right) \left(\Phi_2^\dagger \mathcal{V}^\mu\right) + \left[h_{\mathcal{V}}^{(3)} \left(\mathcal{V}_\mu^\dagger \Phi_2\right) \left(\mathcal{V}^{\dagger\mu} \Phi_2\right) + \text{h.c.}\right]$$

$$+ \left[g_{\mathcal{S}\mathcal{V}} \Phi_2^\dagger \left(D_\mu \mathcal{S}\right) \mathcal{V}^\mu + g_{\mathcal{S}\mathcal{V}}' \left(D_\mu \Phi_2\right)^\dagger \mathcal{S} \mathcal{V}^\mu + \text{h.c.}\right] . \tag{4.40}$$
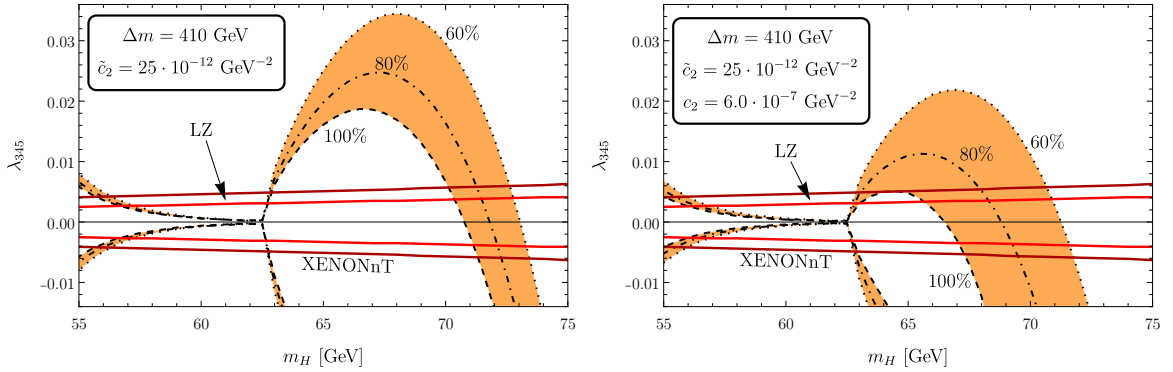
Figure 4.10: Parameter space for $0.6 \leq \Omega_{\text{DM}} h^2 / (\Omega_{\text{DM}} h^2)_{\text{obs}} \leq 1$ in terms of the DM mass m_H and the Higgs portal coupling λ_{345} for fixed mass splitting Δm and Wilson coefficients $\tilde{c}_2$, c_2 ($c_2 = 0$ if not stated differently). The inner boundary corresponds to the full amount of DM. The red, solid lines enclose the parameter space in agreement with the XENONnT and LZ DMDD constraints. Taken from Ref. [3] and see further details on the DM investigation in Ref. [1].

The operators are generated at tree level in case of a heavy vector field $\mathcal{V}_\mu : (\mathbf{1}, \mathbf{2}, 1)$, as depicted in the upper left diagram in Fig. 4.11. In this case the vector $\mathcal{V}_\mu$ must transform under the aforementioned $\mathbb{Z}_2$ symmetry as $\mathcal{V}_\mu \rightarrow -\mathcal{V}_\mu$. Instead of adding just one field, a UV theory with the aforementioned vector and a scalar singlet $\mathcal{S}$ leads to additional contributions at loop level.

Owing to the operators in the first line of Eq. (4.40), the UV extension with the heavy vector naturally generates the CP-conserving operators $\Phi_2^\dagger \Phi_2 W_{\mu\nu}^I W^{I\mu\nu}$ and $\Phi_2^\dagger \Phi_2 B_{\mu\nu} B^{\mu\nu}$ at tree level. Loop-suppressed realizations are possible via the other CP-conserving operators. Remarkably, the CP-conserving operator receives contributions proportional to $|\gamma_\mathcal{V}|^2$, which might motivate the hierarchy $c_2 \gg \tilde{c}_2$ of the Wilson coefficients.

In general, this UV completion generates the operator $\Phi_2^\dagger \sigma^I \Phi_2 \widetilde{W}_{\mu\nu}^I B^{\mu\nu}$ in addition. Here we assume a vanishing coupling and expect that the qualitative findings do not get altered by including this operator.

Lastly, a possible UV realization of the operators could involve heavy, vector-like fermions instead of bosons. Generating the effective operators requires a gauge singlet $N : (\mathbf{1}, \mathbf{1}, 0)$ and the $SU(2)_L$ doublet $\Delta_{(L,R)} : (\mathbf{1}, \mathbf{2}, -1)$. The operators read

$$\mathcal{L}_{N,\Delta} \supset \overline{N} i \slashed{D} N + \overline{\Delta} i \slashed{D} \Delta - \left[y_{N\Delta} \, \overline{N_R} \widetilde{\Phi}_2^\dagger \Delta_L + y_{\Delta N} \, \overline{\Delta_R} \Phi_2 N_L + \text{h.c.} \right] . \qquad (4.41)$$
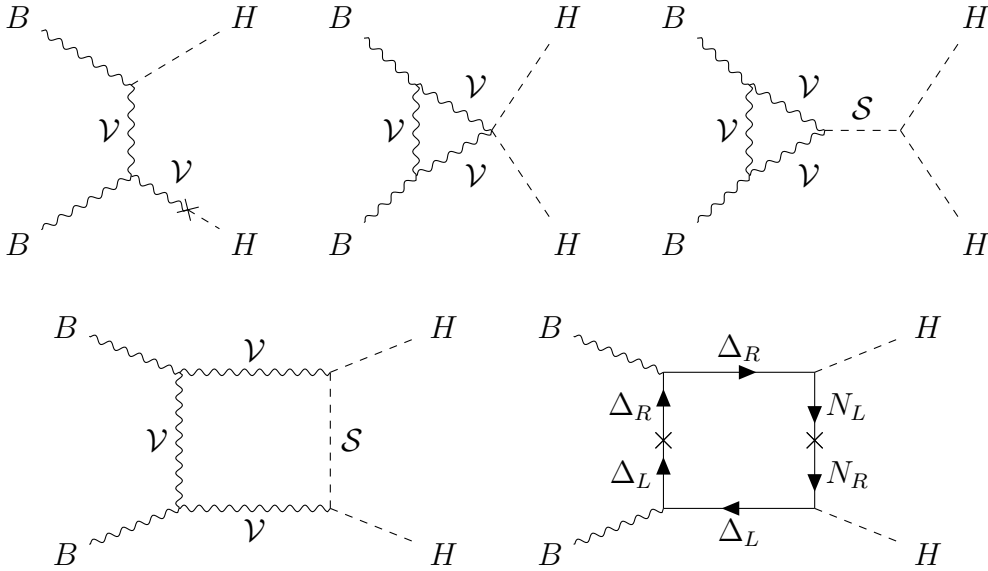
Figure 4.11: Example diagrams for realizing the effective operators in the low-mass regime, including a vector $\mathcal{V}_\mu$, a scalar singlet $\mathcal{S}$, and two vector-like fermions N, Δ.

Further UV completions include, for instance, fermions transforming as $SU(2)_L$ triplets.

Summarizing the findings so far, our scenario accounts for the measured baryon asymmetry as well as the DM relic abundance in the broader DM mass range. Both is not possible in the original IDM as the IDM does neither provide a BSM source of CP violation nor the broader DM mass window due to inefficient DM annihilations in this range.

Comments on the High-Mass Regime

The analysis of the IDMEFT so far featured the $D = 6$ operator for the DM relic abundance and the baryon asymmetry in the DM mass regime in the vicinity of the resonance at $m_H = m_h/2$. But what about the other possible mass range at $m_H \gtrsim 500 \, \text{GeV}$? According to the results in Ref. [1], this mass regime does not provide the parameter space for a two-step EWPhT and the effective operator in Eq. (4.31) can therefore not be used to generate the baryon asymmetry of the Universe. However, a strong first-order EWPhT is possible and the CP-violating SMEFT operator $\tilde{c}_1|\Phi_1|^2 V_{\mu\nu}\widetilde{V}^{\mu\nu}$ can be applied instead. However, there is in fact the problem that the parameter space for the strong first-order EWPhT does not lead to the measured DM relic abundance (*cf.* Fig. 7 in Ref. [1]) as the model requires a quasi-degenerate mass spectrum of the scalars from the inert doublet Φ_2 for the measured DM relic abundance [1, 261]. Mass splittings of $\Delta m \gtrsim 10 \, \text{GeV}$ between the DM particle H and the other BSM scalars lead to sizable cross sections for the DM annihilations into pairs of longitudinally polarized gauge bosons and consequently to underabundant DM [1]. This is in conflict with the mass splitting $\Delta m \sim 200 \, \text{GeV}$ for a strong first-order EWPhT. Additional effective operators might ameliorate this problem by modifying interactions between the DM particle and SM gauge bosons. The effective operators which modify the DM annihilations into longitudinally polarized gauge bosons read

$$\begin{aligned}
\mathcal{L}_{\text{BSM}} \supset{}& C_1 \left|\Phi_1\right|^2 \left(D_\mu\Phi_2\right)^\dagger D^\mu\Phi_2 + C_2 \left|\Phi_2\right|^2 \left(D_\mu\Phi_1\right)^\dagger D^\mu\Phi_1 \\
&+ C_3 \left[\Phi_1^\dagger\Phi_2 \left(D_\mu\Phi_1\right)^\dagger D^\mu\Phi_2 + \text{h.c.}\right] + C_4 \left[\Phi_1^\dagger\Phi_2 \left(D_\mu\Phi_2\right)^\dagger D^\mu\Phi_1 + \text{h.c.}\right] .
\end{aligned} \quad (4.42)$$

Although the Wilson coefficients C_3 and C_4 can be complex in principle and might pose new source of CP violation, we assume real Wilson coefficients C_i for the sake of simplicity. According to our findings, negative Wilson coefficients result in an enhanced DM relic abundance. In fact, the behaviour of the total cross section is determined by an interplay between reducing the contributions of the DM annihilations into EW

gauge bosons and increasing the annihilations into a pair of either SM Higgs bosons or top quarks. Sampling the Wilson coefficients leads for example to the benchmark points

$$C_1 = -5.4\,\text{TeV}^{-2} \quad , \quad C_3 = -3.1\,\text{TeV}^{-2} \quad , \quad C_4 = -3.2\,\text{TeV}^{-2} \tag{4.43}$$

with $C_2 \approx 0$. The resulting parameter space for these Wilson coefficients with a mass splitting $\Delta m \sim 120\,\text{GeV} \gg 10\,\text{GeV}$ is shown in Fig. 4.12 and confronted with the currently most stringent limits from DMDD experiments and theoretical constraints from vacuum stability.

Note that this is an improvement but not enough to realize a strong first-order EWPhT in this model since the mass splitting is too small. Nevertheless, the expansion of the viable DM region to significantly larger mass splittings is an important first step towards a realistic model of baryogenesis and DM side by side for DM masses far beyond the resonance regime. Considering possible UV completions, further operators like $|\Phi_1|^6$ can enhance the EWPhT (see Refs. [196, 197, 282, 283]) and collectively give rise to a strong first-order EWPhT in this mass regime. Yet, in light of the beauty of minimality, this mass regime is arguably a less attractive scenario for DM and baryogenesis in the IDM framework than the mass regime discussed before.

Before studying potential UV completions of this mass regime, we shall examine the new IDMEFT operators in Eq. (4.42) which include the SM gauge covariant derivative and thus the gauge fields. Due to the large DM mass the center-of-mass energy of the
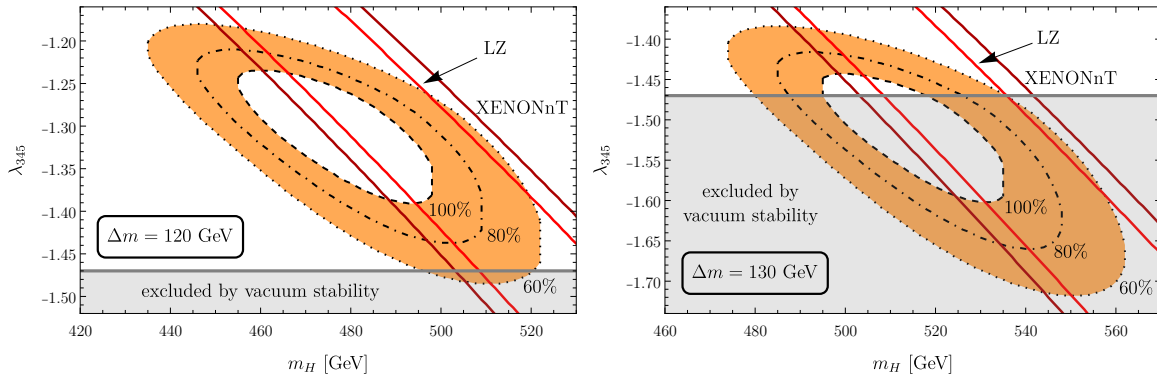
Figure 4.12: Parameter space for $0.6 \leq \Omega_{\text{DM}}h^2/(\Omega_{\text{DM}}h^2)_{\text{obs}} \leq 1$, with respect to the DM mass m_H, the Higgs portal coupling λ_{345}, and the mass splittings Δm. We assume $\tilde{c}_2 = 0$, since this operator is not capable of generating the baryon asymmetry in this mass regime. Adopting the results from Ref. [258], the Higgs portal coupling is bounded from below, $\lambda_{345} > -2\sqrt{\lambda_1 4\pi/3} \approx -1.47$. Taken from Ref. [3].

DM annihilation process is much larger than the masses of the SM gauge bosons and the Goldstone boson equivalence theorem applies. The Goldstone boson equivalence theorem says that the longitudinal polarization states of the gauge bosons dominate the cross sections for high energies (see, *e.g.*, Ref. [9]). Therefore, we shall consider only the longitudinal components of the gauge bosons which are the Goldstone bosons G^0 and $G^\pm$ from the SM Higgs doublet.

In the following, we shall discuss the individual operators and present the dependence of the thermally averaged DM annihilation cross sections in Fig. 4.13. For this we consider the interactions between two DM fields H and either the SM Higgs boson h and the Goldstone bosons $G^{0,\pm}$.

The cross sections were computed with the public `micrOMEGAs` package which is based on the mathematical `CalcHEP` code [284–287] and takes only interactions with up to four fields into account. Therefore, we shall restrict the analysis of relevant interaction terms to this.

The first operator, which corresponds to the Wilson coefficient C_1, leads to the interaction terms

$$|\Phi_1|^2 \, |D_\mu \Phi_2|^2 \supset \frac{1}{4} \partial_\mu H \partial^\mu H \left(h^2 + 2vh + G^0 G^0 + 2G^+ G^- \right) . \qquad (4.44)$$

As shown in Fig. 4.13, the sign of the Wilson coefficient C_1 impacts the DM annihilation cross section for large values of $|C_1|$ because of interference effects. Not surprisingly, the contribution of this IDMEFT operator tends to zero towards smaller values of the Wilson coefficient and the DM annihilation cross sections for positive and negative Wilson coefficients converge towards the annihilation cross section predicted by the original IDM.

The second IDMEFT operator reads

$$|\Phi_2|^2 \, |D_\mu \Phi_1|^2 \supset \frac{1}{4} H^2 \left(\partial_\mu h \partial^\mu h + \partial_\mu G^0 \partial^\mu G^0 + 2\partial_\mu G^- \partial^\mu G^+ \right) . \qquad (4.45)$$

The shape of the four curves as well as the dependence on the sign of the Wilson coefficient is qualitatively the same for the two IDMEFT operators associated with C_1 and C_2. Note that the minima of the DM annihilation cross sections for $HH \to ZZ$ and $HH \to W^+ W^-$ for each operator are located at the same values of the Wilson coefficients because the contributions of the DM annihilation channels (four-point interaction, s- and t-channel, and u-channel if necessary) for both DM annihilation processes are equal.

Lastly, the third and fourth operators, associated with C_3 and C_4, respectively, involve the interactions

$$\Phi_1^\dagger \Phi_2 \left(D_\mu \Phi_1\right)^\dagger D^\mu \Phi_2 + \text{h.c.} \supset \frac{1}{2}\partial_\mu H \left(Hh\partial^\mu h + vH\partial^\mu h - HG^0\partial^\mu G^0 + vA\partial^\mu G^0\right)$$
$$+ \frac{v}{2}H \left(\partial_\mu G^0\partial^\mu A + \partial_\mu G^-\partial^\mu H^+ + \partial_\mu G^+\partial^\mu H^-\right) \quad (4.46)$$

$$\Phi_1^\dagger \Phi_2 \left(D_\mu \Phi_2\right)^\dagger D^\mu \Phi_1 + \text{h.c.} \supset \frac{1}{2}\partial_\mu H \left(Hh\partial^\mu h + vH\partial^\mu h + HG^0\partial^\mu G^0 - vA\partial^\mu G^0\right)$$
$$+ \frac{v}{2}H \left(\partial_\mu G^0\partial^\mu A + \partial_\mu G^-\partial^\mu H^+ + \partial_\mu G^+\partial^\mu H^-\right) \quad (4.47)$$

and the DM annihilation cross sections in Fig. 4.13 feature qualitative differences compared to the first two operators. The two IDMEFT operators in Eqs. (4.46) and (4.47) are identical except for two interaction terms involving the neutral Goldstone boson G^0.
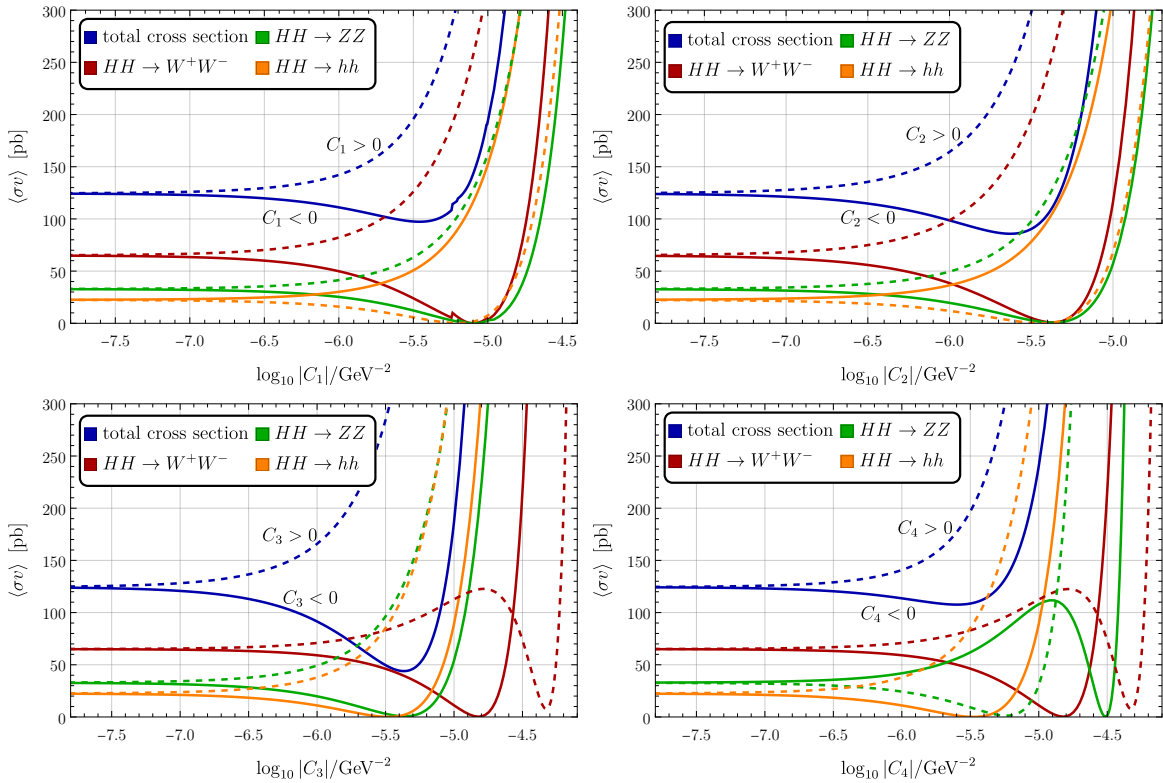
Figure 4.13: Thermally averaged DM annihilation cross section $\langle \sigma v \rangle$ in terms of the Wilson coefficients C_i for the DM mass $m_H = 490\,\text{GeV}$, the mass difference $\Delta m = 120\,\text{GeV}$ between the DM scalar and the other, equally heavy scalars from the inert Higgs doublet, and the Higgs portal coupling $\lambda_{345} = -1.3$. Taken from Ref. [3].

71

Therefore, the DM annihilation cross sections for hh and W^+W^- in the final state are the same for these two IDMEFT operator, whereas the process $HH \to ZZ$ is modified.

In addition to the DM annihilation cross section, the reader may wonder whether and to what extent the IDMEFT operators affect the spin-independent DMDD cross section σ_{SI}. The SI scattering processes are mediated by the SM Higgs boson exclusively. Besides the contribution from the original IDM and the IDMEFT operator associated with C_1, the last two effective operators contribute to the SI DMDD cross section via the momenta. The contribution of these two operators is

$$(C_3 + C_4)\left(p_{1,\mu}p_2^\mu - p_{1,\mu}p_3^\mu\right) \propto p_{1,\mu}p_1^\mu. \tag{4.48}$$

With the momentum p_1 of the SM Higgs boson and $p_{2,3}$ being the DM particles' momenta, the term on the right-hand side results from momentum conservation in the HHh-interaction. Due to the fact that `micrOMEGAs` computes the SI scattering cross section σ_{SI} in the limit of vanishing momentum transfer, *i.e.* $p_{1,\mu}p_1^\mu = 0$, the contributions of the IDMEFT operators associated with $C_{3,4}$ are absent in our numerical results. This approximation is reasonable because the momentum transfer in DM-nucleus scattering processes is $\sim \mathcal{O}\left(10 - 100\right)$ MeV $\ll m_h$ [10]. Summarizing the recent findings, only the first effective operator contributes to the SI DMDD cross section whose dependence on the sign of C_1 and the Higgs portal coupling λ_{345} is presented in Fig. 4.14. The plots show that the possible window for the Wilson coefficient $C_1 = \lambda/\Lambda^2$ for a specific Higgs portal coupling is rather small. While the other two values for the Higgs
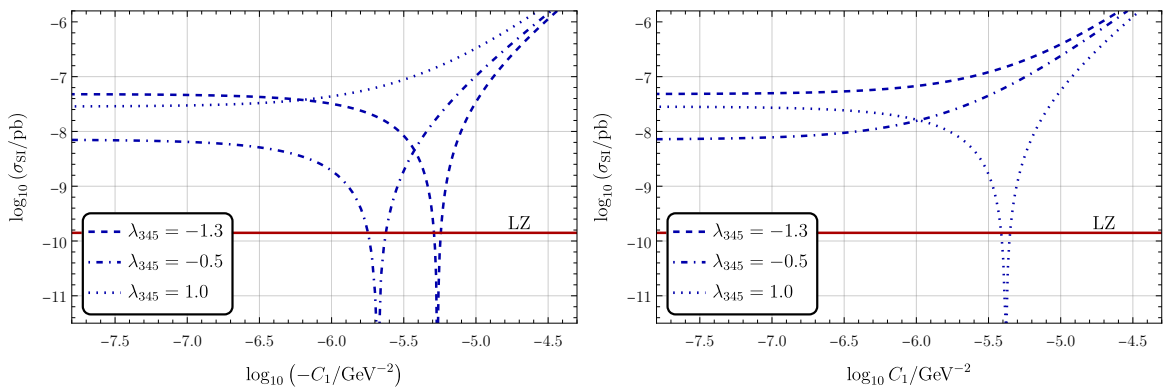
Figure 4.14: Spin-independent DMDD cross section σ_{SI} in terms of the negative (*left*) and positive (*right*) Wilson coefficient C_1. The DM mass is $m_H = 490\,\mathrm{GeV}$, the mass splitting $\Delta m = 120\,\mathrm{GeV}$, and the Higgs portal coupling λ_{345} is shown in the plots. The DMDD cross sections are confronted with the latest LZ limits [110].

portal coupling serve as subjects of comparison, the coupling $\lambda_{345} = -1.3$ was found in Fig. 4.12 and results in the energy scale $\Lambda \approx 4.5\,\mathrm{TeV}$ for $\lambda \sim \mathcal{O}(-0.01)$.

Before finishing this chapter and in spite of the finding that this mass regime and the effective operators in Eq. (4.42) are not as well motivated as the effective operators in Eq. (4.31) for smaller DM mass, we shall proceed the same way as we did for the effective operator in the small DM mass regime and provide an overview of possible realizations beyond the cutoff scale. For this we make use of the summary in Ref. [281] which we used already for the other DM mass regime.

As a reminder, the inert doublet Φ_2 transforms non-trivially under the discrete $\mathbb{Z}_2$ symmetry. Considering the operators

$$-\mathcal{L}_{\mathcal{B},\mathcal{W}} \supset \left[\left(g_{\mathcal{B}}^{D1} \right) \mathcal{B}^\mu \Phi_2^\dagger i D_\mu \Phi_1 + \left(g_{\mathcal{B}}^{D2} \right) \mathcal{B}^\mu \Phi_1^\dagger i D_\mu \Phi_2 + \mathrm{h.c.} \right]$$

$$+ \left[\left(g_{\mathcal{W}}^{D1} \right) \mathcal{W}^{I\mu} \Phi_2^\dagger \frac{\sigma^I}{2} i D_\mu \Phi_1 + \left(g_{\mathcal{W}}^{D2} \right) \mathcal{W}^{I\mu} \Phi_1^\dagger \frac{\sigma^I}{2} i D_\mu \Phi_2 + \mathrm{h.c.} \right] . \qquad (4.49)$$

with the vectors $\mathcal{B}_\mu : (\mathbf{1}, \mathbf{1}, 0)$ and $\mathcal{W}_\mu^I : (\mathbf{1}, \mathbf{3}, 0)$ transforming as a singlet and a triplet with respect to $SU(2)_L$, respectively, these heavy fields must transform in the same way under the discrete Z_2 symmetry as the inert doublet. Hence, the fields must transform as $\mathcal{B}_\mu \to -\mathcal{B}_\mu$ and $\mathcal{W}_\mu^I \to -\mathcal{W}_\mu^I$ under the $\mathbb{Z}_2$ symmetry to generate the first three IDMEFT operators from Eq. (4.42).

The fourth operator from Eq. (4.42), however, requires a very similar set of renormalizable operators and heavy vectors that are invariant under the $\mathbb{Z}_2$ transformation. The set of operators reads

$$-\mathcal{L}_{\mathcal{B}',\mathcal{W}'} \supset \left[\left(g_{\mathcal{B}'}^{D1} \right) \mathcal{B}'^\mu \Phi_1^\dagger i D_\mu \Phi_1 + \left(g_{\mathcal{B}'}^{D2} \right) \mathcal{B}'^\mu \Phi_2^\dagger i D_\mu \Phi_2 + \mathrm{h.c.} \right]$$

$$+ \left[\left(g_{\mathcal{W}'}^{D1} \right) \mathcal{W}'^{I\mu} \Phi_1^\dagger \frac{\sigma^I}{2} i D_\mu \Phi_1 + \left(g_{\mathcal{W}'}^{D2} \right) \mathcal{W}'^{I\mu} \Phi_2^\dagger \frac{\sigma^I}{2} i D_\mu \Phi_2 + \mathrm{h.c.} \right] \qquad (4.50)$$

with the primed vectors being in the same representations as the vectors for the other set of operators above. The relevant tree-level diagrams for the matching of the UV theory onto the IDMEFT are presented in Fig. 4.15.

Discussion

The results from this investigation can be understood as a motivating *first step* an accurate calculation of the baryon asymmetry. Consequently, deploying the estimate from Ref. [270] suffers from the uncertainty that it omits the precise dynamics of the sphaleron processes in the vicinity of the bubble wall. One way towards an accurate calculation was outlined, *e.g.*, in Ref. [288]. Considering the center of the bubble wall at the space coordinate $z = 0$ and the broken EW symmetry in the region with $z \ll 0$, the gradient of the difference n_B of the number densities of baryons and antibaryons obeys the diffusion equation. It reads

$$\partial_z n_B = \frac{3\Gamma_{\rm sph}}{2v_{\rm wall}} \left(N_c \mu_L T^2 - \mathcal{A} n_B \right) \tag{4.51}$$

with the sphaleron rate $\Gamma_{\rm sph}$ for different temperature regimes given in Eqs. (4.11) and (4.12), the number of colors N_c, the chemical potential μ_L of LH quarks in front of the bubble wall, and the parameter $\mathcal{A} = 15/2$ governed by the number of fermions in thermal equilibrium during the sphaleron processes. With this, the asymmetry parameter η can be inferred from Ref. [288] and is given by

$$\eta \equiv \frac{n_B\left(z \to -\infty\right)}{n_\gamma} = \frac{3N_c T^2}{2n_\gamma v_{\rm wall}} \int_{-\infty}^{+\infty} {\rm d}z \, \Gamma_{\rm sph} \mu_L e^{-\frac{3\mathcal{A}}{2v_{\rm wall}} \int_{-\infty}^{z} {\rm d}z' \, \Gamma_{\rm sph}} . \tag{4.52}$$

The chemical potential μ_L of the LH quarks is increased by an enhanced interaction strength of CP-violating processes and must be calculated meticulously for a reliable result. For this the relation between the effective, CP-violating operator and the chemical potential must be derived. Moreover, an accurate calculation requires a careful analysis of the bubble dynamics, including the wall velocity and the profile of the bubble wall with a finite thickness. The latter governs the z-dependent sphaleron rate $\Gamma_{\rm sph}$.
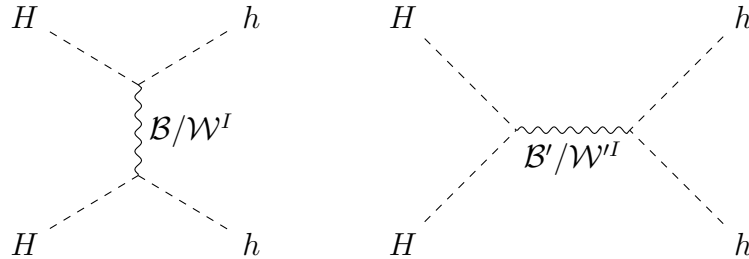
Figure 4.15: Example diagrams for realizations of the effective vertices in Eq. (4.42), induced by a heavy vector singlet $\mathcal{B}^{(\prime)}$ or vector triplet $\mathcal{W}^{(\prime)I}$. Taken from Ref. [3].

A precise calculation of the baryon asymmetry for the effective, CP-violating operator has not been performed to our knowledge, but would be enlightening to assess quantitatively the quality of the estimate and the results we presented above.

In conclusion, this chapter demonstrated the possibility to account for the baryon asymmetry of the Universe in scalar DM models via an EFT approach and presented a couple of potential UV realizations. Recalling the list of shortcomings of the SM, the reader might wonder whether there is a connection between the presence of DM and the neutrino properties that allows to determine the latter experimentally. This shall be the subject of the next chapter.

Chapter 5

Neutrino Properties from Dark Matter Annihilations

For this last chapter before the conclusion, we shall still consider a theory with a dark sector but put the motivation of explaining the baryon asymmetry of the Universe aside. We rather turn to the puzzling observation of neutrino oscillation and the consequence of *massive* neutrinos.[1] Before presenting a few models for explaining the tiny – but finite – neutrino masses in Section 5.2 and discussing our results on the potential for inferring neutrino properties from studying DM annihilations in the consecutive sections, we shall first elaborate on the theoretical and experimental motivation for this study.

5.1 Theoretical and Experimental Background of Neutrino Properties

As we have seen already above in the introduction to the SM and the discussion on the EW sector in Chapter 1, the SM provides remarkably successful predictions, *e.g.* for the masses of the EW gauge bosons. The prediction of exactly massless neutrinos, however, is experimentally disproved by the discovery of non-zero masses and mixings. Unlike the other fermions in the SM which are charged under $SU(3)_c \times U(1)_Q$, the SM neutrinos are a singlet under this gauge group. The SM contains only LH neutrinos which reside in the same $SU(2)_L$ doublets as their associated charged lepton siblings. Therefore, the only neutrino Majorana mass term in agreement with the SM gauge group and particle content would be the bilinear operator $\overline{L^c}L \equiv L^T C L$ with the charge conjugation

---

[1]In this context the term 'massive' refers to a *finite* mass.

operator $C \equiv i\gamma_2\gamma_0$ [289]. However, the lepton number symmetry would be violated by two units by this operator and thus forbids this term in the SM. Moreover, as we have seen in Section 4.1, the global symmetry $U(1)_{B-L}$ is exact and consequently prevents this bilinear operator from being generated by non-perturbative effects [10]. Hence, the SM neutrinos are exactly massless – which contradicts the experimentally confirmed neutrino oscillations. The experimental evidence for at least two massive neutrinos via neutrino oscillation measurements, which culminated in the Nobel Prize for Kajita and McDonald in 2015, reshaped the notion of neutrinos substantially [290, 291]. The SM falls short also in this point and the search for BSM physics is in order.

Before we provide a brief overview of potential particle physics models for the generation of neutrino masses and elaborate on two specific neutrino mass models, we shall begin with the theoretical foundation of neutrinos and their masses (see, e.g., Refs. [292, 293] for overviews).

Analogously to the CKM matrix in the quark sector, the weak and mass eigenstates of the neutrinos are not identical. The corresponding Pontecorvo-Maki-Nakagawa-Sakata (PMNS) mixing matrix for Dirac neutrino reads [10]

$$
V_{\mathrm{PMNS}}^{\mathrm{D}} = \begin{pmatrix} c_{12}c_{13} & s_{12}c_{13} & s_{13}e^{-i\delta_{\mathrm{CP}}} \\ -s_{12}c_{23} - c_{12}s_{23}s_{13}e^{i\delta_{\mathrm{CP}}} & c_{12}c_{23} - s_{12}s_{23}s_{13}e^{i\delta_{\mathrm{CP}}} & s_{23}c_{13} \\ s_{12}s_{23} - c_{12}c_{23}s_{13}e^{i\delta_{\mathrm{CP}}} & -c_{12}s_{23} - s_{12}c_{23}s_{13}e^{i\delta_{\mathrm{CP}}} & c_{23}c_{13} \end{pmatrix} \tag{5.1}
$$

with the short-hand notation $s_{ij} \equiv \sin\theta_{ij}$, $c_{ij} \equiv \cos\theta_{ij}$, and the CP-violating Dirac phase δ_{CP}. The PMNS matrix for the case of Dirac neutrinos contains $3(n-2)$ angles and $2n-5$ physical phases, where $n = 3$ is the number of massive neutrinos we shall consider in the tree-level investigation below [10]. For Majorana neutrinos, the number of physical phases is $3(n-2)$ and the PMNS matrix for this scenario is given by

$$
V_{\mathrm{PMNS}}^{\mathrm{M}} = V_{\mathrm{PMNS}}^{\mathrm{D}} \times \mathcal{D}^{\mathrm{M}} \equiv V_{\mathrm{PMNS}}^{\mathrm{D}} \times \mathrm{diag}\left(1, e^{i\varphi_1/2}, e^{i\varphi_2/2}\right) \tag{5.2}
$$

with the two Majorana phases $\varphi_{1,2}$. The entries of the neutrino mass matrix for three massive neutrinos are hence given by [294]

$$
(m_\nu)_{ij} = \left[V_{\mathrm{PMNS}}^{\mathrm{M}} \, \mathrm{diag}\left(m_1, m_2, m_3\right) \left(V_{\mathrm{PMNS}}^{\mathrm{M}}\right)^T \right]_{ij} . \tag{5.3}
$$

This PMNS matrix describes how the neutrino flavors mix with each other to create the respective mass eigenstates. As the latter are those that propagate in spacetime, the PMNS matrix plays a prime role in neutrino oscillations and mixings and determin-

ing its parameters is key for understanding the nature of neutrinos. The neutrino sector is described by nine parameters in total which are the three mixing angles θ_{12}, θ_{23}, θ_{13}, two mass differences Δm_{21}^2, $\Delta m_{3\ell}^2$ with $\ell = 1(2)$ for NH (IH), the lightest neutrino mass $m_0 \equiv m_{1(3)}$ for normal mass hierarchy (inverted mass hierarchy), and three CP phases δ_{CP}, $\varphi_{1,2}$. While the mass differences Δm_{21}^2, $\Delta m_{3\ell}^2$ are fairly precisely known by the measurement of solar and atmospheric neutrinos, respectively, the mass *hierarchy* of the neutrino masses is yet unknown. It can be either the normal hierarchy with $m_1 < m_2 < m_3$ or the inverted hierarchy with $m_3 < m_1 < m_2$. The first five neutrino parameters have been experimentally determined very accurately (*cf.* Tab. 5.1). Experimental data could in principle allow to determine the Dirac CP phase δ_{CP}, but the results from the long-baseline T2K [296] and NOνA [297] experiments are yet inconclusive. More data for better statistics as well as mitigating systematic uncertainties with the help of future, improved experimental setups might help narrow down the range. In the subsequent analysis we adopt the best-fit values from the *NuFIT* group which has specialized on analyses of the neutrino oscillation measurements in light of three massive neutrinos in the SM (see, *e.g.*, Refs. [295, 298, 299] for recent publications). The remaining three neutrino parameters are the absolute neutrino mass scale m_0 and the two Majorana phases φ_1, φ_2 which cannot be specified by neutrino oscillation experiments.

Neutrino oscillations occur as the weak eigenstates of the neutrinos are not identical to their mass eigenstates. The neutrino flavor eigenstates with the flavor index α can be expressed in terms of the three mass eigenstates with the mass index i as [10]

$$|\nu_\alpha\rangle = \sum_{i=1}^{3} \left(V_{\mathrm{PMNS}}^{\mathrm{M}}\right)_{\alpha i}^* |\nu_i\rangle \; . \tag{5.4}$$

Neutrino Parameter	Normal Mass Hierarchy	Inverted Mass Hierarchy
$\Delta m_{21}^2 / \left(10^{-5}\,\mathrm{eV}^2\right)$	7.42	7.42
$\Delta m_{3\ell}^2 / \left(10^{-3}\,\mathrm{eV}^2\right)$	2.517	-2.498
$\sin^2\theta_{12}$	0.304	0.304
$\sin^2\theta_{23}$	0.573	0.575
$\sin^2\theta_{13}$	0.02219	0.02238
$\delta_{\mathrm{CP}}/^\circ$	197_{-24}^{+27}	282_{-30}^{+26}

Table 5.1: Summary of the best-fit neutrino oscillation parameters with SuperKamiokande atmospheric neutrino data [295]. The difference between m_3^2 and m_ℓ^2 depends on the mass hierarchy with $\ell = 1(2)$ for NH(IH).

The probability to find a neutrino with the flavor β after being produced in flavor α is thus given by [10]

$$P_{\alpha\beta} = |\langle \nu_\beta | \nu_\alpha(t) \rangle|^2 = \left| \sum_{i,j=1}^{3} \left(V_{\mathrm{PMNS}}^{\mathrm{M}}\right)_{\alpha i}^* \left(V_{\mathrm{PMNS}}^{\mathrm{M}}\right)_{\beta j} \langle \nu_j | \nu_i(t) \rangle \right|^2 . \tag{5.5}$$

The *ansatz* of a plane wave, $|\nu_j(t)\rangle = e^{-iE_j t} |\nu_j(t=0)\rangle$ and of a relativistic neutrino leads to the oscillation probability [10]

$$P_{\alpha\beta} = \delta_{\alpha\beta} - 4 \sum_{i<j}^{3} \mathrm{Re}\left[\left(V_{\mathrm{PMNS}}^{\mathrm{M}}\right)_{\alpha i} \left(V_{\mathrm{PMNS}}^{\mathrm{M}}\right)_{\beta i}^* \left(V_{\mathrm{PMNS}}^{\mathrm{M}}\right)_{\alpha j}^* \left(V_{\mathrm{PMNS}}^{\mathrm{M}}\right)_{\beta j} \right] \sin^2 \frac{\Delta m_{ij}^2 L}{4E}$$

$$+ 2 \sum_{i<j}^{3} \mathrm{Im}\left[\left(V_{\mathrm{PMNS}}^{\mathrm{M}}\right)_{\alpha i} \left(V_{\mathrm{PMNS}}^{\mathrm{M}}\right)_{\beta i}^* \left(V_{\mathrm{PMNS}}^{\mathrm{M}}\right)_{\alpha j}^* \left(V_{\mathrm{PMNS}}^{\mathrm{M}}\right)_{\beta j} \right] \sin \frac{\Delta m_{ij}^2 L}{2E} \tag{5.6}$$

with the difference of the squared masses $\Delta m_{ij}^2 \equiv m_i^2 - m_j^2$. The oscillation length in vacuum is given by [10]

$$L_{ij}^{\mathrm{osc}} = \frac{4\pi E}{|\Delta m_{ij}^2|} . \tag{5.7}$$

The oscillation probability described above applies to neutrino propagating in vacuum. Measurements of solar neutrinos and the unexpected result in the counts of electron neutrinos led to the idea that the matter along the way impacts the neutrino oscillation. The Mikheyev–Smirnov–Wolfenstein (MSW) effect successfully accounts for the neutrino propagation in varying matter densities [300, 301].

Besides confirming the mere fact that at least two of the three SM neutrinos are massive, neutrino oscillation experiments offer insights in the mass differences between the different states. What this type of experiments is not sensitive to is the Majorana phases, the absolute neutrino mass scale m_0, and the sign of the mass differences. The CP phases are interesting to know as they would show whether the CP symmetry is violated also in the SM lepton sector. In the following we shall briefly discuss three experimental approaches for determining the absolute neutrino mass scale as well as the mass hierarchy.

Concerning the mass m_0 of the lightest active neutrino, one approach is the precise measurement of the electron energy spectrum of the β decay. Regardless of the nature of the neutrinos (*i.e.*, whether it is a Dirac or Majorana particle), the emission of a massive

neutrino impacts the part of the energy spectrum near the end point and thus provides information about the neutrino mass for sufficiently good energy resolution [292]. The effective electron neutrino mass is defined as

$$m_\beta \overset{\text{def}}{=} \sqrt{\sum_i m_i \left| V_{\text{PMNS}}^{\text{M}} \right|_{ei}^2} \tag{5.8}$$

and the currently best limit from these β decay experiments is $m_\beta < 0.8\,\text{eV}$, set by the KATRIN collaboration [302].

Another approach is the precise analysis of the CMB. The sum of the neutrino masses is experimentally constrained by Planck [75], extended Baryon Oscillation Spectroscopy Survey (eBOSS) [303], Atacama Cosmology Telescope (ACT) [304], and Dark Energy Spectroscopic Instrument (DESI) [305]. The limits read

$$\sum_i m_i < \begin{cases} 0.12\,\text{eV} & \text{for Planck (95\% C.L.)} \\ 0.12\,\text{eV} & \text{for ATC (95\% C.L.)} \\ 0.082\,\text{eV} & \text{for Planck} + \text{eBOSS (95\% C.L.)} \\ 0.072\,\text{eV} & \text{for Planck} + \text{DESI (95\% C.L.)} \end{cases} \tag{5.9}$$

and allow to infer the upper bounds on the absolute neutrino mass scale with the precise measurements of the neutrino mass differences.

A third possibility to determine the neutrino mass scale as well as the neutrino mass hierarchy and to gain insights into the nature of neutrinos is the search for neutrinoless double β decay ($0\nu\beta\beta$). The coincident β decay with only two instead of four leptons in the final state is only possible if the neutrino is a Majorana particle and annihilates (*cf.* Fig. 5.1). The two possible mass hierarchies as well as the mass of the lightest neutrino result in different $0\nu\beta\beta$ rates which is possible for Majorana neutrinos only (see, *e.g.*, Ref. [306]). Strong limits on the characteristic time scale $T_{1/2}^{0\nu\beta\beta}$ are set by KamLAND-Zen [307] for ^{136}Xe and the GERDA collaboration [308] for ^{76}Ge,

$$T_{1/2}^{0\nu\beta\beta} > \begin{cases} 1.07 \times 10^{26}\,\text{yr} & \text{for KamLAND-Zen} \\ 1.8 \times 10^{26}\,\text{yr} & \text{for GERDA} \end{cases}. \tag{5.10}$$

It is worth mentioning that the discovery of $0\nu\beta\beta$ was claimed in the early 2000s by parts of the Heidelberg-Moscow collaboration [309–311] for ^{76}Ge and disputed in Refs. [312–315]. Comparing to the lower limits for the characteristic time scale in

Eq. (5.10), the announced lifetime $T_{1/2}^{0\nu\beta\beta} \sim \mathcal{O}(10^{25})$ yr is ruled out by the GERDA experiment (see Ref. [315] for the time scale).

As shown in the Feynman diagram in Fig. 5.1, the $0\nu\beta\beta$ rate is dictated by the effective Majorana neutrino mass m_{ee} which is defined as

$$m_{ee} = \left| \sum_i m_i \left(V_{\mathrm{PMNS}}^{\mathrm{M}} \right)_{ei}^2 \right| \tag{5.11}$$

with the sum over the three SM neutrino flavors. The absence of a signal corresponds to a small $0\nu\beta\beta$ rate and thus to a small effective Majorana neutrino mass. The characteristic time scales in Eq. (5.10) can be translated into [307, 308]

$$m_{ee} < \begin{cases} 61 - 165\,\mathrm{meV} & \text{for KamLAND-Zen} \\ 79 - 180\,\mathrm{meV} & \text{for GERDA} \end{cases}. \tag{5.12}$$

The uncertainties stem from the calculation of the involved nuclear matrix elements [10]. The dependence of the effective Majorana neutrino mass on the lightest neutrino mass m_0 is depicted in the left panel of Fig. 5.1. With future experiments pushing the limits on the effective Majorana neutrino mass and on the absolute neutrino mass scale towards smaller values, the neutrino mass hierarchy can be determined. Note that a positive signal in $0\nu\beta\beta$ experiments indicates lepton number violation but does not unambiguously lead to the value of the effective Majorana neutrino mass m_{ee} since
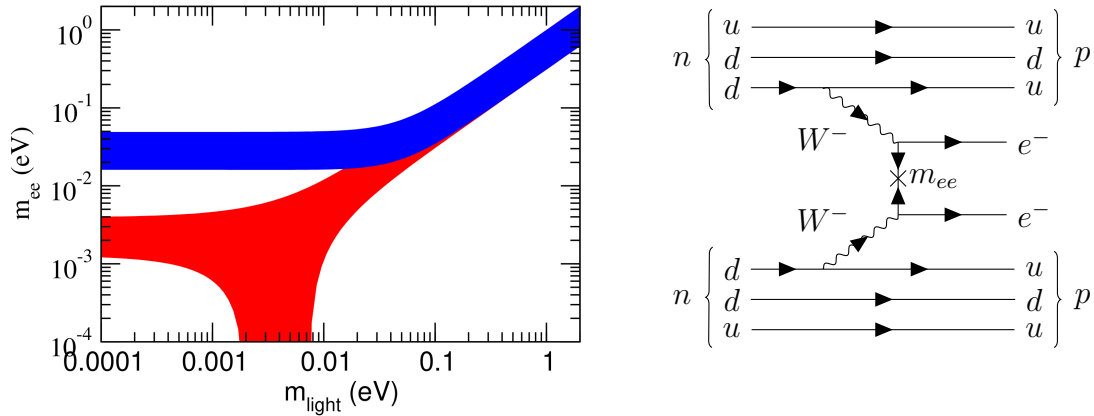
Figure 5.1: *Left*: Dependence of the effective Majorana neutrino mass m_{ee} on the neutrino mass scale $m_{\mathrm{light}} \equiv m_0$. The bands correspond to normal (red) and inverted (blue) neutrino mass hierarchy. Figure taken from Ref. [10]. *Right*: Lowest-order neutrinoless double-β decay.

additional, new lepton number-violating interactions can contribute to the rate and hence to the effective m_{ee} (see, *e.g.*, Refs. [316, 317] for details).

5.2   Overview of Neutrino Mass Models

The evidence for massive neutrinos is overwhelming and an extension of the SM to account for this fact is in order. One straightforward extension is the introduction of RH neutrinos. Since the neutrino carries neither color nor electric charge and RH fermions do not participate in weak interactions, *i.e.* transform as singlets under $SU(2)_L$, the RH neutrino is a full singlet with respect to the SM gauge group. With the RH neutrinos at hand and inspired by the mass-generating interactions of the other SM fermions, tiny Yukawa couplings of the order $y^\nu \lesssim \mathcal{O}(10^{-13})$ could explain Dirac neutrino masses. As such a small coupling parameter seems unnatural and new physics would be expected to explain *these small couplings*, other, more natural explanations become appealing and shall be discussed in the next section. Moreover, the RH neutrinos are singlets and Majorana mass terms are therefore not prohibited by any symmetry.

The lowest-dimensional operator for a Majorana neutrino mass at $D = 5$ is the so-called Weinberg operator $LL\Phi\Phi$ [318]. Even higher-dimensional operators can be built by adding the singlet $\Phi^\dagger\Phi$. Models with $LL\Phi\Phi(\Phi^\dagger\Phi)$ for $D = 7$ and $LL\Phi\Phi(\Phi^\dagger\Phi)^2$ for $D = 9$ operators are presented in Refs. [319–323]. An overview of a wealth of neutrino mass models alongside potential searches at colliders can be found, *e.g.*, in Ref. [324].

Before we delve into the analysis of two specific neutrino mass models, we shall first provide an overview of $D = 5$ neutrino mass models. They can be divided into two categories: tree-level and radiative neutrino mass models. The latter explain the neutrino masses by loop processes and are appealing for the experimental evidence of the smallness of the neutrino masses.

Tree-level mass models

First, we shed light on three prominent neutrino mass models which have been extensively discussed in the literature. The neutrino mass-generating processes are shown in Fig. 5.2. Remarkably, the Weinberg operator can be realized by renormalizable operators in only three ways: (*i*) the lepton doublet L_i and the Higgs doublet Φ form a fermion singlet, (*ii*) the two lepton doublets $L_{i,j}$ form a scalar triplet, and lastly (*iii*) the lepton doublet L_i and the Higgs doublet Φ form a fermion triplet [325]. These three possibilities are described in the following.

Type-I seesaw model

One possible, minimal extension of the SM is a model in which n copies of the right-handed neutrino N_R are added to the leptonic sector with three active neutrinos. The RH neutrino is a full SM singlet, *i.e.* $N_R : (\mathbf{1}, \mathbf{1}, 0)$, and heavy for a sufficiently large suppression of the SM neutrino mass. The relevant operators are

$$-\mathcal{L} \supset \frac{1}{2} \sum_{i,j} M_{ij} \overline{N_R^c} N_R + y_i^\nu \overline{L} \widetilde{\Phi} N_{R,i} + \text{h.c.} \tag{5.13}$$

with the $3 \times n$ Yukawa matrices y_i^ν and the $n \times n$ matrix M. See Refs. [326–330] for details.

Type-II seesaw model

In contrast to the previous model, the type-II seesaw model features a scalar $SU(2)_L$ triplet with the weak hypercharge $Y = 0$ or $Y = 2$ (see, *e.g.*, Refs. [331–335] for recent studies). The latter case is appealing for its doubly charged scalar which can be looked for in ongoing and future collider experiments. For this reason we shall focus on this scenario below in Section 5.3.

The neutrino masses can be generated with the operators

$$-\mathcal{L} \supset \mu_\Delta^2 \text{Tr} \left(\Delta^\dagger \Delta \right) + \lambda |\Phi|^2 \text{Tr} \left(\Delta^\dagger \Delta \right) + i y_{ij} \overline{L_i^c} \sigma_2 \Delta L_j + i \mu_{\Phi\Delta} \Phi^T \sigma_2 \Delta^\dagger \Phi + \text{h.c.} \tag{5.14}$$

Type-III seesaw model

The third type of seesaw model, proposed in Ref. [325, 336], features a leptonic $SU(2)_L$ triplet $\Sigma : (\mathbf{1}, \mathbf{3}, 0)$ as the extension of the SM. The operators connecting the BSM
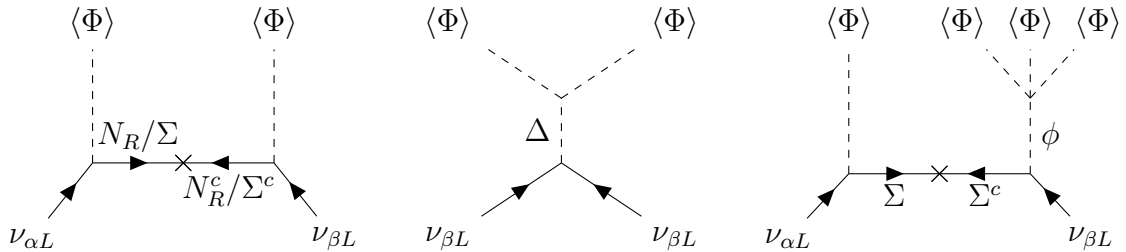
Figure 5.2: Tree-level processes for neutrino mass generation in the type-I, -II, and -III seesaw models. The first two diagrams are associated with the Weinberg operator $LL\Phi\Phi$, while the third one corresponds to an example for a $D = 7$ operator.

lepton triplet with the SM neutrino via the Higgs vev as well as breaking lepton number by two units are given by

$$-\mathcal{L} \supset \mu_\Sigma \text{Tr}\left(\overline{\Sigma_L^c}\Sigma_L\right) + y_\Sigma \overline{L^c}\Sigma_L \widetilde{\Phi} + \text{h.c.}. \tag{5.15}$$

The resulting neutrino mass is $m_\nu \sim y_\Sigma^2 v_\Phi^2/(2\mu_\Sigma)$ [324]. The process responsible for neutrino mass generation is shown in Fig. 5.2.

Radiative neutrino mass models

The processes for possible radiative neutrino mass models are shown in Fig. 5.3 in which small Majorana neutrino masses can emerge at the loop-level and the combination of loop as well as chirality suppression can give rise to a potentially smaller new physics scale. Generally speaking, this class of models does not require an extended fermion content but typically features BSM scalars.

Scotogenic model

Extending the SM by a set of RH neutrinos $N_R : (\mathbf{1}, \mathbf{1}, 0)$ and a second doublet $\Phi_2 : (\mathbf{1}, \mathbf{2}, 1)$ which all transform in the same, non-trivial way under a discrete $\mathbb{Z}_2$ symmetry, the neutrino masses can be generated at one-loop level. See Refs. [337, 338] for details and the operators

$$-\mathcal{L} \supset \frac{1}{2}\sum_{i,j} M_{ij}\overline{N_{R,i}^c}N_{R,j} + y_i\overline{L}\widetilde{\Phi}_2 N_{R,i} + \lambda|\Phi_1|^2|\Phi_2|^2 \tag{5.16}$$

give rise to the neutrino masses.
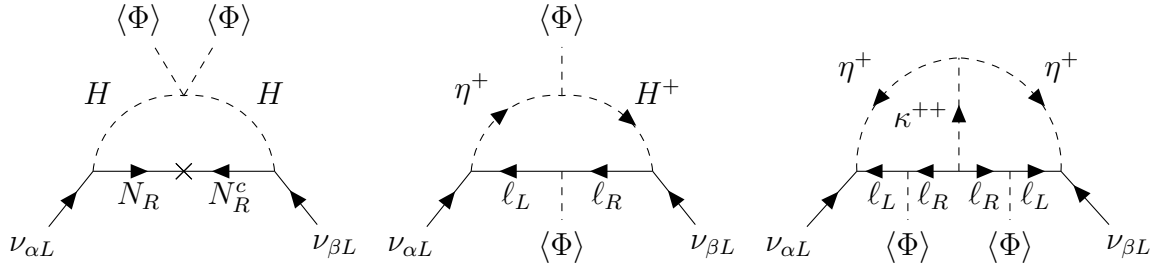
Figure 5.3: Diagrams for selected radiative neutrino mass models: scotogenic model (*left*) with the neutral scalar from the $\mathbb{Z}_2$-odd doublet Φ_2, Zee model (*center*) with the physical charged scalar H^+ from Φ_2, and Zee-Babu model (*right*).

Zee model

Another example is the Zee model in which the singly charged BSM scalar is responsible for neutrino masses and mixings. In this framework the scalar sector comprises two Higgs doublets $\Phi_{1,2} : (\mathbf{1}, \mathbf{2}, 1)$ and a charged scalar singlet $\eta^+ : (\mathbf{1}, \mathbf{1}, 2)$. See Refs. [339, 340] for the details and the relevant operators are

$$-\mathcal{L} \supset y_\eta \varepsilon_{ab} \overline{L_a^c} \eta^+ L_b + y_2 \overline{L} \Phi_2 \ell_R + \mu \Phi_2 \eta^+ \widetilde{\Phi}_1 + \text{h.c.} \qquad (5.17)$$

with the $SU(2)_L$ indices a, b in the first term.

Zee-Babu model

In comparison to the SM, the particle spectrum is extended only by two scalar $SU(2)_L$ singlet fields, $i.e.$ $\eta^+ : (\mathbf{1}, \mathbf{1}, 2)$ and $\kappa^{++} : (\mathbf{1}, \mathbf{1}, 4)$, which carry electric charge one and two, respectively. See Refs. [340, 341] for the proposals. The neutrino masses are generated via an interplay of the operators

$$-\mathcal{L} \supset f_{\alpha\beta} \overline{L_\alpha^{ac}} L_\beta^b \varepsilon_{ab} \eta^+ + g_{\alpha\beta} \overline{\ell_{\alpha,R}^c} \ell_{\beta,R} \kappa^{++} + \mu \eta^+ \eta^+ \kappa^{--} + \text{h.c.} \qquad (5.18)$$

and we shall discuss this neutrino mass model below in Section 5.4 as an example.

In the following two sections we shall investigate two specific neutrino mass models which simultaneously account for the DM relic abundance.

5.3 Dark Matter Mediators in Type-II Seesaw

In the first model of consideration, the scalar sector of the type-II seesaw model with the scalar $SU(2)_L$ triplet $\Delta : (\mathbf{1}, \mathbf{3}, 2)$ is furnished by a complex singlet $S : (\mathbf{1}, \mathbf{1}, 0)$ which transforms as $S \to -S$ under a discrete, stabilizing $\mathbb{Z}_2$ symmetry and thus poses a suitable DM candidate in this framework. The interesting operators of this model read

$$\mathcal{L} \supset \sum_\phi (D_\mu \phi)^\dagger (D_\mu \phi) - \mu_\Phi^2 \Phi^\dagger \Phi - \lambda_\Phi \left| \Phi^\dagger \Phi \right|^2 - \mu_S^2 S^\dagger S - \lambda_S \left(S^\dagger S \right)^2 - \mu_\Delta^2 \text{Tr} \left(\Delta^\dagger \Delta \right)$$

$$- \lambda_{S\Delta} S^\dagger S \text{Tr} \left(\Delta^\dagger \Delta \right) - \lambda_{S\Phi} S^\dagger S \Phi^\dagger \Phi - \lambda_{\Phi\Delta} \left[\Phi^\dagger \Phi \text{Tr} \left(\Delta^\dagger \Delta \right) - \kappa_{\Phi\Delta} \left| \Phi^\dagger \Delta \right|^2 \right]$$

$$- \mu_{\Phi\Delta} \left(i \Phi^T \sigma_2 \Delta^\dagger \Phi + \text{h.c.} \right) - \lambda_\Delta \left[\text{Tr}^2 \left(\Delta^\dagger \Delta \right) + \kappa_\Delta \text{Tr} \left(\Delta^\dagger \Delta \Delta^\dagger \Delta \right) \right] , \qquad (5.19)$$

where the sum is over the scalar multiplets $\phi = \Phi, \Delta, S$, and the SM Higgs doublet Φ and scalar triplet Δ can be written as

$$\Phi = \frac{1}{\sqrt{2}} \begin{pmatrix} \sqrt{2}G^+ \\ v_\Phi + h + iG^0 \end{pmatrix} \quad , \quad \Delta = \frac{1}{\sqrt{2}} \begin{pmatrix} \Delta^+ & \sqrt{2}\Delta^{++} \\ v_\Delta + \Delta_R^0 + i\Delta_I^0 & -\Delta^+ \end{pmatrix} \quad (5.20)$$

with the usual would-be Goldstones $G^\pm$ and G^0 (*cf.* Eq. (1.11)). Moreover, we assign the lepton number $L(\Delta) = -2$ to the triplet scalar. After EWSB, the neutral components of the scalar multiplets Φ and Δ obtain finite vevs v_Φ and v_Δ, respectively, which are related to each other via $v_\Phi^2 + 2v_\Delta^2 = v^2 \approx (246\,\text{GeV})^2$ [335]. The analytical expressions for the masses can be found in Appendix E.1. The vev v_Δ is determined by the minimization condition as

$$v_\Delta \approx \frac{\mu_{\Phi\Delta} v_\Phi^2}{\sqrt{2}\mu_\Delta^2} \qquad (5.21)$$

and precise measurements of the EW parameter $\rho = 1.00038(20)$ [10], defined at tree level as $\rho \equiv m_W^2 / (m_Z^2 \cos^2 \theta_W)$, severely constrain the model parameters. In the present scenario, the ρ parameter is modified by the triplet vev and reads $\rho = (v_\Phi^2 + 2v_\Delta^2)/(v_\Phi^2 + 4v_\Delta^2)$ which in turn leads to the constraint $v_\Delta \lesssim 2\,\text{GeV} \ll v_\Phi$. The hierarchy of the two scalar vevs constrains the mixing of the respective two weak eigenstates from the scalar $SU(2)_L$ multiplets and demonstrates that the weak eigenstates virtually equal their corresponding mass eigenstates [342]. Note that the triplet vev in Eq. (5.21) is proportional to the lepton number-violating parameter $\mu_{\Phi\Delta}$. Hence, a small vev v_Δ leads to a small ratio $\mu_{\Phi\Delta}/\mu_\Delta$ and zero vev results in lepton number-restoration as $\mu_{\Phi\Delta} \to 0$; the lepton number-violating parameter is hence 't Hooft natural [335, 343].

The link between the scalar triplet and the neutrinos is established by the Yukawa interactions

$$-\mathcal{L} \supset i\,(y_{L\Delta})_{\alpha\beta}\,\overline{L_\alpha^c}\sigma_2\Delta L_\beta + \text{h.c.} \qquad (5.22)$$

with the Hermitian 3×3 Yukawa matrix $y_{L\Delta}$ and the LH lepton doublets L_α, where α denotes the flavor index for e, μ, τ. While the triplet vev does not contribute to a mass of any electrically charged SM fermion as gauge and Lorentz invariance forbid further operators involving the scalar triplet and fermion fields, it is proportional to the generated Majorana neutrino mass, *i.e.*

$$(m_\nu)_{\alpha\beta} = \sqrt{2}v_\Delta\,(y_{L\Delta})_{\alpha\beta} \;. \qquad (5.23)$$

Combining Eqs. (5.3) and (5.23), the Yukawa matrix is completely determined by the neutrino oscillation parameters and can be cast as

$$(y_{L\Delta})_{\alpha\beta} = \frac{1}{\sqrt{2}v_\Delta} \left[V_{\text{PMNS}}^{\text{M}} \operatorname{diag}(m_1, m_2, m_3) \left(V_{\text{PMNS}}^{\text{M}}\right)^T \right]_{\alpha\beta}. \tag{5.24}$$

Consequently, determining these Yukawa couplings in experiments might give valuable insights into the nature of neutrinos as it would allow to constrain the Majorana and Dirac CP phases or to infer the possible range of the neutrino mass scale m_0. As found, *e.g.*, in Ref. [294] for a slightly different notation, the elements of the Yukawa matrix $y_{L\Delta}$ can be written in terms of the neutrino oscillation parameters and the triplet vev,

$$(y_{L\Delta})_{ee} = \frac{1}{\sqrt{2}v_\Delta} \left(m_1 c_{12}^2 c_{13}^2 + m_2 c_{13}^2 s_{12}^2 e^{i\varphi_1} + m_3 s_{13}^2 e^{i(\varphi_2 - 2\delta_{\text{CP}})} \right),$$

$$(y_{L\Delta})_{e\mu} = \frac{1}{\sqrt{2}v_\Delta} \Big[-m_1 c_{12} c_{13} \left(s_{12} c_{23} + c_{12} s_{13} s_{23} e^{i\delta_{\text{CP}}} \right)$$
$$+ m_2 c_{13} s_{12} e^{i\varphi_1} \left(c_{12} c_{23} - s_{12} s_{13} s_{23} e^{i\delta_{\text{CP}}} \right) + m_3 s_{13} s_{23} c_{13} e^{i(\varphi_2 - \delta_{\text{CP}})} \Big],$$

$$(y_{L\Delta})_{e\tau} = \frac{1}{\sqrt{2}v_\Delta} \Big[m_1 c_{12} c_{13} \left(s_{12} s_{23} - c_{12} c_{23} s_{13} e^{i\delta_{\text{CP}}} \right)$$
$$- m_2 c_{13} s_{12} e^{i\varphi_1} \left(c_{12} s_{23} + s_{12} s_{13} c_{23} e^{i\delta_{\text{CP}}} \right) + m_3 s_{13} c_{23} c_{13} e^{i(\varphi_2 - \delta_{\text{CP}})} \Big],$$

$$(y_{L\Delta})_{\mu\mu} = \frac{1}{\sqrt{2}v_\Delta} \Big[m_1 \left(s_{12} c_{23} + c_{12} s_{23} s_{13} e^{i\delta_{\text{CP}}} \right)^2$$
$$+ m_2 e^{i\varphi_1} \left(c_{12} c_{23} - s_{12} s_{13} s_{23} e^{i\delta_{\text{CP}}} \right)^2 + m_3 c_{13}^2 s_{23}^2 e^{i\varphi_2} \Big],$$

$$(y_{L\Delta})_{\mu\tau} = \frac{1}{\sqrt{2}v_\Delta} \Big[m_1 \left(c_{12} c_{23} s_{13} e^{i\delta_{\text{CP}}} - s_{12} s_{23} \right) \left(s_{12} c_{23} + c_{12} s_{23} s_{13} e^{i\delta_{\text{CP}}} \right)$$
$$+ m_2 e^{i\varphi_1} \left(c_{12} s_{23} + s_{12} c_{23} s_{13} e^{i\delta_{\text{CP}}} \right) \left(s_{12} s_{23} s_{13} e^{i\delta_{\text{CP}}} - c_{12} c_{23} \right)$$
$$+ m_3 c_{13}^2 c_{23} s_{23} e^{i\varphi_2} \Big],$$

$$(y_{L\Delta})_{\tau\tau} = \frac{1}{\sqrt{2}v_\Delta} \Big[m_1 \left(s_{12} s_{23} - c_{12} c_{23} s_{13} e^{i\delta_{\text{CP}}} \right)^2$$
$$+ m_2 e^{i\varphi_1} \left(c_{12} s_{23} + s_{12} s_{13} c_{23} e^{i\delta_{\text{CP}}} \right)^2 + m_3 c_{13}^2 c_{23}^2 e^{i\varphi_2} \Big]. \tag{5.25}$$

Unlike the SM, the type-II seesaw model predicts charged lepton flavor violation (cLFV) which stems from the off-diagonal terms of the BSM Yukawa matrix $y_{L\Delta}$. For this reason, dedicated search strategies are being conducted to probe the SM prediction. Leptonic decays like $\ell_\alpha^- \to \ell_\beta^+ \ell_\gamma^- \ell_\delta^-$ and $\ell_\alpha^- \to \ell_\beta^- \gamma$ (with the lepton flavor indices α, β, γ, and δ) with the leading contributions arising at tree and one-loop level, respectively, via the doubly charged scalar are suitable for those searches (see, e.g., Refs. [334, 335] for overviews). A brief summary of these cLFV observables alongside the resulting constraints for the neutrino mass matrix entries $(m_\nu)_{ij}$, BSM scalar mass, and triplet vev is presented in Tab. 5.2.

Typically, the fields of the scalar triplet Δ feature a mass splitting which can be categorized into two hierarchical configurations:

$$\text{Configuration 1} \ : \ m_{\Delta^0} \geq m_{\Delta^+} \geq m_{\Delta^{++}} \tag{5.26}$$

$$\text{Configuration 2} \ : \ m_{\Delta^{++}} > m_{\Delta^+} > m_{\Delta^0} \,. \tag{5.27}$$

According to the decay phase diagram in Ref. [331], the doubly charged scalar predominantly decays into a pair of same-sign charged leptons for $v_\Delta \lesssim 10^{-4}\,\text{GeV}$. The smaller the triplet vev, the larger the mass difference between the triplet scalars can be without changing the dominant decay mode. For larger triplet vevs the decay of the scalars

cLFV observable	Constraints
$\text{BR}\left(\mu^- \to e^+e^-e^-\right) < 1.0 \times 10^{-12}$	$\left\|(m_\nu)_{e\mu}\,(m_\nu)_{ee}\right\| / \left(m_{\Delta^{++}}^2 v_\Delta^2\right) < (145\,\text{TeV})^{-2}$
$\text{BR}\left(\tau^- \to e^+e^-e^-\right) < 2.7 \times 10^{-8}$	$\left\|(m_\nu)_{e\tau}\,(m_\nu)_{ee}\right\| / \left(m_{\Delta^{++}}^2 v_\Delta^2\right) < (7.4\,\text{TeV})^{-2}$
$\text{BR}\left(\tau^- \to e^+e^-\mu^-\right) < 1.8 \times 10^{-8}$	$\left\|(m_\nu)_{e\tau}\,(m_\nu)_{e\mu}\right\| / \left(m_{\Delta^{++}}^2 v_\Delta^2\right) < (9.8\,\text{TeV})^{-2}$
$\text{BR}\left(\tau^- \to e^+\mu^-\mu^-\right) < 1.7 \times 10^{-12}$	$\left\|(m_\nu)_{e\tau}\,(m_\nu)_{\mu\mu}\right\| / \left(m_{\Delta^{++}}^2 v_\Delta^2\right) < (8.3\,\text{TeV})^{-2}$
$\text{BR}\left(\tau^- \to \mu^+e^-e^-\right) < 1.5 \times 10^{-8}$	$\left\|(m_\nu)_{\mu\tau}\,(m_\nu)_{ee}\right\| / \left(m_{\Delta^{++}}^2 v_\Delta^2\right) < (8.6\,\text{TeV})^{-2}$
$\text{BR}\left(\tau^- \to \mu^+\mu^-e^-\right) < 2.7 \times 10^{-8}$	$\left\|(m_\nu)_{\mu\tau}\,(m_\nu)_{e\mu}\right\| / \left(m_{\Delta^{++}}^2 v_\Delta^2\right) < (8.8\,\text{TeV})^{-2}$
$\text{BR}\left(\tau^- \to \mu^+\mu^-\mu^-\right) < 2.1 \times 10^{-8}$	$\left\|(m_\nu)_{\mu\tau}\,(m_\nu)_{\mu\mu}\right\| / \left(m_{\Delta^{++}}^2 v_\Delta^2\right) < (7.9\,\text{TeV})^{-2}$
$\text{BR}\left(\mu \to e\gamma\right) < 4.2 \times 10^{-13}$	$(8+r)\left\|m_\nu^\dagger m_\nu\right\|_{e\mu} / \left(m_{\Delta^{++}}^2 v_\Delta^2\right) < (15.3\,\text{TeV})^{-2}$
$\text{BR}\left(\tau \to e\gamma\right) < 3.3 \times 10^{-8}$	$(8+r)\left\|m_\nu^\dagger m_\nu\right\|_{e\tau} / \left(m_{\Delta^{++}}^2 v_\Delta^2\right) < (0.6\,\text{TeV})^{-2}$
$\text{BR}\left(\tau \to \mu\gamma\right) < 4.4 \times 10^{-8}$	$(8+r)\left\|m_\nu^\dagger m_\nu\right\|_{\mu\tau} / \left(m_{\Delta^{++}}^2 v_\Delta^2\right) < (0.56\,\text{TeV})^{-2}$

Table 5.2: Constraints on Yukawa couplings from cLFV processes. The experimental limits at 90% C.L. are taken from Refs. [344–348] and the constraints from Ref. [334]. The mass ratio is defined as $r \equiv m_{\Delta^{++}}^2 / m_{\Delta^+}^2$. Table can be found in Ref. [4].

into (off-shell) gauge bosons dominates. In the subsequent analysis we shall consider the scenario in which Δ^{++} is not heavier than the other fields from the triplet with a negligible mass difference between the doubly charged scalar and the other scalars from the triplet and set $v_\Delta \ll 10^{-4}\,\text{GeV}$ to make sure that the scalars from the triplet decay exclusively into leptons. As presented in Ref. [335] for example, the decay rate of the doubly charged triplet scalar Δ^{++} reads

$$\Gamma\left(\Delta^{++} \to \ell_\alpha^+ \ell_\beta^+\right) = \frac{m_{\Delta^{++}}}{4\pi\left(1 + \delta_{\alpha\beta}\right)} |\left(y_{L\Delta}\right)_{\alpha\beta}|^2 \tag{5.28}$$

and the branching ratio (BR) for the decay into lepton flavors is given by

$$\text{BR}\left(\Delta^{++} \to \ell_\alpha^+ \ell_\beta^+\right) = \frac{|\left(y_{L\Delta}\right)_{\alpha\beta}|^2}{1 + \delta_{\alpha\beta}} \Big/ \sum_{a \leq b} \frac{|\left(y_{L\Delta}\right)_{ab}|^2}{1 + \delta_{ab}}, \tag{5.29}$$

in which the Kronecker delta δ_{ij} takes care of identical leptons.

Taking the best-fit values for the three neutrino mixing angles θ_{12}, θ_{23}, θ_{13} and the two mass differences Δm_{21}^2, $\Delta m_{3\ell}^2$, the branching ratio $\text{BR}(\Delta^{++} \to \ell_\alpha^+ \ell_\beta^+)$ are presented in Fig. 5.4 in terms of the neutrino mass scale m_0, the Dirac CP phase δ_{CP}, and the Majorana phases $\varphi_{1,2}$. For the sake of simplicity, the two Majorana phases are assumed to equal each other. The slight asymmetry of the branching ratio with respect to the Majorana phases is caused by $\delta_{\text{CP}} \bmod \pi \neq 0$ with the best-fit value for the Dirac CP phase from Tab. 5.1. Remarkably, the dependence of the branching ratios for different lepton channels on the neutrino mass parameters is significantly influenced by the absolute neutrino mass as well as by the Majorana phases, whereas not so much by the Dirac CP phase. However, also for the Dirac CP phase the branching ratios vary for the different lepton channels. As a result, considering the leptonic decays and their branching ratios might help decipher the nature of the neutrino mass hierarchy in experiments which are sufficiently sensitive to the different branching ratios.

As a closing remark on this specific neutrino mass model, the qualitative findings for the type-II seesaw model can be transferred to other tree-level seesaw models briefly described in the previous section. Alongside the type-II seesaw model which generates the Majorana neutrino masses via the Weinberg operator $LL\Phi\Phi$, we shall discuss the tree-level $D = 7$ neutrino mass model, known as the BNT model (consult, *e.g.*, [319, 349–351] for more details), in which the Majorana neutrino masses arise from the vev of the $SU(2)_L$ quadruplet ϕ (*cf.* Fig. 5.2). Besides the neutral scalar, this quadruplet comprises scalars with electric charge three, two, and one.

5.4 Dark Matter Mediators in the Zee-Babu Model

Next we shall examine the Zee-Babu model as an example for radiative neutrino mass models. It features the electrically charged BSM scalars $\eta^+ : (\mathbf{1}, \mathbf{1}, 2)$ and $\kappa^{++} : (\mathbf{1}, \mathbf{1}, 4)$ which serve as DM mediators in this framework. As in the type-II seesaw framework,
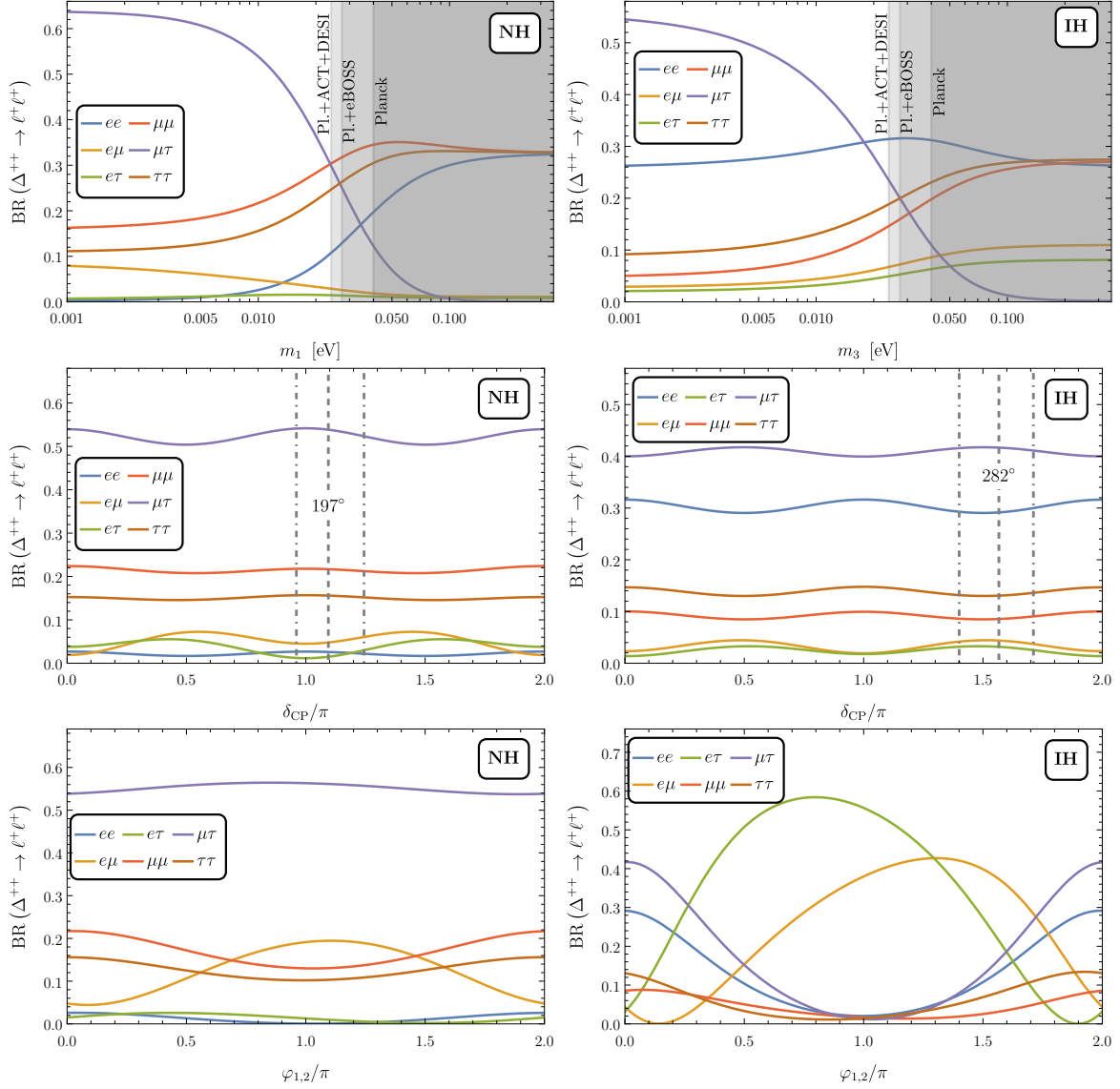
Figure 5.4: Dependence of the branching ratios on free neutrino oscillation parameters in type-II seesaw framework. The BSM vev is set to $v_\Delta = 10^{-5}\,\mathrm{GeV}$, and we choose $\delta_{\mathrm{CP}} = 197°\,(282°)$ for NH (IH) as the central values of the CP phase (*cf.* Tab. 5.1). The neutrino mass scale is set to $m_0 = 0.01\,\mathrm{eV}$ and the Majorana phases to $\varphi_{1,2} = 0$ if not stated otherwise. Taken from Ref. [4].

a complex scalar singlet $S = (s + ia)/\sqrt{2}$ with the same transformation properties with respect to a discrete $\mathbb{Z}_2$ symmetry is included and plays the role of the DM candidate. The Lagrangian of the scalar sector with the sum over the scalars $\phi = \Phi, S, \eta^+, \kappa^{++}$ is given by

$$
\begin{aligned}
\mathcal{L} \supset \sum_\phi & \left(D_\mu \phi\right)^\dagger \left(D^\mu \phi\right) - \mu_\phi^2 \phi^\dagger \phi - \lambda_\phi \left(\phi^\dagger \phi\right)^2 - \left(\mu_{\eta\kappa} \eta^+ \eta^+ \kappa^{--} + \text{h.c.}\right) \\
& - \lambda_{S\Phi} S^\dagger S |\Phi|^2 - \lambda_{\Phi\eta} \eta^- \eta^+ |\Phi|^2 - \lambda_{\Phi\kappa} \kappa^{--} \kappa^{++} |\Phi|^2 - \lambda_{\eta\kappa} \eta^- \eta^+ \kappa^{--} \kappa^{++} \\
& - \lambda_{S\eta} \eta^- \eta^+ S^\dagger S - \lambda_{S\kappa} \kappa^{--} \kappa^{++} S^\dagger S
\end{aligned}
\tag{5.30}
$$

with the definition of the SM Higgs doublet Φ in Eq. (1.11). The portal terms in the last line connect the DM scalar S with the charged BSM scalars. The analytical expressions for the masses can be found in Appendix E.2. The Yukawa interactions between the SM leptons and the electrically charged BSM scalar fields η^+ and κ^{++} are described by

$$
\mathcal{L} \supset f_{\alpha\beta} \overline{L_\alpha^{ac}} L_\beta^b \varepsilon_{ab} \eta^+ + g_{\alpha\beta} \overline{\ell_{\alpha,R}^c} \ell_{\beta,R} \kappa^{++} + \text{h.c.} ,
\tag{5.31}
$$

where $L_\alpha^{(c)}$ and $\ell_\alpha^{(c)}$ denote the (charge conjugated) LH lepton doublet and RH lepton singlet, respectively, with the flavor index α [352]. The indices of the Levi-Civita tensor ε_{ab} correspond to $SU(2)_L$ indices. Unlike the symmetric matrix g, the Yukawa matrix f is antisymmetric in flavor space due to the antisymmetric Levi-Civita tensor ε_{ab} and the relation $\overline{L_\alpha^{ac}} L_\beta^b = \overline{L_\beta^{bc}} L_\alpha^a$ (*cf.* Ref. [353] for instance).

Analogously to the type-II seesaw model, the DM mediators are assigned the lepton number $L(\eta^+) = L(\kappa^{++}) = -2$ to. Consequently, the term $\mu_{\eta\kappa} \eta^+ \eta^+ \kappa^{--}$ in Eq. (5.30) softly breaks the non-anomalous global symmetry $U(1)_{B-L}$ symmetry by two units and thus gives rise to Majorana neutrino masses at two-loop level (*cf.* Fig. 5.3). The neutrino mass matrix in terms of the SM Yukawa matrix y and the BSM Yukawa matrices f, g can be found, *e.g.*, in Refs. [354, 355] and reads

$$
m_\nu = \frac{8 \mu_{\eta\kappa} v^2}{(16\pi^2)^2 m_\eta^2} \, f \, y \, g^\dagger \, y^T \, f^T \, \mathcal{I}\left(\frac{m_\kappa^2}{m_\eta^2}\right) ,
\tag{5.32}
$$

where the loop integral function can be written as [352]

$$
\mathcal{I}(r) = -\int_0^1 \mathrm{d}z \int_0^{1-z} \mathrm{d}y \, \frac{1}{z + (r-1)y + y^2} \log \frac{y(1-y)}{z + ry} .
\tag{5.33}
$$

Following the results of Refs. [354, 356, 357] and using the short-hand notation $r \equiv m_\kappa^2/m_\eta^2$, this integral can be approximated in certain limits,

$$
\mathcal{I}(r) \approx
\begin{cases}
\frac{1}{r}\left(\log^2 r + \frac{\pi^2}{3} - 1\right) & \text{for } r \gg 1 \\
\frac{\pi^2}{3} & \text{for } r \to 0
\end{cases}.
\tag{5.34}
$$

The agreement between the numerical evaluaton of the integral in Eq. (5.33) and the known limits from the literature is demonstrated in Fig. 5.5. The plot can also help estimate whether the approximations are applicable for a given mass configuration.

The neutrino mass matrix in Eq. (5.32) is peculiar as it features the antisymmetric BSM Yukawa matrix f, which consequently leads to $\det m_\nu = 0$ of the neutrino mass matrix. As a result, the Zee-Babu model predicts the lightest neutrino to be massless while the other two are evidently massive [354].

The relation between the neutrino mass matrix m_ν in this model and the PMNS matrix in Eq. (5.1) leads to a connection between the neutrino oscillation parameters and the BSM Yukawa couplings. The neutrino mass matrix for the mass hierarchies $\mathcal{H} \in \{\mathrm{NH}, \mathrm{IH}\}$ reads

$$
m_\nu^\mathcal{H} = V_{\mathrm{PMNS}}^{\mathrm{D}} \, \mathcal{D}_\nu^\mathcal{H} \left(V_{\mathrm{PMNS}}^{\mathrm{D}}\right)^T ,
\tag{5.35}
$$

with the diagonal matrices $\mathcal{D}_\nu^{\mathrm{NH}} = \mathrm{diag}\,(0, m_2 e^{i\varphi}, m_3)$ and $\mathcal{D}_\nu^{\mathrm{IH}} = \mathrm{diag}\,(m_1, m_2 e^{i\varphi}, 0)$ for normal and inverted mass hierarchy, respectively. As shown in Ref. [354], ratios of the
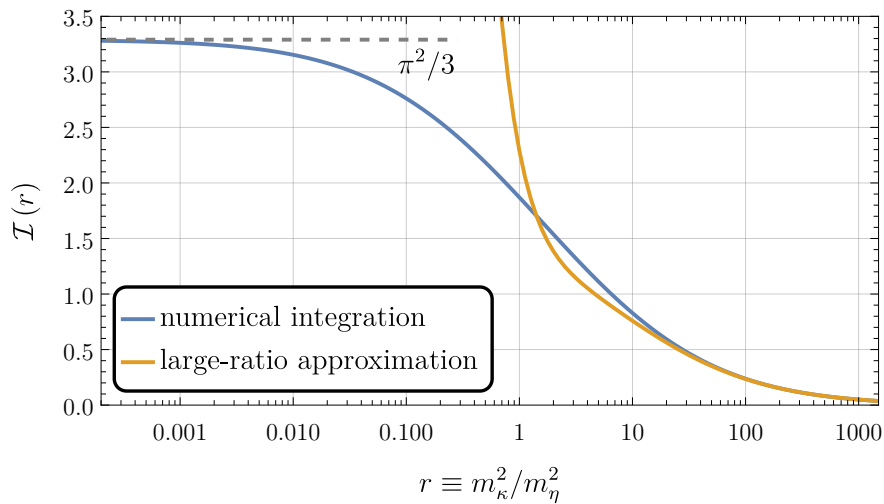
Figure 5.5: Comparison of the approximations for small and large mass ratios r to the numerical integration.

entries of the antisymmetric matrix f can be written in terms of the neutrino oscillation parameters. The eigenvector $\boldsymbol{f}_{\lambda=0} = (f_{\mu\tau}, -f_{e\tau}, f_{e\mu})$ of the matrix f, corresponding to the eigenvalue $\lambda = 0$, is also an eigenvector of the neutrino mass matrix. Exploiting that, one finds for the normal neutrino mass hierarchy the relation

$$\frac{f_{e\tau}}{f_{\mu\tau}} = t_{12}\frac{c_{23}}{c_{13}} + t_{13}s_{23}e^{-i\delta_{\text{CP}}} \quad , \quad \frac{f_{e\mu}}{f_{\mu\tau}} = t_{12}\frac{s_{23}}{c_{13}} - t_{13}c_{23}e^{-i\delta_{\text{CP}}} \tag{5.36}$$

and

$$\frac{f_{e\tau}}{f_{\mu\tau}} = -\frac{s_{23}}{t_{13}}e^{-i\delta_{\text{CP}}} \quad , \quad \frac{f_{e\mu}}{f_{\mu\tau}} = \frac{c_{23}}{t_{13}}e^{-i\delta_{\text{CP}}} \tag{5.37}$$

for the inverted hierarchy. In analogy to the other trigonometric functions, we define $t_{ij} \equiv \tan\theta_{ij}$ in the expressions above. In the following analysis, we shall use the entry $f_{e\mu}$ as the free model parameter which governs – together with the neutrino oscillation parameters – the other two entries of the antisymmetric Yukawa matrix f. Notice that the ratios of the Yukawa parameters in the IH are inversely proportional to the very small parameter $\sin^2\theta_{13} \ll \sin^2\theta_{23} \approx \cos^2\theta_{23}$ (cf. Tab. 5.1). The resulting large ratio of Yukawa coupling parameters leads to either a very small $f_{\mu\tau}$ or to very large $f_{e\tau}, f_{e\mu}$. In foresight to the experimental constraints that will be discussed below, either scenario results in conflicts with the cLFV constraints which consequently render the inverted neutrino mass hierarchy in this particular neutrino mass model unlikely. Therefore, we shall focus on the normal mass hierarchy in the analysis below.

While the antisymmetric Yukawa matrix f is determined by the neutrino oscillation parameters with one additional free parameter (here $f_{e\mu}$), the symmetric Yukawa matrix g needs three input parameters that shall be $g_{ee}, g_{e\mu}, g_{e\tau}$. To find the expressions for the other three entries of the matrix, let us first define $\xi \equiv \mu_{\eta\kappa}v^2 / \left(32\pi^4 m_\eta^2\right) \mathcal{I}\left(m_\kappa^2/m_\eta^2\right)$ and consider the neutrino mass matrix with in Eq. (5.32). Following Ref. [354], one possible set of equations is

$$(m_\nu)_{22} = \frac{2\xi}{v^2}\left(f_{e\mu}^2 g_{ee}^* m_e^2 - 2f_{e\mu}f_{\mu\tau}g_{e\tau}^* m_e m_\tau + f_{\mu\tau}^2 g_{\tau\tau}^* m_\tau^2\right) \tag{5.38}$$

$$(m_\nu)_{23} = \frac{2\xi}{v^2}\left(f_{e\mu}f_{e\tau}g_{ee}^* m_e^2 + f_{e\mu}f_{\mu\tau}g_{e\mu}^* m_e m_\mu - f_{e\tau}f_{\mu\tau}g_{e\tau}^* m_e m_\tau - f_{\mu\tau}^2 g_{\mu\tau}^* m_\mu m_\tau\right) \tag{5.39}$$

$$(m_\nu)_{33} = \frac{2\xi}{v^2}\left(f_{e\tau}^2 g_{ee}^* m_e^2 + 2f_{e\tau}f_{\mu\tau}g_{e\mu}^* m_e m_\mu + f_{\mu\tau}^2 g_{\mu\mu}^* m_\mu^2\right) . \tag{5.40}$$

These entries of the neutrino mass matrix are predicted by the Zee-Babu model and can be compared to those of the neutrino mass matrix in Eq. (5.3). The two possible

neutrino mass hierarchies give rise to two different sets of expressions: the set for the normal neutrino mass hierarchy is given by

$$\left(m_\nu^{\text{NH}}\right)_{22} = m_3 c_{13}^2 s_{23}^2 + m_2 e^{i\varphi} \left(c_{12}c_{23} - s_{12}s_{13}s_{23}e^{i\delta_{\text{CP}}}\right)^2 \tag{5.41}$$

$$\left(m_\nu^{\text{NH}}\right)_{23} = m_3 c_{13}^2 s_{23}c_{23} - m_2 e^{i\varphi} \left(c_{12}s_{23} + s_{12}s_{13}c_{23}e^{i\delta_{\text{CP}}}\right)\left(c_{12}c_{23} - s_{12}s_{13}s_{23}e^{i\delta_{\text{CP}}}\right) \tag{5.42}$$

$$\left(m_\nu^{\text{NH}}\right)_{33} = m_3 c_{13}^2 c_{23}^2 + m_2 e^{i\varphi} \left(c_{12}s_{23} + s_{12}s_{13}c_{23}e^{i\delta_{\text{CP}}}\right)^2 , \tag{5.43}$$

while it reads

$$\left(m_\nu^{\text{IH}}\right)_{22} = m_1 \left(s_{12}c_{23} + c_{12}s_{13}s_{23}e^{i\delta_{\text{CP}}}\right)^2 + m_2 e^{i\varphi} \left(c_{12}c_{23} - s_{12}s_{13}s_{23}e^{i\delta_{\text{CP}}}\right)^2 \tag{5.44}$$

$$\left(m_\nu^{\text{IH}}\right)_{23} = m_1 \left(-s_{12}s_{23} + c_{12}s_{13}c_{23}e^{i\delta_{\text{CP}}}\right)\left(s_{12}c_{23} + c_{12}s_{13}s_{23}e^{i\delta_{\text{CP}}}\right)$$
$$+ m_2 e^{i\varphi} \left(-c_{12}c_{23} + s_{12}s_{13}s_{23}e^{i\delta_{\text{CP}}}\right)\left(c_{12}s_{23} + s_{12}s_{13}c_{23}e^{i\delta_{\text{CP}}}\right) \tag{5.45}$$

$$\left(m_\nu^{\text{IH}}\right)_{33} = m_1 \left(s_{12}s_{23} - c_{12}s_{13}c_{23}e^{i\delta_{\text{CP}}}\right)^2 + m_2 e^{i\varphi} \left(c_{12}s_{23} + s_{12}s_{13}c_{23}e^{i\delta_{\text{CP}}}\right)^2 \tag{5.46}$$

for the inverted mass hierarchy. Solving this set of equations gives

$$g_{\mu\mu}^{*\mathcal{H}} = \frac{v^2}{2f_{\mu\tau}^2 m_\mu^2 \xi}\left(m_\nu^{\mathcal{H}}\right)_{33} - \frac{f_{e\tau}m_e}{f_{\mu\tau}^2 m_\mu}\left(f_{e\tau}g_{ee}^*\frac{m_e}{m_\mu} + 2f_{\mu\tau}g_{e\mu}^*\right) \tag{5.47}$$

$$g_{\mu\tau}^{*\mathcal{H}} = \frac{f_{e\mu}m_e\left(f_{e\tau}g_{ee}^* m_e + f_{\mu\tau}g_{e\mu}^* m_\mu\right)}{f_{\mu\tau}^2 m_\mu m_\tau} - \frac{f_{e\tau}g_{e\tau}^* m_e}{f_{\mu\tau}m_\mu} - \frac{v^2}{2f_{\mu\tau}^2 m_\mu m_\tau \xi}\left(m_\nu^{\mathcal{H}}\right)_{23} \tag{5.48}$$

$$g_{\tau\tau}^{*\mathcal{H}} = \frac{v^2}{2f_{\mu\tau}^2 m_\tau^2 \xi}\left(m_\nu^{\mathcal{H}}\right)_{22} - \frac{f_{e\mu}m_e}{f_{\mu\tau}^2 m_\tau}\left(f_{e\mu}g_{ee}^*\frac{m_e}{m_\tau} - 2f_{\mu\tau}g_{e\tau}^*\right) \tag{5.49}$$

for both hierarchies $\mathcal{H} \in \{\text{NH, IH}\}$. These findings are in agreement with Ref. [354] if one assumes negligibly small Yukawa couplings g_{ee}, $g_{e\mu}$, and $g_{e\tau}$.

Before investigating the ramifications of these Yukawa matrices, we shall first summarize the theoretical and experimental constraints for the entries of the Yukawa matrices f, g, as well as on the cubic coupling $\mu_{\eta\kappa}$. They are presented in Tabs. 5.3 and 5.4.

Theoretical constraints

For staying within the perturbative regime, we restrict $|f_{ij}|, |g_{ij}| < 3$. Adopting the results from Ref. [356], the requirement that the tree-level quartic couplings must be larger than the effective couplings (while respecting perturbativity) allows to set the

upper bound

$$
\mu_{\eta\kappa} \leq
\begin{cases}
\left(3 \times 2\pi^2\right)^{1/4} m_\eta & \text{for } m_\kappa \ll m_\eta \\
\left(3 \times 6\pi^2\right)^{1/4} m_\eta & \text{for } m_\kappa \approx m_\eta \\
\left(3 \times 24\pi^2\right)^{1/4} m_\eta & \text{for } m_\kappa \gg m_\eta
\end{cases}
\tag{5.50}
$$

on the cubic coupling. A more conservative bound emerges from avoiding a charge-breaking vacuum [358], which is

$$
\mu_{\eta\kappa} \lesssim \sqrt{20\pi} \max\left(m_\eta, m_\kappa\right) .
\tag{5.51}
$$

Experimental constraints

Severe constraints on the BSM scalar masses and Yukawa coupling are set by searches for cLFV processes. They include searches for flavor-changing decays of one charged lepton to one or three charged leptons, for muonium-antimuonium conversion, for the violation of lepton universality, as well as measurements of the anomalous magnetic dipole moment of the electron and muon. In spite of the current tension between the SM prediction and the experimental value for the anomalous magnetic dipole moment of the muon (see, *e.g.*, Refs. [359–361]), we shall adopt the value from Ref. [362] for this analysis.

The doubly charged scalar κ^{++} induces cLFV interactions at tree level. The absence of signals for those cLFV decays strongly constrains the combination of the doubly charged scalar mass and the associated Yukawa couplings g_{ij}. The rate of a cLFV decay into three charged leptons, normalized to the SM decay into a lighter charged lepton and a pair of neutrinos, is given by [354, 363]

$$
\frac{\Gamma\left(\ell_i^- \to \ell_j^+ \ell_k^- \ell_l^-\right)}{\Gamma\left(\ell_i^- \to \ell_j^- \overline{\nu}\nu\right)} = \frac{\left|g_{ij} g_{kl}^*\right|^2}{2\left(1 + \delta_{kl}\right) G_F^2 m_\kappa^4}
\tag{5.52}
$$

with Fermi's constant G_F.

Searches for transitions from muonium (bound state of μ^+ and e^-) to antimuonium, which are mediated by the doubly charged scalar at tree level, lead to additional constraints. Taking the expression from Ref. [354], the effective coupling for the transition reads

$$
G_{\mathrm{M\overline{M}}} = -\frac{g_{ee} g_{\mu\mu}^*}{\sqrt{32} m_\kappa^2} .
\tag{5.53}
$$

The bound $|G_{\mathrm{M\overline{M}}}| < 3 \times 10^{-3} G_F$ can be translated to the constraint [354, 362]

$$\frac{|g_{ee}g_{\mu\mu}^*|}{(m_\kappa/\mathrm{GeV})^2} < 1.97 \times 10^{-7} \,. \tag{5.54}$$

The tree-level constraints we consider in the following analysis are presented in Tab. 5.3.

Next, we shall discuss constraints from one-loop contributions of the BSM scalars. The normalized cLFV decay rate at one-loop level can be expressed as

$$\frac{\Gamma\left(\ell_i^- \to \ell_j^- \gamma\right)}{\Gamma\left(\ell_i^- \to \ell_j^- \overline{\nu}\nu\right)} = \frac{\alpha}{48\pi G_F^2}\left[\left(\frac{\left(f^\dagger f\right)_{ij}}{m_\eta^2}\right)^2 + 16\left(\frac{\left(g^\dagger g\right)_{ij}}{m_\kappa^2}\right)^2\right] \tag{5.55}$$

with the electromagnetic fine-structure constant α.

Another constraint for a loop-level process is set by measurements of the magnetic dipole moment of the electron and muon. The Zee-Babu model predicts contributions to the anomalous magnetic dipole moment, given by

$$\delta a_i = -\frac{m_i^2}{24\pi^2}\left[\frac{\left(f^\dagger f\right)_{ii}}{m_\eta^2} + 4\frac{\left(g^\dagger g\right)_{ii}}{m_\kappa^2}\right] \tag{5.56}$$

with the anomalous magnetic dipole moment $a_i \equiv (g_i - 2)/2$ [354]. These constraints on the Yukawa couplings are summarized in Tab. 5.4.

Lastly, we shall summarize the constraints on lepton flavor universality. The singly charged scalar mediates the decay of a charged lepton. Measurements of the de-

Experiment (90% C.L.)	Bound (90% C.L.)
$\mathrm{BR}\left(\mu^- \to e^+e^-e^-\right) < 1.0 \times 10^{-12}$	$\left\|g_{e\mu}g_{ee}^*\right\|/m_\kappa^2 < 2.33 \times 10^{-11}\,\mathrm{GeV}^{-2}$
$\mathrm{BR}\left(\tau^- \to e^+e^-e^-\right) < 2.7 \times 10^{-8}$	$\left\|g_{e\tau}g_{ee}^*\right\|/m_\kappa^2 < 9.07 \times 10^{-9}\,\mathrm{GeV}^{-2}$
$\mathrm{BR}\left(\tau^- \to e^+e^-\mu^-\right) < 1.8 \times 10^{-8}$	$\left\|g_{e\tau}g_{e\mu}^*\right\|/m_\kappa^2 < 5.23 \times 10^{-9}\,\mathrm{GeV}^{-2}$
$\mathrm{BR}\left(\tau^- \to e^+\mu^-\mu^-\right) < 1.7 \times 10^{-8}$	$\left\|g_{e\tau}g_{\mu\mu}^*\right\|/m_\kappa^2 < 7.20 \times 10^{-9}\,\mathrm{GeV}^{-2}$
$\mathrm{BR}\left(\tau^- \to \mu^+e^-e^-\right) < 1.5 \times 10^{-8}$	$\left\|g_{\mu\tau}g_{ee}^*\right\|/m_\kappa^2 < 6.85 \times 10^{-9}\,\mathrm{GeV}^{-2}$
$\mathrm{BR}\left(\tau^- \to \mu^+\mu^-e^-\right) < 2.7 \times 10^{-8}$	$\left\|g_{\mu\tau}g_{e\mu}^*\right\|/m_\kappa^2 < 6.50 \times 10^{-9}\,\mathrm{GeV}^{-2}$
$\mathrm{BR}\left(\tau^- \to \mu^+\mu^-\mu^-\right) < 2.1 \times 10^{-8}$	$\left\|g_{\mu\tau}g_{\mu\mu}^*\right\|/m_\kappa^2 < 8.11 \times 10^{-9}\,\mathrm{GeV}^{-2}$

Table 5.3: Constraints on the Yukawa couplings from cLFV processes at tree-level. See Refs. [344, 345] for the experimental limits and Ref. [362] for the bounds. Table can be found in Ref. [4].

cays $\ell_i \to \ell_j \bar{\nu} \nu$ allow to constrain the ratio of the entries of the BSM Yukawa matrix f and the mass of the singly charged scalar. The constraints with 3σ uncertainty range read [51, 362]

$$\frac{g_\tau}{g_\mu} = \left| \frac{1 + |f_{e\tau}|^2 v^2/m_\eta^2}{1 + |f_{e\mu}|^2 v^2/m_\eta^2} \right| = 1.0009 \pm 0.0014 \tag{5.57}$$

$$\frac{g_\tau}{g_e} = \left| \frac{1 + |f_{\mu\tau}|^2 v^2/m_\eta^2}{1 + |f_{e\mu}|^2 v^2/m_\eta^2} \right| = 1.0027 \pm 0.0014 \tag{5.58}$$

$$\frac{g_\mu}{g_e} = \left| \frac{1 + |f_{\mu\tau}|^2 v^2/m_\eta^2}{1 + |f_{e\tau}|^2 v^2/m_\eta^2} \right| = 1.0019 \pm 0.0014 \,. \tag{5.59}$$

With this we close the overview of the theoretical and experimental constrains and focus on the calculation of the branching ratios for the BSM scalar decays into different lepton flavors. The branching ratios for the singly and doubly charged scalars are given by

$$\text{BR}\left(\eta^+ \to \ell_i^+ \nu_j \right) = |f_{ij}|^2 / \sum_{a \leq b} |f_{ab}|^2 \tag{5.60}$$

$$\text{BR}\left(\kappa^{++} \to \ell_i^+ \ell_j^+ \right) = \frac{|g_{ij}|^2}{1 + \delta_{ij}} / \sum_{a \leq b} \frac{|g_{ab}|^2}{1 + \delta_{ab}} \,. \tag{5.61}$$

Their dependence on the Dirac CP phase δ_{CP} and the Majorana phase φ is presented in Fig. 5.6. The reader may bear in mind that the Zee-Babu predicts a massless

Experiment (90% C.L.)	Bound (90% C.L.)	
$\text{BR}\left(\mu \to e\gamma \right) < 4.2 \times 10^{-13}$	$\frac{|f_{e\tau}^* f_{\mu\tau}|^2}{(m_\eta/\text{GeV})^4} + 16 \frac{|g_{ee}^* g_{e\mu} + g_{e\mu}^* g_{\mu\mu} + g_{e\tau}^* g_{\mu\tau}|^2}{(m_\kappa/\text{GeV})^4}$	$< 1.10 \times 10^{-18}$
$\text{BR}\left(\tau \to e\gamma \right) < 3.3 \times 10^{-8}$	$\frac{|f_{e\mu}^* f_{\mu\tau}|^2}{(m_\eta/\text{GeV})^4} + 16 \frac{|g_{ee}^* g_{e\tau} + g_{e\mu}^* g_{\mu\tau} + g_{e\tau}^* g_{\tau\tau}|^2}{(m_\kappa/\text{GeV})^4}$	$< 4.85 \times 10^{-13}$
$\text{BR}\left(\tau \to \mu\gamma \right) < 4.4 \times 10^{-8}$	$\frac{|f_{e\mu}^* f_{e\tau}|^2}{(m_\eta/\text{GeV})^4} + 16 \frac{|g_{e\mu}^* g_{e\tau} + g_{\mu\mu}^* g_{\mu\tau} + g_{\mu\tau}^* g_{\tau\tau}|^2}{(m_\kappa/\text{GeV})^4}$	$< 6.65 \times 10^{-13}$
$\delta a_e = 2.8 \times 10^{-13}$	$\frac{|f_{e\mu}|^2 + |f_{e\tau}|^2}{(m_\eta/\text{GeV})^2} + 4 \frac{|g_{ee}|^2 + |g_{e\mu}|^2 + |g_{e\tau}|^2}{(m_\kappa/\text{GeV})^2}$	$< 2.53 \times 10^{-4}$
$\delta a_\mu = 2.61 \times 10^{-9}$	$\frac{|f_{e\mu}|^2 + |f_{\mu\tau}|^2}{(m_\eta/\text{GeV})^2} + 4 \frac{|g_{e\mu}|^2 + |g_{\mu\mu}|^2 + |g_{\mu\tau}|^2}{(m_\kappa/\text{GeV})^2}$	$< 5.53 \times 10^{-5}$

Table 5.4: Constraints on the Yukawa couplings from cLFV processes at loop level and measurements of the anomalous magnetic moments. The experimental limits are quoted from Refs. [346, 347] and the expressions for the bounds are taken from Ref. [354, 362]. Table can be found in Ref. [4].

lightest neutrino, *i.e.* $m_0 = 0$, and consequently the neutrino mass spectrum is fully determined by the measurements of the mass differences listed in Tab. 5.1. Notice that the symmetries of the BSM Yukawa matrices manifest themselves in the decay channels: While the singly charged BSM scalar decays (governed by the antisymmetric matrix f) inevitably violate charged lepton flavor, the doubly charged scalar can decay into same-flavor leptons (here predominantly into two muons for the selected benchmark point) as the corresponding BSM Yukawa matrix g is symmetric and can therefore feature non-zero diagonal entries.

With the values for the three mixing angles θ_{12}, θ_{23}, θ_{13} and the two mass differences Δm^2_{21}, $\Delta m^2_{3\ell}$ the plots show that the Dirac CP phase as well as the Majorana phase clearly modify the branching ratios of the BSM scalar decays. The benchmark points for the following analysis are listed in Tab. 5.5.

Similar to the type-II seesaw model, our qualitative findings for the Zee-Babu model can be applied to other radiative neutrino mass models like those discussed above. The BSM Yukawa matrices and hence the branching ratios of the decays of the charged
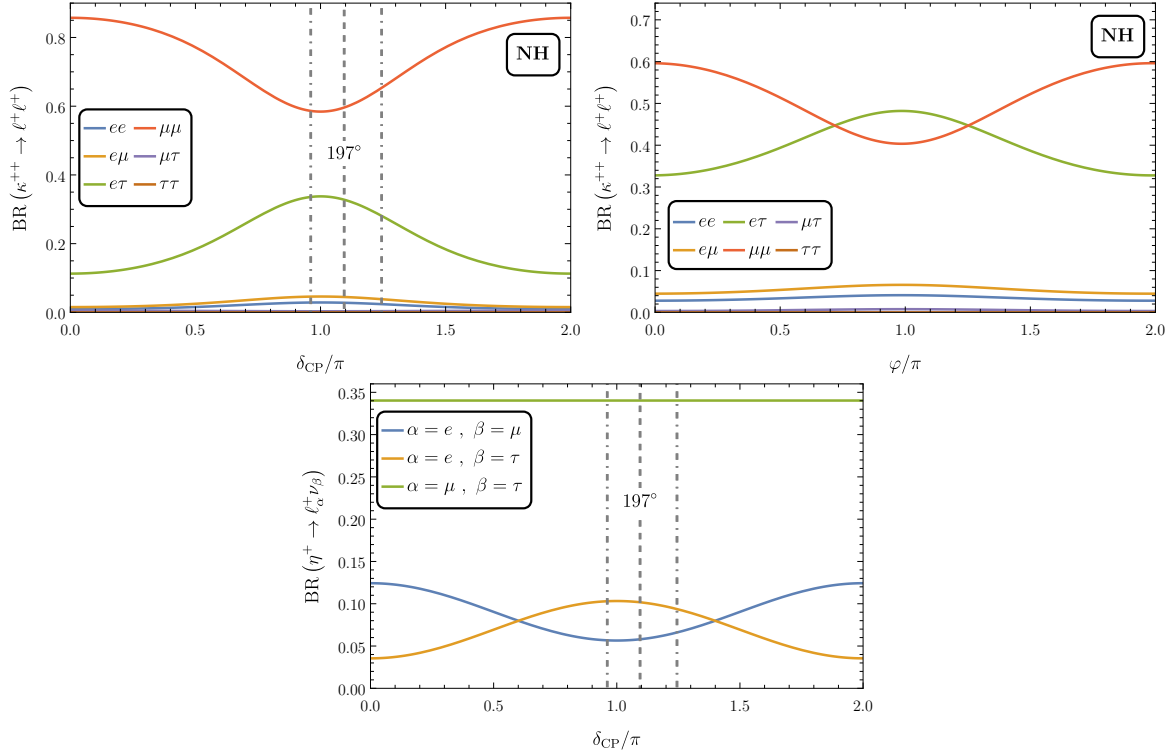
Figure 5.6: Branching ratios to different lepton flavors for the benchmark point BM1 in Zee-Babu model. The top panel is for doubly charged scalars, and the bottom panel is for singly charged scalars. Taken from Ref. [4].

BSM scalars into leptons are governed by the neutrino parameters. If these scalars serve as a scalar-neutrino portal for scalar DM, one can expect lepton flavor-specific observables in collider experiments and in cosmic ray positron spectra from the BSM Yukawa matrices.

5.5   Dark Matter Phenomenology

After having introduced the two neutrino mass models alongside their respective characteristics and constraints both from the theoretical and from the experimental perspective, we shall investigate these model in light of the DM phenomenology next. As outlined in the Lagrangian for the type-II seesaw framework in Eq. (5.19) and for the Zee-Babu framework in Eq. (5.30), the DM particle in these models is assumed to be a complex scalar singlet and stabilized by a discrete $\mathbb{Z}_2$ symmetry. In the following discussion, we shall focus on the WIMP mass regime.

Both models feature the Higgs portal $S^\dagger S \Phi^\dagger \Phi$ which connects the dark sector with the SM sector. It prescribes both DM annihilation into one or two Higgs bosons (the former is possible only after EWSB) and Higgs-mediated scattering processes off nuclei for instance. DMDD experiments like XENONnT and LZ provide strong constraints on DM-nucleon scattering cross sections in the WIMP mass regime such that the

Benchmark Points	BM1 (min-μ)	BM2 (pure-μ)	BM3 (pure-μ)
m_κ [TeV]	9	9	1
m_η [TeV]	29	55	13
$\mu_{\eta\kappa}$ [TeV]	65	99	35
$f_{e\mu}$	0.13	0.068	-0.079
g_{ee}	0.038	-0.0014	0.0010
$g_{e\mu}$	0.034	-0.0012	0.00051
$g_{e\tau}$	-0.092	0.00049	-0.00066
BR_{ee}	0.042	$< 10^{-3}$	$< 10^{-3}$
$\mathrm{BR}_{e\mu}$	0.067	$< 10^{-3}$	$< 10^{-3}$
$\mathrm{BR}_{e\tau}$	0.500	$< 10^{-3}$	$< 10^{-3}$
$\mathrm{BR}_{\mu\mu}$	0.388	0.982	0.982
$\mathrm{BR}_{\mu\tau}$	0.007	0.018	0.005
$\mathrm{BR}_{\tau\tau}$	$< 10^{-3}$	$< 10^{-3}$	$< 10^{-3}$

Table 5.5: Benchmark points for Zee-Babu model including the branching ratios for decays into the different leptonic final states. The Majorana phase is assumed to be $\varphi = \pi$. Table can be found in Ref. [4].

corresponding coupling cannot be substantial. In the following analysis we assume this coupling parameter to be effectively zero. Yet, the dark sector is in fact coupled to the SM particle bath, owing to the rich scalar sector of the neutrino mass models. The type-II seesaw framework contains the portal term $\lambda_{S\Delta} S^\dagger S \mathrm{Tr}\left(\Delta^\dagger \Delta\right)$, while the Zee-Babu framework features the terms $\lambda_{S\eta} \eta^+ \eta^- S^\dagger S$ and $\lambda_{S\kappa} \kappa^{++} \kappa^{--} S^\dagger S$. These portal terms lead to the thermally averaged DM annihilation cross section

$$\langle \sigma v \rangle_{S^\dagger S \to M^\dagger M} \simeq \frac{\lambda_{SM}^2 \sqrt{1 - m_M^2/m_S^2}}{32\pi m_S^2} \tag{5.62}$$

for the annihilation into a pair of mediators M. The BSM coupling parameter λ_{SM} is identified as $\lambda_{SM} = \sqrt{3}\lambda_{S\Delta}$ in the type-II seesaw framework (provided the triplet scalars are degenerate in mass and using $v_\Delta \ll v_\Phi$) and $\lambda_{SM} = \lambda_{S\eta} = \lambda_{S\kappa}$ in the Zee-Babu model.[2] For complex scalar DM the observed DM relic abundance require

$$\langle \sigma v \rangle \simeq 4 \times 10^{-26} \,\mathrm{cm^3 \, s^{-1}} \tag{5.63}$$

the thermally averaged annihilation cross section (see, *e.g.*, Ref. [364]).

For the following DM analysis we shall restrict the numerical results to the type-II seesaw framework but can transfer the findings to the other model, as discussed before.

The DM relic abundance with respect to the BSM scalar masses and portal coupling is presented in Fig. 5.7. The plot shows the parameter space for a substantial proportion of the measured DM relic abundance for different values of the portal coupling parameter $\lambda_{S\Delta}$. The resulting parameter space is confronted with present as well as potentially near-future collider bounds on the triplet mass and with the portal couplings $\lambda_{S\Delta} \in \{\sqrt{4\pi}, 4\pi\}$ which are generally relevant in the context of perturbativity constraints. The computation of the DM relic abundance was performed with the public `micrOMEGAs` package and the results are applicable to the Zee-Babu framework via the aforementioned re-scaling of the portal coupling.

For the discussion of Fig. 5.7 we shall focus on two mass regimes. The mass hierarchy $m_\Delta \ll m_S$ leads to a maximum DM mass for fixed portal coupling and the value of the maximum DM mass can be derived from $\langle \sigma v \rangle \sim \lambda_{S\Delta}^2/m_S^2$ which follows from Eq. (5.62) in this specific mass regime. While keeping the portal coupling parameter

---

[2]The factor $\sqrt{3}$ stems from the four four-point DM annihilations with two featuring identical particles in the respective final state.

and the DM mass fixed, an increasing mediator mass leads to a smaller DM annihilation cross section and in turn to an enhanced DM relic abundance. This behaviour is reflected by the 'knee' that each band features. The parameter space in the mass regime in which the DM and mediator masses are close to each other is very slim. The DM annihilations are Boltzmann-suppressed at $m_\Delta \gtrsim m_S$ and the parameter space approximately follows the line of degenerate masses. The reader may observe that the allowed parameter space dives deeper into the region with $m_\Delta > m_S$, the larger the portal coupling parameter $\lambda_{S\Delta}$ is. In fact, this is expected as the Boltzmann suppression in this regime is compensated for by the larger portal coupling strength.

Applying lower bounds on the mediator mass from experimental searches constrains the possible DM mass range. The most severe constraints on the mediator mass by the ATLAS collaboration exclude $m_{\Delta^{++}} \equiv m_\Delta \lesssim 870\,\mathrm{GeV}$ [365] with present LHC data, under the assumption of exclusive decays into electrically charged leptons. In addition to this (present) constraint, Fig. 5.7 features two projected bounds for potentially future collider experiments. A future $\mu^+\mu^-$-collider with $\sqrt{s} = 3\,\mathrm{TeV}$ center-of-mass energy and the integrated luminosity $\mathcal{L}_{\mathrm{int}} = 1\,\mathrm{ab}^{-1}$ could raise the lower bound for the mass of the doubly charged scalar to $m_{\Delta^{++}} \lesssim 1.45\,\mathrm{TeV}$ [366], while the high-energy
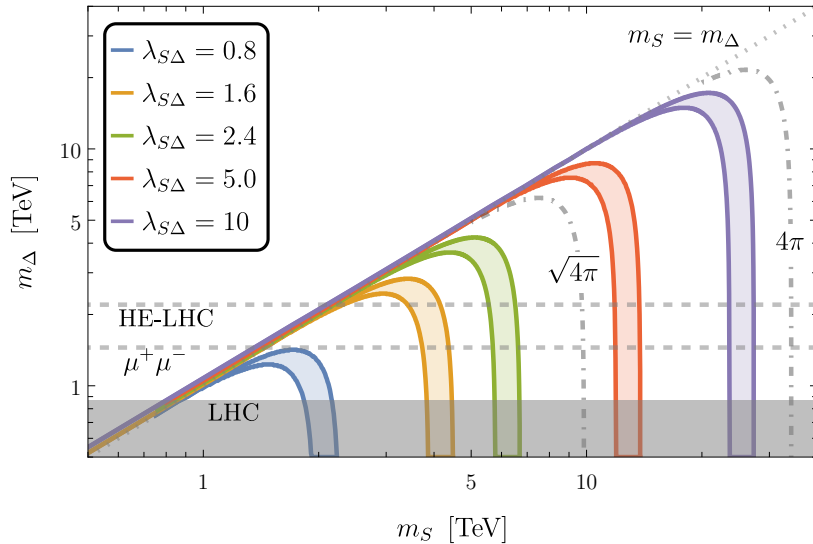
Figure 5.7: Parameter space for a DM relic abundance $0.75 \leq \Omega_{\mathrm{DM}}h^2/(\Omega_{\mathrm{DM}}h^2)_{\mathrm{obs}} \leq 1$ with the portal coupling $\lambda_{S\Delta}$ and degenerate masses m_Δ of the fields in the Δ triplet. The BSM vev is set to $v_\Delta = 10^{-5}\,\mathrm{GeV}$. The shaded parameter space is subject to present LHC bounds. The dashed lines correspond to projected bounds of a future $\mu^+\mu^-$ collider and the HE-LHC (see text for details). Taken from Ref. [4].

LHC (HE-LHC) with a nominal center-of-mass energy $\sqrt{s} = 27\,\text{TeV}$ and an integrated luminosity $\mathcal{L}_{\text{int}} = 15\,\text{ab}^{-1}$ could rule out $m_{\Delta^{++}} < 2.2\,\text{TeV}$ [367].

To summarize the result for the DM phenomenology, the DM mass can be in the range $1\,\text{TeV} \lesssim m_S \lesssim \mathcal{O}(10)\,\text{TeV}$.[3] The lower limit is set by present LHC limits, whereas the upper bound is subject to the transition from perturbative to non-perturbative interactions.

In the next section we shall explore DMID signatures in light of neutrino mass models. The guiding question shall be whether it could be possible to extract information about neutrino parameters like the Majorana phase(s) or about the mass hierarchy from cosmic ray spectra.

5.6 Connection to Dark Matter Indirect Detection

In the following, the DM annihilation process $S^\dagger S \to M^\dagger M$ with the subsequent decay of the mediator M into a pair of leptons, $M \to \ell_i \ell_j (\ell_i \nu_j)$, shall be examined in light of the question whether flavorful couplings of the charged neutrino-portal mediators introduced in Sections 5.3 and 5.4 gain insights into the neutrino oscillation parameters.

As we shall see for DMID, the interactions between the scalar DM S and the scalar mediators from the scalar triplet Δ on the one hand and the interactions between the mediators and different lepton flavors on the other hand influence the spectrum of cosmic ray positrons expected from DM annihilation in our Galaxy. Thanks to this connection between DM annihilation and production of SM leptons via BSM scalar mediators, the neutrino oscillation parameters govern flavor-specific DM annihilation signatures (*cf.* Fig. 5.8) and measuring these signatures might facilitate to learn more about the neutrino properties.

The couplings of the DM mediator to the leptons govern the production rate of primary leptons e, μ, τ. A signal of DM annihilation would average over many annihilation events and DMID is consequently not sensitive to the individual mediator branching ratios, but rather to the mean number $\langle n_{\ell^+}^M \rangle$ of charged leptons ℓ^+ produced in one decay of the mediator M. With $\ell \neq \ell', \ell''$ and the doubly charged mediator M^{++}, the average number of leptons per mediator decay reads

$$\langle n_{\ell^+}^{M^{++}} \rangle \equiv 2 \times \text{BR}\left(M^{++} \to \ell^+ \ell^+\right) + \text{BR}\left(M^{++} \to \ell^+ \ell'^+\right) + \text{BR}\left(M^{++} \to \ell^+ \ell''^+\right), \tag{5.64}$$

---

[3]Note that also the DM mass in the Higgs resonance regime is viable but was not focused on here in particular.

where the factor 2 in the first term accounts for the production of two same-sign charged leptons. This particular decay is not possible for the singly charged mediator, that is why the mean number of leptons for its decay is

$$\langle n_{\ell^+}^{M^+} \rangle \equiv \mathrm{BR}\left(M^+ \to \ell^+ \nu_\ell\right) + \mathrm{BR}\left(M^+ \to \ell^+ \nu_{\ell'}\right) + \mathrm{BR}\left(M^+ \to \ell^+ \nu_{\ell''}\right) . \tag{5.65}$$

These formulae apply to the scalar mediators introduced in Sections 5.3 and 5.4 and the results for the type-II seesaw and Zee-Babu model are presented in Figs. 5.9 and 5.10, respectively.

Summing up the contributions results in loss of information which is encoded in the individual branching ratios (*cf.* Figs. 5.4 and 5.6). Since collider studies are sensitive to the latter, these two experimental strategies serve as complementary approaches. Yet, Figs. 5.9 and 5.10 feature sensitivity to the different scenarios which might allow to obtain further information about the neutrino mass hierarchy and neutrino CP phases from ongoing and future DMID experiments.

We shall focus on the type-II seesaw model in Fig. 5.9 first. While the mean number of produced μ and τ starkly differs from the number of electrons for the normal neutrino mass hierarchy, the individual mean numbers are almost insensitive to the neutrino parameters. The inverted mass hierarchy, however, features more promising results for the Majorana phases which are taken equal, *i.e.* $\varphi_1 = \varphi_2$ for simplicity. The other two neutrino parameters are still almost unaffected by a variation of the respective neutrino parameter.

Unlike the situation in the type-II seesaw framework, the mean number of charged leptons in the Zee-Babu model is not fully determined but rather contains additional free model parameters which can be chosen within the range allowed by theoretical and experimental constraints. Different choices of these parameters lead to different mean
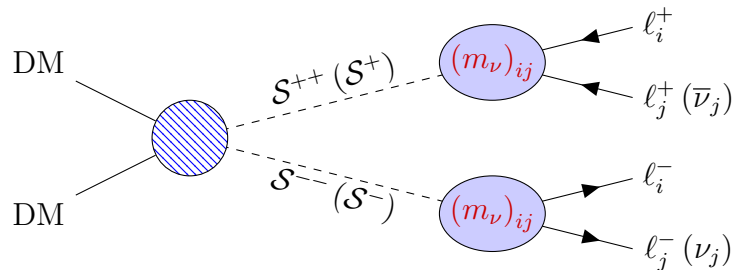
Figure 5.8: Schematic diagram for Dark Matter annihilations to SM leptons via generic, doubly (singly) charged scalars $\mathcal{S}^{\pm\pm}$ ($\mathcal{S}^\pm$). Image taken from Ref. [4].

numbers of charged leptons, which in turn give rise to bands of possible mean numbers of charged leptons instead of lines. These bands are shown in Fig. 5.10 for the decay of both BSM scalars. The doubly charged mediator decays predominantly into a pair of same-sign μ^+. Increasing the mediator mass widens the range of possible numbers of charged leptons in the final stance and thus enhances the sensitivity with respect to the neutrino parameters. The decay of the singly charged mediator η^+ is insensitive to the Majorana phase and leads ultimately to a virtually constant mean number of
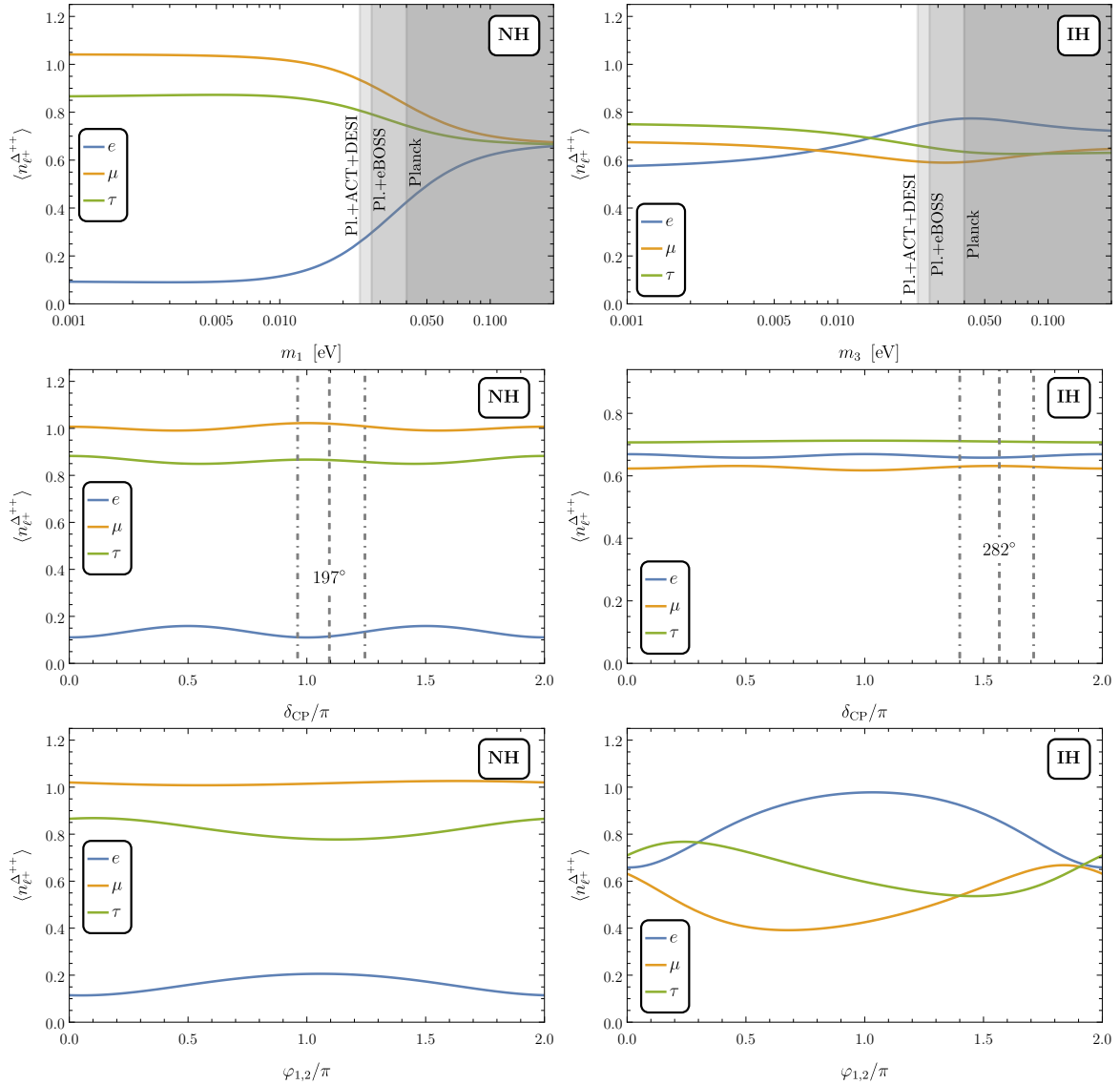
Figure 5.9: Mean number of lepton species $\langle n_{\ell^+}^{\Delta^{++}} \rangle$ per Δ^{++} decay in the type-II seesaw scenario. The parameter assignment is the same as for Fig. 5.4. Taken from Ref. [4].

electrons for any value of the Dirac CP phase. The variation of the mean numbers of the other two charged leptons seems to be too small to allow a clear discrimination in an experiment.
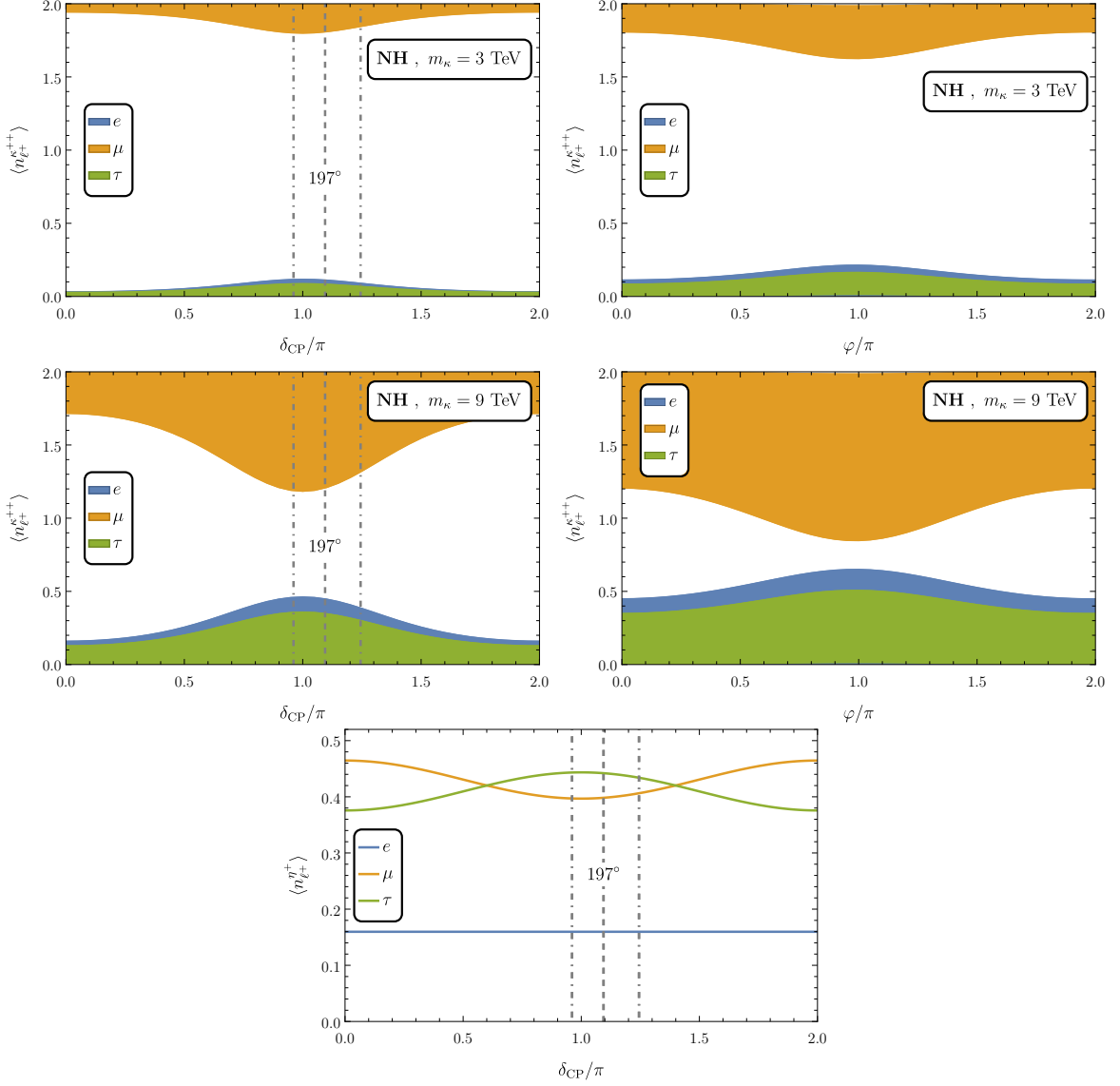
Figure 5.10: Mean number of leptons with the Dirac CP phase as given in Tab. 5.1 and the Majorana phase $\varphi = 0$ if not stated otherwise. *Top rows:* Bands of possible mean numbers of leptons in the decay of κ^{++}. The free Yukawa couplings in f, g as well as the cubic coupling $\mu_{\eta\kappa}$ are sampled. The parameter points satisfy the theoretical and experimental constraints. The plots in the left column contain information on the central value of δ_{CP} (dashed) as well as its 1σ uncertainty range (dot-dashed). *Bottom:* Mean numbers of leptons in the decay of η^+. Taken from Ref. [4].

Although the sensitivity of the mean number of charged values is not impressively great for some neutrino parameters, one can hope that the remaining scenarios lead to distinguishable positron spectra in DMID experiments. For this we consider the benchmark points given in Tab. 5.6 which are partially based on Tab. 5.5.

The measure in DMID experiments is the flux of the cosmic positrons which originate from DM annihilation processes in the Milky Way and propagate all the way to the detector site. The measured flux $\mathrm{d}\Phi_{e^+}/\mathrm{d}E = v_{e^+}n/(4\pi)$ of these cosmic rays depends on the positron velocity v_{e^+} and the cosmic ray density $n = \mathrm{d}N/(\mathrm{d}E\mathrm{d}^3x)$. Assuming cosmic rays with the energy E_0 originating from DM annihilation, the cosmic ray source term reads

$$Q\left(E_0, \vec{x}_0\right) = \frac{1}{4}\frac{\langle\sigma v\rangle\,\rho_{\mathrm{DM}}^2\left(\vec{x}_0\right)}{m_{\mathrm{DM}}^2}\left.\frac{\mathrm{d}N_{\mathrm{ann}}}{\mathrm{d}E}\right|_{E=E_0}, \tag{5.66}$$

where $\langle\sigma v\rangle$ is the thermally averaged DM annihilation cross section and $\mathrm{d}N_{\mathrm{ann}}/\mathrm{d}E$ is the positron spectrum per DM annihilation [4]. For the profile of the DM halo around the Milky Way we assume the Navarro–Frenk–White (NFW) profile [368] which reads

$$\rho_{\mathrm{NFW}}\left(r\right) = \rho_{\mathrm{gal}}\frac{r_{\mathrm{gal}}}{r}\left(1 + \frac{r}{r_{\mathrm{gal}}}\right)^{-2} \tag{5.67}$$

BM	BR_{ee}	$\mathrm{BR}_{e\mu}$	$\mathrm{BR}_{e\tau}$	$\mathrm{BR}_{\mu\mu}$	$\mathrm{BR}_{\mu\tau}$	$\mathrm{BR}_{\tau\tau}$	$\langle n_{e^\pm}\rangle$	$\langle n_{\mu^\pm}\rangle$	$\langle n_{\tau^\pm}\rangle$
SS-II NH	0.03	0.05	0.02	0.22	0.54	0.16	0.12	1.02	0.86
SS-II NH φ	~ 0	0.19	0.01	0.13	0.56	0.10	0.21	1.02	0.78
SS-II IH	0.29	0.04	0.03	0.09	0.42	0.13	0.66	0.63	0.71
SS-II IH φ	0.02	0.38	0.56	0.02	0.01	0.01	0.98	0.43	0.60
ZB-κ pure-μ	~ 0	~ 0	~ 0	0.98	0.02	~ 0	~ 0	1.98	0.02
ZB-κ min-μ	0.04	0.07	0.50	0.39	0.01	~ 0	0.65	0.85	0.50
ZB-η	0	0.06	0.10	0	0.34	0	0.16	0.40	0.44

Table 5.6: Benchmark points for branching ratios and mean number of leptons in type-II seesaw (SS-II) and Zee-Babu models. The benchmark points for the type-II seesaw model correspond to the two neutrino mass hierarchies and either $\varphi_{1,2} = 0$ or $\varphi_{1,2} = \pi$ (the latter case is labelled with φ), while the neutrino mass scale $m_{1,3} = 0.01\,\mathrm{eV}$ and the Dirac CP phase is taken from Tab. 5.1. The benchmark points for the Zee-Babu model correspond to NH, $m_1 = 0$, $\varphi = \pi$, and Dirac CP phase as given in Tab. 5.1. Example model parameters are presented in Tab. 5.5.

with the characteristic length scale $r_{\mathrm{gal}} = 24.42\,\mathrm{kpc}$ and $\rho_{\mathrm{gal}} = 0.184\,\mathrm{GeV\,cm^{-3}}$, resulting in a local DM density of $\rho_{\odot} = 0.3\,\mathrm{GeV/cm^3}$ at the position of the Sun [369].

To investigate the dependence of the positron spectra on the mean number of charged leptons predicted by the different scenarios in Tab. 5.6, we compute the positron spectra $\mathrm{d}N_{\mathrm{ann}}/\mathrm{d}E$ after cosmic ray propagation and shall discuss two scenarios: the first describes DM annihilation in the smooth Galactic DM halo, obeying the NFW profile, and the second features DM annihilation in a DM subhalo rather close to the detector site ($0.1\,\mathrm{kpc}$ distance) with a luminosity $10^{62}\,\mathrm{GeV^2\,cm^{-3}}$ in addition to the DM halo. The resulting positron spectra are shown in Fig. 5.11. The predictions are confronted with the current experimental data set by AMS-02 and with the projected spectrum for AMS-100.[4] While the positron flux expected from DM annihilations in the DM halo is not detectable since the background is much higher than the contributions from DM annihilations, a dense DM subhalo close to the detector site might cause a signal in the future AMS-100 experiment. For the benchmark points we selected in Tab. 5.6 the contributions from the type-II seesaw framework with inverted

---

[4]The Alpha Magnetic Spectrometer (AMS-02) is a present module of the International Space Station, designed to measure the flux of, *e.g.*, antimatter like positrons and antiprotons (*cf.* Refs. [370, 371]). Unlike its predecessor, AMS-100 is a detector designed to be mounted on a standalone spacecraft and to operate at the Sun-Earth Lagrange Point 2. The beginning of the science program is scheduled for 2030. See Ref. [372] for details.
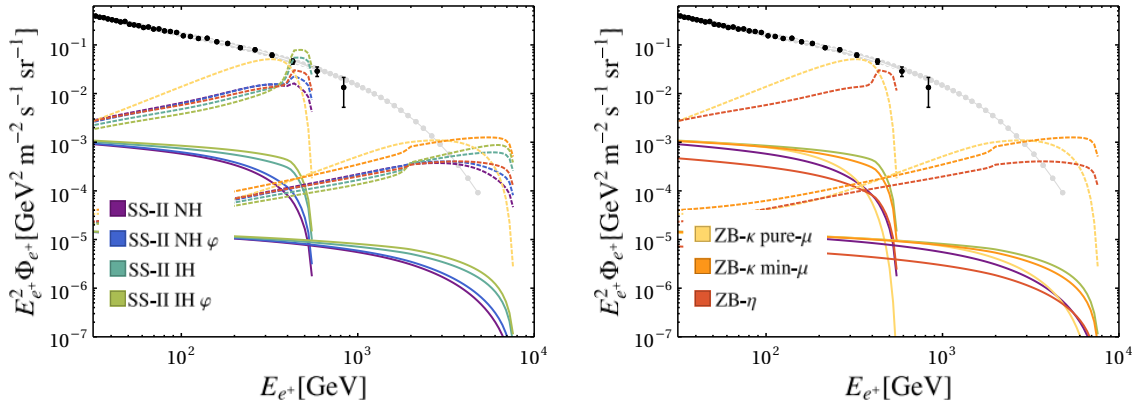
Figure 5.11: Local cosmic ray positron flux for different neutrino mass models and mass configurations. The solid lines correspond to the signal expected from the DM halo (obeying the NFW profile here), whereas the dashed lines show the positron flux for a nearby DM subhalo. The fluxes are compared to current AMS-02 data (black dots) and to an AMS-100 projection (gray). Each plot contains the results for the two mass configurations $M_{\mathrm{DM}}/m_{\mathrm{mediator}} = 1/0.99,\ 10/8\,\mathrm{TeV}$. Taken from Ref. [4].

neutrino mass hierarchy cause a flux which would be visible in the present data. As a consequence, these two benchmark points can be ruled out in this setting, which demonstrates the capability of cosmic ray measurements to help distinguish between different scenarios. However, the positron spectrum alone cannot identify the neutrino mass models since multiple models can predict the same signal. Nonetheless, this degeneracy can be broken by performing additional, complementary measurements. Hence we shall close this chapter with the collider analysis in the following section.

5.7   Collider Complementarity

Unlike the previous section, this section is dedicated to promising collider signatures and the potential of the LHC to help specify the neutrino oscillation parameters which are not already accurately determined. Here we are interested in the Drell-Yan processes with four electrically charged leptons in the final state. We shall begin with the type-II seesaw framework first and the collider signature of interest is shown in Fig. 5.12.

The number of events with this particular signature is predicted to be

$$N_{\text{events}} = \sigma_{\text{prod}} \times \mathcal{L}_{\text{int}} \times \text{BR}\left(\Delta^{++} \to \ell_a^+ \ell_b^+\right) \times \text{BR}\left(\Delta^{--} \to \ell_c^- \ell_d^-\right) \tag{5.68}$$

for a given integrated luminosity $\mathcal{L}_{\text{int}}$ and the branching ratios calculated above in Eq. (5.29). The production cross section σ_{prod} of the mediators must be computed before we can analyze the dependence on the neutrino oscillation parameters. For this we implement our model into the `FeynRules` package and compute the production cross section for the Drell-Yan plus photon fusion pair production mode of Δ^{++} by
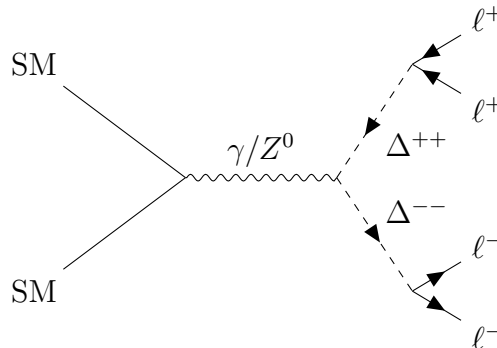
Figure 5.12: Drell-Yan process involving doubly charged scalars which decay into the four final-state charged leptons.

using the Monte Carlo event generator `MadGraph5_aMC@NLO`. For maximising the signal efficiency, we apply the following acceptance criteria in the analysis: (i) a lower bound on the transverse momentum $p_T(\ell^\pm) > 15\,\mathrm{GeV}$ of the charged leptons, (ii) an upper bound on the pseudorapidity $|\eta(\ell^\pm)| < 2.5$ which is defined as $\eta \equiv -\log\tan(\theta/2)$ with the relative angle θ between the spatial momentum of the particle and the beam axis, and ultimately (iii) a veto on any opposite-sign dilepton pair with an invariant mass near the Z boson mass, *i.e.* $|M(\ell^+\ell^-) - M_Z| > 15\,\mathrm{GeV}$, to diminish the risk of accepting Z-mediated processes and thus to avoid spurious contributions to the production cross section of the doubly charged scalar. As a results, the reconstruction of the invariant mass for a same-sign lepton pair produces a prominent peak at the mass of the doubly charged mediator without any SM background. By examining signals such as $pp \to \Delta^{++}\Delta^{--} \to e^+e^+e^-e^-/\mu^+\mu^+\mu^-\mu^-/e^+\mu^+e^-\mu^-$, there is substantial potential to obtain complementary information on neutrino oscillation parameters at the High-Luminosity LHC (HL-LHC). We do not take τ leptons in the final state into account since the identification efficiency for electrons and muons at colliders is considerably higher than the efficiency for the short-lived τ leptons.

To assess the potential of observing the discussed four-lepton process at the collider, we calculate the significance via

$$\mathcal{S} \equiv N_{\mathrm{events}}/\sqrt{N_{\mathrm{events}} + N_{\mathrm{bkg}}} \tag{5.69}$$

with the predicted number of BSM events from Eq. (5.68) and the expected number N_{bkg} of background events. Since this process is essentially free of any SM background contributions, the significance scales with $\sqrt{N_{\mathrm{events}}}$. The decay modes of the doubly charged scalar mediators into the different lepton flavors depend on the neutrino mass scale and the three CP phases. The sensitivity $\mathcal{S}$ for different integrated luminosities and final states is illustrated in Fig. 5.13 for varying neutrino mass scale and Majorana phase. The solid contours indicate different sensitivities for the integrated luminosity $\mathcal{L}_{\mathrm{int}} = 3\,\mathrm{ab}^{-1}$ of the high-luminosity LHC (HL-LHC), while the red dashed contours correspond to the integrated luminosities $\mathcal{L}_{\mathrm{int}} = 1\,\mathrm{ab}^{-1}$ and $\mathcal{L}_{\mathrm{int}} = 10\,\mathrm{ab}^{-1}$. In addition to the neutrino oscillation parameters, we compare the sensitivities for normal and inverted neutrino mass hierarchy. It is evident from Fig. 5.13 that the predicted sensitivities significantly vary for the two neutrino mass hierarchies. Beginning with the neutrino mass scale $m_0 \equiv m_{1,(3)}$ for NH (IH) and the process $pp \to e^+e^+e^-e^-$, the detection sensitivity is low for the Majorana phases $\varphi_{1,2} \approx \pi$, while the sensitivities evolve differently towards smaller/larger Majorana phases for the two mass hierar-

chies. In the case of inverted neutrino mass hierarchy, the sensitivity increases towards smaller/larger Majorana phases, virtually regardless of the absolute neutrino mass m_3. On the contrary, the sensitivity depends on m_1 in the normal neutrino mass hierarchy. The current upper limits on the absolute mass scale, however, rules out already the parameter space that features a significant range of sensitivities (*cf.* Fig. 5.4 for instance) and leaves the parameter space for the sensitivity $\mathcal{S} \leq 1\sigma$ open. The sensitivity is more appealing in the processes which involve muons in the final state. Most promising is the process with $e^+\mu^+e^-\mu^-$ in the final state and an inverted neutrino mass hierarchy as this features a 5σ sensitivity for the HL-LHC for the parameter space that is not ruled out by neutrino mass experiments.

In a analogous way, the statistical sensitivity can be examined for other sets of neutrino oscillation parameters. Fig. 5.14 illustrates the sensitivities of doubly charged
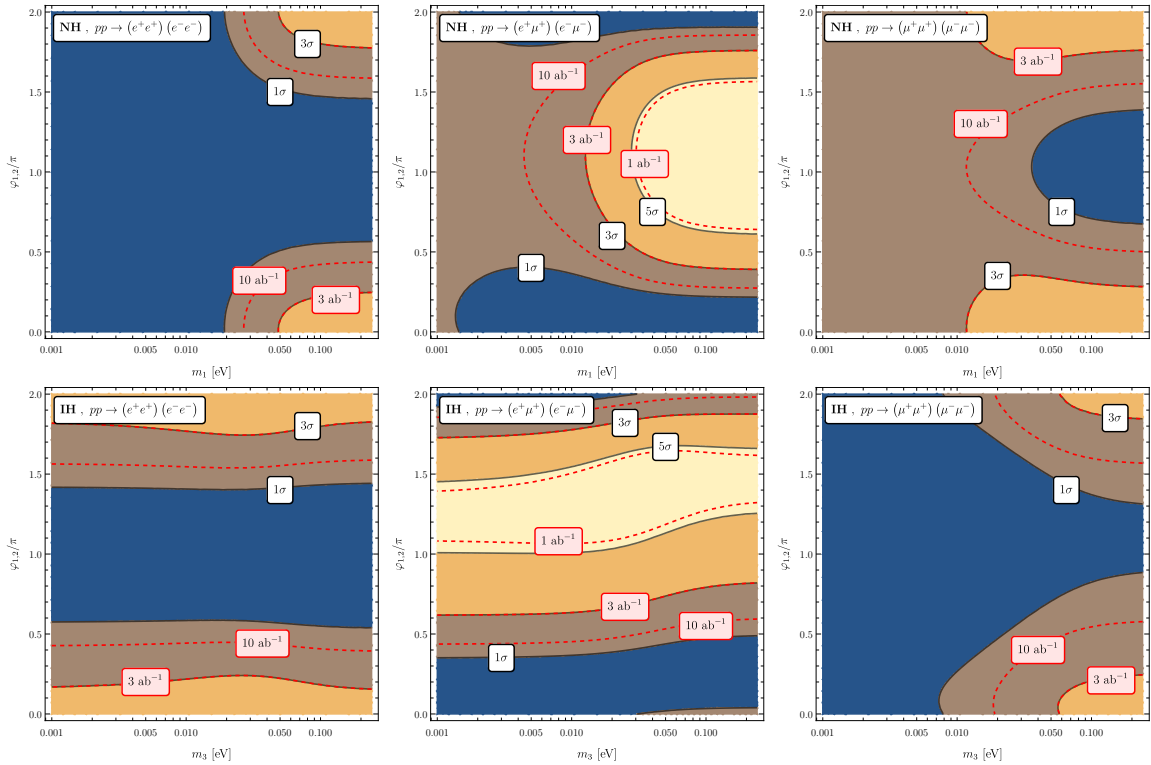
Figure 5.13: Sensitivities at HL-LHC for neutrino oscillation parameters with respect to the neutrino mass scale m_0 and the Majorana phase φ (we assume $\varphi_1 = \varphi_2 \equiv \varphi$ and the Dirac CP phase from Tab. 5.1) in the type-II seesaw model for a fixed mediator mass $m_\Delta = 1\,\mathrm{TeV}$. The contours indicate the statistical significance at $\mathcal{L}_{\mathrm{int}} = 3\,\mathrm{ab}^{-1}$ and the red, dashed lines show the 3σ contours for different integrated luminosities. Taken from Ref. [4].

scalars at the HL-LHC as a function of the Majorana phases $\varphi_{1,2}$ and the mediator mass m_Δ in the type-II seesaw model for different integrated luminosities. Unlike in the previous figure, the contour for the integrated luminosity $\mathcal{L}_{\mathrm{int}} = 139\,\mathrm{fb}^{-1}$ of the current LHC can be shown. The plots again show the statistical sensitivity for different channels and the two neutrino mass hierarchies. The heavier the doubly charged mediator Δ^{++}, the smaller is the sensitivity as the production cross section σ_{prod} decreases exponentially with the mediator mass for a fixed beam energy and the expected number of events in Eq. (5.68) decreases accordingly. Remarkably though, the sensitivity tends for $\varphi_{1,2} \approx \pi$ towards smaller mediator masses for the processes with a same-flavor final state, while the sensitivity for these Majorana phases tends towards large mediator masses for the mixed-flavor final state. The qualitative behaviour of the sensitivity for the six different cases can be inferred from the branching ratios illustrated in Fig. 5.4. It becomes evident from Fig. 5.14 that a doubly charged scalar from the triplet Δ with
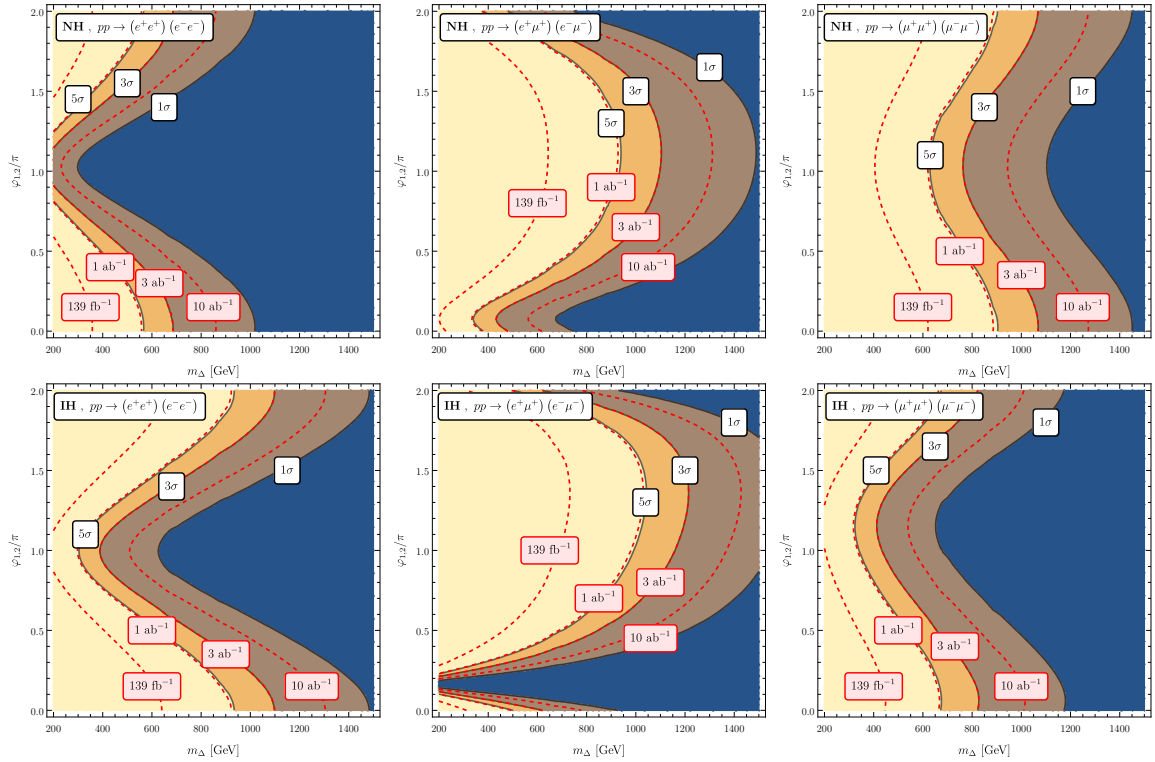
Figure 5.14: Sensitivities of doubly charged scalars at HL-LHC as a function of Majorana phase φ in the type-II seesaw framework. The Dirac CP phase is taken from Tab. 5.1 and the neutrino mass scale is set to $m_0 = 0.1\,\mathrm{eV}$. The contours indicate the statistical significance at $\mathcal{L}_{\mathrm{int}} = 3\,\mathrm{ab}^{-1}$ and the red dashed lines show the 3σ contours for different integrated luminosities. Taken from Ref. [4].

a mass $m_\Delta \lesssim 1.5\,\text{TeV}$ can be probed at the HL-LHC with an integrated luminosity of $10\,\text{ab}^{-1}$.

As the last set of plots in the type-II seesaw model, we investigate the dependence of the sensitivity with respect to the mediator mass and the Dirac CP phase δ_{CP} in Fig. 5.15. Again the contours for the integrated luminosities as well as for the statistical sensitivities are presented. The oscillatory behaviour of the sensitivity with respect to the Dirac CP phase is evident and originates from the oscillating branching ratios shown in Fig. 5.4. Similar to the discussion of the dependence on the absolute neutrino mass scale, the channel with a mixed-flavor final state seems to be the promising channel as the change in the gradient with respect to the Dirac CP phase is large for a mediator mass $300\,\text{GeV} \lesssim m_\Delta \lesssim 800\,\text{GeV}$. On the downside, lower limits on the mass of the doubly charged scalar from the scalar triplet Δ might rule out this parameter space.
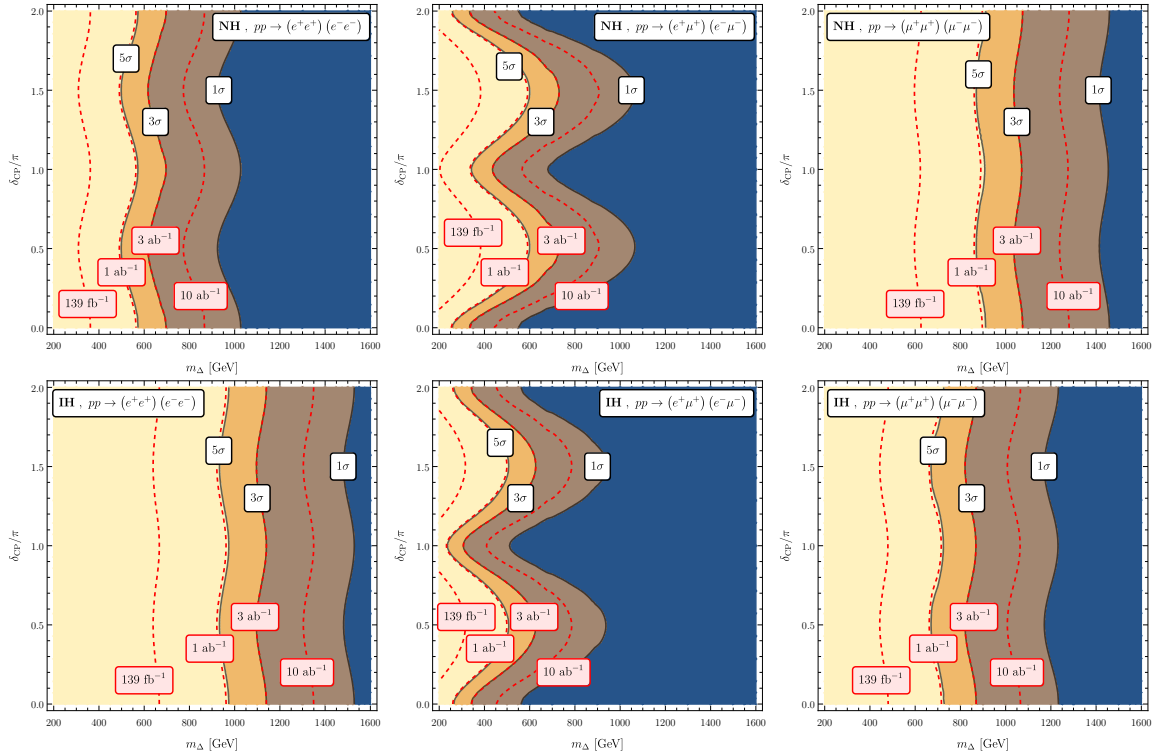
Figure 5.15: Sensitivities of doubly charged scalars at HL-LHC as a function of Dirac CP phase δ_{CP} in the type-II seesaw framework with the neutrino mass scale $m_0 = 0.1\,\text{eV}$ and the Majorana phase $\varphi = 0$. The contours indicate the statistical significance at $\mathcal{L}_{\text{int}} = 3\,\text{ab}^{-1}$ and the red dashed lines show the 3σ contours for different integrated luminosities. Taken from Ref. [4].

Lastly, we shall briefly examine the statistical sensitivity for the Zee-Babu model. Notably, the four-muons final state is the prominent channel while the other two channels are not promising due to the small branching ratios (*cf.* Fig. 5.6). The results for the dependence of the sensitvity on the two CP phases in the Zee-Babu model are shown in Fig. 5.16. The sensitivity is virtually independent of the two CP phases in the Zee-Babu model and mildly dependent on the mediator mass m_κ.

Concluding this chapter, we investigated the dependence of the positron flux as one of the DMID observables and of the collider cross sections for four leptons in the final state with charged lepton flavor violation on the neutrino oscillation parameters in the light of two neutrino mass models. The qualitative results for the former are very similar for the two models and require a nearby DM subhalo for enhancing the flux to be detectable. The predicted positron flux from DM annihilations in the Galactic DM halo is by several orders of magnitude smaller than the observed/predicted background, so that no discrimination between signal and background is feasible. The findings in the collider analysis feature great differences for the detection significance in
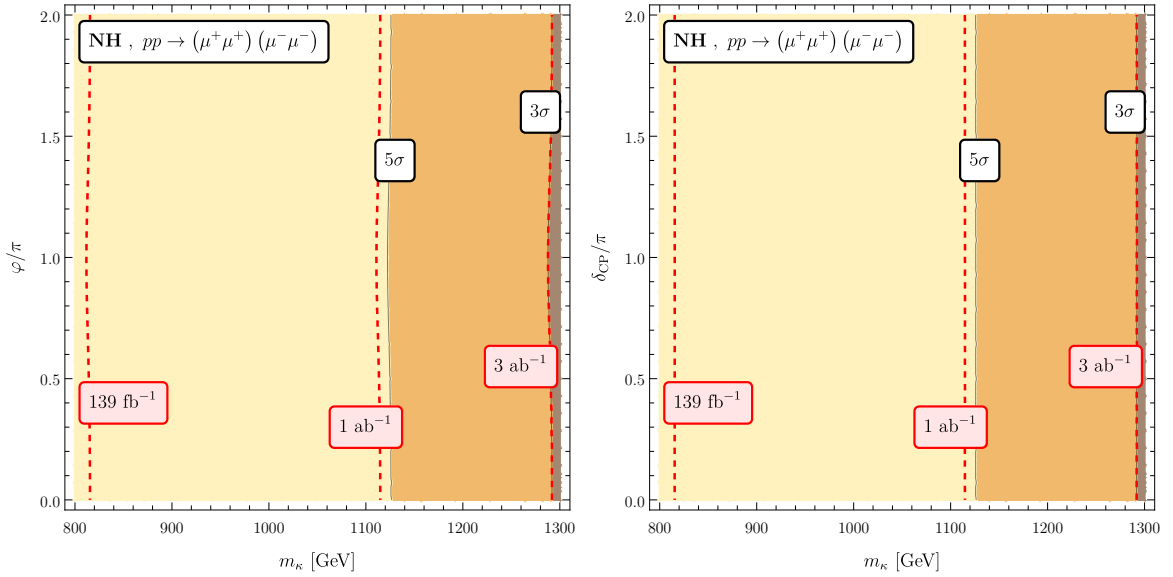
Figure 5.16: Sensitivities of doubly charged scalars at HL-LHC as a function of the neutrino CP phases δ_{CP}, φ, and the mediator mass m_κ in the Zee-Babu model for BM3 from Tab. 5.5. The Dirac CP phase is given by Tab. 5.1 and the Majorana phases $\varphi = 0$ if not stated otherwise. The contours indicate the statistical significance at $\mathcal{L}_{\mathrm{int}} = 3\,\mathrm{ab}^{-1}$, and the red dashed lines show the 3σ contours for different integrated luminosities.

different channels and is therefore promising for future analyses. These channels with the aforementioned selection rules for the invariant mass *etc.* are appealing for setting severe constraints on the mass of the doubly charged mediator in terms of the neutrino oscillation parameter in the type-II seesaw model. The dependence of the detection significance on the neutrino oscillation parameters is virtually absent in the Zee-Babu model, but the dependence on the mediator mass can be deployed for mass constraints. A more accurate detection significance would require a full-fledged detector analysis which is beyond the scope of this project but worthwhile for potential future analyses.

Chapter 6

Summary & Conclusion

In this thesis we investigated several open questions which the SM cannot account for and were outlined in the introduction to the SM and to DM in Chapters 1 and 2, respectively.

Making use of the advantages of the EFT framework, we presented in Chapter 3 an eDMEFT as a first attempt to improve DM studies at colliders in light of the HEFT, that allows to describe, *e.g.*, interactions between fermionic DM and the SM particles. The appealing advantages of our approach are (*i*) the minimal theoretical bias with respect to the representations both of the SM Higgs multiplet and of the two scalar mediators which in general allows to map numerous UV theories onto this eDMEFT and (*ii*) the possibility to allow for resonant enhancement due to the exchange of the mediators. As a first demonstration of the concept, we compare the eDMEFT to a simple extension of the SM, whose scalar degrees of freedom serve as mediators between the dark and the SM sectors. The results for the DM relic abundance and the mono-h and mono-Z signatures meet our expectations. Afterwards, we investigated the capabilities of the eDMEFT to describe an extension of the well-studied 2HDM to a satisfying level of accuracy. The extended 2HDM features more than two scalars that can mediate DM annihilations. We pointed out differences between two scenarios in this UV theory and explained the discrepancies in the predictions for the DM relic abundance. Lastly, we provided suggestions for improving the analysis.

The feature of the EFT framework to describe in principle a plethora of UV theories motivated the investigation of a model for baryogenesis in Chapter 4. We studied the IDM, which serves as a motivated and well-studied DM theory, with an additional, higher-dimensional CP-violating operator in order to account for the lack of CP violation in the SM. We find that the EFT with this CP-violating operator can account

for the baryon asymmetry of the Universe via a multi-step EWPhT and the evolution of the BSM vev without spoiling the findings for the DM relic abundance. Due to the inert nature of the inert Higgs doublet at low temperatures (at today's temperatures in particular), the arguably dominant contribution to the predicted lepton EDM occurs at two-loop level and thus eludes detection in eEDM searches by JILA for instance. Remarkably though, the projected limits by the ACME III experiment cover a fraction of the parameter space in the IDMEFT, so that the predictions of this EFT get scrutinized. We identified parameter space in two DM mass regimes in which the lightest scalar from the BSM Higgs doublet serves as the DM candidate and the baryon asymmetry of the Universe can be generated (or is poised to be generated via additional higher-dimensional operators). Eventually, possible UV realizations for the two DM mass regimes have been discussed.

The last Chapter 5 addressed the open question of the origin of neutrino masses and the resulting mixing of the flavor eigenstates. In purpose of the experimental determination of neutrino properties, we investigated the potential of DMID in light of the free neutrino oscillation parameters and the neutrino mass hierarchy in the framework of the type-II seesaw and Zee-Babu model as two well-known neutrino mass models. We found that the positron spectrum from DM annihilations in a nearby DM subhalo changes for different scenarios of the neutrino mass models and can be substantially larger than the expected positron background. In addition, we studied the detection significance of the two models for the free neutrino oscillation parameters and the mass hierarchy and compared the results for different collider luminosities.

In conclusion, the results of this thesis should be understood as positive indications for the possibility of systematically investigating DM models in the context of the presented eDMEFT framework as well as for the feasibility of probing model predictions thanks to the great progress in sensitivity and accuracy both in low-energy (*e.g.* ℓEDM searches) and high-energy experiments (*e.g.* colliders or DMID). One can indeed stay optimistic about the future of particle physics. Metaphorically speaking, doors might get closed by experimental and theoretical findings, but others do open instead.

Appendix A

Processes for eDMEFT Analysis

The purpose of this appendix is providing an overview of important and potentially interesting processes for comparison between a UV model and the eDMEFT. While the processes in Tab. are important for constraints, those in Tab. include interesting collider signatures.

Category	Process	Model parameter
IHD	h → $\mathcal{S}_i$ ... $\mathcal{S}_i$	$\lambda_{2,0}^{(1)}, \lambda_{1,1}^{(1)}, \lambda_{0,2}^{(1)}, \lambda_{3,0}^{(1)}, \lambda_{2,1}^{(1)}, \lambda_{1,2}^{(1)}, \lambda_{0,3}^{(1)},$ $\lambda_{4,0}^{(1)}, \lambda_{3,1}^{(1)}, \lambda_{2,2}^{(1)}, \lambda_{1,3}^{(1)}, \lambda_{0,4}^{(1)}$
EWPO	Z → $\mathcal{S}_i$ ... $\mathcal{S}_i$	$s1_{1,0}^{(0)}, s1_{0,1}^{(0)}, s1_{2,0}^{(0)}, s1_{1,1}^{(0)}, s1_{0,2}^{(0)} + (s1 \leftrightarrow s2)$
	V ~~ V (tadpole loop)	$\kappa_{0,0}^{(2)}, \kappa_{2,0}^{(0)}, \kappa_{0,2}^{(0)}$
	V ~~ V (gauge loop)	$\kappa_{0,0}^{(1)}, \kappa_{1,0}^{(0)}, \kappa_{0,1}^{(0)}$
	V ~~ V (scalar loop)	$s_{0,0}^{(1)}, s_{1,0}^{(0)}, s_{0,1}^{(0)} + (s \leftrightarrow s1 \leftrightarrow s2)$
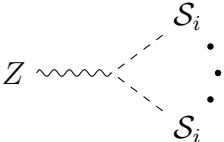
Table A.1: Relevant Wilson coefficients for invisible SM Higgs decay (IHD) and EW precision observables (EWPO) for the EW gauge bosons $V = W^{\pm}, Z$. Dashed propagators correspond to the SM Higgs h and BSM scalars $\mathcal{S}_i$.

Category	Process	Model parameter
τ pair production	$g,g \to \mathcal{S}_i \to \tau^-\tau^+$ (and q-triangle loop diagram with $\mathcal{S}_i$)	$c_G^{\mathcal{S}_i},(c_\ell)_{1,0}^{(0)},(c_\ell)_{0,1}^{(0)}$ $+ (c_q)_{1,0}^{(0)},(c_q)_{0,1}^{(0)}$
Mono-jet	$g,g \to \mathcal{S}_i \to \chi\overline{\chi} + g$, $+\ q$-loop	$c_G^{\mathcal{S}_i},\ y_{1,0}^{(0)},\ y_{0,1}^{(0)} + q\text{-loop}$
Higgs pair production	$g,g \to \mathcal{S}_i \to h\,h$, $+\ q$-loop	$c_G^{\mathcal{S}_i},\ \lambda_{1,0}^{(2)},\ \lambda_{0,1}^{(2)} + q\text{-loop}$
Mono-h	$g,g \to h/\mathcal{S}_i \to \mathcal{S}_i + h$, $+\ q$-loop	$c_G^{\mathcal{S}_i},\tilde{c}_G^{\mathcal{S}_i},\lambda_{1,0}^{(2)},\ \lambda_{0,1}^{(2)},\lambda_{2,0}^{(1)},\lambda_{1,1}^{(1)},\lambda_{0,2}^{(1)},$ $+q\text{-loop}$
Di-boson resonance	$g,g \to h/\mathcal{S}_i \to Z/W^+ + Z/W^-$, $+\ q$-loop	$c_G^{\mathcal{S}_i},c_W^{\mathcal{S}_i},c_B^{\mathcal{S}_i},\kappa_{0,0}^{(1)},\kappa_{1,0}^{(0)},\kappa_{0,1}^{(0)}$ $+q\text{-loop}$
Mono-Z	$g,g \to h/\mathcal{S}_i \to h/\mathcal{S}_i + Z$, $+\ q$-loop	$c_G^{\mathcal{S}_i},\tilde{c}_G^{\mathcal{S}_i},s_{1,0}^{(0)},s_{0,1}^{(0)},s1_{0,0}^{(1)},$ $s1_{0,1}^{(0)},s2_{0,0}^{(1)},s2_{1,0}^{(0)}$ $+q\text{-loop}$

Table A.2: Important Wilson coefficients for collider searches. The tilde indicates an interaction with pseudoscalar mediator.

Appendix B

Relations for Model Parameters

This chapter is devoted to presenting the matching conditions for the eDMEFT and the respective UV model. The Lagrangian of the eDMEFT is defined in Eq. (3.12). The Wilson coefficients not listed here are not present in the matching.

B.1 SM + Complex Scalar Singlet + Fermionic Singlets

We find the following relations:

$$\mu_S^2 = -\frac{m_s^2 c_\theta^2 v_s + m_h^2 s_\theta^2 v_s + \left(m_h^2 - m_s^2\right) s_\theta c_\theta v_h}{2v_s} \tag{B.1}$$

$$\mu_\Phi^2 = -\frac{m_h^2 c_\theta^2 v_h + m_s^2 s_\theta^2 v_h + \left(m_h^2 - m_s^2\right) s_\theta c_\theta v_s}{2v_h} \tag{B.2}$$

$$\mu_a^2 = \frac{m_a^2}{2} \tag{B.3}$$

$$\lambda_S = \frac{m_h^2 s_\theta^2 + m_s^2 c_\theta^2}{2v_s^2} \tag{B.4}$$

$$\lambda_\Phi = \frac{m_h^2 c_\theta^2 + m_s^2 s_\theta^2}{2v_h^2} \tag{B.5}$$

$$\lambda_{\Phi S} = \frac{m_h^2 - m_s^2}{2v_h v_s} s_{2\theta} \tag{B.6}$$

$$y_{\chi S} = \sqrt{2}\frac{m_\chi}{v_s} \tag{B.7}$$

$$y_{\mathcal{Q}S} = \sqrt{2}\frac{m_\mathcal{Q}}{v_s} \tag{B.8}$$

APPENDIX B.   RELATIONS FOR MODEL PARAMETERS

The matching conditions for the UV model, presented in Section 3.3.1, are given in this section of the appendix.

$$(c_{u,d,\ell})_{0,0}^{(1)} = c_\theta/v_h \tag{B.9}$$

$$(c_{u,d,\ell})_{1,0}^{(0)} = -s_\theta/v_h \tag{B.10}$$

$$y_{0,0}^{(1)} = \frac{s_\theta}{2\sqrt{2}} y_{\chi S} \tag{B.11}$$

$$y_{1,0}^{(0)} = \frac{c_\theta}{2\sqrt{2}} y_{\chi S} \tag{B.12}$$

$$y_{0,1}^{(0)} = \frac{y_{\chi S}}{\sqrt{2}} \tag{B.13}$$

$$\kappa_{0,0}^{(1)} = 2c_\theta/v_h \tag{B.14}$$

$$\kappa_{1,0}^{(0)} = -2s_\theta/v_h \tag{B.15}$$

$$\kappa_{0,0}^{(2)} = c_\theta^2/v_h^2 \tag{B.16}$$

$$\kappa_{1,0}^{(1)} = -s_{2\theta}/v_h^2 \tag{B.17}$$

$$\kappa_{2,0}^{(0)} = s_\theta^2/v_h \tag{B.18}$$

$$c_h^B = 3 \sum_{\mathcal{Q}=\mathcal{T},\mathcal{B}} Q_\mathcal{Q}^2 m_\mathcal{Q} \frac{m_h^2 + \left(m_h^2 - 4m_\mathcal{Q}^2\right) \arcsin^2 \frac{m_h}{2m_\mathcal{Q}}}{m_h^4} y_{\mathcal{Q}S} s_\theta \tag{B.19}$$

$$c_h^G = 2 \sum_{\mathcal{Q}=\mathcal{T},\mathcal{B}} m_\mathcal{Q} \frac{m_h^2 + \left(m_h^2 - 4m_\mathcal{Q}^2\right) \arcsin^2 \frac{m_h}{2m_\mathcal{Q}}}{m_h^4} y_{\mathcal{Q}S} s_\theta \tag{B.20}$$

$$c_{\mathcal{S}_1}^B = 3 \sum_{\mathcal{Q}=\mathcal{T},\mathcal{B}} Q_\mathcal{Q}^2 m_\mathcal{Q} \frac{m_{\mathcal{S}_1}^2 + \left(m_{\mathcal{S}_1}^2 - 4m_\mathcal{Q}^2\right) \arcsin^2 \frac{m_{\mathcal{S}_1}}{2m_\mathcal{Q}}}{m_{\mathcal{S}_1}^4} y_{\mathcal{Q}S} c_\theta \tag{B.21}$$

$$c_{\mathcal{S}_1}^G = 2 \sum_{\mathcal{Q}=\mathcal{T},\mathcal{B}} m_\mathcal{Q} \frac{m_{\mathcal{S}_1}^2 + \left(m_{\mathcal{S}_1}^2 - 4m_\mathcal{Q}^2\right) \arcsin^2 \frac{m_{\mathcal{S}_1}}{2m_\mathcal{Q}}}{m_{\mathcal{S}_1}^4} y_{\mathcal{Q}S} c_\theta \tag{B.22}$$

$$c_{\mathcal{S}_2}^B = 4 \sum_{\mathcal{Q}=\mathcal{T},\mathcal{B}} Q_\mathcal{Q}^2 \frac{m_\mathcal{Q} y_{\mathcal{Q}S}}{\sqrt{2} m_{\mathcal{S}_2}^2} c_\theta \arcsin^2 \frac{m_{\mathcal{S}_2}}{2m_\mathcal{Q}} \tag{B.23}$$

$$c_{\mathcal{S}_2}^G = 2 \sum_{\mathcal{Q}=\mathcal{T},\mathcal{B}} \frac{m_\mathcal{Q} y_{\mathcal{Q}S}}{\sqrt{2} m_{\mathcal{S}_2}^2} c_\theta \arcsin^2 \frac{m_{\mathcal{S}_2}}{2m_\mathcal{Q}} \tag{B.24}$$

$$\lambda_{0,0}^{(2)} = \frac{m_h^2}{2} \tag{B.25}$$

$$\lambda_{2,0}^{(0)} = \frac{m_s^2}{2} \tag{B.26}$$

$$\lambda_{0,2}^{(0)} = \mu_a^2 \tag{B.27}$$

$$\lambda_{0,0}^{(3)} = \frac{m_h^2}{2v_h v_s} \left(v_h s_\theta^3 + v_s c_\theta^3 \right) \tag{B.28}$$

$$\lambda_{1,0}^{(2)} = \frac{m_s^2 + 2m_h^2}{4v_h v_s} \left(v_h s_\theta - v_s c_\theta \right) s_{2\theta} \tag{B.29}$$

$$\lambda_{2,0}^{(1)} = \frac{m_s^2 + 2m_h^2}{4v_h v_s} \left(v_h c_\theta + v_s s_\theta \right) s_{2\theta} \tag{B.30}$$

$$\lambda_{0,2}^{(1)} = \frac{m_h^2 s_\theta}{2v_s} \tag{B.31}$$

$$\lambda_{3,0}^{(0)} = \frac{m_s^2}{2v_h v_s} \left(v_h c_\theta^3 - v_s s_\theta^3 \right) \tag{B.32}$$

$$\lambda_{1,2}^{(0)} = \frac{m_s^2 c_\theta}{2v_s} \tag{B.33}$$

$$\lambda_{0,0}^{(4)} = \frac{m_h^2 v_s^2 c_\theta^6 + m_s^2 v_s^2 c_\theta^4 s_\theta^2 + 2\left(m_h^2 - m_s^2\right) v_h v_s s_\theta^3 c_\theta^3 + m_s^2 v_h^2 c_\theta^2 s_\theta^4 + m_h^2 v_h^2 s_\theta^6}{8v_h^2 v_s^2} \tag{B.34}$$

$$\lambda_{3,0}^{(1)} = \frac{\left(3m_h^2 + m_s^2\right)\left(v_s c_\theta + v_h s_\theta\right) + \left(m_h^2 - m_s^2\right)\left(v_s c_{3\theta} - v_h s_{3\theta}\right)}{16v_h^2 v_s^2} \left(v_h s_\theta - v_s c_\theta \right) s_{2\theta} \tag{B.35}$$

$$\lambda_{2,0}^{(2)} = \frac{6\left(m_h^2 - m_s^2\right) v_h v_s c_{4\theta} + 6\left(m_h^2 + m_s^2\right)\left(v_h^2 + v_s^2\right) s_{2\theta}}{32v_h^2 v_s^2}$$
$$- \frac{\left(m_h^2 - m_s^2\right)\left(3\left(v_h^2 - v_s^2\right) s_{4\theta} - 2v_h v_s\right)}{32v_h^2 v_s^2} \tag{B.36}$$

$$\lambda_{0,2}^{(2)} = \frac{\left(m_h^2 - m_s^2\right) v_s c_\theta^3 + m_s^2 v_h c_\theta^2 s_\theta + m_h^2 v_h s_\theta^3}{4v_h v_s^2} s_\theta \tag{B.37}$$

$$\lambda_{3,0}^{(1)} = \frac{\left(m_h^2 + 3m_s^2\right) v_h c_\theta + \left(m_s^2 - m_h^2\right) v_h c_{3\theta} - 4v_s s_\theta \left(m_h^2 c_\theta^2 + m_s^2 s_\theta^2\right)}{16v_h^2 v_s^2} \left(v_h c_\theta + v_s s_\theta \right)$$
$$\tag{B.38}$$

$$\lambda_{1,2}^{(1)} = \frac{m_s^2 v_h c_\theta^2 + \left(m_s^2 - m_h^2\right) s_\theta c_\theta v_s + m_h^2 v_h s_\theta^2}{4v_h v_s^2} s_{2\theta} \tag{B.39}$$

$$\lambda_{4,0}^{(0)} = \frac{m_s^2 v_h^2 c_\theta^6 + m_h^2 v_h^2 c_\theta^4 s_\theta^2 + 2\left(m_h^2 - m_s^2\right) v_h v_s s_\theta^3 c_\theta^3 + m_h^2 v_s^2 c_\theta^2 s_\theta^4 + m_s^2 v_s^2 s_\theta^6}{8v_h^2 v_s^2} \tag{B.40}$$

$$\lambda_{2,2}^{(0)} = \frac{\left(m_h^2 - m_s^2\right) v_s s_\theta^3 + m_h^2 v_h s_\theta^2 c_\theta + m_s^2 v_h c_\theta^3}{4v_h v_s^2} c_\theta \tag{B.41}$$

$$\lambda_{0.4}^{(0)} = \frac{m_s^2 c_\theta^2 + m_h^2 s_\theta^2}{8v_s^2} \tag{B.42}$$

B.2   2HDM + Pseudoscalar + Fermionic DM

We find the following relations:

$$M_{11}^2 = \left(2m_{H^\pm}^2 - m_H^2 - \lambda_3 v^2\right) \sin^2\beta - \frac{1}{2}m_h^2 \cos 2\beta \tag{B.43}$$

$$M_{22}^2 = \left(2m_{H^\pm}^2 - m_H^2 - \lambda_3 v^2\right) \cos^2\beta + \frac{1}{2}m_h^2 \cos 2\beta \tag{B.44}$$

$$M_{12}^2 = -\frac{1}{2}\left(m_h^2 - m_H^2 + 2m_{H^\pm}^2 - \lambda_3 v^2\right) \sin 2\beta \tag{B.45}$$

$$M_{PP}^2 = m_A^2 \sin^2\theta + m_a^2 \cos^2\theta - \left(\lambda_{11P} \cos^2\beta + \lambda_{22P} \sin^2\beta\right) v^2 \tag{B.46}$$

$$\lambda_1 = \frac{1}{v^2}\left(m_h^2 - \left(m_h^2 - 2m_H^2 + 2m_{H^\pm}^2 - \lambda_3 v^2\right) \tan^2\beta\right) \tag{B.47}$$

$$\lambda_2 = \frac{m_h^2}{v^2 \sin^2\beta} - \frac{2m_h^2 - 2m_H^2 + 2m_{H^\pm}^2 - \lambda_3 v^2}{v^2} \cot^2\beta \tag{B.48}$$

$$\lambda_4 = \frac{1}{v^2}\left(m_h^2 - m_H^2 - \lambda_3 v^2 + m_A^2 \cos^2\theta + m_a^2 \sin^2\theta\right) \tag{B.49}$$

$$\lambda_5 = \frac{1}{v^2}\left(m_h^2 - m_H^2 + 2m_{H^\pm}^2 - \lambda_3 v^2 - m_A^2 \cos^2\theta - m_a^2 \sin^2\theta\right) \tag{B.50}$$

$$\mu_{12P} = -\frac{m_a^2 - m_A^2}{2v} \sin 2\theta \tag{B.51}$$

The matching conditions for the Wilson coefficients and the UV model parameters are given in the remainder.

Neutral scalar from second doublet

$$(c_{u,d,\ell})_{1,0}^{(0)} = \epsilon_{u,d,\ell}/v \tag{B.52}$$

$$(c_u)_{0,1}^{(0)} = -\,(c_{d,\ell})_{0,1}^{(0)} = -s_\theta \epsilon_{u,d,\ell}/v \tag{B.53}$$

$$y_{0,1}^0 = y_{\chi P} c_\theta \tag{B.54}$$

$$\kappa_{0,0}^{(1)} = 2/v \tag{B.55}$$

$$\kappa_{0,0}^{(2)} = \kappa_{2,0}^{(0)} = 1/v^2 \tag{B.56}$$

$$\kappa_{0,2}^{(0)} = s_\theta^2/v^2 \tag{B.57}$$

$$(s_1)_{0,1}^{(0)} = -\,(s_2)_{1,0}^{(0)} = -2s_\theta/v^2 \tag{B.58}$$

$$\lambda_{0,0}^{(2)} = \frac{\lambda_2 s_\beta^2 + \lambda_{345} c_\beta^2}{2} v^2 \tag{B.59}$$

$$\lambda_{2,0}^{(0)} = \frac{\lambda_2 - \lambda_{345}}{2} s_\beta^2 v^2 - \frac{M_{12}^2}{s_{2\beta}} \tag{B.60}$$

$$\lambda_{0,2}^{(0)} = \frac{1}{2} \left[\left(M_P^2 + \left(\lambda_{11P} c_\beta^2 + \lambda_{22P} s_\beta^2 \right) v^2 \right) c_\theta^2 - \mu_{12P} s_{2\theta} v - \left(\lambda_5 v^2 + \frac{M_{12}^2}{s_{2\beta}} \right) s_\theta^2 \right] \tag{B.61}$$

$$\lambda_{0,0}^{(3)} = \frac{\lambda_2 s_\beta^2 + \lambda_{345} c_\beta^2}{2} v \tag{B.62}$$

$$\lambda_{2,0}^{(1)} = \frac{3 \left(\lambda_2 - \lambda_{345} \right) s_\beta^2 + \lambda_{345}}{2} v \tag{B.63}$$

$$\lambda_{0,2}^{(1)} = \left(\lambda_{11P} c_\beta^2 + \lambda_{22P} s_\beta^2 \right) c_\theta^2 v + \frac{\lambda_2 s_\beta^2 + \lambda_{345} c_\beta^2 - 2\lambda_5}{2} s_\theta^2 v - \frac{\mu_{12P} s_{2\theta}}{2} \tag{B.64}$$

$$\lambda_{3,0}^{(0)} = \frac{\lambda_2 - \lambda_{345}}{8 c_\beta^2} s_{4\beta} v \tag{B.65}$$

$$\lambda_{1,2}^{(0)} = \frac{\lambda_{345} - \lambda_2}{2} \left(t_\beta - s_{2\beta} \right) s_\theta^2 v - \frac{\lambda_{11P} - \lambda_{22P}}{2} c_\theta^2 s_{2\beta} v \tag{B.66}$$

$$\tag{B.67}$$

$$\lambda_{0,0}^{(4)} = \frac{\lambda_{345} c_\beta^2 + \lambda_2 s_\beta^2}{8} \tag{B.68}$$

$$\lambda_{2,0}^{(2)} = \frac{3 \left(\lambda_2 - \lambda_{345} \right) s_\beta^2 + \lambda_{345}}{4} \tag{B.69}$$

$$\lambda_{0,2}^{(2)} = \frac{\left(\lambda_{11P} c_\beta^2 + \lambda_{22P} s_\beta^2 \right) c_\theta^2 + \left(\lambda_{345} c_\beta^2 + \lambda_2 s_\beta^2 - 2\lambda_5 \right) s_\theta^2}{2} \tag{B.70}$$

$$\lambda_{3,0}^{(1)} = \frac{\lambda_2 - \lambda_{345}}{8 c_\beta^2} s_{4\beta} \tag{B.71}$$

$$\lambda_{1,2}^{(1)} = \frac{\lambda_{22P} - \lambda_{11P}}{2} s_{2\beta} c_\theta^2 - \frac{\lambda_{345} - \lambda_2}{2} \left(s_{2\beta} - t_\beta \right) s_\theta^2 \tag{B.72}$$

$$\lambda_{4,0}^{(0)} = \frac{1}{8} \left[\lambda_{345} - \left(\lambda_2 - \lambda_{345} \right) \left(3 s_\beta^2 - \frac{1}{c_\beta^2} \right) \right] \tag{B.73}$$

$$\lambda_{2,2}^{(0)} = \frac{\lambda_{11P} s_\beta^2 + \lambda_{22P} c_\beta^2}{2} c_\theta^2 + \left[\frac{\lambda_{345}}{4} + \frac{\lambda_2 - \lambda_{345}}{16 c_\beta^2} \left(1 + 3 c_{2\beta}^2 \right) \right] s_\theta^2 \tag{B.74}$$

$$\lambda_{0,4}^{(0)} = \frac{\lambda_P}{4} c_\theta^4 + \frac{\lambda_{11P} s_\beta^2 + \lambda_{22P} c_\beta^2}{8} s_{2\theta}^2 + \left[\frac{\lambda_{345}}{8} + \frac{\lambda_2 - \lambda_{345}}{32 c_\beta^2} \left(1 + 3 c_{2\beta}^2 \right) \right] s_\theta^4 \tag{B.75}$$

Neutral pseudoscalar from second doublet

$$\lambda_{0,0}^{(2)} = \frac{\lambda_2 s_\beta^2 + \lambda_{345} c_\beta^2}{2} v^2 \tag{B.76}$$

$$\lambda_{2,0}^{(0)} = \frac{1}{2}\left[\left(M_P^2 + \left(\lambda_{11P} c_\beta^2 + \lambda_{22P} s_\beta^2\right) v^2\right) s_\theta^2 + \mu_{12P} s_{2\theta} v - \left(\lambda_5 v^2 + \frac{2M_{12}^2}{s_{2\beta}}\right) c_\theta^2\right] \tag{B.77}$$

$$\lambda_{1,1}^{(0)} = -\left(\frac{\lambda_{11P} c_\beta^2 + \lambda_{22P} s_\beta^2 + \lambda_5}{2} v^2 + \frac{M_2^2}{2} + \frac{M_{12}^2}{s_{2\beta}}\right) s_{2\theta} + \mu_{12P}\left(1 - 2c_\theta^2 v\right) v \tag{B.78}$$

$$\lambda_{0,2}^{(0)} = \frac{1}{2}\left[\left(M_P^2 + \left(\lambda_{11P} c_\beta^2 + \lambda_{22P} s_\beta^2\right) v^2\right) c_\theta^2 - \mu_{12P} s_{2\theta} v - \left(\lambda_5 v^2 + \frac{2M_{12}^2}{s_\theta^2}\right) s_\theta^2\right] \tag{B.79}$$

$$\lambda_{0,0}^{(3)} = \frac{\lambda_2 s_\beta^2 + \lambda_{345} c_\beta^2}{2} v \tag{B.80}$$

$$\lambda_{2,0}^{(1)} = \left(\lambda_{11P} c_\beta^2 + \lambda_{22P} s_\beta^2\right) s_\theta^2 v + \frac{\lambda_2 s_\beta^2 + \lambda_{345} c_\beta^2 - 2\lambda_5}{2} c_\theta^2 v + \frac{\mu_{12P}}{2} s_{2\theta} \tag{B.81}$$

$$\lambda_{1,1}^{(1)} = -\frac{1}{2}\left(2\left(\lambda_{11P} c_\beta^2 + \lambda_{22P} s_\beta^2\right) s_\theta^2 - \lambda_{345} c_\beta^2 - \lambda_2 s_\beta^2 + 2\lambda_5\right) s_{2\theta} v - \mu_{12P} c_{2\theta} \tag{B.82}$$

$$\lambda_{0,2}^{(1)} = \left(\lambda_{11P} c_\beta^2 + \lambda_{22P} s_\beta^2\right) c_\theta^2 v + \frac{\lambda_2 s_\beta^2 + \lambda_{345} c_\beta^2 - 2\lambda_5}{2} s_\theta^2 v - \frac{\mu_{12P}}{2} s_{2\theta} \tag{B.83}$$

$$\lambda_{0,0}^{(4)} = \frac{\lambda_{345} c_\beta^2 + \lambda_2 s_\beta^2}{8} \tag{B.84}$$

$$\lambda_{2,0}^{(2)} = \frac{1}{4}\left[\left(\lambda_2 s_\beta^2 + \lambda_{345} c_\beta^2 - 2\lambda_5\right) c_\theta^2 + 2\left(\lambda_{11P} c_\beta^2 + \lambda_{22P} s_\beta^2\right) s_\theta^2\right] \tag{B.85}$$

$$\lambda_{1,1}^{(2)} = -\frac{1}{4}\left[\left(2\lambda_{11P} - \lambda_{345}\right) c_\beta^2 + \left(2\lambda_{22P} - \lambda_2\right) s_\beta^2 + 2\lambda_5\right] s_{2\theta} \tag{B.86}$$

$$\lambda_{0,2}^{(2)} = \frac{1}{4}\left[\left(\lambda_2 s_\beta^2 + \lambda_{345} c_\beta^2 - 2\lambda_5\right) s_\theta^2 + 2\left(\lambda_{11P} c_\beta^2 + \lambda_{22P} s_\beta^2\right) c_\theta^2\right] \tag{B.87}$$

$$\lambda_{4,0}^{(0)} = \frac{1}{8}\left[\lambda_2 c_\beta^4 c_\theta^4 + 2\lambda_P s_\theta^4 + 2\left(\lambda_{345} c_\theta^2 s_\beta^2 + 2\lambda_{22P} s_\theta^2\right) c_\beta^2 c_\theta^2 \right.$$
$$\left. + s_\beta^2\left(\lambda_{11P} s_{2\theta}^2 + \left(\lambda_{345} c_{2\beta} + \lambda_2 s_\beta^2\right) c_\theta^4 t_\beta^2\right)\right] \tag{B.88}$$

$$\lambda_{3,1}^{(0)} = \frac{1}{4}\left[2\left(\lambda_1 s_\beta^4 + \lambda_2 c_\beta^4 + 2\lambda_{345} s_\beta^2 c_\beta^2\right) s_\theta c_\theta^3 - 4\lambda_P c_\theta s_\theta^3 - \left(\lambda_{11P} s_\beta^2 + \lambda_{22P} c_\beta^2\right) s_{4\theta}\right] \tag{B.89}$$

$$\lambda_{2,2}^{(0)} = \frac{1}{32}\left[4\lambda_{22P} c_\beta^2\left(1 + 3c_{4\theta}\right) + 24\lambda_2 s_\theta^2 c_\theta^2 c_\beta^4 + 3\left(4\lambda_P + \lambda_{345} s_{2\beta}^2\right) s_{2\theta}^2 \right.$$
$$\left. + 4s_\beta^2\left(\lambda_{11P}\left(1 + 3c_{4\theta}\right) + 6\left(\lambda_{345} c_{2\beta} + \lambda_2 s_\beta^2\right) c_\theta^2 s_\theta^2 t_\beta^2\right)\right] \tag{B.90}$$

$$\lambda_{1,3}^{(0)} = \frac{1}{4}\left[2\left(\lambda_1 s_\beta^4 + \lambda_2 c_\beta^4 + 2\lambda_{345} s_\beta^2 c_\beta^2\right) c_\theta s_\theta^3 - 4\lambda_P s_\theta c_\theta^3 + \left(\lambda_{11P} s_\beta^2 + \lambda_{22P} c_\beta^2\right) s_{4\theta}\right] \tag{B.91}$$

$$\lambda_{0,4}^{(0)} = \frac{1}{8}\left[\lambda_2 c_\beta^4 c_\theta^4 + 2\lambda_P c_\theta^4 + 2\left(\lambda_{345} s_\theta^2 s_\beta^2 + 2\lambda_{22P} c_\theta^2\right) c_\beta^2 s_\theta^2 \right.$$
$$\left. + s_\beta^2\left(\lambda_{11P} s_{2\theta}^2 + \left(\lambda_{345} c_{2\beta} + \lambda_2 s_\beta^2\right) s_\theta^4 t_\beta^2\right)\right] \tag{B.92}$$

$$(c_u)_{1,0}^{(0)} = - (c_{d,\ell})_{1,0}^{(0)} = -c_\theta \epsilon_{d,\ell}/v \tag{B.93}$$

$$(c_u)_{0,1}^{(0)} = - (c_{d,\ell})_{0,1}^{(0)} = -s_\theta \epsilon_{d,\ell}/v \tag{B.94}$$

$$y_{1,0}^{(0)} = -y_{\chi P} s_\theta \tag{B.95}$$

$$y_{0,1}^{(0)} = y_{\chi P} c_\theta \tag{B.96}$$

$$\kappa_{0,0}^{(1)} = 2/v \tag{B.97}$$

$$\kappa_{0,0}^{(2)} = 1/v^2 \tag{B.98}$$

$$\kappa_{2,0}^{(0)} = c_\theta^2/v^2 \tag{B.99}$$

$$\kappa_{1,1}^{(0)} = s_{2\theta}^2/v^2 \tag{B.100}$$

$$\kappa_{0,2}^{(0)} = s_\theta^2/v^2 \tag{B.101}$$

Appendix C

Constraints for UV Models

This appendix is dedicated to present the theoretical and experimental constraints that need to be taken into account for a detailed analysis of the UV models presented in Section 3.3. Note that the purpose of Section 3.3 is the comparison of the eDMEFT to several UV models of different complexity and *not* a full analysis of the UV models. Hence, the lists of constraints in this appendix is not meant to be complete but can be understood as a first attempt of finding open parameter space.

C.1 SM + Complex Scalar Singlet + Fermionic Singlets

Vacuum stability

The leading terms of the potential in Eq. (3.15) can be written as

$$-\mathcal{L} \supset \frac{\lambda_\Phi}{4}\left(h^2 + \frac{\lambda_{\Phi S}}{2\lambda_\Phi}s^2\right)^2 + \frac{4\lambda_\Phi^2\lambda_S - \lambda_{\Phi S}^2\lambda_\Phi}{16\lambda_\Phi^2}s^4 + \lambda_\Phi v h^3 + \lambda_S v s^3\,. \qquad \text{(C.1)}$$

Imposing the intuitive condition on the potential to be bounded from below leads to the constraints

$$\lambda_\Phi > 0 \quad , \quad 4\lambda_\Phi\lambda_S > \lambda_{\Phi S}^2\,. \qquad \text{(C.2)}$$

The last condition stems from the possibility that the s^4 term from the squared parentheses in Eq. (C.1) becomes zero for $s^2 = -2h^2\lambda_\Phi/\lambda_{\Phi S}$ in spite of the positive quartic coupling λ_Φ. Note that $\lambda_S > 0$ is always fulfilled by the constraints in Eq. (C.2).

Invisible Higgs decay

The measurements of the SM Higgs decay width, summarized in Eq. (1.15), result in the branching ratio $\mathrm{BR}\left(h \to \mathrm{inv.}\right) < 0.107$ [373] for the SM Higgs boson decaying into BSM particles. The corresponding partial decay width reads

$$\Gamma_h^{\mathrm{BSM}} = \sum_\phi \Gamma\left(h \to \phi\phi\right) = \sum_\phi \frac{|g_{h\phi\phi}|^2}{32\pi m_h} \sqrt{1 - \frac{4m_\phi^2}{m_h^2}} \tag{C.3}$$

with the kinematically accessible scalars $\phi = s, a$ in the final state. Note that the Higgs decay $h \to as$ is prohibited in this model by the unbroken CP symmetry in the scalar sector and $h \to \chi\chi$ is kinematically forbidden. The couplings are given by

$$g_{hss} = \lambda_{\Phi S}\left(c_\theta^3 v_h + s_\theta^3 v_s\right) - s_{2\theta}\lambda_{\Phi S}\left(v_s c_\theta + v_h s_\theta\right) + 3s_{2\theta}\left(\lambda_S v_s c_\theta + \lambda_\Phi v_h s_\theta\right) \tag{C.4}$$

$$g_{haa} = 2\lambda_S s_\theta v_s + c_\theta \lambda_{\Phi S} v_h \,. \tag{C.5}$$

Perturbativity and perturbative unitarity

Perturbative unitarity restricts the couplings in two-to-two interactions between scalars, scalar and gauge bosons, and only gauge bosons both in the initial and in the final state. Following the discussion in the appendix of Ref. [374], the general expression of the scattering amplitude

$$\mathcal{M}^{(ab)} = 16\pi i \sum_{J \geq 0} \left(2J + 1\right) a_J^{(ab)}\left(s\right) P_J\left(\cos\theta\right) \tag{C.6}$$

with the indices a, b for the initial and final states, respectively, the Legendre polynomials P_J and the scattering angle θ simplifies in the high-energy limit, such that

$$a_0^{(ab)} = -\frac{i}{16\pi}\mathcal{M}^{(ab)} \quad \text{and} \quad a_J^{(ab)} = 0 \quad \forall J \geq 1\,. \tag{C.7}$$

The states for the different electric charges Q read

$$Q = 2: \quad \left(G^+ G^+ / \sqrt{2}\right) \tag{C.8}$$

$$Q = 1: \quad \left(G^+ h\right), \left(G^+ G^0\right), \left(G^+ s\right), \left(G^+ a\right) \tag{C.9}$$

$$Q = 0: \quad \left(G^+ G^-\right), \left(G^0 G^0 / \sqrt{2}\right), \left(hh/\sqrt{2}\right), \left(ss/\sqrt{2}\right), \left(aa/\sqrt{2}\right),$$
$$\left(hG^0\right), (hs), (ha), \left(G^0 s\right), \left(G^0 a\right), (sa) \tag{C.10}$$

and the Hermitian scattering matrices $\mathcal{M}_Q$ are given by

$$\mathcal{M}_2 = \mathrm{diag}\left(2\lambda_\Phi\right) \tag{C.11}$$

$$\mathcal{M}_1 = \mathrm{diag}\left(2\lambda_\Phi, 2\lambda_\Phi, \lambda_{\Phi S}, \lambda_{\Phi S}\right) \tag{C.12}$$

$$\mathcal{M}_0 = \mathrm{diag}\left(A_{5\times5}, 2\lambda_\Phi, \lambda_{\Phi S}, \lambda_{\Phi S}, \lambda_{\Phi S}, \lambda_{\Phi S}, 2\lambda_{\Phi S}\right) \tag{C.13}$$

with the symmetric submatrix

$$A_{5\times5} = \begin{pmatrix} 4\lambda_\Phi & \times & \times & \times & \times \\ \sqrt{2}\lambda_\Phi & 3\lambda_\Phi & \times & \times & \times \\ \sqrt{2}\lambda_\Phi & \lambda_\Phi & 3\lambda_\Phi & \times & \times \\ \lambda_{\Phi S}/\sqrt{2} & \lambda_{\Phi S}/2 & \lambda_{\Phi S}/2 & 3\lambda_S & \times \\ \lambda_{\Phi S}/\sqrt{2} & \lambda_{\Phi S}/2 & \lambda_{\Phi S}/2 & \lambda_S & 3\lambda_S \end{pmatrix} . \tag{C.14}$$

Determining the (trivial) eigenvalues of the scattering matrices $\mathcal{M}_Q$ leads to the constraints for perturbative unitarity by requiring $|\mathrm{Re}\, a_0^{(ab)}| \leq 1/2$.

C.2   2HDM + Pseudoscalar + Fermionic DM

Perturbativity and perturbative unitarity

The results for this section can be found in Refs. [155, 375–377]. Demanding that the eigenvalues of the scattering matrix are bounded from above to preserve perturbative unitarity, the constraints read

$$|\lambda_{11P}|\,,\,|\lambda_{22P}|\,,\,|\lambda_3 \pm \lambda_4|\,,\,\frac{1}{2}|\lambda_3 \pm \lambda_5|\,,\,\frac{1}{2}|\lambda_3 + 2\lambda_4 \pm 3\lambda_5| < 4\pi \tag{C.15}$$

$$\left|\frac{1}{2}\left(\lambda_1 + \lambda_2 \pm \sqrt{(\lambda_1 - \lambda_2)^2 + 4\lambda_{4,5}^2}\right)\right|\,,\,|x_j| < 8\pi \tag{C.16}$$

with x_j being the three solutions of the equation

$$\begin{aligned} 0 = {} & x^3 - 3\left(\lambda_P + \lambda_1 + \lambda_2\right)x^2 \\ & + \left[9\left(\lambda_1 + \lambda_2\right)\lambda_P - 4\left(\lambda_{11P}^2 + \lambda_{22P}^2 + \lambda_3^2 + \lambda_3\lambda_4\right) - \lambda_4^2 + 9\lambda_1\lambda_2\right]x \\ & + 12\left(\lambda_{11P}^2\lambda_2 + \lambda_{22P}^2\lambda_1\right) - 8\lambda_{11P}\lambda_{22P}\left(2\lambda_3 + \lambda_4\right) \\ & + 3\lambda_P\left(-9\lambda_1\lambda_2 + 4\lambda_3^2 + 4\lambda_3\lambda_4 + \lambda_4^2\right) . \end{aligned} \tag{C.17}$$

Vacuum stability

Adopting the results from Ref. [378], the constraints form vacuum stability are given by

$$\lambda_{1,2,P} > 0 \,, \ \overline{\lambda}_{12} \equiv \lambda_3 + \sqrt{\lambda_1 \lambda_2} + \min\left(0, \lambda_4 - |\lambda_5|\right) > 0 \,, \ \overline{\lambda}_{jP} \equiv \sqrt{\frac{\lambda_j \lambda_P}{2}} + \lambda_{jjP} > 0$$

$$\sqrt{\frac{\lambda_1 \lambda_2 \lambda_P}{2}} + \lambda_{11P}\sqrt{\lambda_2} + \lambda_{22P}\sqrt{\lambda_1} + \left(\overline{\lambda}_{12} - \sqrt{\lambda_1 \lambda_2}\right)\sqrt{\frac{\lambda_P}{2}} + \sqrt{2\overline{\lambda}_{12}\overline{\lambda}_{1P}\overline{\lambda}_{2P}} > 0 \tag{C.18}$$

with $j = 1, 2$. Moreover, as discussed in Ref. [155], the coupling parameter λ_3 is bounded from below for the hierarchy $m_A \gg m_a$ by

$$\lambda_3 > \frac{m_A^2 - m_a^2}{v^2}\sin^2\theta - \frac{m_h^2}{v^2}\cot^2 2\beta \,, \tag{C.19}$$

which restricts the eigenvalues of the scattering amplitude matrix for this hierarchy to fulfill [379]

$$\frac{1}{v^2}\left| \Delta - \frac{m_A^2 - m_a^2}{8}\left(1 - \cos 4\theta\right) \pm \sqrt{\Delta^2 + \frac{\left(m_A^2 - m_a^2\right)^2}{8}\left(1 - \cos 4\theta\right)} \right| < 8\pi \tag{C.20}$$

with the short-hand notation

$$\Delta \equiv -\frac{2m_{12}^2}{\sin 2\beta} - m_{H^\pm}^2 - \frac{m_h^2}{2} + 2m_W^2 \,. \tag{C.21}$$

Invisible Higgs decay

The partial decay widths

$$\Gamma\left(h \to AA\right) = \frac{|g_{hAA}|^2}{32\pi m_h}\sqrt{1 - \frac{4m_A^2}{m_h^2}} \tag{C.22}$$

$$\Gamma\left(h \to aA\right) = \frac{|g_{haA}|^2}{16\pi m_h^3}\sqrt{\left(m_h^2 - (m_a - m_A)^2\right)\left(m_h^2 - (m_a + m_A)^2\right)} \tag{C.23}$$

$$\Gamma\left(h \to aa\right) = \frac{|g_{haa}|^2}{32\pi m_h}\sqrt{1 - \frac{4m_a^2}{m_h^2}} \tag{C.24}$$

with the couplings

$$g_{hAA} = \frac{m_h^2 + 4m_{H^\pm}^2 - 2m_A^2 - 2m_H^2 - 2\lambda_3 v^2}{v} c_\theta^2 - 2\left(\lambda_{11P}c_\beta^2 + \lambda_{22P}s_\beta^2\right) s_\theta^2 v \qquad (C.25)$$

$$g_{haH} = \frac{s_{2\theta}}{2v}\left(m_h^2 + 4m_{H^\pm}^2 - 2m_H^2 - m_A^2 - m_a^2 \right.$$
$$\left. + \left(\lambda_{11P} - \lambda_{22P}\right)c_{2\beta}v^2 + \left(\lambda_{11P} + \lambda_{22P} - 2\lambda_3\right)v^2\right) \qquad (C.26)$$

$$g_{haa} = \frac{2m_a^2 + 2m_H^2 - 4m_{H^\pm}^2 - m_h^2 + 2\lambda_3 v^2}{v} s_\theta^2 + 2\left(\lambda_{11P}c_\beta^2 + \lambda_{22P}s_\beta^2\right) c_\theta^2 v. \qquad (C.27)$$

B physics observables

Measurements of branching ratios of B mesons put strong constraints on the mass of the electrically charged scalar. The results in 2018 presented by the Heavy Flavor Averaging Group show $\mathrm{BR}\left(b \to s\gamma\right) = (3.32 \pm 0.15) \times 10^{-4}$ [380] which excludes masses $m_{H^\pm} \lesssim 800\,\mathrm{GeV}$ [381].[1]

Electroweak precision tests

The precise measurements of the masses of the massive EW gauge bosons allow to constrain new-physics contributions. The contribution to the ρ parameter is given by

$$\Delta\rho = \frac{\alpha_{\mathrm{QED}}\left(m_Z^2\right)}{16\pi^2 m_W^2 \left(1 - m_W^2/m_Z^2\right)} \left[f\left(m_{H^\pm}^2, m_H^2\right) + c_\theta^2 \left(f\left(m_{H^\pm}^2, m_A^2\right) - f\left(m_A^2, m_H^2\right)\right)\right.$$
$$\left. + s_\theta^2 \left(f\left(m_{H^\pm}^2, m_P^2\right) - f\left(m_P^2, m_H^2\right)\right)\right] \qquad (C.28)$$

with the function $f\left(x, y\right) = x + y - \frac{2xy}{x-y}\log\frac{x}{y}$.

Further constraints are those on the Peskin-Takeuchi parameters which are given by the central values with SM parameters (see Ref. [383] and references therein)

$$\mathcal{O}^{\mathrm{SM}} \equiv (S, T, U)^{\mathrm{SM}} = (0.04, 0.09, -0.02) \qquad (C.29)$$

and the experimentally allowed range is dictated by

$$\chi^2 = \sum_{i,j} \left(\mathcal{O}_i - \mathcal{O}_i^{\mathrm{SM}}\right) \left(\sigma_i V_{ij} \sigma_j\right)^{-1} \left(\mathcal{O}_j - \mathcal{O}_j^{\mathrm{SM}}\right) \qquad (C.30)$$

---

[1]The author of this thesis is aware of the latest measurement [51] of the branching ratio which suggests a slightly larger value with a larger uncertainty. Consequently, the lower bound on possible $m_{H^\pm}$ is reduced, as discussed in Ref. [382]. In the present analysis we keep the stronger constraint.

with the standard deviation and symmetric covariance matrix

$$\sigma = (0.11, 0.14, 0.11) \quad , \quad V = \begin{pmatrix} 1 & \times & \times \\ 0.92 & 1 & \times \\ -0.68 & -0.87 & 1 \end{pmatrix} . \tag{C.31}$$

The mass differences between the fields from the singlet and second doublet affect the Peskin-Takeuchi parameters. In the alignment limit they can be written as [383–385]

$$\mathcal{O}_1 \equiv S = -\frac{1}{4\pi} \left[g\left(m_{H^\pm}^2, m_{H^\pm}^2\right) - c_\theta^2 g\left(m_H^2, m_A^2\right) - s_\theta^2 g\left(m_H^2, m_a^2\right) \right] \tag{C.32}$$

$$\mathcal{O}_2 \equiv T = \frac{\Delta\rho}{\alpha_{\text{QED}}} \tag{C.33}$$

$$\mathcal{O}_3 \equiv U = -\frac{1}{4\pi} \left[g\left(m_{H^\pm}^2, m_{H^\pm}^2\right) + c_\theta^2 g\left(m_H^2, m_A^2\right) + s_\theta^2 g\left(m_H^2, m_a^2\right) \right.$$
$$\left. - g\left(m_{H^\pm}^2, m_H^2\right) - c_\theta^2 g\left(m_{H^\pm}^2, m_A^2\right) - s_\theta^2 g\left(m_{H^\pm}^2, m_a^2\right) \right] \tag{C.34}$$

with the function

$$g(x, y) = -\frac{1}{3} \left(\frac{4}{3} - \frac{x \log x - y \log y}{x - y} - \frac{x + y}{(x - y)^2} f(x, y) \right) . \tag{C.35}$$

The dependence of the maximally possible mass splitting between the new-physics scale Λ and the pseudoscalar A on the scale Λ is shown in Fig. C.1.
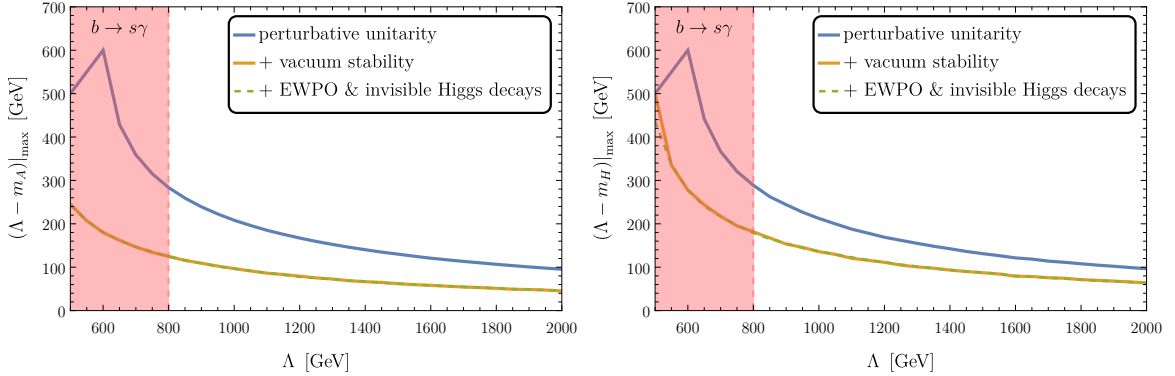
Figure C.1: Maximum mass splitting between doublet scalars and the doublet pseudoscalar with respect to the new-physics scale Λ in the presence of different constraints. The electrically charged scalar resides at the new-physics scale and the two scenarios differ from each other by $m_H = \Lambda$ (*left*) and $m_A = \Lambda$ (*right*). The mass of the singlet pseudoscalar is restricted to $m_a < m_A$.

Appendix D

Calculation of the Lepton EDM

In this appendix we shall present the full calculation of the ℓEDM for the SMEFT and IDMEFT operators. This follows the presentation in our publication [3] very closely.

The low-energy effective operator for the ℓEDM is given by

$$\mathcal{L}_{\text{eff}}^{\ell\text{EDM}} = -\frac{i}{2} d_\ell \, \overline{\ell} \sigma^{\mu\nu} \gamma^5 \ell F_{\mu\nu} = -\frac{i}{2} d_\ell \left(\overline{\ell_L} \sigma^{\mu\nu} \ell_R - \overline{\ell_R} \sigma^{\mu\nu} \ell_L \right) F_{\mu\nu} \tag{D.1}$$

with $\sigma^{\mu\nu} \equiv i\left[\gamma^\mu, \gamma^\nu\right]/2$, the electromagnetic field strength tensor $F_{\mu\nu} = \partial_\mu A_\nu - \partial_\nu A_\mu$, and the usual chiral projections $\ell_{L,R} \equiv (1 \mp \gamma^5)/2\,\ell$ of the lepton ℓ (*cf.* Refs. [210, 212]).

As we shall see below, we will evaluate the loop integrals by following the dimensional regularization scheme. This, however, affects the anti-commutation properties of the γ^5 matrix in general. Here we deploy the 'naive dimensional regularization scheme' [210, 386, 387] in which these anti-commutation properties are unchanged for any number of space-time dimensions. The γ^5 matrix can be written in terms of the other γ^μ matrices and the Levi-Civita symbol $\varepsilon^{\mu\nu\rho\sigma}$ as $\gamma^5 \equiv -i\varepsilon^{\mu\nu\rho\sigma}\gamma_\mu\gamma_\nu\gamma_\rho\gamma_\sigma/4!$ with $\varepsilon^{0123} = 1$.

In the remainder we consider a lepton with mass m_ℓ, electric charge Q_ℓ in units of the elementary charge e, incoming momentum p_1, and outgoing momentum k_1, as well as an incoming photon with momentum p_2.

D.1   SM Effective Operator

The tree-level interaction between the photon and the lepton does not induce a chirality flip of the latter and hence not contribute to the ℓEDM due to the structure of the operator in Eq. (D.1). At leading order in perturbation theory the SMEFT operator connects the incoming photon via a loop (including SM Higgs boson h and either

a photon γ or a Z boson) with the lepton. The process is depicted in Fig. D.1. Taking different coefficients for the terms into account, *i.e.* $\tilde{c}_{hW} \neq \tilde{c}_{hB}$ in general, the SMEFT operator becomes

$$\mathcal{L} \supset |\Phi_1|^2 \left(\tilde{c}_{hW} W^I_{\mu\nu} \widetilde{W}^{I\mu\nu} + \tilde{c}_{hB} B_{\mu\nu} \widetilde{B}^{\mu\nu} \right) \tag{D.2}$$

$$\supset 2\varepsilon^{\mu\nu\rho\sigma} v h \partial_\mu A_\nu [\underbrace{\left(\tilde{c}_{hW} \sin^2\theta_W + \tilde{c}_{hB} \cos^2\theta_W \right)}_{\equiv \tilde{c}_\gamma} \partial_\rho A_\sigma + \underbrace{\left(\tilde{c}_{hW} - \tilde{c}_{hB} \right)}_{\equiv \tilde{c}_Z} \sin 2\theta_W \partial_\rho Z_\sigma] \tag{D.3}$$

and gives rise to the two Feynman diagrams.

Let us first focus on the left-hand Feynman diagram in Fig. D.1 with a mediating photon and one specific chirality configuration. The matrix element is given by

$$i\mathcal{M}_\gamma = 4 m_\ell Q_\ell e \, \tilde{c}_\gamma \, \overline{u_L}(k_1) \int \frac{\mathrm{d}^d q}{(2\pi)^d} \frac{\left(\slashed{p}_1 - \slashed{q} + m_\ell \right) \gamma_\beta q_\alpha \varepsilon^{\alpha\beta\kappa\nu} p_{2,\kappa} \epsilon_\nu(p_2)}{\left[(q + p_2)^2 - m_h^2 \right] q^2 \left[(q - p_1)^2 - m_\ell^2 \right]} u_R(p_1) . \tag{D.4}$$

Deploying the identity $\gamma_\lambda \gamma_\beta = \left(\{\gamma_\lambda, \gamma_\beta\} + [\gamma_\lambda, \gamma_\beta] \right)/2 = g_{\lambda\beta} - i\sigma_{\lambda\beta}$, omitting the term proportional to the lepton mass (and thus suppressed) in the numerator, and introducing the short-hand notation $\Xi_{a,b} \equiv (q + a)^2 - b^2$ for the factors in the denominator from the propagators allow us to rephrase the matrix element as

$$i\mathcal{M}_\gamma \supset 4 m_\ell Q_\ell e \, \tilde{c}_\gamma \, \overline{u_L}(k_1) \int_q \frac{(p_1 - q)^\lambda q_\alpha}{\Xi_{p_2,m_h} \Xi_{0,0} \Xi_{-p_1,m_\ell}} \left(g_{\lambda\beta} - i\sigma_{\lambda\beta} \right) \varepsilon^{\alpha\beta\kappa\nu} u_R(p_1) p_{2,\kappa} \epsilon_\nu(p_2) . \tag{D.5}$$
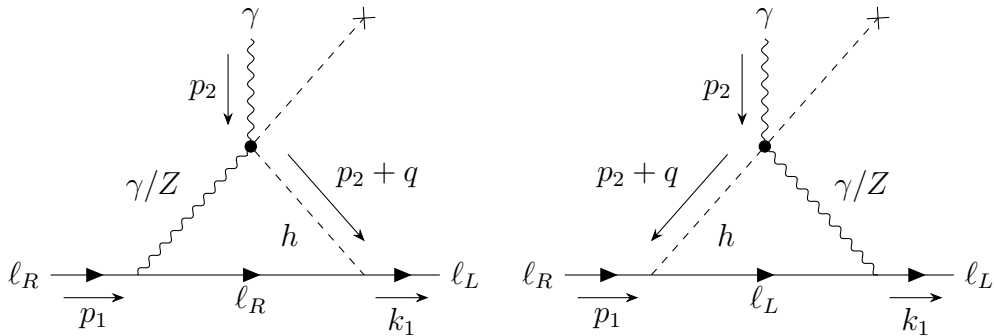
Figure D.1: Feynman diagrams for processes contributing to d_ℓ, including the momentum flow. The dotted vertices correspond to insertions of the $D = 6$ operator and a cross attached to a dashed line indicates the SM Higgs vev entering the vertex factor. The right panel shows the respective 'mirrored' diagram.

As we shall see later, the metric term does not contribute due to the anti-symmetry of the Levi-Civita tensor. Since the integral in Eq. (D.5) will appear frequently in the following calculation, we present its evaluation here once. Introducing the Feynman parameters x, y, z and including $\delta\left(x + y + z - 1\right)$ in the integral measure for the sake of conciseness lead to

$$\int_q \frac{(p_1 - q)^\lambda q_\alpha}{\Xi_{p_2, m_h} \Xi_{0,0} \Xi_{-p_1, m_\ell}} = 2 \int_{x,y,z} \int_{\tilde{q}} \frac{\Theta_\alpha^\lambda}{(\tilde{q}^2 - \Delta)^3} \tag{D.6}$$

with $\Theta_\alpha^\lambda \equiv \left((1 - y) p_1 - \tilde{q} + x p_2\right)^\lambda \left(\tilde{q} - x p_2 + y p_1\right)_\alpha$. Employing $p_1^2 = k_1^2 = m_\ell^2$ and $p_2^2 = 0$, the shifted momentum $\tilde{q}$ and momentum-independent remnant Δ read

$$\tilde{q} \equiv q + x p_2 - y p_1 \quad , \quad \Delta \equiv x m_h^2 + y^2 m_\ell^2 \ . \tag{D.7}$$

Since the denominator of the integrand is symmetric with respect to the integration momentum $\tilde{q}$ upon sign flip, terms in the numerator which are linear in $\tilde{q}$ vanish after integration and only those terms containing either the product $\tilde{q}^\lambda \tilde{q}_\alpha$ or a $\tilde{q}$-independent numerator remain. After a Wick rotation to Euclidean spacetime, the former leads via dimensional regularization to

$$I_\alpha^\lambda \overset{\text{def}}{=} \mu^{2\epsilon} \int \frac{\mathrm{d}^d \tilde{q}}{(2\pi)^d} \frac{-\tilde{q}^\lambda \tilde{q}_\alpha}{(\tilde{q}^2 - \Delta)^3} = -i \frac{\mu^{2\epsilon}}{d} \int \frac{\mathrm{d}^d \tilde{q}_E}{(2\pi)^d} \frac{\tilde{q}_E^2 g_\alpha^\lambda}{(\tilde{q}_E^2 + \Delta)^3} = \frac{-i g_\alpha^\lambda \Gamma(\epsilon)}{4 (4\pi)^{d/2}} \left(\frac{\mu^2}{\Delta}\right)^\epsilon \tag{D.8}$$

in $d = 4 - 2\epsilon$ spacetime dimensions. The latter ($\tilde{q}$-independent numerator), on the other hand, becomes

$$I_0 \overset{\text{def}}{=} -i \mu^{2\epsilon} \int \frac{\mathrm{d}^d \tilde{q}_E}{(2\pi)^d} \frac{C_\alpha^\lambda(x, y)}{(\tilde{q}_E^2 + \Delta)^3} = -i \mu^{2\epsilon} \frac{C_\alpha^\lambda(x, y)}{(4\pi)^{d/2}} \frac{\Gamma(1 + \epsilon)}{\Gamma(3) \Delta^{1+\epsilon}} \tag{D.9}$$

with $C_\alpha^\lambda(x, y) \equiv \left((1 - y) p_1 + x p_2\right)^\lambda \left(y p_1 - x p_2\right)_\alpha$. Considering only the $\tilde{q}$-dependent numerator in the integrand, as the contributions from I_0 are further suppressed in $m_\ell^2 / m_h^2 \ll 1$, one gets in the $\overline{\text{MS}}$ renormalization scheme

$$i\mathcal{M}_\gamma \supset 8 m_\ell Q_\ell e\, \tilde{c}_\gamma\, \overline{u_L}(k_1) \int_{x,y,z} I_\alpha^\lambda \left(g_{\lambda\beta} - i\sigma_{\lambda\beta}\right) \varepsilon^{\alpha\beta\kappa\nu} u_R(p_1) p_{2,\kappa} \epsilon_\nu(p_2)$$

$$= -\frac{m_\ell Q_\ell e \tilde{c}_\gamma}{8\pi^2} \int_{x,y,z} \log \frac{\mu^2}{\Delta}\, \overline{u_L}(k_1) \sigma_{\alpha\beta} \varepsilon^{\alpha\beta\kappa\nu} u_R(p_1) p_{2,\kappa} \epsilon_\nu(p_2) + \mathcal{O}(\varepsilon) \ . \tag{D.10}$$

APPENDIX D. CALCULATION OF THE LEPTON EDM

In practice, the divergence and constant term arising from the dimensional regularization are absorbed by the SMEFT counterterm operator $\overline{\ell_L}\sigma^{\mu\nu}\Phi_1 e_R \left(B_{\mu\nu} + \sigma^I/2\, W^I_{\mu\nu} \right)$ with the Pauli matrices σ^a. Alternatively, one could just cut off the loop integral at the new-physics scale.

Owing to the identities

$$\varepsilon^{\alpha\beta\kappa\nu}\sigma_{\alpha\beta} \equiv -2i\gamma^5\sigma^{\kappa\nu}, \quad \left[\gamma^5, \sigma^{\kappa\nu}\right] = 0 \, , \tag{D.11}$$

$$\sigma^{\mu\nu}F_{\mu\nu} = \frac{i}{2}\left[\gamma^\mu, \gamma^\nu\right](\partial_\mu A_\nu - \partial_\nu A_\mu) = 2\sigma^{\mu\nu}\partial_\mu A_\nu \, , \tag{D.12}$$

the EDM parameter $d_\ell^{(1)}$ for the first diagram can now be extracted from the matrix element as

$$i\mathcal{M}_\gamma \supset \underbrace{-\frac{m_\ell Q_\ell e \tilde{c}_\gamma}{4\pi^2}\int_{x,y,z}\log\frac{\mu^2}{\Delta}}_{=d_\ell^{(1)} \text{ from Eq. (D.1)}}\overline{u_L}(k_1)\sigma^{\kappa\nu}\underbrace{\gamma^5 u_R(p_1)}_{=u_R(p_1)}(-ip_{2,\kappa})\,\epsilon_\nu(p_2)\, , \tag{D.13}$$

and reads

$$\left(\frac{d_\ell^{(1)}}{e}\right)_\gamma = -\frac{m_\ell Q_\ell \tilde{c}_\gamma}{4\pi^2}\int_0^1 \mathrm{d}x \int_0^{1-x} \mathrm{d}y \,\, \log\frac{\mu^2}{xm_h^2 + y^2 m_\ell^2}\, . \tag{D.14}$$

The contribution $d_\ell^{(2)}$ of the 'mirrored' diagram (see right-hand diagram in Fig. D.1) is equal to the first one. Hence, expanding in $m_\ell \ll m_h$ eventually gives rise to the ℓEDM for the photon-mediated processes, reading

$$\left(\frac{d_\ell}{e}\right)_\gamma = \left(\frac{d_\ell^{(1)}}{e}\right)_\gamma + \left(\frac{d_\ell^{(2)}}{e}\right)_\gamma = -m_\ell Q_\ell\left(\frac{3}{8\pi^2} + \frac{1}{2\pi^2}\log\frac{\mu}{m_h}\right)\tilde{c}_\gamma\, . \tag{D.15}$$

Next, we consider the process mediated by a Z boson that couples to the RH lepton. The matrix element reads

$$i\mathcal{M}_Z = 2m_\ell \frac{gc_R}{\cos\theta_W}\tilde{c}_Z \sin 2\theta_W \int_q \frac{\overline{u_L}(k_1)\left(\slashed{p}_1 - \slashed{q} + m_\ell\right)\gamma_\beta q_\alpha \varepsilon^{\alpha\beta\kappa\nu}u_R(p_1)\,p_{2,\kappa}\epsilon_\nu(p_2)}{\left[(q+p_2)^2 - m_h^2\right](q^2 - m_Z^2)\left[(q-p_1)^2 - m_\ell^2\right]}$$

$$\supset \underbrace{-\frac{m_\ell c_R e \tilde{c}_Z}{4\pi^2}\int_{x,y,z}\log\frac{\mu^2}{xm_h^2 + zm_Z^2}}_{=d_\ell^{(1)} \text{ from Eq. (D.1)}}\overline{u_L}(k_1)\gamma^5\sigma^{\kappa\nu}u_R(p_1)(-ip_{2,\kappa})\,\epsilon_\nu(p_2)\, , \tag{D.16}$$

138

where we have, similar to the procedure above, introduced Feynman parameters, performed a Wick rotation, neglected the lepton mass, and taken the term proportional to the squared momentum in the integral into account (as shown explicitly above). Evaluating the integral for the massive mediator,

$$\int_0^1 dx \int_0^{1-x} dz \, \log \frac{\mu^2}{xm_h^2 + zm_Z^2} = \frac{3}{4} + \frac{m_Z^4 \log \frac{\mu^2}{m_Z^2} - 2m_h^2 m_Z^2 \log \frac{\mu^2}{m_Z m_h} + m_h^4 \log \frac{\mu^2}{m_h^2}}{2 \left(m_h^2 - m_Z^2\right)^2}$$

$$= \frac{3}{4} + \frac{\left(m_Z^2 - m_h^2\right)^2 \log \frac{\mu^2}{m_h^2} + 2m_Z^2 \left(m_Z^2 - m_h^2\right) \log \frac{m_h}{m_Z}}{2 \left(m_h^2 - m_Z^2\right)^2}$$

$$= \frac{3}{4} + \log \frac{\mu}{m_h} + \frac{m_Z^2}{m_Z^2 - m_h^2} \log \frac{m_h}{m_Z} \, , \tag{D.17}$$

and taking the 'mirrored' diagram into account, results in

$$\left(\frac{d_\ell}{e}\right)_Z = -m_\ell \left[\frac{c_L + c_R}{4\pi^2} \int_{x,y,z} \log \frac{\mu^2}{xm_h^2 + zm_Z^2}\right] \tilde{c}_Z$$

$$= -m_\ell \left[\frac{3 \left(T_{3,\ell} - 2Q_\ell \sin^2 \theta_W\right)}{16\pi^2} + \frac{T_{3,\ell} - 2Q_\ell \sin^2 \theta_W}{4\pi^2} \log \frac{\mu}{m_h}\right.$$

$$\left. + \frac{T_{3,\ell} - 2Q_\ell \sin^2 \theta_W}{4\pi^2} \frac{m_Z^2}{m_Z^2 - m_h^2} \log \frac{m_h}{m_Z}\right] \tilde{c}_Z \, , \tag{D.18}$$

where we have used $c_L + c_R = T_{3,\ell} - 2Q_\ell \sin^2 \theta_W$. Consequently, the full contribution to the ℓEDM ultimately reads

$$\frac{d_\ell}{e} = -m_\ell \left[\frac{3T_{3,\ell}}{16\pi^2} + \frac{T_{3,\ell}}{4\pi^2} \log \frac{\mu}{m_h} + \frac{\left(T_{3,\ell} - 2Q_\ell \sin^2 \theta_W\right) m_Z^2}{4\pi^2 \left(m_Z^2 - m_h^2\right)} \log \frac{m_h}{m_Z}\right] \tilde{c}_{hW} \tag{D.19a}$$

$$- m_\ell \left[\frac{3 \left(2Q_\ell - T_{3,\ell}\right)}{16\pi^2} + \frac{2Q_\ell - T_{3,\ell}}{4\pi^2} \log \frac{\mu}{m_h} - \frac{\left(T_{3,\ell} - 2Q_\ell \sin^2 \theta_W\right) m_Z^2}{4\pi^2 \left(m_Z^2 - m_h^2\right)} \log \frac{m_h}{m_Z}\right] \tilde{c}_{hB} \, . \tag{D.19b}$$

Taking degenerate Wilson coefficient, *i.e.* $\tilde{c}_{hB} = \tilde{c}_{hW} = \tilde{c}_1$, the ℓEDM results in

$$\frac{d_\ell}{e} = -\frac{m_\ell Q_\ell}{8\pi^2} \left(3 + 4\log\frac{\mu}{m_h} \right) \tilde{c}_1 \,, \tag{D.20}$$

which matches the finding in Ref. [210].

D.2 IDM Effective Operator

Similar to the SMEFT operator in Eq. (D.2), the IDMEFT provides CP-violating operators and hence contributes to ℓEDMs. The operators can be written as

$$\mathcal{L} \supset |\Phi_2|^2 \left(\tilde{c}_{HW} W_{\mu\nu}^I \widetilde{W}^{I\mu\nu} + \tilde{c}_{HB} B_{\mu\nu} \widetilde{B}^{\mu\nu} \right) \tag{D.21a}$$

$$\supset H^2 \partial_\mu A_\nu \left[\left(\tilde{c}_{HW} \sin^2\theta_W + \tilde{c}_{HB} \cos^2\theta_W \right) \partial_\rho A_\sigma + \left(\tilde{c}_{HW} - \tilde{c}_{HB} \right) \sin 2\theta_W \partial_\rho Z_\sigma \right] \varepsilon^{\mu\nu\rho\sigma} \,. \tag{D.21b}$$

As the inert Higgs doublet does not acquire a vev at $T \approx 0$, the contribution to the ℓEDM occurs at two-loop level for the first time: a loop with H, A, or $H^\pm$ connects the effective vertex to the SM Higgs boson. With the momenta specified in the left-hand diagram in Fig. D.2, the corresponding matrix element for a mediating photon and an H-loop reads

$$i\mathcal{M}_\gamma = \frac{4}{S} i m_\ell Q_\ell e \tilde{c}_\gamma' \lambda_{345} \, p_{2,\rho} \epsilon_\sigma \left(p_2 \right)$$

$$\times \underbrace{\int_{q_1} \frac{\overline{u_L}(k_1) \left(\slashed{p}_1 - \slashed{q}_1 + m_\ell \right) \gamma_\nu q_{1,\mu} \varepsilon^{\mu\nu\rho\sigma} u_R(p_1)}{\left[(p_1 - q_1)^2 - m_\ell^2 \right] \left[(q_1 + p_2)^2 - m_h^2 \right] q_1^2}}_{\overset{\text{def}}{=} \overline{u_L}(k_1) I_1^{\rho\sigma} u_R(p_1)} \underbrace{\int_{q_2} \frac{1}{\left[(q_1 - q_2 + p_2)^2 - m_H^2 \right] \left[q_2^2 - m_H^2 \right]}}_{\overset{\text{def}}{=} I_2} \tag{D.22}$$

with the symmetry factor $S = 2$ and the short-hand notation $\tilde{c}_\gamma' \equiv \tilde{c}_{HW} \sin^2\theta_W + \tilde{c}_{HB} \cos^2\theta_W$.

Introducing the Feynman parameter x_2 allows us to write the second integral as

$$I_2 = \int_{\tilde{q}_2} \int_{x_2} \frac{1}{\left(\tilde{q}_2^2 - \Delta_2 \right)^2} \tag{D.23}$$

with the shifted momentum $\tilde{q}_2 = q_2 - x_2 (q_1 + p_2)$ and $\Delta_2 = m_H^2 - x_2 (1 - x_2)(q_1 + p_2)^2$.

A Wick rotation leads to

$$I_2 = i \int_{x_2} \int_{\tilde{q}_{2,E}} \frac{1}{\left(\tilde{q}_{2,E}^2 + \Delta_2\right)^2} = i \frac{\Gamma(\epsilon)}{(4\pi)^{d/2}} \int_{x_2} \left(\frac{\mu^2}{\Delta_2}\right)^{\epsilon}. \tag{D.24}$$

The Feynman parameters y_1, z_1 for the first integral lead to

$$I_1^{\rho\sigma} I_2 = 2 \int_{y_1,z_1} \int_{\tilde{q}_1} \frac{\left[(1-y_1)\not{p}_1 - \not{\tilde{q}}_1 + z_1\not{p}_2 + m_\ell\right] \gamma_\nu \left(\tilde{q}_1 + y_1 p_1 - z_1 p_2\right)_\mu \varepsilon^{\mu\nu\rho\sigma}}{\left(\tilde{q}_1^2 - \Delta_1\right)^3} I_2(\tilde{q}_1) \tag{D.25}$$

with $\tilde{q}_1 = q_1 - y_1 p_1 + z_1 p_2$ and $\Delta_1 = z_1 m_h^2 + y_1^2 m_\ell^2$ for the product of two integrals. Analogously to the calculation in Section D.1, we shall keep only the leading term in the numerator which is quadratic in $\tilde{q}_1$ and thereby find

$$I_1^{\rho\sigma} I_2 \supset \frac{-2i\Gamma(\epsilon)}{(4\pi)^{d/2}} \iint_{\tilde{q}_1} \left(\frac{\mu^2}{m_H^2 - x_2(1-x_2)(\tilde{q}_1 + y_1 p_1 + (1-z_1)p_2)^2}\right)^{\epsilon} \frac{\tilde{q}_1^\lambda \tilde{q}_{1,\mu} \varepsilon^{\mu\nu\rho\sigma} \gamma_\lambda \gamma_\nu}{\left(\tilde{q}_1^2 - \Delta_1\right)^3} \tag{D.26}$$

with the first integral over the three Feynman parameters x_2, y_1, z_1. Assuming negligibly small ratios $p_{1,2}/m_H$ leads to

$$I_1^{\rho\sigma} I_2 \supset \frac{-2i\Gamma(\epsilon)}{(4\pi)^{d/2}} \left(\frac{\mu^2}{m_H^2}\right)^{\epsilon} \iint_{\tilde{q}_1} \left(1 - x_2(1-x_2)\frac{\tilde{q}_1^2}{m_H^2}\right)^{-\epsilon} \frac{\tilde{q}_1^\lambda \tilde{q}_{1,\mu} \varepsilon^{\mu\nu\rho\sigma} \gamma_\lambda \gamma_\nu}{\left(\tilde{q}_1^2 - \Delta_1\right)^3}. \tag{D.27}$$
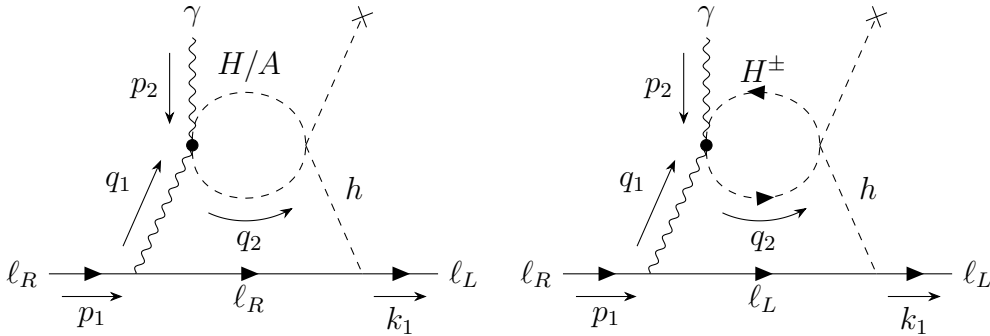
Figure D.2: Two-loop contribution to the ℓEDM from the BSM operator $|\Phi_2|^2 F_{\mu\nu}\widetilde{F}^{\mu\nu}$. The incoming vector boson is (by definition) a photon, but the internal one can be either a photon or a Z boson.

This integral can be simplified by

$$I_1^{\rho\sigma} I_2 = \frac{4i\Gamma\left(\epsilon\right)}{(4\pi)^{d/2} d} \left(\frac{\mu^2}{m_H^2}\right)^\epsilon \iint_{\tilde{q}_1} \left(1 - x_2\left(1 - x_2\right)\frac{\tilde{q}_1^2}{m_H^2}\right)^{-\epsilon} \frac{\tilde{q}_1^2}{\left(\tilde{q}_1^2 - \Delta_1\right)^3}\gamma^5\sigma^{\rho\sigma} \ , \quad \text{(D.28)}$$

where we applied the relation in Eq. (D.11). Evaluating this integral in Euclidean space results in

$$I_1^{\rho\sigma} I_2 \supset \int_{x_2,y_1,z_1} \left(\frac{-\frac{2}{\epsilon} + 3 + 4\gamma_E - 2\log\frac{16\pi^2\mu^4\Delta_1^2}{x_2(1-x_2)m_H^8}}{1024\pi^4\epsilon} + F(m_H) + \mathcal{O}\left(\epsilon\right)\right)\gamma^5\sigma^{\rho\sigma} \ .$$
$$\text{(D.29)}$$

The divergences can be eliminated by introducing the appropriate SMEFT counterterms $\overline{\ell_L}\sigma^{\mu\nu}\Phi_1 e_R \left(B_{\mu\nu} + \sigma^I/2\, W_{\mu\nu}^I\right) + \text{h.c.}$ as in the previous section, so that we can focus solely on the finite, mass-dependent part $F(m)$ of the integral. The resulting matrix element then reads

$$i\mathcal{M} \supset \underbrace{-\frac{4}{S}m_\ell Q_\ell e\tilde{c}_\gamma'\lambda_{345}\int_{x_2,y_1,z_1} F\left(m\right)}_{=d_\ell} \ \overline{u_L}\left(k_1\right)\gamma^5\sigma^{\mu\nu}u_R\left(p_1\right)\left(-ip_{2,\mu}\right)\epsilon_\nu\left(p_2\right) \quad \text{(D.30)}$$

with the IDMEFT Wilson coefficient $\tilde{c}_\gamma'$ defined at the scale m_H, while being agnostic about its nature. Note that we assume that the corrections induced by lepton masses are negligible, since they the leptons are substantially lighter than the scalars.

Taking the contributions of H, A, and $H^\pm$ into account, together with their respective symmetry factors ($S = 2$ for H, A; $S = 1$ for $H^\pm$), we find with degenerate BSM non-DM fields for the ℓEDM parameter

$$\frac{d_\ell}{e} = -2\left[\lambda_{345}\int F\left(m_H\right) + \left(\bar{\lambda}_{345} + \lambda_3\right)\int F\left(m_{A,H^\pm}\right)\right]m_\ell Q_\ell\tilde{c}_\gamma'$$

$$= -2m_\ell Q_\ell\tilde{c}_\gamma'\left(\lambda_{345}\int\left[F\left(m_H\right) + 2F\left(m_{A,H^\pm}\right)\right] + 4\frac{m_{A,H^\pm}^2 - m_H^2}{v^2}\int F\left(m_{A,H^\pm}\right)\right) \ .$$
$$\text{(D.31)}$$

As we chose $\tilde{c}_{HW} = \tilde{c}_{HB}$ for simplicity, where the Z contribution to the ℓEDM vanishes, we do not derive the Z contribution in the IDMEFT. Considering the parameters $\mu = m_H = 71\,\text{GeV}$, the degenerate non-DM masses $m_{A,H^\pm} = 481\,\text{GeV}$, $\lambda_{345} = -0.002$,

and the Wilson coefficient $\tilde{c}_2 \equiv \tilde{c}'_\gamma = 25\,\mathrm{PeV}^{-2}$, we find after numerical integration

$$\left|\frac{d_\ell}{e}\right|_{\mu=m_H} \approx \begin{cases} 6.7 \cdot 10^{-17}\,\mathrm{GeV}^{-1} \text{ for } \ell = e \\ 1.4 \cdot 10^{-14}\,\mathrm{GeV}^{-1} \text{ for } \ell = \mu \\ 2.3 \cdot 10^{-13}\,\mathrm{GeV}^{-1} \text{ for } \ell = \tau \end{cases} , \tag{D.32}$$

and running the ℓEDM parameter down to $\mu = m_\ell$ results in

$$\left|\frac{d_\ell}{e}\right|_{\mu=m_\ell} \approx \begin{cases} 5.9 \cdot 10^{-17}\,\mathrm{GeV}^{-1} \text{ for } \ell = e \\ 1.3 \cdot 10^{-14}\,\mathrm{GeV}^{-1} \text{ for } \ell = \mu \\ 2.2 \cdot 10^{-13}\,\mathrm{GeV}^{-1} \text{ for } \ell = \tau \end{cases} . \tag{D.33}$$

These results for the ℓEDM induces by the IDMEFT operators are to be compared to the experimental limits.

Appendix E

Analytical Expressions for Neutrino Mass Models

Here we provide a few analytical formulae for the type-II seesaw model as well as the Zee-Babu model.

E.1 Type-II Seesaw Model

Calculating the derivatives of the potential in Eq. (5.19), *i.e.*

$$\frac{\partial V}{\partial h}\bigg|_{\text{min}} = \lambda_\Phi v_\Phi^3 + \mu_\Phi^2 v_\Phi + \frac{(1 + \kappa_{\Phi\Delta})\,\lambda_{\Phi\Delta}v_\Delta - 2\sqrt{2}\mu_{\Phi\Delta}}{2}v_\Phi v_\Delta \overset{!}{=} 0 \tag{E.1}$$

$$\frac{\partial V}{\partial \Delta_R^0}\bigg|_{\text{min}} = \lambda_\Delta\,(1 + \kappa_\Delta)\,v_\Delta^3 + \mu_\Delta^2 v_\Delta + \frac{(1 + \kappa_{\Phi\Delta})\,\lambda_{\Phi\Delta}}{2}v_\Delta v_\Phi^2 - \frac{v_\Phi^2 \mu_{\Phi\Delta}}{\sqrt{2}} \overset{!}{=} 0 \tag{E.2}$$

we find for the minimization conditions

$$\mu_\Phi^2 = -\lambda_\Phi v_\Phi^2 - \frac{(1 + \kappa_{\Phi\Delta})\,\lambda_{\Phi\Delta}v_\Delta - 2\sqrt{2}\mu_{\Phi\Delta}}{2}v_\Delta \tag{E.3}$$

$$\mu_\Delta^2 = \frac{v_\Phi^2 \mu_{\Phi\Delta}}{\sqrt{2}v_\Delta} - (1 + \kappa_\Delta)\,\lambda_\Delta v_\Delta^2 - \frac{(1 + \kappa_{\Phi\Delta})\,\lambda_{\Phi\Delta}}{2}v_\Phi^2\,. \tag{E.4}$$

The second derivatives of the potential, evaluated at the minimum, thus lead to the following mass spectrum of the theory:

$$m_h^2 = 2\lambda_\Phi v_\Phi^2 \quad , \quad m_{\Delta_I^0} = \frac{v_\Phi^2 \mu_{\Phi\Delta}}{\sqrt{2} v_\Delta} \quad , \quad m_{s,a}^2 = \mu_S^2 + \frac{\lambda_{S\Phi} v_\Phi^2 + \lambda_{S\Delta} v_\Delta^2}{2}$$

$$m_{\Delta_R^0} = m_{\Delta_I^0} + 2\left(1 + \kappa_\Delta\right)\lambda_\Delta v_\Delta^2 \quad , \quad m_{\Delta^+}^2 = m_{\Delta_I^0} - \frac{\kappa_{\Phi\Delta}\lambda_{\Phi\Delta}}{4} v_\Phi^2$$

$$m_{\Delta^{++}}^2 = m_{\Delta_I^0} - \frac{\kappa_{\Phi\Delta}\lambda_{\Phi\Delta} v_\Phi^2 + 2\kappa_\Delta \lambda_\Delta v_\Delta^2}{2} \, . \tag{E.5}$$

E.2 Zee-Babu Model

The derivative of the potential in Eq. (5.30) with respect to the Higgs field reads

$$\frac{\partial V}{\partial h} = \lambda_\Phi v^3 + \mu_\Phi^2 v \overset{!}{=} 0 \tag{E.6}$$

and the minimization condition hence reads

$$\mu_\Phi^2 = -\lambda_\Phi v^2 \, . \tag{E.7}$$

The mass spectrum of this model is then given by

$$m_h^2 = 2\lambda_\Phi^2 v \quad , \quad m_\eta^2 = \mu_\eta^2 + \frac{\lambda_{\Phi\eta}}{2} v^2$$

$$m_\kappa^2 = \mu_\kappa^2 + \frac{\lambda_{\Phi\kappa}}{2} v^2 \quad , \quad m_{s,a}^2 = \mu_S^2 + \frac{\lambda_{S\Phi}}{2} v^2 \, . \tag{E.8}$$

Bibliography

[1] S. Fabian, F. Goertz and Y. Jiang, *Dark matter and nature of electroweak phase transition with an inert doublet*, *JCAP* **09** (2021) 011 [2012.12847].

[2] S. Fabian, *Study of the inert doublet model in the light of dark matter physics and electroweak phase transition*, 2020.

[3] M.D. Astros, S. Fabian and F. Goertz, *Minimal Inert Doublet benchmark for dark matter and the baryon asymmetry*, *JCAP* **02** (2024) 052 [2307.01270].

[4] S. Bhattacharya, S. Fabian, J. Herms and S. Jana, *Flavor-Specific Dark Matter Signatures through the Lens of Neutrino Oscillations*, 2407.09614.

[5] M.E. Peskin and D.V. Schroeder, *An Introduction to quantum field theory*, Addison-Wesley, Reading, USA (1995).

[6] L. Alvarez-Gaume and M.A. Vazquez-Mozo, *An invitation to quantum field theory*, vol. 839 (2012), 10.1007/978-3-642-23728-7.

[7] M. Thomson, *Modern particle physics*, Cambridge University Press, New York (2013), 10.1017/CBO9781139525367.

[8] M.D. Schwartz, *Quantum Field Theory and the Standard Model*, Cambridge University Press (3, 2014).

[9] P. Langacker, *The Standard Model and Beyond*, Taylor & Francis (2017), 10.1201/b22175.

[10] Particle Data Group collaboration, *Review of Particle Physics*, *PTEP* **2022** (2022) 083C01.

[11] E. Noether, *Invariante variationsprobleme*, *Nachrichten von der Gesellschaft der Wissenschaften zu Göttingen, Mathematisch-Physikalische Klasse* **1918** (1918) 235.

[12] S.L. Glashow, *Partial Symmetries of Weak Interactions*, *Nucl. Phys.* **22** (1961) 579.

[13] A. Salam, *Weak and Electromagnetic Interactions*, *Conf. Proc. C* **680519** (1968) 367.

[14] S. Weinberg, *A Model of Leptons*, *Phys. Rev. Lett.* **19** (1967) 1264.

[15] W. Bernreuther, *CP violation and baryogenesis*, *Lect. Notes Phys.* **591** (2002) 237 [`hep-ph/0205279`].

[16] A.A. Anselm and A.A. Johansen, *Baryon nonconservation in standard model and Yukawa interaction*, *Nucl. Phys. B* **407** (1993) 313.

[17] A.A. Anselm and A.A. Johansen, *Can electroweak theta term be observable?*, *Nucl. Phys. B* **412** (1994) 553 [`hep-ph/9305271`].

[18] M. Dine, *TASI lectures on the strong CP problem*, in *Theoretical Advanced Study Institute in Elementary Particle Physics (TASI 2000): Flavor Physics for the Millennium*, pp. 349–369, 6, 2000 [`hep-ph/0011376`].

[19] J. Goldstone, A. Salam and S. Weinberg, *Broken Symmetries*, *Phys. Rev.* **127** (1962) 965.

[20] F. Englert and R. Brout, *Broken Symmetry and the Mass of Gauge Vector Mesons*, *Phys. Rev. Lett.* **13** (1964) 321.

[21] P.W. Higgs, *Broken Symmetries and the Masses of Gauge Bosons*, *Phys. Rev. Lett.* **13** (1964) 508.

[22] G.S. Guralnik, C.R. Hagen and T.W.B. Kibble, *Global Conservation Laws and Massless Particles*, *Phys. Rev. Lett.* **13** (1964) 585.

[23] G.S. Guralnik, *The History of the Guralnik, Hagen and Kibble development of the Theory of Spontaneous Symmetry Breaking and Gauge Particles*, *Int. J. Mod. Phys. A* **24** (2009) 2601 [`0907.3466`].

[24] ATLAS collaboration, *Constraints on the Higgs boson self-coupling from single- and double-Higgs production with the ATLAS detector using pp collisions at s=13 TeV*, *Phys. Lett. B* **843** (2023) 137745 [`2211.01216`].

[25] CMS collaboration, *A portrait of the Higgs boson by the CMS experiment ten years after the discovery.*, *Nature* **607** (2022) 60 [`2207.00043`].

[26] ATLAS collaboration, *Evidence of off-shell Higgs boson production from ZZ leptonic decay channels and constraints on its total width with the ATLAS detector*, *Phys. Lett. B* **846** (2023) 138223 [`2304.01532`].

[27] CMS collaboration, *Measurement of the Higgs boson width and evidence of its off-shell contributions to ZZ production*, *Nature Phys.* **18** (2022) 1329 [`2202.06923`].

[28] LHC Higgs Cross Section Working Group collaboration, *Handbook of LHC Higgs Cross Sections: 4. Deciphering the Nature of the Higgs Sector*, `1610.07922`.

[29] ATLAS collaboration, *Search for resonances in diphoton events at $\sqrt{s}$=13 TeV with the ATLAS detector*, *JHEP* **09** (2016) 001 [`1606.03833`].

[30] CMS collaboration, *Search for Resonant Production of High-Mass Photon Pairs in Proton-Proton Collisions at $\sqrt{s}$ =8 and 13 TeV*, *Phys. Rev. Lett.* **117** (2016) 051802 [`1606.04093`].

[31] CMS collaboration, *Search for resonant production of high mass photon pairs using $12.9\,\text{fb}^{-1}$ of proton-proton collisions at $\sqrt{s} = 13$ TeV and combined interpretation of searches at 8 and 13 TeV*, .

[32] ATLAS collaboration, *Search for new phenomena in high-mass diphoton final states using $37\,fb^{-1}$ of proton–proton collisions collected at $\sqrt{s} = 13$ TeV with the ATLAS detector*, *Phys. Lett. B* **775** (2017) 105 [`1707.04147`].

[33] CMS collaboration, *Search for high-mass diphoton resonances in proton–proton collisions at 13 TeV and combination with 8 TeV search*, *Phys. Lett. B* **767** (2017) 147 [`1609.02507`].

[34] LHCb collaboration, *Measurement of Form-Factor-Independent Observables in the Decay $B^0 \to K^{*0}\mu^+\mu^-$*, *Phys. Rev. Lett.* **111** (2013) 191801 [`1308.1707`].

[35] LHCb collaboration, *Test of lepton universality using $B^+ \to K^+\ell^+\ell^-$ decays*, *Phys. Rev. Lett.* **113** (2014) 151601 [`1406.6482`].

[36] B. Capdevila, A. Crivellin and J. Matias, *Review of semileptonic B anomalies*, *Eur. Phys. J. ST* **1** (2023) 20 [2309.01311].

[37] BABAR collaboration, *Evidence for an excess of $\bar{B} \to D^{(*)}\tau^-\bar{\nu}_\tau$ decays*, *Phys. Rev. Lett.* **109** (2012) 101802 [1205.5442].

[38] BABAR collaboration, *Measurement of an Excess of $\bar{B} \to D^{(*)}\tau^-\bar{\nu}_\tau$ Decays and Implications for Charged Higgs Bosons*, *Phys. Rev. D* **88** (2013) 072012 [1303.0571].

[39] LHCB collaboration, *Measurement of the ratio of branching fractions $\mathcal{B}(\bar{B}^0 \to D^{*+}\tau^-\bar{\nu}_\tau)/\mathcal{B}(\bar{B}^0 \to D^{*+}\mu^-\bar{\nu}_\mu)$*, *Phys. Rev. Lett.* **115** (2015) 111803 [1506.08614].

[40] BELLE collaboration, *Measurement of the branching ratio of $\bar{B} \to D^{(*)}\tau^-\bar{\nu}_\tau$ relative to $\bar{B} \to D^{(*)}\ell^-\bar{\nu}_\ell$ decays with hadronic tagging at Belle*, *Phys. Rev. D* **92** (2015) 072014 [1507.03233].

[41] BELLE collaboration, *Measurement of the τ lepton polarization and $R(D^*)$ in the decay $\bar{B} \to D^*\tau^-\bar{\nu}_\tau$*, *Phys. Rev. Lett.* **118** (2017) 211801 [1612.00529].

[42] D. Bigi and P. Gambino, *Revisiting $B \to D\ell\nu$*, *Phys. Rev. D* **94** (2016) 094008 [1606.08030].

[43] F.U. Bernlochner, Z. Ligeti, M. Papucci and D.J. Robinson, *Combined analysis of semileptonic B decays to D and D^*: $R(D^{(*)})$, $|V_{cb}|$, and new physics*, *Phys. Rev. D* **95** (2017) 115008 [1703.05330].

[44] LHCB collaboration, *Test of Lepton Flavor Universality by the measurement of the $B^0 \to D^{*-}\tau^+\nu_\tau$ branching fraction using three-prong τ decays*, *Phys. Rev. D* **97** (2018) 072013 [1711.02505].

[45] S. Jaiswal, S. Nandi and S.K. Patra, *Extraction of $|V_{cb}|$ from $B \to D^{(*)}\ell\nu_\ell$ and the Standard Model predictions of $R(D^{(*)})$*, *JHEP* **12** (2017) 060 [1707.09977].

[46] LHCB collaboration, *Measurement of the ratio of the $B^0 \to D^{*-}\tau^+\nu_\tau$ and $B^0 \to D^{*-}\mu^+\nu_\mu$ branching fractions using three-prong τ-lepton decays*, *Phys. Rev. Lett.* **120** (2018) 171802 [1708.08856].

[47] BELLE collaboration, *Measurement of $\mathcal{R}(D)$ and $\mathcal{R}(D^*)$ with a semileptonic tagging method*, *Phys. Rev. Lett.* **124** (2020) 161803 [1910.05864].

[48] P. Gambino, M. Jung and S. Schacht, *The V_{cb} puzzle: An update*, *Phys. Lett. B* **795** (2019) 386 [1905.08209].

[49] BaBar collaboration, *Extraction of form Factors from a Four-Dimensional Angular Analysis of $\overline{B} \to D^*\ell^-\overline{\nu}_\ell$*, *Phys. Rev. Lett.* **123** (2019) 091801 [1903.10002].

[50] M. Bordone, M. Jung and D. van Dyk, *Theory determination of $\bar{B} \to D^{(*)}\ell^-\bar{\nu}$ form factors at $\mathcal{O}(1/m_c^2)$*, *Eur. Phys. J. C* **80** (2020) 74 [1908.09398].

[51] HFLAV collaboration, *Averages of b-hadron, c-hadron, and τ-lepton properties as of 2021*, *Phys. Rev. D* **107** (2023) 052008 [2206.07501].

[52] I.B. Khriplovich and A.R. Zhitnitsky, *Estimate of the Neutron Electric Dipole Moment in the Weinberg Model of CP Violation*, *Sov. J. Nucl. Phys.* **34** (1981) 95.

[53] I.B. Khriplovich and A.R. Zhitnitsky, *What Is the Value of the Neutron Electric Dipole Moment in the Kobayashi-Maskawa Model?*, *Phys. Lett. B* **109** (1982) 490.

[54] I.B. Khriplovich, *Quark Electric Dipole Moment and Induced θ Term in the Kobayashi-Maskawa Model*, *Phys. Lett. B* **173** (1986) 193.

[55] M. Pospelov and A. Ritz, *Neutron EDM from electric and chromoelectric dipole moments of quarks*, *Phys. Rev. D* **63** (2001) 073015 [hep-ph/0010037].

[56] C. Abel et al., *Measurement of the Permanent Electric Dipole Moment of the Neutron*, *Phys. Rev. Lett.* **124** (2020) 081803 [2001.11966].

[57] A. Ringwald, *Review on Axions*, 4, 2024 [2404.09036].

[58] R.D. Peccei, *The Strong CP problem and axions*, *Lect. Notes Phys.* **741** (2008) 3 [hep-ph/0607268].

[59] L. Di Luzio, M. Giannotti, E. Nardi and L. Visinelli, *The landscape of QCD axion models*, *Phys. Rept.* **870** (2020) 1 [2003.01100].

[60] G. Bertone, D. Hooper and J. Silk, *Particle dark matter: Evidence, candidates and constraints*, *Phys. Rept.* **405** (2005) 279 [hep-ph/0404175].

[61] J. Billard et al., *Direct detection of dark matter—APPEC committee report**, *Rept. Prog. Phys.* **85** (2022) 056201 [`2104.07634`].

[62] G. Bertone and D. Hooper, *History of dark matter*, *Rev. Mod. Phys.* **90** (2018) 045002 [`1605.04909`].

[63] W.J.G. de Blok, *The Core-Cusp Problem*, *Adv. Astron.* **2010** (2010) 789293 [`0910.3538`].

[64] J.N. Bahcall, C. Flynn and A. Gould, *Local dark matter from a carefully selected sample*, *Astrophys. J.* **389** (1992) 234.

[65] F. Zwicky, *On the Masses of Nebulae and of Clusters of Nebulae*, *Astrophys. J.* **86** (1937) 217.

[66] W. Tucker, P. Blanco, S. Rappoport, L. David, D. Fabricant, E.E. Falco et al., *1e0657-56: a contender for the hottest known cluster of galaxies*, *Astrophys. J. Lett.* **496** (1998) L5 [`astro-ph/9801120`].

[67] M. Markevitch, A.H. Gonzalez, L. David, A. Vikhlinin, S. Murray, W. Forman et al., *A Textbook example of a bow shock in the merging galaxy cluster 1E0657-56*, *Astrophys. J. Lett.* **567** (2002) L27 [`astro-ph/0110468`].

[68] D. Clowe, A. Gonzalez and M. Markevitch, *Weak lensing mass reconstruction of the interacting cluster 1E0657-558: Direct evidence for the existence of dark matter*, *Astrophys. J.* **604** (2004) 596 [`astro-ph/0312273`].

[69] D. Clowe, M. Bradac, A.H. Gonzalez, M. Markevitch, S.W. Randall, C. Jones et al., *A direct empirical proof of the existence of dark matter*, *Astrophys. J. Lett.* **648** (2006) L109 [`astro-ph/0608407`].

[70] M. Bradac, D. Clowe, A.H. Gonzalez, P. Marshall, W. Forman, C. Jones et al., *Strong and weak lensing united. III. Measuring the mass distribution of the merging galaxy cluster 1E0657-56*, *Astrophys. J.* **652** (2006) 937 [`astro-ph/0608408`].

[71] M. Bradac, S.W. Allen, T. Treu, H. Ebeling, R. Massey, R.G. Morris et al., *Revealing the properties of dark matter in the merging cluster MACSJ0025.4-1222*, *Astrophys. J.* **687** (2008) 959 [`0806.2320`].

[72] G. Gamow, *The Evolution of the Universe*, *Nature* **162** (1948) 680.

[73] R.A. Alpher and R. Herman, *Evolution of the Universe*, *Nature* **162** (1948) 774.

[74] A.A. Penzias and R.W. Wilson, *A Measurement of excess antenna temperature at 4080-Mc/s*, *Astrophys. J.* **142** (1965) 419.

[75] PLANCK collaboration, *Planck 2018 results. VI. Cosmological parameters*, *Astron. Astrophys.* **641** (2020) A6 [`1807.06209`].

[76] PLANCK collaboration, *Planck 2018 results. V. CMB power spectra and likelihoods*, *Astron. Astrophys.* **641** (2020) A5 [`1907.12875`].

[77] V. Springel, C.S. Frenk and S.D.M. White, *The large-scale structure of the Universe*, *Nature* **440** (2006) 1137 [`astro-ph/0604561`].

[78] M. Milgrom, *MOND: A pedagogical review*, Acta Phys. Polon. B **32** (2001) 3613 [`astro-ph/0112069`].

[79] B. Famaey and S. McGaugh, *Modified Newtonian Dynamics (MOND): Observational Phenomenology and Relativistic Extensions*, *Living Rev. Rel.* **15** (2012) 10 [`1112.3960`].

[80] B. Paczynski, *Gravitational microlensing by the galactic halo*, *Astrophys. J.* **304** (1986) 1.

[81] K. Griest, *Galactic Microlensing as a Method of Detecting Massive Compact Halo Objects*, *Astrophys. J.* **366** (1991) 412.

[82] A.M. Green and B.J. Kavanagh, *Primordial Black Holes as a dark matter candidate*, *J. Phys. G* **48** (2021) 043001 [`2007.10722`].

[83] B. Carr, K. Kohri, Y. Sendouda and J. Yokoyama, *Constraints on primordial black holes*, *Rept. Prog. Phys.* **84** (2021) 116902 [`2002.12778`].

[84] B.J. Carr and A.M. Green, *The History of Primordial Black Holes*, `2406.05736`.

[85] J. Silk et al., *Particle Dark Matter: Observations, Models and Searches*, Cambridge Univ. Press, Cambridge (2010), 10.1017/CBO9780511770739.

[86] S. Profumo, *An Introduction to Particle Dark Matter*, World Scientific (2017), 10.1142/q0001.

[87] S.D. McDermott, H.-B. Yu and K.M. Zurek, *Turning off the Lights: How Dark is Dark Matter?*, *Phys. Rev. D* **83** (2011) 063509 [`1011.2907`].

[88] L. Randall, J. Scholtz and J. Unwin, *Cores in Dwarf Galaxies from Fermi Repulsion*, *Mon. Not. Roy. Astron. Soc.* **467** (2017) 1515 [1611.04590].

[89] S. Tremaine and J.E. Gunn, *Dynamical Role of Light Neutral Leptons in Cosmology*, *Phys. Rev. Lett.* **42** (1979) 407.

[90] M. Cirelli, A. Strumia and J. Zupan, *Dark Matter*, 2406.01705.

[91] M. Markevitch, A.H. Gonzalez, D. Clowe, A. Vikhlinin, L. David, W. Forman et al., *Direct constraints on the dark matter self-interaction cross-section from the merging galaxy cluster 1E0657-56*, *Astrophys. J.* **606** (2004) 819 [astro-ph/0309303].

[92] G. Steigman and M.S. Turner, *Cosmological Constraints on the Properties of Weakly Interacting Massive Particles*, *Nucl. Phys. B* **253** (1985) 375.

[93] M. Pospelov, A. Ritz and M.B. Voloshin, *Secluded WIMP Dark Matter*, *Phys. Lett. B* **662** (2008) 53 [0711.4866].

[94] G. Arcadi, M. Dutra, P. Ghosh, M. Lindner, Y. Mambrini, M. Pierre et al., *The waning of the WIMP? A review of models, searches, and constraints*, *Eur. Phys. J. C* **78** (2018) 203 [1703.07364].

[95] G. Arcadi, D. Cabo-Almeida, M. Dutra, P. Ghosh, M. Lindner, Y. Mambrini et al., *The Waning of the WIMP: Endgame?*, 2403.15860.

[96] K. Griest and D. Seckel, *Three exceptions in the calculation of relic abundances*, *Phys. Rev. D* **43** (1991) 3191.

[97] J. Edsjo and P. Gondolo, *Neutralino relic density including coannihilations*, *Phys. Rev. D* **56** (1997) 1879 [hep-ph/9704361].

[98] PANDAX collaboration, *First Measurement of Solar ^8B Neutrino Flux through Coherent Elastic Neutrino-Nucleus Scattering in PandaX-4T*, 2407.10892.

[99] E. Aprile et al., *First Measurement of Solar ^8B Neutrinos via Coherent Elastic Neutrino-Nucleus Scattering with XENONnT*, 2408.02877.

[100] L.J. Hall, K. Jedamzik, J. March-Russell and S.M. West, *Freeze-In Production of FIMP Dark Matter*, *JHEP* **03** (2010) 080 [0911.1120].

154

[101] N. Bernal, M. Heikinheimo, T. Tenkanen, K. Tuominen and V. Vaskonen, *The Dawn of FIMP Dark Matter: A Review of Models and Constraints*, *Int. J. Mod. Phys. A* **32** (2017) 1730023 [1706.07442].

[102] J. Jaeckel and A. Ringwald, *The Low-Energy Frontier of Particle Physics*, *Ann. Rev. Nucl. Part. Sci.* **60** (2010) 405 [1002.0329].

[103] P.W. Graham, I.G. Irastorza, S.K. Lamoreaux, A. Lindner and K.A. van Bibber, *Experimental Searches for the Axion and Axion-Like Particles*, *Ann. Rev. Nucl. Part. Sci.* **65** (2015) 485 [1602.00039].

[104] R.D. Peccei and H.R. Quinn, *CP Conservation in the Presence of Instantons*, *Phys. Rev. Lett.* **38** (1977) 1440.

[105] R.D. Peccei and H.R. Quinn, *Constraints Imposed by CP Conservation in the Presence of Instantons*, *Phys. Rev. D* **16** (1977) 1791.

[106] P. Arias, D. Cadamuro, M. Goodsell, J. Jaeckel, J. Redondo and A. Ringwald, *WISPy Cold Dark Matter*, *JCAP* **06** (2012) 013 [1201.5902].

[107] C.B. Adams et al., *Axion Dark Matter*, in *Snowmass 2021*, 3, 2022 [2203.14923].

[108] J.L. Feng, *Dark Matter Candidates from Particle Physics and Methods of Detection*, *Ann. Rev. Astron. Astrophys.* **48** (2010) 495 [1003.0904].

[109] XENON collaboration, *First Dark Matter Search with Nuclear Recoils from the XENONnT Experiment*, *Phys. Rev. Lett.* **131** (2023) 041003 [2303.14729].

[110] LZ collaboration, *First Dark Matter Search Results from the LUX-ZEPLIN (LZ) Experiment*, *Phys. Rev. Lett.* **131** (2023) 041002 [2207.03764].

[111] COSINE-100 collaboration, *Strong constraints from COSINE-100 on the DAMA dark matter results using the same sodium iodide target*, *Sci. Adv.* **7** (2021) abk2699 [2104.03537].

[112] PandaX-II collaboration, *Results of dark matter search using the full PandaX-II exposure*, *Chin. Phys. C* **44** (2020) 125001 [2007.15469].

[113] XMASS collaboration, *A direct dark matter search in XMASS-I*, *Phys. Lett. B* **789** (2019) 45 [1804.02180].

[114] D.Y. Akimov et al., *WIMP-nucleon cross-section results from the second science run of ZEPLIN-III*, *Phys. Lett. B* **709** (2012) 14 [1110.4769].

[115] DARKSIDE collaboration, *Search for Dark-Matter–Nucleon Interactions via Migdal Effect with DarkSide-50*, *Phys. Rev. Lett.* **130** (2023) 101001 [2207.11967].

[116] CRESST collaboration, *First results from the CRESST-III low-mass dark matter program*, *Phys. Rev. D* **100** (2019) 102002 [1904.00498].

[117] F. Ruppin, J. Billard, E. Figueroa-Feliciano and L. Strigari, *Complementarity of dark matter detectors in light of the neutrino background*, *Phys. Rev. D* **90** (2014) 083510 [1408.3581].

[118] C.A.J. O'Hare, *New Definition of the Neutrino Floor for Direct Dark Matter Searches*, *Phys. Rev. Lett.* **127** (2021) 251802 [2109.03116].

[119] H. Georgi, *Effective field theory*, *Ann. Rev. Nucl. Part. Sci.* **43** (1993) 209.

[120] K. Crowther, *Effective Spacetime: Understanding Emergence in Effective Field Theory and Quantum Gravity*, Springer International Publishing, Cham (2016), 10.1007/978-3-319-39508-1.

[121] I. Brivio and M. Trott, *The Standard Model as an Effective Field Theory*, *Phys. Rept.* **793** (2019) 1 [1706.08945].

[122] A.V. Manohar, *Introduction to Effective Field Theories*, 1804.05863.

[123] T. Appelquist and J. Carazzone, *Infrared Singularities and Massive Fields*, *Phys. Rev. D* **11** (1975) 2856.

[124] R. Contino, A. Falkowski, F. Goertz, C. Grojean and F. Riva, *On the Validity of the Effective Field Theory Approach to SM Precision Tests*, *JHEP* **07** (2016) 144 [1604.06444].

[125] G. Isidori, F. Wilsch and D. Wyler, *The standard model effective field theory at work*, *Rev. Mod. Phys.* **96** (2024) 015006 [2303.16922].

[126] W. Buchmuller and D. Wyler, *Effective Lagrangian Analysis of New Interactions and Flavor Conservation*, *Nucl. Phys. B* **268** (1986) 621.

[127] B. Grzadkowski, M. Iskrzynski, M. Misiak and J. Rosiek, *Dimension-Six Terms in the Standard Model Lagrangian*, *JHEP* **10** (2010) 085 [`1008.4884`].

[128] M. Bjørn and M. Trott, *Interpreting W mass measurements in the SMEFT*, *Phys. Lett. B* **762** (2016) 426 [`1606.06502`].

[129] E. Bagnaschi, J. Ellis, M. Madigan, K. Mimasu, V. Sanz and T. You, *SMEFT analysis of m_W*, *JHEP* **08** (2022) 308 [`2204.05260`].

[130] J. Fan, L. Li, T. Liu and K.-F. Lyu, *W-boson mass, electroweak precision tests, and SMEFT*, *Phys. Rev. D* **106** (2022) 073010 [`2204.04805`].

[131] F.-Z. Chen, Q. Wen and F. Xu, *Correlating $B \to K^{(*)}\nu\bar{\nu}$ and flavor anomalies in SMEFT*, `2401.11552`.

[132] T. Alanne and F. Goertz, *Extended Dark Matter EFT*, *Eur. Phys. J. C* **80** (2020) 446 [`1712.07626`].

[133] N.D. Christensen and C. Duhr, *FeynRules - Feynman rules made easy*, *Comput. Phys. Commun.* **180** (2009) 1614 [`0806.4194`].

[134] N.D. Christensen, P. de Aquino, C. Degrande, C. Duhr, B. Fuks, M. Herquet et al., *A Comprehensive approach to new physics simulations*, *Eur. Phys. J. C* **71** (2011) 1541 [`0906.2474`].

[135] A. Alloul, N.D. Christensen, C. Degrande, C. Duhr and B. Fuks, *FeynRules 2.0 - A complete toolbox for tree-level phenomenology*, *Comput. Phys. Commun.* **185** (2014) 2250 [`1310.1921`].

[136] G. Belanger, F. Boudjema, A. Pukhov and A. Semenov, *microOMEGAs_3: A program for calculating dark matter observables*, *Comput. Phys. Commun.* **185** (2014) 960 [`1305.0237`].

[137] G. Bélanger, F. Boudjema, A. Goudelis, A. Pukhov and B. Zaldivar, *micrOMEGAs5.0 : Freeze-in*, *Comput. Phys. Commun.* **231** (2018) 173 [`1801.03509`].

[138] J. Alwall, M. Herquet, F. Maltoni, O. Mattelaer and T. Stelzer, *MadGraph 5 : Going Beyond*, *JHEP* **06** (2011) 128 [`1106.0522`].

[139] J. Alwall, R. Frederix, S. Frixione, V. Hirschi, F. Maltoni, O. Mattelaer et al., *The automated computation of tree-level and next-to-leading order differential cross sections, and their matching to parton shower simulations*, *JHEP* **07** (2014) 079 [1405.0301].

[140] J. Ellis, *TikZ-Feynman: Feynman diagrams with TikZ*, *Comput. Phys. Commun.* **210** (2017) 103 [1601.05437].

[141] H.E. Haber, G.L. Kane and T. Sterling, *The Fermion Mass Scale and Possible Effects of Higgs Bosons on Experimental Observables*, *Nucl. Phys. B* **161** (1979) 493.

[142] G.C. Branco, P.M. Ferreira, L. Lavoura, M.N. Rebelo, M. Sher and J.P. Silva, *Theory and phenomenology of two-Higgs-doublet models*, *Phys. Rept.* **516** (2012) 1 [1106.0034].

[143] G. Bhattacharyya and D. Das, *Scalar sector of two-Higgs-doublet models: A minireview*, *Pramana* **87** (2016) 40 [1507.06424].

[144] I.P. Ivanov, *Building and testing models with extended Higgs sectors*, *Prog. Part. Nucl. Phys.* **95** (2017) 160 [1702.03776].

[145] S. Dawson, C. Englert and T. Plehn, *Higgs Physics: It ain't over till it's over*, *Phys. Rept.* **816** (2019) 1 [1808.01324].

[146] ATLAS collaboration, *Combined measurements of Higgs boson production and decay using up to 139 fb^{-1} of proton-proton collision data at $\sqrt{s} = 13$ TeV collected with the ATLAS experiment*, .

[147] A. Pich and P. Tuzon, *Yukawa Alignment in the Two-Higgs-Doublet Model*, *Phys. Rev. D* **80** (2009) 091702 [0908.1554].

[148] P. Tuzon and A. Pich, *The Aligned two-Higgs Doublet model*, *Acta Phys. Polon. Supp.* **3** (2010) 215 [1001.0293].

[149] A. Pich, *Flavour constraints on multi-Higgs-doublet models: Yukawa alignment*, *Nucl. Phys. B Proc. Suppl.* **209** (2010) 182 [1010.5217].

[150] A. Peñuelas and A. Pich, *Flavour alignment in multi-Higgs-doublet models*, *JHEP* **12** (2017) 084 [1710.02040].

[151] S. Gori, H.E. Haber and E. Santos, *High scale flavor alignment in two-Higgs doublet models and its phenomenology*, *JHEP* **06** (2017) 110 [`1703.05873`].

[152] M.D. Campos, D. Cogollo, M. Lindner, T. Melo, F.S. Queiroz and W. Rodejohann, *Neutrino Masses and Absence of Flavor Changing Interactions in the 2HDM from Gauge Principles*, *JHEP* **08** (2017) 092 [`1705.05388`].

[153] G. Arcadi, S. Profumo, F.S. Queiroz and C. Siqueira, *Right-handed Neutrino Dark Matter, Neutrino Masses, and non-Standard Cosmology in a 2HDM*, *JCAP* **12** (2020) 030 [`2007.07920`].

[154] G. Arcadi, G. Busoni, T. Hugle and V.T. Tenorth, *Comparing 2HDM + Scalar and Pseudoscalar Simplified Models at LHC*, *JHEP* **06** (2020) 098 [`2001.10540`].

[155] G. Arcadi, N. Benincasa, A. Djouadi and K. Kannike, *Two-Higgs-doublet-plus-pseudoscalar model: Collider, dark matter, and gravitational wave signals*, *Phys. Rev. D* **108** (2023) 055010 [`2212.14788`].

[156] PARTICLE DATA GROUP collaboration, *Review of Particle Physics*, *PTEP* **2020** (2020) 083C01.

[157] J.M. Cline, *Baryogenesis*, in *Les Houches Summer School - Session 86: Particle Physics and Cosmology: The Fabric of Spacetime*, 9, 2006 [`hep-ph/0609145`].

[158] B.D. Fields, K.A. Olive, T.-H. Yeh and C. Young, *Big-Bang Nucleosynthesis after Planck*, *JCAP* **03** (2020) 010 [`1912.01132`].

[159] L. Canetti, M. Drewes and M. Shaposhnikov, *Matter and Antimatter in the Universe*, *New J. Phys.* **14** (2012) 095012 [`1204.4186`].

[160] A.D. Sakharov, *Violation of CP Invariance, C asymmetry, and baryon asymmetry of the universe*, *Pisma Zh. Eksp. Teor. Fiz.* **5** (1967) 32.

[161] V.A. Kostelecky and N. Russell, *Data Tables for Lorentz and CPT Violation*, *Rev. Mod. Phys.* **83** (2011) 11 [`0801.0287`].

[162] G. 't Hooft, *Symmetry Breaking Through Bell-Jackiw Anomalies*, *Phys. Rev. Lett.* **37** (1976) 8.

[163] N.S. Manton, *Topology in the Weinberg-Salam Theory*, *Phys. Rev. D* **28** (1983) 2019.

[164] F.R. Klinkhamer and N.S. Manton, *A Saddle Point Solution in the Weinberg-Salam Theory*, *Phys. Rev. D* **30** (1984) 2212.

[165] J.H. Christenson, J.W. Cronin, V.L. Fitch and R. Turlay, *Evidence for the 2π Decay of the K_2^0 Meson*, *Phys. Rev. Lett.* **13** (1964) 138.

[166] A.G. Cohen, D.B. Kaplan and A.E. Nelson, *Progress in electroweak baryogenesis*, *Ann. Rev. Nucl. Part. Sci.* **43** (1993) 27 [`hep-ph/9302210`].

[167] V.A. Rubakov and M.E. Shaposhnikov, *Electroweak baryon number nonconservation in the early universe and in high-energy collisions*, *Usp. Fiz. Nauk* **166** (1996) 493 [`hep-ph/9603208`].

[168] A.I. Vainshtein, V.I. Zakharov, V.A. Novikov and M.A. Shifman, *ABC's of Instantons*, *Sov. Phys. Usp.* **25** (1982) 195.

[169] V.A. Kuzmin, V.A. Rubakov and M.E. Shaposhnikov, *On the Anomalous Electroweak Baryon Number Nonconservation in the Early Universe*, *Phys. Lett. B* **155** (1985) 36.

[170] M. Quiros, *Finite temperature field theory and phase transitions*, in *ICTP Summer School in High-Energy Physics and Cosmology*, pp. 187–259, 1, 1999 [`hep-ph/9901312`].

[171] D.J. Weir, *Gravitational waves from a first order electroweak phase transition: a brief review*, *Phil. Trans. Roy. Soc. Lond. A* **376** (2018) 20170126 [`1705.01783`].

[172] A. Kosowsky, M.S. Turner and R. Watkins, *Gravitational waves from first order cosmological phase transitions*, *Phys. Rev. Lett.* **69** (1992) 2026.

[173] M. Kamionkowski, A. Kosowsky and M.S. Turner, *Gravitational radiation from first order phase transitions*, *Phys. Rev. D* **49** (1994) 2837 [`astro-ph/9310044`].

[174] C. Grojean and G. Servant, *Gravitational Waves from Phase Transitions at the Electroweak Scale and Beyond*, *Phys. Rev. D* **75** (2007) 043507 [`hep-ph/0607107`].

[175] L. Leitao, A. Megevand and A.D. Sanchez, *Gravitational waves from the electroweak phase transition*, *JCAP* **10** (2012) 024 [`1205.3070`].

[176] L. Dolan and R. Jackiw, *Symmetry Behavior at Finite Temperature*, *Phys. Rev. D* **9** (1974) 3320.

[177] N.K. Nielsen, *On the Gauge Dependence of Spontaneous Symmetry Breaking in Gauge Theories*, *Nucl. Phys. B* **101** (1975) 173.

[178] R. Fukuda and T. Kugo, *Gauge Invariance in the Effective Action and Potential*, *Phys. Rev. D* **13** (1976) 3469.

[179] W. Fischler and R. Brout, *Gauge Invariance in Spontaneously Broken Symmetry*, *Phys. Rev. D* **11** (1975) 905.

[180] M. Laine, *Gauge dependence of the high temperature two loop effective potential for the Higgs field*, *Phys. Rev. D* **51** (1995) 4525 [`hep-ph/9411252`].

[181] D. Metaxas and E.J. Weinberg, *Gauge independence of the bubble nucleation rate in theories with radiative symmetry breaking*, *Phys. Rev. D* **53** (1996) 836 [`hep-ph/9507381`].

[182] D. Boyanovsky, D. Brahm, R. Holman and D.S. Lee, *The Gauge invariant effective potential: Equilibrium and nonequilibrium aspects*, *Phys. Rev. D* **54** (1996) 1763 [`hep-ph/9603337`].

[183] H.H. Patel and M.J. Ramsey-Musolf, *Baryon Washout, Electroweak Phase Transition, and Perturbation Theory*, *JHEP* **07** (2011) 029 [`1101.4665`].

[184] C. Wainwright, S. Profumo and M.J. Ramsey-Musolf, *Gravity Waves from a Cosmological Phase Transition: Gauge Artifacts and Daisy Resummations*, *Phys. Rev. D* **84** (2011) 023521 [`1104.5487`].

[185] D.E. Morrissey and M.J. Ramsey-Musolf, *Electroweak baryogenesis*, *New J. Phys.* **14** (2012) 125003 [`1206.2942`].

[186] K. Kajantie, M. Laine, K. Rummukainen and M.E. Shaposhnikov, *Is there a hot electroweak phase transition at $m_H \gtrsim m_W$?*, *Phys. Rev. Lett.* **77** (1996) 2887 [`hep-ph/9605288`].

[187] F. Karsch, T. Neuhaus, A. Patkos and J. Rank, *Critical Higgs mass and temperature dependence of gauge boson masses in the SU(2) gauge Higgs model*, *Nucl. Phys. B Proc. Suppl.* **53** (1997) 623 [`hep-lat/9608087`].

[188] M. Gurtler, E.-M. Ilgenfritz and A. Schiller, *Where the electroweak phase transition ends*, *Phys. Rev. D* **56** (1997) 3888 [`hep-lat/9704013`].

[189] K. Rummukainen, M. Tsypin, K. Kajantie, M. Laine and M.E. Shaposhnikov, *The Universality class of the electroweak theory*, *Nucl. Phys. B* **532** (1998) 283 [hep-lat/9805013].

[190] F. Csikor, Z. Fodor and J. Heitger, *Endpoint of the hot electroweak phase transition*, *Phys. Rev. Lett.* **82** (1999) 21 [hep-ph/9809291].

[191] Y. Aoki, F. Csikor, Z. Fodor and A. Ukawa, *The Endpoint of the first order phase transition of the SU(2) gauge Higgs model on a four-dimensional isotropic lattice*, *Phys. Rev. D* **60** (1999) 013001 [hep-lat/9901021].

[192] M. D'Onofrio, K. Rummukainen and A. Tranberg, *Sphaleron Rate in the Minimal Standard Model*, *Phys. Rev. Lett.* **113** (2014) 141602 [1404.3565].

[193] M. D'Onofrio and K. Rummukainen, *Standard model cross-over on the lattice*, *Phys. Rev. D* **93** (2016) 025003 [1508.07161].

[194] C. Jarlskog, *A Basis Independent Formulation of the Connection Between Quark Mass Matrices, CP Violation and Experiment*, *Z. Phys. C* **29** (1985) 491.

[195] C. Jarlskog, *Commutator of the Quark Mass Matrices in the Standard Electroweak Model and a Measure of Maximal CP Nonconservation*, *Phys. Rev. Lett.* **55** (1985) 1039.

[196] D. Bodeker, L. Fromme, S.J. Huber and M. Seniuch, *The Baryon asymmetry in the standard model with a low cut-off*, *JHEP* **02** (2005) 026 [hep-ph/0412366].

[197] C. Grojean, G. Servant and J.D. Wells, *First-order electroweak phase transition in the standard model with a low cutoff*, *Phys. Rev. D* **71** (2005) 036001 [hep-ph/0407019].

[198] SUPER-KAMIOKANDE collaboration, *Search for proton decay via $p \to \mu^+ K^0$ in 0.37 megaton-years exposure of Super-Kamiokande*, *Phys. Rev. D* **106** (2022) 072003 [2208.13188].

[199] SUPER-KAMIOKANDE collaboration, *Search for proton decay via $p \to e^+ \pi^0$ and $p \to \mu^+ \pi^0$ with an enlarged fiducial volume in Super-Kamiokande I-IV*, *Phys. Rev. D* **102** (2020) 112011 [2010.16098].

[200] R. Barbier et al., *R-parity violating supersymmetry*, *Phys. Rept.* **420** (2005) 1 [hep-ph/0406039].

[201] K.S. Babu, R.N. Mohapatra and S. Nasri, *Post-Sphaleron Baryogenesis*, *Phys. Rev. Lett.* **97** (2006) 131301 [`hep-ph/0606144`].

[202] K.S. Babu, P.S. Bhupal Dev, E.C.F.S. Fortes and R.N. Mohapatra, *Post-Sphaleron Baryogenesis and an Upper Limit on the Neutron-Antineutron Oscillation Time*, *Phys. Rev. D* **87** (2013) 115019 [`1303.6918`].

[203] L. Calibbi, G. Ferretti, D. Milstead, C. Petersson and R. Pöttgen, *Baryon number violation in supersymmetry: n-n̄ oscillations as a probe beyond the LHC*, *JHEP* **05** (2016) 144 [`1602.04821`].

[204] R.N. Mohapatra, *Neutron-Anti-Neutron Oscillation: Theory and Phenomenology*, *J. Phys. G* **36** (2009) 104006 [`0902.0834`].

[205] D.G. Phillips, II et al., *Neutron-Antineutron Oscillations: Theoretical Status and Experimental Prospects*, *Phys. Rept.* **612** (2016) 1 [`1410.1100`].

[206] SUPER-KAMIOKANDE collaboration, *Neutron-antineutron oscillation search using a 0.37 megaton-years exposure of Super-Kamiokande*, *Phys. Rev. D* **103** (2021) 012008 [`2012.02607`].

[207] M. Baldo-Ceolin et al., *A New experimental limit on neutron - anti-neutron oscillations*, *Z. Phys. C* **63** (1994) 409.

[208] F. Backman et al., *The development of the NNBAR experiment*, *JINST* **17** (2022) P10046 [`2209.09011`].

[209] D.G. Ang, *Progress towards an improved measurement of the electric dipole moment of the electron*, Ph.D. thesis, Harvard U., 2023.

[210] J. Kley, T. Theil, E. Venturini and A. Weiler, *Electric dipole moments at one-loop in the dimension-6 SMEFT*, *Eur. Phys. J. C* **82** (2022) 926 [`2109.15085`].

[211] M.S. Safronova, D. Budker, D. DeMille, D.F.J. Kimball, A. Derevianko and C.W. Clark, *Search for New Physics with Atoms and Molecules*, *Rev. Mod. Phys.* **90** (2018) 025008 [`1710.01833`].

[212] J. Aebischer, W. Dekens, E.E. Jenkins, A.V. Manohar, D. Sengupta and P. Stoffer, *Effective field theory interpretation of lepton magnetic and electric dipole moments*, *JHEP* **07** (2021) 107 [`2102.08954`].

[213] E.M. Purcell and N.F. Ramsey, *On the Possibility of Electric Dipole Moments for Elementary Particles and Nuclei*, *Phys. Rev.* **78** (1950) 807.

[214] P. Sandars, *The electric dipole moment of an atom*, *Physics Letters* **14** (1965) 194.

[215] Y. Ema, T. Gao and M. Pospelov, *Standard Model Prediction for Paramagnetic Electric Dipole Moments*, *Phys. Rev. Lett.* **129** (2022) 231801 [2202.10524].

[216] M. Pospelov and A. Ritz, *CKM benchmarks for electron electric dipole moment experiments*, *Phys. Rev. D* **89** (2014) 056006 [1311.5537].

[217] T.S. Roussy et al., *An improved bound on the electron's electric dipole moment*, *Science* **381** (2023) adg4084 [2212.11841].

[218] X. Wu, P. Hu, Z. Han, D.G. Ang, C. Meisenhelder, G. Gabrielse et al., *Electrostatic focusing of cold and heavy molecules for the ACME electron EDM search*, *New J. Phys.* **24** (2022) 073043 [2204.05906].

[219] W. Bernreuther and M. Suzuki, *The electric dipole moment of the electron*, *Rev. Mod. Phys.* **63** (1991) 313.

[220] Muon (g-2) collaboration, *An Improved Limit on the Muon Electric Dipole Moment*, *Phys. Rev. D* **80** (2009) 052008 [0811.1207].

[221] M. Abe et al., *A New Approach for Measuring the Muon Anomalous Magnetic Moment and Electric Dipole Moment*, *PTEP* **2019** (2019) 053C02 [1901.03047].

[222] M. Sakurai et al., *muEDM: Towards a Search for the Muon Electric Dipole Moment at PSI Using the Frozen-spin Technique*, *JPS Conf. Proc.* **37** (2022) 020604 [2201.06561].

[223] K. Murai, F. Takahashi, M. Yamada and W. Yin, *Can baryon asymmetry be explained by a large initial value before inflation?*, *Phys. Rev. D* **108** (2023) 083518 [2307.03049].

[224] G. Elor et al., *New Ideas in Baryogenesis: A Snowmass White Paper*, in *Snowmass 2021*, 3, 2022 [2203.05010].

[225] G.A. White, *A Pedagogical Introduction to Electroweak Baryogenesis*, .

[226] M. Fukugita and T. Yanagida, *Baryogenesis Without Grand Unification*, *Phys. Lett. B* **174** (1986) 45.

[227] W. Buchmuller, R.D. Peccei and T. Yanagida, *Leptogenesis as the origin of matter*, *Ann. Rev. Nucl. Part. Sci.* **55** (2005) 311 [`hep-ph/0502169`].

[228] S. Davidson, E. Nardi and Y. Nir, *Leptogenesis*, *Phys. Rept.* **466** (2008) 105 [`0802.2962`].

[229] G.C. Branco, R.G. Felipe and F.R. Joaquim, *Leptonic CP Violation*, *Rev. Mod. Phys.* **84** (2012) 515 [`1111.5332`].

[230] A. Ibarra, *Leptogenesis from heavy right-handed neutrino decay*, *Indian J. Phys.* **97** (2023) 3287.

[231] A. Matsumoto et al., *EMPRESS. VIII. A New Determination of Primordial He Abundance with Extremely Metal-poor Galaxies: A Suggestion of the Lepton Asymmetry and Implications for the Hubble Tension*, *Astrophys. J.* **941** (2022) 167 [`2203.09617`].

[232] M. Kawasaki and K. Murai, *Lepton asymmetric universe*, *JCAP* **08** (2022) 041 [`2203.09713`].

[233] I.M. Oldengott and D.J. Schwarz, *Improved constraints on lepton asymmetry from the cosmic microwave background*, *EPL* **119** (2017) 29001 [`1706.01705`].

[234] F. Gao, J. Harz, C. Hati, Y. Lu, I.M. Oldengott and G. White, *Baryogenesis and first-order QCD transition with gravitational waves from a large lepton asymmetry*, `2407.17549`.

[235] M.E. Shaposhnikov, *Possible Appearance of the Baryon Asymmetry of the Universe in an Electroweak Theory*, *JETP Lett.* **44** (1986) 465.

[236] M.E. Shaposhnikov, *Baryon Asymmetry of the Universe in Standard Electroweak Theory*, *Nucl. Phys. B* **287** (1987) 757.

[237] N. Turok and J. Zadrozny, *Electroweak baryogenesis in the two doublet model*, *Nucl. Phys. B* **358** (1991) 471.

[238] A.E. Nelson, D.B. Kaplan and A.G. Cohen, *Why there is something rather than nothing: Matter from weak interactions*, *Nucl. Phys. B* **373** (1992) 453.

[239] M. Trodden, *Electroweak baryogenesis*, *Rev. Mod. Phys.* **71** (1999) 1463 [`hep-ph/9803479`].

[240] J.M. Cline, K. Kainulainen and M. Trott, *Electroweak Baryogenesis in Two Higgs Doublet Models and B meson anomalies*, *JHEP* **11** (2011) 089 [`1107.3559`].

[241] X. Gan, A.J. Long and L.-T. Wang, *Electroweak sphaleron with dimension-six operators*, *Phys. Rev. D* **96** (2017) 115018 [`1708.03061`].

[242] J. de Vries, M. Postma, J. van de Vis and G. White, *Electroweak Baryogenesis and the Standard Model Effective Field Theory*, *JHEP* **01** (2018) 089 [`1710.04061`].

[243] M.I. Dias Astros, *CP-Violation in the inert doublet model: Dark Matter and Baryogenesis*, 2022.

[244] N.G. Deshpande and E. Ma, *Pattern of Symmetry Breaking with Two Higgs Doublets*, *Phys. Rev. D* **18** (1978) 2574.

[245] R. Barbieri, L.J. Hall and V.S. Rychkov, *Improved naturalness with a heavy Higgs: An Alternative road to LHC physics*, *Phys. Rev. D* **74** (2006) 015007 [`hep-ph/0603188`].

[246] L. Lopez Honorez, E. Nezri, J.F. Oliver and M.H.G. Tytgat, *The Inert Doublet Model: An Archetype for Dark Matter*, *JCAP* **02** (2007) 028 [`hep-ph/0612275`].

[247] L. Lopez Honorez and C.E. Yaguna, *The inert doublet model of dark matter revisited*, *JHEP* **09** (2010) 046 [`1003.3125`].

[248] L. Lopez Honorez and C.E. Yaguna, *A new viable region of the inert doublet model*, *JCAP* **01** (2011) 002 [`1011.1411`].

[249] I.F. Ginzburg, K.A. Kanishev, M. Krawczyk and D. Sokolowska, *Evolution of Universe to the present inert phase*, *Phys. Rev. D* **82** (2010) 123533 [`1009.4593`].

[250] T.A. Chowdhury, M. Nemevsek, G. Senjanovic and Y. Zhang, *Dark Matter as the Trigger of Strong Electroweak Phase Transition*, *JCAP* **02** (2012) 029 [`1110.5334`].

[251] D. Borah and J.M. Cline, *Inert Doublet Dark Matter with Strong Electroweak Phase Transition*, *Phys. Rev. D* **86** (2012) 055001 [1204.4722].

[252] G. Gil, P. Chankowski and M. Krawczyk, *Inert Dark Matter and Strong Electroweak Phase Transition*, *Phys. Lett. B* **717** (2012) 396 [1207.0084].

[253] M. Gustafsson, S. Rydbeck, L. Lopez-Honorez and E. Lundstrom, *Status of the Inert Doublet Model and the Role of multileptons at the LHC*, *Phys. Rev. D* **86** (2012) 075019 [1206.6316].

[254] A. Arhrib, Y.-L.S. Tsai, Q. Yuan and T.-C. Yuan, *An Updated Analysis of Inert Higgs Doublet Model in light of the Recent Results from LUX, PLANCK, AMS-02 and LHC*, *JCAP* **06** (2014) 030 [1310.0358].

[255] N. Blinov, J. Kozaczuk, D.E. Morrissey and C. Tamarit, *Electroweak Baryogenesis from Exotic Electroweak Symmetry Breaking*, *Phys. Rev. D* **92** (2015) 035012 [1504.05195].

[256] N. Blinov, S. Profumo and T. Stefaniak, *The Electroweak Phase Transition in the Inert Doublet Model*, *JCAP* **07** (2015) 028 [1504.05949].

[257] A. Ilnicka, M. Krawczyk and T. Robens, *Inert Doublet Model in light of LHC Run I and astrophysical data*, *Phys. Rev. D* **93** (2016) 055026 [1508.01671].

[258] A. Belyaev, G. Cacciapaglia, I.P. Ivanov, F. Rojas-Abatte and M. Thomas, *Anatomy of the Inert Two Higgs Doublet Model in the light of the LHC and non-LHC Dark Matter Searches*, *Phys. Rev. D* **97** (2018) 035011 [1612.00511].

[259] J. Kalinowski, W. Kotlarski, T. Robens, D. Sokolowska and A.F. Zarnecki, *Benchmarking the Inert Doublet Model for e^+e^- colliders*, *JHEP* **12** (2018) 081 [1809.07712].

[260] Y.-L.S. Tsai, V.Q. Tran and C.-T. Lu, *Confronting dark matter co-annihilation of Inert two Higgs Doublet Model with a compressed mass spectrum*, *JHEP* **06** (2020) 033 [1912.08875].

[261] J. Kalinowski, T. Robens, D. Sokolowska and A.F. Zarnecki, *IDM Benchmarks for the LHC and Future Colliders*, *Symmetry* **13** (2021) 991 [2012.14818].

[262] B. Grzadkowski, O.M. Ogreid, P. Osland, A. Pukhov and M. Purmohammadi, *Exploring the CP-Violating Inert-Doublet Model*, *JHEP* **06** (2011) 003 [1012.4680].

[263] M. Krawczyk, N. Darvishi and D. Sokolowska, *The Inert Doublet Model and its extensions*, *Acta Phys. Polon. B* **47** (2016) 183 [1512.06437].

[264] A. Cordero-Cid, J. Hernández-Sánchez, V. Keus, S. Moretti, D. Rojas-Ciofalo and D. Sokołowska, *Collider signatures of dark CP-violation*, *Phys. Rev. D* **101** (2020) 095023 [2002.04616].

[265] I. Baldes and G. Servant, *High scale electroweak phase transition: baryogenesis \& symmetry non-restoration*, *JHEP* **10** (2018) 053 [1807.08770].

[266] P. Meade and H. Ramani, *Unrestored Electroweak Symmetry*, *Phys. Rev. Lett.* **122** (2019) 041802 [1807.07578].

[267] A. Glioti, R. Rattazzi and L. Vecchi, *Electroweak Baryogenesis above the Electroweak Scale*, *JHEP* **04** (2019) 027 [1811.11740].

[268] O. Matsedonskyi and G. Servant, *High-Temperature Electroweak Symmetry Non-Restoration from New Fermions and Implications for Baryogenesis*, *JHEP* **09** (2020) 012 [2002.05174].

[269] N. Benincasa, L. Delle Rose, K. Kannike and L. Marzola, *Multi-step phase transitions and gravitational waves in the inert doublet model*, *JCAP* **12** (2022) 025 [2205.06669].

[270] M. Dine, P. Huet, R.L. Singleton, Jr and L. Susskind, *Creating the baryon asymmetry at the electroweak phase transition*, *Phys. Lett. B* **257** (1991) 351.

[271] A.G. Cohen and D.B. Kaplan, *Thermodynamic Generation of the Baryon Asymmetry*, *Phys. Lett. B* **199** (1987) 251.

[272] A.G. Cohen and D.B. Kaplan, *SPONTANEOUS BARYOGENESIS*, *Nucl. Phys. B* **308** (1988) 913.

[273] A.G. Cohen, D.B. Kaplan and A.E. Nelson, *Spontaneous baryogenesis at the weak phase transition*, *Phys. Lett. B* **263** (1991) 86.

[274] M. Dine, P. Huet and R.L. Singleton, Jr., *Baryogenesis at the electroweak scale*, *Nucl. Phys. B* **375** (1992) 625.

[275] A. Azatov and M. Vanvlasselaer, *Bubble wall velocity: heavy physics effects*, *JCAP* **01** (2021) 058 [2010.02590].

[276] A. Azatov, M. Vanvlasselaer and W. Yin, *Baryogenesis via relativistic bubble walls*, *JHEP* **10** (2021) 043 [2106.14913].

[277] M. Mangano, ed., *Physics at the FCC-hh, a 100 TeV pp collider*, 1710.06353.

[278] A. Celis, J. Fuentes-Martin, A. Vicente and J. Virto, *DsixTools: The Standard Model Effective Field Theory Toolkit*, *Eur. Phys. J. C* **77** (2017) 405 [1704.04504].

[279] J. Fuentes-Martin, P. Ruiz-Femenia, A. Vicente and J. Virto, *DsixTools 2.0: The Effective Field Theory Toolkit*, *Eur. Phys. J. C* **81** (2021) 167 [2010.16341].

[280] S. Banerjee, F. Boudjema, N. Chakrabarty, G. Chalons and H. Sun, *Relic density of dark matter in the inert doublet model beyond leading order: The heavy mass case*, *Phys. Rev. D* **100** (2019) 095024 [1906.11269].

[281] J. de Blas, J.C. Criado, M. Perez-Victoria and J. Santiago, *Effective description of general extensions of the Standard Model: the complete tree-level dictionary*, *JHEP* **03** (2018) 109 [1711.10391].

[282] C. Delaunay, C. Grojean and J.D. Wells, *Dynamics of Non-renormalizable Electroweak Symmetry Breaking*, *JHEP* **04** (2008) 029 [0711.2511].

[283] F. Goertz, *Electroweak Symmetry Breaking without the μ^2 Term*, *Phys. Rev. D* **94** (2016) 015013 [1504.00355].

[284] A. Pukhov, E. Boos, M. Dubinin, V. Edneral, V. Ilyin, D. Kovalenko et al., *CompHEP: A Package for evaluation of Feynman diagrams and integration over multiparticle phase space*, hep-ph/9908288.

[285] CompHEP collaboration, *CompHEP 4.4: Automatic computations from Lagrangians to events*, *Nucl. Instrum. Meth. A* **534** (2004) 250 [hep-ph/0403113].

[286] A. Pukhov, *CalcHEP 2.3: MSSM, structure functions, event generation, batchs, and generation of matrix elements for other packages*, hep-ph/0412191.

[287] A. Belyaev, N.D. Christensen and A. Pukhov, *CalcHEP 3.4 for collider physics within and beyond the Standard Model*, *Comput. Phys. Commun.* **184** (2013) 1729 [1207.6082].

[288] S. Bruggisser, T. Konstandin and G. Servant, *CP-violation for Electroweak Baryogenesis from Dynamical CKM Matrix*, *JCAP* **11** (2017) 034 [`1706.08534`].

[289] E.K. Akhmedov, *Neutrino physics*, in *ICTP Summer School in Particle Physics*, pp. 103–164, 6, 1999 [`hep-ph/0001264`].

[290] T. Kajita, *Nobel Lecture: Discovery of atmospheric neutrino oscillations*, *Rev. Mod. Phys.* **88** (2016) 030501.

[291] A.B. McDonald, *Nobel Lecture: The Sudbury Neutrino Observatory: Observation of flavor change for solar neutrinos*, *Rev. Mod. Phys.* **88** (2016) 030502.

[292] R.N. Mohapatra et al., *Theory of neutrinos: A White paper*, *Rept. Prog. Phys.* **70** (2007) 1757 [`hep-ph/0510213`].

[293] M.C. Gonzalez-Garcia and M. Maltoni, *Phenomenology with Massive Neutrinos*, *Phys. Rept.* **460** (2008) 1 [`0704.1800`].

[294] A.G. Akeroyd, M. Aoki and H. Sugiyama, *Probing Majorana Phases and Neutrino Mass Spectrum in the Higgs Triplet Model at the CERN LHC*, *Phys. Rev. D* **77** (2008) 075010 [`0712.4019`].

[295] I. Esteban, M.C. Gonzalez-Garcia, M. Maltoni, T. Schwetz and A. Zhou, *The fate of hints: updated global analysis of three-flavor neutrino oscillations*, *JHEP* **09** (2020) 178 [`2007.14792`].

[296] T2K collaboration, *Measurements of neutrino oscillation parameters from the T2K experiment using 3.6×10^{21} protons on target*, *Eur. Phys. J. C* **83** (2023) 782 [`2303.03222`].

[297] NOvA collaboration, *Improved measurement of neutrino oscillation parameters by the NOvA experiment*, *Phys. Rev. D* **106** (2022) 032004 [`2108.08219`].

[298] I. Esteban, M.C. Gonzalez-Garcia, M. Maltoni, I. Martinez-Soler and T. Schwetz, *Updated fit to three neutrino mixing: exploring the accelerator-reactor complementarity*, *JHEP* **01** (2017) 087 [`1611.01514`].

[299] I. Esteban, M.C. Gonzalez-Garcia, A. Hernandez-Cabezudo, M. Maltoni and T. Schwetz, *Global analysis of three-flavour neutrino oscillations: synergies and tensions in the determination of θ_{23}, δ_{CP}, and the mass ordering*, *JHEP* **01** (2019) 106 [`1811.05487`].

[300] L. Wolfenstein, *Neutrino Oscillations in Matter*, *Phys. Rev. D* **17** (1978) 2369.

[301] S.P. Mikheyev and A.Y. Smirnov, *Resonance Amplification of Oscillations in Matter and Spectroscopy of Solar Neutrinos*, Sov. J. Nucl. Phys. **42** (1985) 913.

[302] KATRIN collaboration, *Direct neutrino-mass measurement with sub-electronvolt sensitivity*, *Nature Phys.* **18** (2022) 160 [2105.08533].

[303] S. Brieden, H. Gil-Marín and L. Verde, *Model-agnostic interpretation of 10 billion years of cosmic evolution traced by BOSS and eBOSS data*, *JCAP* **08** (2022) 024 [2204.11868].

[304] ACT collaboration, *The Atacama Cosmology Telescope: DR6 Gravitational Lensing Map and Cosmological Parameters*, *Astrophys. J.* **962** (2024) 113 [2304.05203].

[305] DESI collaboration, *DESI 2024 VI: Cosmological Constraints from the Measurements of Baryon Acoustic Oscillations*, 2404.03002.

[306] F.T. Avignone, III, S.R. Elliott and J. Engel, *Double Beta Decay, Majorana Neutrinos, and Neutrino Mass*, *Rev. Mod. Phys.* **80** (2008) 481 [0708.1033].

[307] KAMLAND-ZEN collaboration, *Search for Majorana Neutrinos near the Inverted Mass Hierarchy Region with KamLAND-Zen*, *Phys. Rev. Lett.* **117** (2016) 082503 [1605.02889].

[308] GERDA collaboration, *Final Results of GERDA on the Search for Neutrinoless Double-β Decay*, *Phys. Rev. Lett.* **125** (2020) 252502 [2009.06079].

[309] H.V. Klapdor-Kleingrothaus, A. Dietz, H.L. Harney and I.V. Krivosheina, *Evidence for neutrinoless double beta decay*, *Mod. Phys. Lett. A* **16** (2001) 2409 [hep-ph/0201231].

[310] H.V. Klapdor-Kleingrothaus, I.V. Krivosheina, A. Dietz and O. Chkvorets, *Search for neutrinoless double beta decay with enriched Ge-76 in Gran Sasso 1990-2003*, *Phys. Lett. B* **586** (2004) 198 [hep-ph/0404088].

[311] H.V. Klapdor-Kleingrothaus and I.V. Krivosheina, *The evidence for the observation of 0nu beta beta decay: The identification of 0nu beta beta events from the full spectra*, *Mod. Phys. Lett. A* **21** (2006) 1547.

[312] Y.G. Zdesenko, F.A. Danevich and V.I. Tretyak, *Has neutrinoless double beta decay of Ge-76 been really observed?*, *Phys. Lett. B* **546** (2002) 206.

[313] C.E. Aalseth et al., *Comment on 'Evidence for neutrinoless double beta decay'*, *Mod. Phys. Lett. A* **17** (2002) 1475 [`hep-ex/0202018`].

[314] F. Feruglio, A. Strumia and F. Vissani, *Neutrino oscillations and signals in beta and 0nu2beta experiments*, *Nucl. Phys. B* **637** (2002) 345 [`hep-ph/0201291`].

[315] B. Schwingenheuer, *Status and prospects of searches for neutrinoless double beta decay*, *Annalen Phys.* **525** (2013) 269 [`1210.7432`].

[316] W. Rodejohann, *Neutrino-less Double Beta Decay and Particle Physics*, *Int. J. Mod. Phys. E* **20** (2011) 1833 [`1106.1334`].

[317] S.M. Bilenky and C. Giunti, *Neutrinoless Double-Beta Decay: a Probe of Physics Beyond the Standard Model*, *Int. J. Mod. Phys. A* **30** (2015) 1530001 [`1411.4791`].

[318] S. Weinberg, *Cosmological Production of Baryons*, *Phys. Rev. Lett.* **42** (1979) 850.

[319] K.S. Babu, S. Nandi and Z. Tavartkiladze, *New Mechanism for Neutrino Mass Generation and Triply Charged Higgs Bosons at the LHC*, *Phys. Rev. D* **80** (2009) 071702 [`0905.2710`].

[320] F. Bonnet, D. Hernandez, T. Ota and W. Winter, *Neutrino masses from higher than d=5 effective operators*, *JHEP* **10** (2009) 076 [`0907.3143`].

[321] I. Picek and B. Radovcic, *Novel TeV-scale seesaw mechanism with Dirac mediators*, *Phys. Lett. B* **687** (2010) 338 [`0911.1374`].

[322] R. Cepedello, M. Hirsch and J.C. Helo, *Lepton number violating phenomenology of d = 7 neutrino mass models*, *JHEP* **01** (2018) 009 [`1709.03397`].

[323] G. Anamiati, O. Castillo-Felisola, R.M. Fonseca, J.C. Helo and M. Hirsch, *High-dimensional neutrino masses*, *JHEP* **12** (2018) 066 [`1806.07264`].

[324] Y. Cai, T. Han, T. Li and R. Ruiz, *Lepton Number Violation: Seesaw Models and Their Collider Tests*, *Front. in Phys.* **6** (2018) 40 [`1711.02180`].

[325] E. Ma, *Pathways to naturally small neutrino masses*, *Phys. Rev. Lett.* **81** (1998) 1171 [`hep-ph/9805219`].

[326] P. Minkowski, $\mu \to e\gamma$ *at a Rate of One Out of* 10^9 *Muon Decays?*, *Phys. Lett. B* **67** (1977) 421.

[327] T. Yanagida, *Horizontal gauge symmetry and masses of neutrinos*, *Conf. Proc. C* **7902131** (1979) 95.

[328] R.N. Mohapatra and G. Senjanovic, *Neutrino Mass and Spontaneous Parity Nonconservation*, *Phys. Rev. Lett.* **44** (1980) 912.

[329] M. Gell-Mann, P. Ramond and R. Slansky, *Complex Spinors and Unified Theories*, *Conf. Proc. C* **790927** (1979) 315 [`1306.4669`].

[330] J. Schechter and J.W.F. Valle, *Neutrino Masses in SU(2) x U(1) Theories*, *Phys. Rev. D* **22** (1980) 2227.

[331] A. Melfo, M. Nemevsek, F. Nesti, G. Senjanovic and Y. Zhang, *Type II Seesaw at LHC: The Roadmap*, *Phys. Rev. D* **85** (2012) 055018 [`1108.4416`].

[332] M. Mitra, S. Niyogi and M. Spannowsky, *Type-II Seesaw Model and Multilepton Signatures at Hadron Colliders*, *Phys. Rev. D* **95** (2017) 035042 [`1611.09594`].

[333] Y. Du, A. Dunbrack, M.J. Ramsey-Musolf and J.-H. Yu, *Type-II Seesaw Scalar Triplet Model at a 100 TeV pp Collider: Discovery and Higgs Portal Coupling Determination*, *JHEP* **01** (2019) 101 [`1810.09450`].

[334] R. Primulando, J. Julio and P. Uttayarat, *Scalar phenomenology in type-II seesaw model*, *JHEP* **08** (2019) 024 [`1903.02493`].

[335] S. Mandal, O.G. Miranda, G. Sanchez Garcia, J.W.F. Valle and X.-J. Xu, *Toward deconstructing the simplest seesaw mechanism*, *Phys. Rev. D* **105** (2022) 095020 [`2203.06362`].

[336] R. Foot, H. Lew, X.G. He and G.C. Joshi, *Seesaw Neutrino Masses Induced by a Triplet of Leptons*, *Z. Phys. C* **44** (1989) 441.

[337] Z.-j. Tao, *Radiative seesaw mechanism at weak scale*, *Phys. Rev. D* **54** (1996) 5693 [`hep-ph/9603309`].

[338] E. Ma, *Verifiable radiative seesaw mechanism of neutrino mass and dark matter*, *Phys. Rev. D* **73** (2006) 077301 [`hep-ph/0601225`].

[339] A. Zee, *A Theory of Lepton Number Violation, Neutrino Majorana Mass, and Oscillation*, *Phys. Lett. B* **93** (1980) 389.

[340] A. Zee, *Quantum Numbers of Majorana Neutrino Masses*, *Nucl. Phys. B* **264** (1986) 99.

[341] K.S. Babu, *Model of 'Calculable' Majorana Neutrino Masses*, *Phys. Lett. B* **203** (1988) 132.

[342] Y. Cheng, X.-G. He, F. Huang, J. Sun and Z.-P. Xing, *Electroweak precision tests for triplet scalars*, *Nucl. Phys. B* **989** (2023) 116118 [`2208.06760`].

[343] N. Craig, *Naturalness: past, present, and future*, *Eur. Phys. J. C* **83** (2023) 825 [`2205.05708`].

[344] SINDRUM collaboration, *Search for the Decay $\mu^+ \to e^+e^+e^-$*, *Nucl. Phys. B* **299** (1988) 1.

[345] K. Hayasaka et al., *Search for Lepton Flavor Violating Tau Decays into Three Leptons with 719 Million Produced Tau+Tau- Pairs*, *Phys. Lett. B* **687** (2010) 139 [`1001.3221`].

[346] BaBar collaboration, *Searches for Lepton Flavor Violation in the Decays $\tau^+ \to e^+\gamma$ and $\tau^+ \to \mu^+\gamma$*, *Phys. Rev. Lett.* **104** (2010) 021802 [`0908.2381`].

[347] MEG collaboration, *Search for the lepton flavour violating decay $\mu^+ \to \mathrm{e}^+\gamma$ with the full dataset of the MEG experiment*, *Eur. Phys. J. C* **76** (2016) 434 [`1605.05081`].

[348] Particle Data Group collaboration, *Review of Particle Physics*, *Phys. Rev. D* **98** (2018) 030001.

[349] S. Bhattacharya, S. Jana and S. Nandi, *Neutrino Masses and Scalar Singlet Dark Matter*, *Phys. Rev. D* **95** (2017) 055003 [`1609.03274`].

[350] K. Ghosh, S. Jana and S. Nandi, *Neutrino Mass Generation at TeV Scale and New Physics Signatures from Charged Higgs at the LHC for Photon Initiated Processes*, *JHEP* **03** (2018) 180 [`1705.01121`].

[351] T. Ghosh, S. Jana and S. Nandi, *Neutrino mass from Higgs quadruplet and multicharged Higgs searches at the LHC*, *Phys. Rev. D* **97** (2018) 115037 [`1802.09251`].

[352] D. Aristizabal Sierra and M. Hirsch, *Experimental tests for the Babu-Zee two-loop model of Majorana neutrino masses*, *JHEP* **12** (2006) 052 [`hep-ph/0609307`].

[353] E. Akhmedov, *Majorana neutrinos and other Majorana particles:Theory and experiment*, (2014) [`1412.3320`].

[354] M. Nebot, J.F. Oliver, D. Palao and A. Santamaria, *Prospects for the Zee-Babu Model at the CERN LHC and low energy experiments*, *Phys. Rev. D* **77** (2008) 093013 [`0711.0483`].

[355] D. Schmidt, T. Schwetz and H. Zhang, *Status of the Zee–Babu model for neutrino mass and possible tests at a like-sign linear collider*, *Nucl. Phys. B* **885** (2014) 524 [`1402.2251`].

[356] K.S. Babu and C. Macesanu, *Two loop neutrino mass generation and its experimental consequences*, *Phys. Rev. D* **67** (2003) 073010 [`hep-ph/0212058`].

[357] K.L. McDonald and B.H.J. McKellar, *Evaluating the two loop diagram responsible for neutrino mass in Babu's model*, `hep-ph/0309270`.

[358] J. Herrero-Garcia, M. Nebot, N. Rius and A. Santamaria, *The Zee–Babu model revisited in the light of new data*, *Nucl. Phys. B* **885** (2014) 542 [`1402.4491`].

[359] F. Jegerlehner and A. Nyffeler, *The Muon g-2*, *Phys. Rept.* **477** (2009) 1 [`0902.3360`].

[360] Muon g-2 collaboration, *Measurement of the Positive Muon Anomalous Magnetic Moment to 0.46 ppm*, *Phys. Rev. Lett.* **126** (2021) 141801 [`2104.03281`].

[361] Muon g-2 collaboration, *Measurement of the Positive Muon Anomalous Magnetic Moment to 0.20 ppm*, *Phys. Rev. Lett.* **131** (2023) 161802 [`2308.06230`].

[362] A. Jueid, T.A. Chowdhury, S. Nasri and S. Saad, *Probing Zee-Babu states at muon colliders*, *Phys. Rev. D* **109** (2024) 075011 [`2306.01255`].

[363] J. Bernabeu, A. Pich and A. Santamaria, *CP Phases in the Charged Current and Higgs Sectors for Majorana Neutrinos*, *Z. Phys. C* **30** (1986) 213.

[364] G. Steigman, B. Dasgupta and J.F. Beacom, *Precise Relic WIMP Abundance and its Impact on Searches for Dark Matter Annihilation*, *Phys. Rev. D* **86** (2012) 023506 [1204.3622].

[365] ATLAS collaboration, *Search for doubly charged Higgs boson production in multi-lepton final states with the ATLAS detector using proton–proton collisions at $\sqrt{s} = 13$ TeV*, *Eur. Phys. J. C* **78** (2018) 199 [1710.09748].

[366] S.P. Maharathy and M. Mitra, *Type-II see-saw at $\mu+\mu-$ collider*, *Phys. Lett. B* **844** (2023) 138105 [2304.08732].

[367] R. Padhan, D. Das, M. Mitra and A. Kumar Nayak, *Probing doubly and singly charged Higgs bosons at the pp collider HE-LHC*, *Phys. Rev. D* **101** (2020) 075050 [1909.10495].

[368] J.F. Navarro, C.S. Frenk and S.D.M. White, *A Universal density profile from hierarchical clustering*, *Astrophys. J.* **490** (1997) 493 [astro-ph/9611107].

[369] M. Cirelli, G. Corcella, A. Hektor, G. Hutsi, M. Kadastik, P. Panci et al., *PPPC 4 DM ID: A Poor Particle Physicist Cookbook for Dark Matter Indirect Detection*, *JCAP* **03** (2011) 051 [1012.4515].

[370] D. Maurin, F. Melot and R. Taillet, *A database of charged cosmic rays*, *Astron. Astrophys.* **569** (2014) A32 [1302.5525].

[371] AMS collaboration, *The Alpha Magnetic Spectrometer (AMS) on the international space station: Part II — Results from the first seven years*, *Phys. Rept.* **894** (2021) 1.

[372] S. Schael et al., *AMS-100: The next generation magnetic spectrometer in space – An international science platform for physics and astrophysics at Lagrange point 2*, *Nucl. Instrum. Meth. A* **944** (2019) 162561 [1907.04168].

[373] ATLAS collaboration, *Combination of searches for invisible decays of the Higgs boson using 139 fb−1 of proton-proton collision data at s=13 TeV collected with the ATLAS experiment*, *Phys. Lett. B* **842** (2023) 137963 [2301.10731].

[374] A. Arhrib, R. Benbrik, M. Chabab, G. Moultaka, M.C. Peyranere, L. Rahili et al., *The Higgs Potential in the Type II Seesaw Model*, *Phys. Rev. D* **84** (2011) 095005 [1105.1925].

[375] S. Kanemura, Y. Okada, E. Senaha and C.P. Yuan, *Higgs coupling constants as a probe of new physics*, *Phys. Rev. D* **70** (2004) 115002 [hep-ph/0408364].

[376] D. Bečirević, E. Bertuzzo, O. Sumensari and R. Zukanovich Funchal, *Can the new resonance at LHC be a CP-Odd Higgs boson?*, *Phys. Lett. B* **757** (2016) 261 [1512.05623].

[377] A. Barroso, P.M. Ferreira, I.P. Ivanov and R. Santos, *Metastability bounds on the two Higgs doublet model*, *JHEP* **06** (2013) 045 [1303.5098].

[378] K. Kannike, *Vacuum Stability Conditions From Copositivity Criteria*, *Eur. Phys. J. C* **72** (2012) 2093 [1205.3781].

[379] D. Goncalves, P.A.N. Machado and J.M. No, *Simplified Models for Dark Matter Face their Consistent Completions*, *Phys. Rev. D* **95** (2017) 055027 [1611.04593].

[380] HFLAV collaboration, *Averages of b-hadron, c-hadron, and τ-lepton properties as of 2018*, *Eur. Phys. J. C* **81** (2021) 226 [1909.12524].

[381] M. Misiak, A. Rehman and M. Steinhauser, *Towards $\overline{B} \to X_s\gamma$ at the NNLO in QCD without interpolation in m_c*, *JHEP* **06** (2020) 175 [2002.01548].

[382] T. Biekötter, D. Fontes, M. Mühlleitner, J.C. Romão, R. Santos and J.a.P. Silva, *Impact of new experimental data on the C2HDM: the strong interdependence between LHC Higgs data and the electron EDM*, *JHEP* **05** (2024) 127 [2403.02425].

[383] G. Arcadi, G. Busoni, D. Cabo-Almeida and N. Krishnan, *Is there a (Pseudo)Scalar at 95 GeV?*, 2311.14486.

[384] H.E. Haber and D. O'Neil, *Basis-independent methods for the two-Higgs-doublet model III: The CP-conserving limit, custodial symmetry, and the oblique parameters S, T, U*, *Phys. Rev. D* **83** (2011) 055017 [1011.6188].

[385] S. Kanemura, Y. Okada, H. Taniguchi and K. Tsumura, *Indirect bounds on heavy scalar masses of the two-Higgs-doublet model in light of recent Higgs boson searches*, *Phys. Lett. B* **704** (2011) 303 [1108.3297].

[386] A.J. Buras, *Weak Hamiltonian, CP violation and rare decays*, in *Les Houches Summer School in Theoretical Physics, Session 68: Probing the Standard Model of Particle Interactions*, pp. 281–539, 6, 1998 [`hep-ph/9806471`].

[387] A. Denner and S. Dittmaier, *Electroweak Radiative Corrections for Collider Physics*, *Phys. Rept.* **864** (2020) 1 [`1912.06823`].